A Numerical Study of the Effect of Viscoelasticity on Cavitation and Bubble Dynamics

Steven John Lind [1]
Supervised by Prof. T. N. Phillips

July 14, 2010

[1]Department of Mathematics, Cardiff University, CF24 4AG, United Kingdom

Acknowledgements

First and foremost I wish to thank my supervisor, Professor Tim Phillips, for his support and guidance over the course of my studies. Your door has always been open and I very much appreciate everything you have done. It has been both a pleasure and privilege working with you.

I also want to thank Dr. Oliver Harlen and Prof. Russell Davies for agreeing to examine this thesis.

I gratefully acknowledge the funding I received from the Engineering and Physical Sciences Research Council of the United Kingdom, through grant EP/C513037.

I wish to thank the members of the Fluids Group at Cardiff for providing such an active and stimulating research environment, and in particular Dr. Peter Bollada, for the many helpful discussions over the last few years.

To all those who have ever worked in and around M/2.05 over the last few years, thank you for making Cardiff such an enjoyable place to work.

Finally, to my family and Laura, thank you for your unwavering support and encouragement. I never tell you enough how much you all mean to me. This thesis is dedicated to you all.

DECLARATION

This work has not previously been accepted in substance for any degree and is not concurrently submitted in candidature for any degree.

Signed ..... Date .....

STATEMENT 1

This thesis is being submitted in partial fulfillment of the requirements for the degree of PhD.

Signed ..... Date .....

STATEMENT 2

This thesis is the result of my own independent work/investigation, except where otherwise stated. Other sources are acknowledged by explicit references.

Signed ..... Date .....

STATEMENT 3

I hereby give consent for my thesis, if accepted, to be available for photocopying and for inter-library loan, and for the title and summary to be made available to outside organisations.

Signed ..... Date .....

Summary

In this thesis two different models and numerical methods have been developed to investigate the dynamics of bubbles in viscoelastic fluids. In the interests of gaining crucial initial insights, a simplified system of governing equations is first considered. The ambient fluid around the bubble is considered incompressible and the flow irrotational. Viscoelastic effects are included through the normal stress balance at the bubble surface. The governing equations are then solved using a boundary element method. With regard to spherical bubble collapse, the model captures the behaviour seen in other studies, including the damped oscillation of the bubble radius with time and the existence of an elastic-limit solution. The model is extended in order to investigate multi-bubble dynamics near a rigid wall and a free surface. It is found that viscoelastic effects can prevent jet formation, produce cusped bubble shapes, and generally prevent the catastrophic collapse that is seen in the inviscid cases.

The model is then used to investigate the role of viscoelasticity in the dynamics of rising gas bubbles. The dynamics of bubbles rising in a viscoelastic liquid are characterised by three phenomena: the trailing edge cusp, negative wake, and the rise velocity jump discontinuity. The model predicts the cusp at the trailing end of a rising bubble to a high resolution. However, the irrotational assumption precludes the prediction of the negative wake. The corresponding absence of the jump discontinuity supports the hypothesis that the negative wake is primarily responsible for the jump discontinuity, as mooted in previous studies.

A second model is developed with the intention of gaining further insight into the role of viscoelasticity and corroborating the findings of the first model. This second model employs the full compressible governing equations in a two dimensional domain. The equations are solved using the spectral element method, while the two phases are represented by "marker particles". The results are in qualitative agreement with the first model and confirm that the findings presented are a faithful account of bubble dynamics in viscoelastic fluids.

Contents

List of Figures

Chapter 1

Introduction

1.1 Motivation

This thesis is concerned with the development of numerical methods to investigate the dynamics of bubbles in viscoelastic fluids. When a body of liquid is heated under constant pressure, or when its pressure is reduced at a constant temperature; vapour and/or gas filled bubbles can form and grow. The latter process of rupturing a fluid by a decrease in pressure is often called cavitation [29]. The occurrence of bubbles in Nature and industry is innumerable and their role in fluid systems is one of fundamental importance. A few example industrial systems are combustion engines, pipelines, pumps, and distillation columns [124]. In medicine and biology, bubbles are important in ultrasound [166] and shock-wave lithotripsy [51, 85] procedures. In Nature, besides the world's oceans and rivers being natural bubbly flows, bubbles are utilised by living organisms such as the snapping shrimp in subduing their prey [96].

Many of the fluids in such systems are best described by non-Newtonian, and in particular, viscoelastic models. This is especially true of common biological and industrial fluids such as blood, oils, and lubricants. Briefly, viscoelastic fluids are those which possess characteristics of both the elastic solid and viscous fluid. In 1867 Maxwell first proposed a mathematical model for a viscoelastic material. By combining the concepts of the ideal elastic solid proposed by Hooke (1676) with the ideal viscous fluid proposed by Newton (1687), Maxwell derived the well-known constitutive equation

$$\lambda \frac{\partial \mathbf{T}}{\partial t} + \mathbf{T} = \mu \dot{\boldsymbol{\gamma}}, \tag{1.1}$$

relating the stress $\mathbf{T}$ to the rate of strain (or rate of deformation) $\dot{\boldsymbol{\gamma}}$. The constants of proportionality μ and λ are called the viscosity and relaxation time, respectively. The relaxation time is an important property of viscoelastic materials and, broadly speaking, provides an order of magnitude estimate of the time it takes for the stress to relax to some limiting value. Physically, the relaxation time is associated with the rate at which structures within the material change their configurations. In the case of water the relaxation time is approximately 10^{-12}s, while that of low density polyethylene is about 10s. It is often the case, for example in polymeric liquids, that there will be a range of time constants associated with a range of polymer molecule configurations, and consequently the fluid will have a spectrum of relaxation times. Due to their complex structure, in reality few viscoelastic materials obey the simple linear relationship proposed by Maxwell, particularly in flows with large deformations. In a landmark paper, Oldroyd [109] discussed the use of frame invariant rheological models, suitable for application to all conditions of motion and stress. This set up the framework for the development of non-linear constitutive equations and, to this day, ever more sophisticated rheological models are being proposed to better describe viscoelastic flow behaviour.

The dynamics of viscoelastic fluids are interesting and varied, and can differ greatly from Newtonian fluids. One can then expect the behaviour of bubbles within a viscoelastic fluid to differ drastically from a Newtonian fluid. Despite their prevalence and more interesting dynamics, bubbles in viscoelastic fluids have received little attention compared to their Newtonian counterparts. Theoretical and numerical studies are, in the most part, restricted to spherical bubble dynamics and the solution of the governing non-linear ODE. In reality, bubbles rarely remain spherical. While a multitude of numerical methods have been developed to simulate non-spherical Newtonian dynamics, numerical studies into non-spherical viscoelastic dynamics are sadly lacking. The bubble dynamic process which receives the greatest attention in this thesis is arguably the most important and interesting; that of bubble collapse.

1.2 Bubble Collapse and Cavitation Damage

Bubble collapse occurs implosively and is a catastrophic phenomenon producing high pressures, velocities, temperatures, loud noises and even light [29]. As a result of

such high pressures and velocities, bubble collapse can cause substantial damage to nearby surfaces; so called cavitation damage. As stated by Knapp et al. [84]: "Cavitation is a most unpleasant hydrodynamic phenomenon, whose harmful effects are both widespread and obvious and seriously handicap many phases of science and engineering". Figure 1.1 shows images of a propeller which has succumbed to cavitation damage.

Figure 1.1: Cavitation damage on a propeller blade[1].

One of the first studies of cavitation damage was under commission from the British Admiralty, which wanted research carried out to determine the cause of damage to ship propellers. It was reported that damage was due to "hydraulic blows" to the blades from collapsing cavitation bubbles [18]. The first serious theoretical study of cavitation was undertaken by Lord Rayleigh in 1917 [126]. Considering the collapse of a spherical void in an infinite bath of fluid, it was shown that collapse created high pressures and velocities in close proximity to the bubble surface. For fifty years the development of high pressures was seen as a sufficient reason for cavitation damage. It was not until the pioneering experimental work of Benjamin and Ellis [9] in 1966, that it was realised a more complex dynamic occurred. During collapse near a wall the bubble no longer remains spherical. In fact a high speed liquid jet forms, which can penetrate and thread the bubble and impact upon the wall. The resulting bubble can then have a toroidal form. A simple diagrammatic representation of this process is given in Figure 1.2

Jet velocities during bubble collapse can typically reach 100ms^{-1} [86, 138]. It was subsequently proposed that the impact of this liquid jet upon a nearby surface was the

[1]Picture available for reuse under licence, see http://creativecommons.org/licenses/by-sa/2.5/deed.en

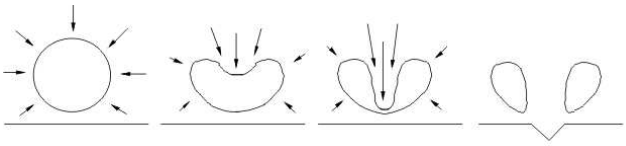

Figure 1.2: Sketch of jet formation and impact during collapse near a rigid wall - and the possible damage that results.

primary mechanism for cavitation damage [158]. More recently it was found that, following jet impact, the subsequent toroidal dynamics can produce large pressure shock waves, which also contribute to cavitation damage [115]. The proposed source of these shock waves is a "splashing effect", which arises from the collision of fluid from the liquid jet with the oppositely directed flow [151]. Hence, whether acting directly or indirectly, jet formation is a major factor in the creation of cavitation damage. Cavitation damage remains a subject of intense research due to its prevalence in many different processes. These include shockwave lithotripsy (cavitation damage can occur on internal organs during the procedure [51]), the flow around hydrofoils [47] and journal bearings [44] (both of which can succumb to cavitation damage) and interestingly, the snapping shrimp (their snapping claw produces bubbles which collapse, stunning their prey [96]).

1.3 Numerical Approaches in the Modelling of Bubble Dynamics

Bubble dynamics falls under the broader subject of multi-phase flows; the bubble is comprised of one phase (gas or vapour), while the ambient fluid comprises of another (liquid). One need not dwell on the importance of multi-phase flows, but their incredible prevalence means that they have been a subject of intense research for decades. Short of analytical solutions but for the simplest cases, a multitude of numerical methods have been developed to simulate their dynamics. Broadly speaking, the numerical methods can be split into two groups; fixed (Eulerian) mesh techniques or moving (Lagrangian) mesh techniques. The main methods within these two groups, and their relative merits, will be briefly discussed.

1.3.1 Eulerian Techniques

Since the computational mesh is fixed, additional functions need to be defined to trace fluid boundaries. These functions can be designed and implemented in such a way as to capture large deformations and coalescence/splitting with ease. The are two distinct approaches - surface tracking methods and volume tracking methods.

Surface Tracking

Surface tracking methods specify a set of marker points or use height functions to describe the surface explicitly. Extensively used techniques include the front tracking method of Unverdi and Tryggvason [156] and the level set method of Osher and Sethian [111]. The front tracking method and the level set method are typically applied in "one-fluid" methods. Briefly, all phases are governed by one set of governing equations with densities and viscosities varying appropriately for each phase (for example the density of the region describing the bubble should be less than the ambient fluid). The front tracking method specifies a series of marker points on the bubble surface. The surface is well defined but the sharp change in variables across the surface is smoothed as information is passed on to the fixed grid. The level set method defines a function ϕ that is zero on the boundary, positive in one phase, and negative in the other. Since the function is advected with the flow and the boundary, ϕ will theoretically retain these values indefinitely. The set of points such that $\phi = 0$ defines the position of the surface, but as with the front tracking method, smoothing is required over the interface when passing information onto the fixed grid. The advantage the level-set method has over the front tracking method is that no special treatment is required when interfaces meet. In the former the interface needs to be reconstructed accordingly, while for the latter the interface is always defined by $\phi = 0$. The level set method, however, suffers from poor mass conservation, with mass being spuriously created or destroyed, especially under significant topological changes of the interface.

The MAC method, originally of Harlow and Welch [64], is not dissimilar to the front tracking method in the respect that the surface is traced by advected marker points. However, marker points are also distributed throughout the fluid bulk, and so the method can be considered more a volume tracking technique rather than surface tracking. Here marker points indicate the position of the fluid interface on the grid and so where the free surface boundary conditions can be applied. In the original implemen-

tation, the free surface boundary conditions were included in a crude manner as no detail regarding the form of the free surface could be deduced (only its whereabouts on the grid). However, this has since been considerably refined. For example, Popinet and Zaleski [121] in their finite volume study, interpolate such marker points using cubic splines - producing a well defined surface allowing for an accurate implementation of the boundary conditions.

Volume Tracking

The most commonly used volume tracking techniques are variations and extensions of the well known "volume of fluid" method (VOF). A volume fraction parameter, f (sometimes called a colour function), is assigned to each of the grid cells such that it is full of liquid if $f = 1$, is empty if $f = 0$, and partially full if $0 < f < 1$. The function f is then calculated at subsequent time steps using an advection equation. As with the level set method, the major benefit is its ability to deal with large deformations and changes in topology without any additional effort. The volume fraction f is simply updated using the advection equation to determine what portion of fluid is in each grid cell. The major problem is that the interface is not explicitly described. There have been a number of methods which infer the interface geometry in a variety of ways, including SLIC (simple line interface calculation), PLIC (piecewise linear interface construction) and ELVIRA (efficient least squares VOF interface reconstruction algorithm). However such techniques can lead to unwanted smoothing of the surface, i.e. "numerical surface tension". Consequently the accuracy of surface tension forces can be significantly affected. Though traditionally used in conjunction with finite difference grids, VOF methods have also been used with finite element methods, see for example [103]. The main benefit of doing so is that boundary conditions on the interface can be implemented in a more natural and physical way using appropriately shaped elements along fluid interfaces. "One fluid" finite difference methods typically accommodate such conditions through an additional body force term in the equation of motion. Different methods exist for calculating this body force, such as the CSF (continuum surface force) method, but these inevitably require smoothing the force over a finite interface.

The marker particle (MP) method of Rider and Kothe [128] bears a semblance to

both the volume of fluid and MAC method. In a similar manner to VOF, a colour function C is updated using the usual advection equation. However, instead of directly tracking volume, massless marker particles are tracked. Each particle is assigned a particular "colour" depending upon the phase in which it resides. Since a particle of fluid will remain of that fluid type (assuming no change in phase), a particle will keep its colour indefinitely. Within fluid-fluid interface regions, where two (or more) differently coloured sets of marker particles reside, an average is taken of the surrounding particles to determine an interpolated colour at the point in question. To accurately describe the different phases, the whole computational domain is filled with a high density of these marker particles, with each being updated to a new position every time step. An obvious disadvantage compared to VOF methods is the additional computational cost in tracking such a large number of particles. The main advantages include the ease of implementation, the trivial extension to compressible flows, and the minimal numerical diffusion of the colour function over time (particle information is never lost). Furthermore, the method retains the VOF's ability to deal with large deformations and topology changes automatically.

1.3.2 Lagrangian and Semi-Lagrangian Techniques

Alternatively, one can eliminate the need for additional phase defining functions through the employment of a moving or Lagrangian mesh technique. Defining the surface of the bubble or drop to be the boundary of the computational domain, one can solve the governing equations and update the mesh to determine the evolution in bubble shape. Generally such an approach allows an accurate implementation of the stress boundary conditions between phases, which is indeed necessary to complete the system of governing equations. In most cases however, and in contrast to many one-field Eulerian models, the gas/vapour phase is not explicitly modelled (but its influence can still be exerted through the boundary conditions).

Finite element methods are a popular choice in solving such moving mesh problems due to their flexibility in handling irregular geometries. However, a limitation of Lagrangian techniques is the development of large distortions in the mesh, as it deforms with the flow. To prevent stretching and distortion of the mesh, and subsequent onset of numerical instability, substantial remeshing has to be undertaken. Appropriate remeshing can be difficult and can itself introduce additional errors in the solution. The Arbitrary Lagrangian Eulerian (ALE) method attempts to alleviate mesh distortion,

by mapping the advecting physical domain onto a computational domain. The computational domain is moved with a velocity that can be different from that of the flow. This allows its deformation to be controlled, enabling it to stay relatively structured even though the physical domain is heavily distorted [124]. In two or more dimensions, Lagrangian and semi-Lagrangian techniques can be quite tricky to implement. Boundary element methods (BEM) have been very popular in describing multiphase flows as the dimensionality of the problem is effectively reduced by one. Not only is this more computationally efficient, but updating and redistributing the mesh is easier to implement. Consequently, BEM methods are adept in handling large flow deformations. However, boundary element methods are best reserved for the numerical solution of linear PDE's. Though it is possible to extend BEM to non-linear equations - this will inevitably involve some domain calculations [59]. As a result, boundary element methods are well suited to solving incompressible and irrotational flows (governed by Laplace's equation: $\nabla^2\phi = 0$), and Stokes flows ($\nabla \cdot \boldsymbol{\sigma} = 0$). The use of boundary element methods in solving Stokes' equation for bubble and drop problems has been investigated by Khayat [75], for example. Khayat looks at several industrial processes, such as cavity flow in polymer solutions with moving boundaries [75] (the polymeric liquid under study is assumed to be of Jeffrey's type), drop deformation in confined flow [76], and extrusion of a viscous fluid through a solid cylinder [77]. Though able to describe extremely slow or viscous flows [43], the Stokes approximation cannot be used to describe high speed cavitation phenomena, such as jet formation and bubble collapse.

In previous studies of non-spherical bubble collapse, the application of Laplace's equation has proven most successful. The problem was first tackled by Plesset and Chapman [119] who assumed an inviscid, incompressible and irrotational fluid, and solved Laplace's equation using a finite difference method. Blake et al. [19] then solved the same model problem using the more efficient and accurate boundary element method. Following experimental observations, axisymmetry was also assumed. Their results show the production of the liquid jet (up until the point of impact upon the lower bubble surface) and bear good agreement with experiment. Subsequent developments to the model include a cubic spline representation of the boundary and the surface functions [46], the inclusion of non-condensible bubble contents [11], the simulation of bursting of bubbles near free surfaces [26], and fully 3D calculations [122,167]. Best [10] also extended the theory to study the dynamics of the toroidal bubble created after the

liquid jet penetrates the cavity. Subsequent numerical studies of the toroidal splashing effect have been reported in [151]. These studies have all assumed the fluid around the bubble to be inviscid. There is a common misconception that an irrotational flow implies an inviscid fluid. Importantly, and as recently stressed by Joseph [70], this is certainly not the case.

1.4 The Direction of this Thesis

In the interests of gaining some crucial insights into viscoelastic bubble dynamics, a simplified system of governing equations is first considered. Given the success of the irrotational boundary element method in describing inviscid bubble collapse, the first course of action is to extend the method to include viscoelastic effects. The assumption is that the viscoelastic (and viscous) effects are important only in the immediate proximity of the bubble surface, with the ambient fluid flow remaining irrotational. This model will allow a valuable and unique insight into dynamics, as well as provide a particularly good approximation to inertia dominated flows, such as jet formation. In such flows viscous/viscoelastic effects are important only in thin boundary layers near the bubble surface.

Indeed, the irrotational flow approximation has provided some very satisfactory results for a range of viscous/viscoelastic bubble and drop phenomena. As mentioned, an irrotational flow does not imply an inviscid fluid; viscous, and indeed viscoelastic effects, still reside and can appear through the boundary conditions. This is a fact that has been reemphasised in a number of recent papers by Joseph and co-workers (see for example [70]). The ability of viscous/viscoelastic irrotational flows to provide good approximations to full solutions arises from the small amount of vorticity generated at the bubble's shear stress-free free surface. As stated by Batchelor [7] p. 366, there is only a small variation in velocity across the boundary layer, and energy dissipation is dominated by the external irrotational flow. Studies where viscous and viscoelastic potential flows have been particularly fruitful are in the study of rising bubbles in viscous liquids [88, 106, 107], capillary instabilities in viscous [56] and Maxwell fluids [57], and in the Rayleigh-Taylor instability of viscoelastic drops [71]. Furthermore, such potential flow approximations are not necessarily restricted to high Reynolds numbers. An analysis of spherical cap bubbles using a viscous potential flow approximation gives

excellent agreement with experiment for Reynolds numbers as low as $Re = 0.1$ [69]. Similarly, agreement between experiment and potential flow calculations for viscous rising bubbles are fairly good for even for $Re \sim O(1)$ [70].

Such is the dearth of numerical research into viscoelastic bubble dynamics, and particularly bubble collapse, that employing an irrotational assumption and solving the simplified system is an important first step. This approach was recommended independently by Brujan [32]. With regard to simulating bubble collapse near rigid boundaries in viscoelastic fluids, Brujan suggests the model proposed here; employing an irrotational approximation in the bulk with viscoelastic effects included at the bubble surface.

Besides being able to provide a faithful approximation to many bubble phenomena, the model can be used to provide other unique and useful insights into viscoelastic bubble dynamics. In particular, the model allows one to ascertain the relative importance of surface and bulk viscoelastic effects, and also (in situations where they are known to occur) the importance of wake structures on dynamics, which are prevented under the irrotational approximation.

The overall aim of the model is to provide valuable and accessible initial insights into bubble dynamics in viscoelastic fluids, using an effective and efficient numerical method. It is an important first step in the development of more sophisticated models.

Following this first venture, and given that the potential flow approximation does preclude an exacting account of the role of viscoelasticity, a second model and numerical method is then developed to describe bubble dynamics in viscoelastic fluids. The intention is to gain further insight into the role of viscoelasticity, but also to support the findings of the boundary element study. Now both the bubble and the ambient fluid are directly modelled, and the full governing equations are solved over the whole fluid domain. Whereas the boundary element method is a fully Lagrangian technique, the second method is (mostly) Eulerian. It is a one-field model with the *compressible* equations of motion being solved on an Eulerian grid using the spectral element method. Compressibility is necessary, given that the fluid within the bubble is now explicitly modelled and requires the ability to change volume during collapse. It is also well known that during collapse compressibility effects can be important in the am-

bient fluid, particularly in the final stages, when collapse velocities are non-negligible compared to the speed of sound [30]. Necessarily, a suitable constitutive equation for compressible viscoelastic fluids will also be discussed. The multiphase description to be employed is the marker particle method described in the previous section. As mentioned, particular benefits of the scheme include the ease of implementation, the trivial extension to compressible flows, the minimal numerical diffusion of the colour function over time, and the ability to deal with large deformations and topology changes automatically.

While particularly good quantitative agreement between the two models is not to be expected (given the notable differences), the extent of their qualitative agreement will be discussed.

1.5 The Outline of this Thesis

This thesis is structured as follows: Chapter 2 introduces the first mathematical model and describes the numerical solution of the governing equations. The numerical scheme is validated through comparison with available analytical solutions. The dynamics of spherical bubble collapse in viscoelastic fluids is discussed and the predictions of the model compared with those of the literature. The majority of the work in this chapter has been published in the Journal of Non-Newtonian Fluid Mechanics [94].

Chapter 3 utilises the model of Chapter 2 and investigates the role of viscoelasticity in the collapse of a bubble near a rigid wall/boundary. The numerical scheme is validated through the comparisons with the results for the inviscid case, which are available in the literature. Viscous and viscoelastic effects are then included and the subsequent dynamics discussed. A version of this chapter has been submitted to Theoretical and Computational Fluid Dynamics [92].

Chapter 4 extends the work of Chapter 3 and looks at the dynamics of two bubbles near a rigid boundary. For in reality bubbles rarely form in single configurations but as a part of large bubble clouds. Consequently, an understanding of the bubble-bubble interaction when near a wall is important.

Chapter 5 investigates the dynamics of a single bubble near a free surface. This is another important situation, particularly in biological applications, where bubbles form near flexible membranes and tissue. Bubble collapse near such surfaces can then result in cell and tissue damage. Furthermore, a study of the role of viscoelasticity is important, as many biological fluids (e.g. blood, plasma) are viscoelastic in nature. A version of this chapter is in preparation for submission to the Journal of Fluid Mechanics [91].

Chapter 6 investigates the dynamics of gas bubbles rising in viscoelastic fluids. It is a fundamental problem of great importance and has received much attention from experimentalists. The dynamics are drastically different to their Newtonian counterparts. Viscoelastic phenomena includes the formation of trailing end cusps, a negative wake, and a jump in the rise velocity for bubbles over a certain volume. The aim is to resolve the debate in the literature over the cause of this "velocity jump discontinuity" seen in experiment. The irrotational assumption precludes the formation of the negative wake, allowing important insights into the dynamics. Much of the work in this chapter is to appear in a paper that has been accepted for publication in the Journal of Non-Newtonian Fluid Mechanics [90].

In Chapter 7, we return to the problem of bubble collapse near a wall. Here however the full compressible governing equations are solved using a spectral element method. A volume-of-fluid-like scheme called the marker particle method is used to track and distinguish the bubble and ambient fluid phases. The results are compared with those of Chapter 3 with the aim of corroborating the previous findings and gaining more insight into the effect of viscoelasticity on cavitation dynamics. A version of this chapter is in preparation for submission to the Journal of Computational Physics [93].

In Chapter 8, the conclusions of the thesis are presented. This includes a summary of the findings, a critical analysis of the numerical methods, and the possibilities for further research.

Chapter 2

Spherical Bubble Collapse in Viscoelastic Fluids

2.1 Introduction

As mentioned in Chapter 1, the dynamics of cavitation bubbles play a crucial role in many different areas of science, medicine and engineering. The importance is reflected in the plethora of studies, both experimental and theoretical, that are available in the literature. Cavitation processes occur frequently in non-Newtonian fluids in industry and in medicine. Given their importance, an understanding of spherical bubble dynamics is an essential first port of call.

2.1.1 The Rayleigh-Plesset Equation

The Rayleigh-Plesset equation is the non-linear ordinary differential equation governing the dynamics of a spherical bubble in a Newtonian fluid. First derived for the inviscid case by Lord Rayleigh [126], with viscous effects introduced by Plesset [120], it can be readily derived by considering the Naiver-Stokes equations in spherical polar co-ordinates.

Consider a spherical bubble of radius $R(t)$, in an infinite domain of fluid with a pressure $p_\infty(t)$ at infinity. The fluid is considered incompressible with a constant density ρ and viscosity μ. It is assumed the bubble contents are homogenous and the pressure $p_b(t)$ uniform. In the spherically symmetric geometry, the Navier-Stokes equations are given by

$$\rho\frac{\partial u}{\partial t}+\rho u\frac{\partial u}{\partial t}=-\frac{\partial p}{\partial r}+\mu\left(\frac{1}{r^2}\frac{\partial}{\partial r}(r^2\frac{\partial u}{\partial r})-\frac{2u}{r^2}\right). \tag{2.1}$$

Conservation of mass requires that

$$u(r,t)=\frac{F(t)}{r^2}. \tag{2.2}$$

In the case of zero mass transfer across the surface, $u(R,t)=dR/dt=\dot{R}$ and so $F(t)=R^2\dot{R}$. This can be shown to be a good approximation even when evaporation or condensation occurs at the interface [29]. Therefore, (2.2) can be written as

$$u(r,t)=\frac{R^2\dot{R}}{r^2}. \tag{2.3}$$

Substituting (2.3) into (2.1) and integrating gives

$$\frac{2R\dot{R}^2+R^2\ddot{R}}{r}-\frac{R^4\dot{R}^2}{2r^4}=\frac{p-p_\infty}{\rho}, \tag{2.4}$$

using the fact that $p\to p_\infty$ when $r\to\infty$.

Now consider the stress boundary condition on the bubble fluid interface: the resultant stress on an infinitely thin lamina radially outwards is given by

$$(\sigma_{rr})_{r=R}+p_b-\frac{2S}{R}, \tag{2.5}$$

where p_b is the pressure inside the bubble and S the surface tension. In the absence of mass transfer, this stress must be zero and hence

$$p=p_b+4\mu\frac{\dot{R}}{R}-\frac{2S}{R}. \tag{2.6}$$

(Since $\sigma_{rr}=-p+2\mu\frac{\partial u}{\partial r}$) Finally, substituting (2.6) into (2.4) gives the Rayleigh-Plesset equation; a description of spherical bubble dynamics in a Newtonian fluid:

$$R\ddot{R}+\frac{3}{2}\dot{R}^2+4\mu\frac{\dot{R}}{R}+\frac{2S}{R}=\frac{p_b-p_\infty}{\rho}. \tag{2.7}$$

For the inviscid case ($\mu=0$), if one neglects surface tension ($S=0$) then (2.7) can be integrated in time to give the form derived by Rayleigh [126]:

$$\dot{R} = \left(\frac{2(p_\infty - p_b)}{3\rho} \left(\frac{R_0^3}{R^3} - 1 \right) \right)^{1/2}. \tag{2.8}$$

From this one can derive the collapse time t_c for a spherical cavity in an inviscid incompressible fluid (the time it takes for $R \to 0$), to give

$$t_c = R_0 \left(\frac{\rho}{6(p_\infty - p_b)} \right)^{1/2} \frac{\Gamma(5/6)\Gamma(1/2)}{\Gamma(4/3)} \approx 0.91468 R_0 \left(\frac{\rho}{(p_\infty - p_b)} \right)^{1/2}. \tag{2.9}$$

The inviscid collapse time t_c allows important comparisons to be made and is a useful time scale for bubble collapse phenomena.

The Rayleigh-Plesset equation (2.7) is a second order, non-linear ODE that can be solved in a straightforward manner using standard numerical techniques. Using a fourth-order Runge-Kutta scheme, the numerical solution of (2.7) can be obtained for different values of viscosity μ (see Fig. 2.1). The effects of surface tension are neglected ($S = 0$) in the interest of determining the effects of fluid rheology on dynamics.

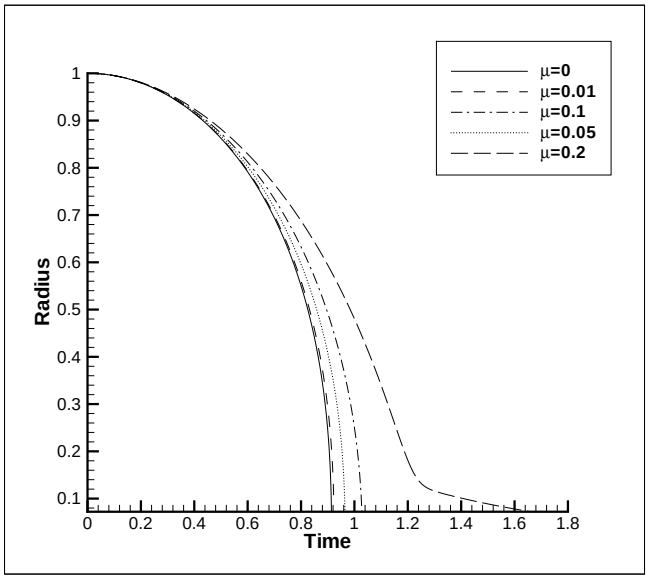

Figure 2.1: Numerical solution of the Rayleigh-Plesset equation for different viscosities.

As expected intuitively, an increase in viscosity results in an increase in the collapse time; the dynamics being increasingly damped in the presence of increasing viscous forces.

2.1.2 Viscoelastic Spherical Bubble Dynamics

In a similar manner to the Newtonian case, a general Rayleigh-Plesset equation can be derived given a general equation of motion with an extra stress tensor $\mathbf{T}$. The spherical symmetry of the system means that all shear stress components are zero and that $T_{\theta\theta} = T_{\varphi\varphi}$. Consequently, the equation of motion is given by

$$\rho\left(\frac{\partial u}{\partial t} + u\frac{\partial u}{\partial r}\right) = -\frac{\partial p}{\partial r} + \left(\frac{\partial T_{rr}}{\partial r} + \frac{2(T_{rr} - T_{\theta\theta})}{r}\right). \tag{2.10}$$

The stress balance on the bubble/fluid surface (again neglecting surface tension) is given by

$$p = p_b + T_{rr}. \tag{2.11}$$

Furthermore, it is commonly assumed that the extra stress tensor is trace free ($T_{ii} = 0$), allowing the stress components to be written in terms of T_{rr} only. Subsequent integration of (2.10) between R and ∞ gives the generalised Rayleigh-Plesset equation:

$$R\ddot{R} + \frac{3}{2}\dot{R}^2 = \frac{p_b - p_\infty}{\rho} - \frac{3}{\rho}\int_R^\infty \frac{T_{rr}}{r}dr \tag{2.12}$$

A primary characteristic of spherical bubble collapse (or expansion) in most viscoelastic fluids, is the damped oscillation of the bubble radius in time. This intuitive effect is due to the competition between inertial, viscous and elastic forces - and occurs only in fluids with characteristically large elasticities, such as the Maxwell and Oldroyd models (it is consequently not seen in a second order fluid [50]).

Many authors have noted this and other effects by solving a generalised Rayleigh-Plesset equation for a range of different constitutive relations. Fogler and Goddard [54] undertook one of the first theoretical studies of collapse in a viscoelastic medium, using a Rayleigh-Plesset equation to solve the problem of a collapsing spherical cavity in a linear Maxwell fluid. For a range of Reynolds and Deborah numbers, the viscoelastic Rayleigh-Plesset equation was solved using finite difference methods. Their results show for very large Deborah numbers the bubble will either oscillate about an equilibrium radius, or collapse without oscillation, depending on some critical value. The important finding of the study is that elasticity in the liquid can significantly retard the collapse of a void and produce large oscillatory motion whenever the relaxation time of the fluid is of the same order of magnitude as the Rayleigh collapse time. Later,

the Jeffreys model was investigated by Ellis and Ting [50] and also Tanasawa and Yang [148]. Again, the oscillation of the bubble radius in time was predicted. It was also noted that, due to the presence of elasticity, viscous damping effects on collapse are less in a viscoelastic fluid than in a purely viscous Newtonian fluid.
More recently Kim [78] investigated collapse in an upper convected Maxwell fluid, and solved the appropriate Rayleigh-Plesset equation using a 1D finite element method. The study notes the "highly oscillatory behaviours observed for moderate to high De". Additionally, it was observed that collapse is faster in the early stages, but slower in the later stages; remarking that this retardation could suppress catastrophic collapse and reduce cavitation damage in viscoelastic fluids.
Many other studies on spherical viscoelastic bubbles exist in the literature. Fogler and Goddard [53] and Allen and Roy [2] have investigated bubble dynamics in an Oldroyd fluid, but with applications to acoustics. Hence, frequency forcing terms were included in the models to study bubble oscillation. Brujan [30] considered the influence of compressibility on the spherical collapse of a bubble in a Jeffreys fluid. The study showed that rebound and the period of oscillation during collapse are significantly less than in the incompressible case, as energy is lost through sound radiation. The important thing to note is that, despite the subtle differences in each study, each one captures the essential viscoelastic dynamics - the damped oscillation of the radius with time.

The Rayleigh-Plesset equation is restrictive in the sense that its solution describes only spherical dynamics. However, some of the most important bubble dynamic processes, such as jet formation, are non-spherical (yet still axisymmetric [19]). In this chapter we present the first of two numerical methods developed in the study of non-spherical viscoelastic bubble collapse. Under the assumption of irrotationality and incompressibility, the mass continuity equation is solved using an axisymmetric boundary element method. An equation of motion is then formulated in terms of a generalised Bernoulli equation. Although developed with the ultimate intention of simulating non-spherical dynamics, in this chapter we present the details of the numerical scheme and its predictions for spherical bubble dynamics only. Non-spherical investigations are reserved for the subsequent chapters. The model is shown to describe all the important spherical phenomena observed in the literature for the well-studied Maxwell fluid. The dynamics of more complicated constitutive equations are also investigated using this method.

In Section 2, the mathematical model and governing equations are presented. In Section 3 the numerical technique for solving the governing equations is described. Then in Section 4, some numerical results are presented for several viscoelastic models detailing the influence of the Deborah and Reynolds numbers on bubble dynamics. Conclusions to the study are presented in Section 5.

2.2 Mathematical Model and Governing Equations

Consider a spherical bubble of initial radius R_0 in an infinite expanse of fluid. Let the fluid domain be labelled Ω with the fluid boundary, or equivalently the bubble surface, labelled $\partial\Omega$. A description of fluid and bubble dynamics can be determined by solution of the equations governing fluid motion; the conservation of mass

$$\frac{D\rho}{Dt} + \rho\nabla \cdot \mathbf{u} = 0, \tag{2.13}$$

and the conservation of momentum,

$$\rho\frac{D\mathbf{u}}{Dt} = -\nabla p + \nabla \cdot \mathbf{T}. \tag{2.14}$$

Here ρ is the fluid density, $\mathbf{u}$ the velocity, p the pressure and $\mathbf{T}$ is the extra stress tensor.

As noted in the theoretical studies of Brujan [30, 31], the effects of compressibility can be important, particularly in the late stages of collapse, when bubble interface velocities become non-negligible compared to the speed of sound in the liquid. Despite this, we follow the majority of other works in the literature, and assume only a small fraction of bubble kinetic energy is radiated away as sound, and so impose incompressibility. Hence the conservation of mass (Equation (2.13)) reduces to,

$$\nabla \cdot \mathbf{u} = 0. \tag{2.15}$$

As stated in Chapter 1, in the interests of gaining some crucial initial insights into viscoelastic bubble dynamics, a simplified system of governing equations is considered. As suggested by Brujan [32], the fluid flow is assumed to be irrotational,

$$\nabla \times \mathbf{u} = 0, \tag{2.16}$$

with viscous and viscoelastic effects included at the bubble surface. Besides allowing

a valuable and unique insight into dynamics, this assumption can provide a faithful approximation, especially in the modelling of inertia dominated phenomena such as jet formation. In such cases it is well known that viscous effects are important only in thin boundary layers near surfaces [7]. The fluid outside of these boundary layers behaves as if it is inviscid and the flow is irrotational. Similarly, in the case of viscoelastic fluids, Beard and Walters [8] and Denn [45] assume such an (effectively) inviscid external flow in their study of viscoelastic boundary layers. In the case of bubbles (and drops), the shear stress-free free surface generates little vorticity and so flow within the boundary layer is only slightly perturbed from irrotationality [7]. Thus, to a good approximation, the bulk of the fluid can be modelled as (effectively) inviscid and irrotational, with viscous and viscoelastic effects appearing through the normal stress boundary condition at the bubble interface.

This approximation has proven extremely fruitful in many studies of viscous and viscoelastic drop and bubble dynamics. These include the study of rising bubbles in viscous liquids [88, 106, 107], capillary instabilities in viscous [56] and Maxwell fluids [57], and in the Rayleigh-Taylor instability of viscoelastic (Oldroyd B) drops [71]. Due to the complexity of some problems, several studies necessarily employ the boundary element method (BEM) in their viscous potential flow solution. Georgescu et al. [60] and Boulton-Stone and co-workers [25, 26] undertake a viscous potential flow study of a bursting bubble near a free surface, with the results of the former showing good agreement with experiment. Similarly Rush and Nadim [135] use a viscous potential BEM in their study of viscous drop oscillation; as do Canot and Davoust [40] in their study of viscous buoyant bubbles near walls. Evidently, the viscous/viscoelastic potential flow approximation has provided a successful description of many multiphase systems, and in many cases gives excellent agreement with experiment.

The success of the description is due to reduced vorticity generation at the free surface, compared to the corresponding no-slip surface. Consequently, not only can the irrotationality of the ambient fluid be maintained, but the potential flow can provide a better than expected approximation at lower Reynolds numbers. An analysis of spherical cap bubbles using a viscous potential flow approximation gives excellent agreement with experiment for Reynolds numbers as low as $Re = 0.1$ [69]. Similarly, agreement between experiment and potential flow calculations for rising bubbles are fairly good

for even for $Re \sim O(1)$ [70].

Besides being able to provide a faithful approximation to many bubble phenomena, the model can be used to provide other unique insights into viscoelastic bubble dynamics. This includes information on the relative importance of surface and bulk viscoelastic effects, and also (in situations where they are known to occur) the importance of wake structures on dynamics, which are prevented under the irrotational approximation. In any case, the model will provide a valuable and accessible first insight into problems that notoriously require complex numerical implementations and excessive computational resources.

The spherical symmetry of the problems studied in this chapter means that the flow is inherently irrotational. However, the analysis presented here is kept completely general and is applicable to any irrotational flow and to non-spherical dynamics. In the interests of primarily studying the viscoelastic effects, the following assumptions are also made: the effects of gravity are negligible and the bubble contents are comprised of a uniform vapour or gas.

Following the assumptions of incompressibility and irrotationality, it follows from the conservation of mass that there exists a velocity potential ϕ which satisfies Laplace's equation:

$$\nabla^2 \phi = 0, \tag{2.17}$$

in the region Ω, exterior to the bubble. By Greens theorem, there exists an integral solution to (2.17), defined in terms of the boundary integral [113]

$$c(\mathbf{p})\phi(\mathbf{p}) = \int_{\partial\Omega} \left(\frac{\partial \phi}{\partial n}(\mathbf{q}) G(\mathbf{p}, \mathbf{q}) - \phi(\mathbf{q}) \frac{\partial G}{\partial n}(\mathbf{p}, \mathbf{q}) \right) dS \tag{2.18}$$

where the constant $c(\mathbf{p})$ is given by

$$c(\mathbf{p}) = \begin{cases} 2\pi & \text{if } \mathbf{p} \in \partial\Omega, \\ 4\pi & \text{if } \mathbf{p} \in \Omega \backslash \partial\Omega \end{cases}$$

In 3D, the Greens function $G(\mathbf{p}, \mathbf{q})$ is given by

$$G(\mathbf{p}, \mathbf{q}) = \frac{1}{|\mathbf{p} - \mathbf{q}|}. \tag{2.19}$$

As mentioned, the boundary $\partial\Omega$ represents the bubble surface. Hence the bubble is represented by a void in the fluid domain Ω and is not explicitly modelled. In reality, bubbles will never be complete voids or vacuums, hence any dynamics associated with the bubble contents are introduced artificially through the boundary conditions on the bubble surface (as in the Rayleigh-Plesset equation).

Given an initial potential ϕ_0 on the bubble surface $\partial\Omega$, the integral equation (2.18) can be solved numerically (details of which will be given later) for the normal velocity to the surface $\frac{\partial\phi}{\partial n}$. The tangential velocity $\frac{\partial\phi}{\partial s}$ can be calculated given the potential ϕ_0, and the surface geometry $\partial\Omega$. Hence the velocity on the surface is completely described. Fluid particles with position vector $\mathbf{x}$ initially on the surface $\partial\Omega$ will remain there. Consequently, the surface can be updated in a Lagrangian manner according to

$$\frac{D\mathbf{x}}{Dt} = \nabla\phi, \quad \mathbf{x} \in \partial\Omega. \tag{2.20}$$

To update the potential ϕ we require an appropriate equation of motion. For an irrotational velocity field $\mathbf{u} = \nabla\phi$, the conservation of momentum (Eqn. (2.14)) can be rewritten as

$$\nabla\left(\rho\frac{\partial\phi}{\partial t} + \frac{\rho}{2}|\nabla\phi|^2 + p\right) = \nabla \cdot \mathbf{T}. \tag{2.21}$$

Hence one can formulate an irrotational equation of motion (a generalised Bernoulli equation) provided that

$$\nabla \cdot \mathbf{T} = \nabla\psi, \tag{2.22}$$

for some real scalar function ψ. So, assuming such a function exists, a Bernoulli equation (of motion) results from the integration of (2.21),

$$\rho\frac{\partial\phi}{\partial t} + \frac{\rho}{2}|\nabla\phi|^2 + p - \psi = C(t). \tag{2.23}$$

Equation (2.22) is not satisfied for general constitutive equations in general irrotational flows [72]. In this study, viscous and viscoelastic effects are confined to the bubble surface. The bulk contribution is negligible in comparison (i.e. $\nabla \cdot \mathbf{T} = 0$) and so the condition on the stress (Eqn. (2.22)) is satisfied by any constant ψ.

If it is assumed that $\phi, \psi \to 0$ as $\mathbf{x} \to \infty$, then by (2.23) $C(t) = p_\infty$, the pressure at infinity. On the surface of the bubble therefore, the following equation holds,

$$p(\mathbf{x}) = -\rho \frac{D\phi}{Dt} + \frac{\rho}{2}|\nabla\phi|^2 + p_\infty, \quad \mathbf{x} \in \partial\Omega. \tag{2.24}$$

Consider an infinitely thin lamina across a segment of the surface. Assuming that there is no mass transfer, the resultant forces must be zero [29] and so we have

$$p_b = -\sigma_{nn}(\mathbf{x}) + S\kappa, \tag{2.25}$$

where p_b is the pressure inside the bubble and σ_{nn} is the normal component of the normal stress vector $\boldsymbol{\sigma} \cdot \mathbf{n}$ at the point $\mathbf{x} \in \partial\Omega$. The surface tension and total curvature of the surface are given by S and κ, respectively. The fluid pressure on the surface $p(\mathbf{x})$ can now be related to the pressure p_b inside the bubble given by (2.25) through

$$p(\mathbf{x}) = p_b + T_{nn}(\mathbf{x}) - S\kappa \quad \mathbf{x} \in \partial\Omega. \tag{2.26}$$

As in Kim [78], we here choose to neglect the effect of surface tension (set $S = 0$) and focus solely on the viscoelastic effects.
Hence a dynamic boundary condition on the bubble surface is given by

$$\rho \frac{D\phi}{Dt} = \frac{\rho}{2}|\mathbf{u}|^2 - T_{nn} + p_\infty - p_b. \tag{2.27}$$

The evolution of ϕ in time can be determined using (2.27). Subsequently, the integral equation (2.18) can be solved to determine $\partial\phi/\partial n$ and hence the velocity field. The particle positions are then updated using (2.20). This serves to determine the new location of the bubble surface and the process is repeated to obtain a complete description of the bubble dynamics.

Bubble Contents

A description of the internal bubble pressure, p_b, requires some consideration. A standard approach is to assume the bubble contents are uniform and contain either some condensible vapour (see, for example, Blake et al. [19]) or non-condensible gas (Best and Kucera [11]). Condensible vapour contents can be adequately approximated by a constant bubble pressure, due to the vapour evaporation during bubble expansion and

condensation during contraction [87]. The non-condensible gas contents are commonly modelled by an adiabatic ideal gas law viz.,

$$p_b = p_v + p_0(V_0/V)^\gamma, \tag{2.28}$$

where V and V_0 are the current and initial volumes of the bubble, respectively, p_v is a constant vapour pressure, and γ is the ratio of specific heats. The presence of these contents induce oscillation in the bubble during collapse, due to the high pressures built up by the internal gas. Consequently, in this chapter we assume a simple constant vapour pressure within the bubble, so the effects of viscoelasticity on dynamics can be clearly seen.

2.2.1 Modelling Newtonian Dynamics

The extra stress tensor $\mathbf{T}$ for a Newtonian fluid is given by

$$\mathbf{T} = \mu\dot{\boldsymbol{\gamma}} = \mu\left((\nabla\mathbf{u}) + (\nabla\mathbf{u})^T\right). \tag{2.29}$$

Under the irrotational assumption, the velocity gradient is symmetric, and hence

$$\mathbf{T} = 2\mu(\nabla\mathbf{u}). \tag{2.30}$$

If the velocity gradient is then expressed in terms of boundary fitted co-ordinates (n, s), where n and s are the normal and arclength, respectively, then using the Frenet formulae, the normal-normal component of the stress T_{nn} can be expressed in the form

$$T_{nn} = 2\mu\frac{\partial^2\phi}{\partial n^2}. \tag{2.31}$$

Therefore the equation of motion for the Newtonian problem is given by

$$\rho\frac{D\phi}{Dt} = \frac{\rho}{2}|\mathbf{u}|^2 - 2\mu\frac{\partial^2\phi}{\partial n^2} + p_\infty - p_b. \tag{2.32}$$

This model has been applied to many different studies in the literature, including jet drop ejection [60], viscous buoyant bubbles near walls [40], and the oscillation of drops with viscous effects [135].

The second normal derivative can be expressed in a more tractable form by making use of Laplace's equation (2.17) expressed in boundary fitted coordinates. Considering

a cylindrical geometry, Laplace's equation can be written as

$$\frac{\partial^2\phi}{\partial n^2} + \frac{\partial^2\phi}{\partial s^2} + \mathcal{C}\frac{\partial\phi}{\partial n} + \frac{1}{r}\left(n_r\frac{\partial\phi}{\partial n} + s_r\frac{\partial\phi}{\partial s}\right) = 0, \tag{2.33}$$

where n_r, s_r are the components of the normal and tangent vectors (in the radial direction), respectively, and $\mathcal{C}$ is the in-plane curvature. On the axis of symmetry ($r = 0$), equation (2.33) becomes

$$\frac{\partial^2\phi}{\partial n^2} + 2\frac{\partial^2\phi}{\partial s^2} + 2\mathcal{C}\frac{\partial\phi}{\partial n} = 0. \tag{2.34}$$

The first normal derivative is found directly from the boundary element method, while the first and second derivatives with respect to arclength are approximated using centred differences. The second normal derivative is thus fully determined from equations (2.33) and (2.34).

As in [19], the variables are non-dimensionalised as follows. Lengths are scaled with respect to the initial bubble radius R_0,

$$r^* = \frac{r}{R_0}, \qquad z^* = \frac{z}{R_0}, \tag{2.35}$$

and time, pressure and the potential are scaled, respectively, according to

$$t^* = \frac{t}{R_0}\left(\frac{p_\infty - p_b}{\rho}\right)^{1/2}, \tag{2.36}$$

$$p^* = \frac{p - p_b}{p_\infty - p_b}, \tag{2.37}$$

$$\phi^* = \frac{\phi}{R_0}\left(\frac{\rho}{p_\infty - p_b}\right)^{1/2}. \tag{2.38}$$

This choice of non-dimensionalisation yields a Reynolds number defined by

$$Re = \frac{R_0((p_\infty - p_b)\rho)^{1/2}}{\mu}. \tag{2.39}$$

Note that our definition of Reynolds number, defined with respect to pressure not velocity, can still permit high speed flow and significant inertia at lower values. Hence the irrotational assumption can still provide a valid approximation to the flow, even if the Reynolds number defined by (2.39) is not particularly large.

So, (re-labelling dimensionless variables without asterisks) the dimensionless Newto-

nian equation of motion reads

$$\frac{D\phi}{Dt} = 1 + \frac{1}{2}|\mathbf{u}|^2 - \frac{2}{Re}\frac{\partial^2\phi}{\partial n^2}. \tag{2.40}$$

2.2.2 Modelling Viscoelastic Effects

Initially we choose to model the viscoelastic effects using the Maxwell rheological model. The reason for this is that the Maxwell model is the simplest model that provides significant elastic effects. The linear version of this model, though fundamentally applicable, is limited since it is only able to describe viscoelastic effects under small deformations [15]. For this reason, the so called "material" Maxwell model will be used to describe the viscoelastic effects. The partial time derivative in the linear model is replaced by a material derivative. This provides us with a more physically astute constitutive relation, which allows for substantial deformation. The material Maxwell model has been applied successfully in other studies of spherical viscoelastic bubble dynamics, including Brujan [30, 31] and Fogler and Goddard [54]. Perhaps the most satisfying feature of the model is that the extra stress tensor on the bubble surface can be calculated with ease, since the material derivative reduces to the ordinary time derivative in the particle reference frame. Furthermore, under the assumption of an irrotational flow, the material derivative also satisfies frame invariance. This can be seen by considering the frame invariant Jaumann derivative, which reduces to the material derivative in an irrotational flow [68].

The constitutive equation for the material Maxwell model is given by

$$\lambda\frac{D\mathbf{T}}{Dt} + \mathbf{T} = \mu\dot{\boldsymbol{\gamma}}. \tag{2.41}$$

Where λ is the relaxation time and μ the viscosity.

The choice of scaling in the previous section yields an additional dimensionless parameter associated with elastic effects: the Deborah number

$$De = \frac{\lambda}{R_0}\left(\frac{\triangle p}{\rho}\right)^{1/2}. \tag{2.42}$$

The dimensionless equation of motion is then,

$$\frac{D\phi}{Dt} = 1 + \frac{1}{2}|\mathbf{u}|^2 - T_{nn}, \tag{2.43}$$

where T_{nn} is found from the constitutive equation

$$De\frac{DT_{nn}}{Dt} + T_{nn} = \frac{1}{Re}\dot{\gamma}_{nn}. \tag{2.44}$$

It is not immediately obvious that T_{nn} satisfies the above equation, given that the boundary fitted co-ordinate system (n, s) is advected with the flow. However, it can be shown that in a general axisymmetric geometry, the material derivative of the normal vector is parallel to the tangent vector [102]. Specifically,

$$\frac{D\mathbf{n}}{Dt} = \left(\mathcal{C}\frac{\partial\phi}{\partial s} - \frac{\partial}{\partial s}\left(\frac{\partial\phi}{\partial n}\right)\right)\mathbf{s}. \tag{2.45}$$

Consequently, given the physical requirement that shear stresses are zero ($\mathbf{n}\cdot\mathbf{T}\cdot\mathbf{s} = 0$) on the bubble free surface,

$$\frac{DT_{nn}}{Dt} = \frac{D\mathbf{n}}{Dt}\cdot\mathbf{T}\cdot\mathbf{n} + \mathbf{n}\cdot\frac{D\mathbf{T}}{Dt}\cdot\mathbf{n} + \mathbf{n}\cdot\mathbf{T}\cdot\frac{D\mathbf{n}}{Dt} = \mathbf{n}\cdot\frac{D\mathbf{T}}{Dt}\cdot\mathbf{n}.$$

Equation (2.44) then follows directly from Equation (2.41).

2.3 Numerical Solution of Governing Equations

Much of the relevant phenomena in cavitation bubble dynamics, such as spherical collapse and jet formation near a boundary, is seen to be axisymmetric [19]. In making this assumption the dimensions of the problem effectively reduce from 3D to 2D, as the third dimension is treated analytically.

In terms of cylindrical polar co-ordinates ($\mathbf{p} = (r_0, 0, z_0)$, $\mathbf{q} = (r, \theta, z)$), the Green's function (2.19) can be written as

$$G(\mathbf{p}, \mathbf{q}) = \frac{1}{[(r + r_0)^2 + (z - z_0)^2 - 4rr_0\cos^2(\theta/2)]^{1/2}}, \tag{2.46}$$

and similarly,

$$\nabla G(\mathbf{p}, \mathbf{q}) = -\frac{(r\cos\theta - r_0, r\sin\theta, z - z_0)}{[(r + r_0)^2 + (z - z_0)^2 - 4rr_0\cos^2(\theta/2)]^{3/2}}. \tag{2.47}$$

The boundary $\partial\Omega$ (the bubble surface) is discretised into N segments and $N+1$ nodes, with nodes 1 and $N + 1$ lying on the axis of symmetry on the top and bottom of the bubble, respectively. The surface variables $r(s)$ and $z(s)$ and the potential $\phi(s)$, are

represented by cubic splines so that

$$q_i(s) = q_{i0} + q_{i1}(s - s_i) + q_{i2}(s - s_i)^2 + q_{i3}(s - s_i)^3, \tag{2.48}$$

for $s_i \leq s \leq s_{i+1}$, $i = 1, \ldots, N$. Note that s_i is the cumulative arclength along the surface from node 1 to i. The choice of cubic spline is essential for the accuracy of the discretisation. Given that both $\phi(s)$ and $z(s)$ are symmetric about the axis of symmetry (even variables with respect to total arclength), their first derivatives with respect to arclength are thus zero on this axis. Therefore, clamped cubic splines are used to represent these variables; enforcing zero derivatives on the axis. The variable $r(s)$ is antisymmetric (odd with respect to total arclength), and hence has a zero second derivative on the axis of symmetry. A natural cubic spline is used to represent $r(s)$ and enforce this requirement. Details on the construction of these splines can be found in Appendix A. The normal derivative of the potential $\frac{\partial \phi}{\partial n}$ is represented linearly with respect to arclength.

Following the above discretisation, the integral solution to the Laplace equation (2.18) can be written as

$$\begin{aligned} c(\mathbf{p}_i)\phi(\mathbf{p}_i) &= \sum_{j=1}^{N} \int_{s_j}^{s_{j+1}} \frac{\partial \phi}{\partial n}(s) \left(\int_0^{2\pi} G(\mathbf{p}_i, s) r(s)\, d\theta \right) ds \\ &- \sum_{j=1}^{N} \int_{s_j}^{s_{j+1}} \phi(s) \left(\int_0^{2\pi} \frac{\partial G}{\partial n}(\mathbf{p}_i, s) r(s)\, d\theta \right) ds \end{aligned} \tag{2.49}$$

The azimuthal integrations can be calculated analytically and give

$$\int_0^{2\pi} G(\mathbf{p}_i, s) r(s)\, d\theta = \frac{4 r(s) K(k(s))}{[(r(s) + r_i)^2 + (z(s) - z_i)^2]^{1/2}}, \tag{2.50}$$

$$\begin{aligned} &\int_0^{2\pi} \frac{\partial G}{\partial n} r(s)\, d\theta = \\ &-4 \frac{r}{[(r + r_i)^2 + (z - z_i)^2]^{3/2}} \left(\left[\frac{dz}{ds}(r + r_i) - \frac{dr}{ds}(z - z_i) - \frac{2 r_i}{k^2} \frac{dz}{ds} \right] \frac{E(k)}{1 - k^2} + \frac{2 r_i}{k^2} \frac{dz}{ds} K(k) \right), \end{aligned} \tag{2.51}$$

where

$$k^2(s) = \frac{4r(s)r_i}{(r(s)+r_i)^2 + (z(s)-z_i)^2}, \tag{2.52}$$

and $K(k)$ and $E(k)$ are complete elliptical integrals of the first and second kind, respectively. These integrals are approximated by

$$\tilde{K}(k) = P(1-k^2) - Q(1-k^2)\log(1-k^2), \tag{2.53}$$

$$\tilde{E}(k) = R(1-k^2) - S(1-k^2)\log(1-k^2), \tag{2.54}$$

where P, Q, R, S are tabulated polynomials [1].
Equation (2.49) can now be written as a system of $N+1$ linear equations thus,

$$c(\mathbf{p}_i)\phi_i + \sum_{j=1}^{N} A_{ij} = \sum_{j=1}^{N}(B_{ij}\psi_j + C_{ij}\psi_{j+1}), \tag{2.55}$$

$i = 1, \ldots, N+1$. Here ψ_j denotes the unknown value of the normal derivative $\frac{\partial\phi}{\partial n}$ at node j. Let $\alpha_i(s)$ and $\beta_i(s)$ denote the azimuthal integrals (2.51) and (2.50) respectively, then the remaining coefficients are

$$A_{ij} = \int_{s_j}^{s_{j+1}} \phi_j(s)\alpha_i(s)\,ds \tag{2.56}$$

$$B_{ij} = \int_{s_j}^{s_{j+1}} \frac{(s_{j+1}-s)}{\Delta s_j}\beta_i(s)\,ds \tag{2.57}$$

$$C_{ij} = \int_{s_j}^{s_{j+1}} \frac{(s-s_j)}{\Delta s_j}\beta_i(s)\,ds \tag{2.58}$$

The integrals are approximated using a 10-point Gaussian quadrature rule. A weak logarithmic singularity occurs whenever integration is done over a segment that contains the collocation point $\mathbf{p}_i$. This integration is then treated separately using a log-Gaussian quadrature rule [142]. Further details on this special treatment can be found in Appendix B.
The resulting matrix system is generally full but is very small compared to other numerical schemes. Hence Gaussian elimination is used to solve the system for ψ_j.

After solving the system (2.55) for the normal velocity, the tangential velocity is determined in order to completely describe the velocity on the surface. Given the potential

ϕ, the tangential velocity and higher derivatives are found from the finite difference formulae for non-uniform grids given in [89]. Typically a fourth or sixth order centred difference scheme is used.

With the velocity fully described on $\partial\Omega$, the bubble surface can now be evolved in a Lagrangian manner over a time step according to (2.20). Similarly, the potential is updated using the equation of motion (2.43). Both equations are integrated using a fourth-order Runge-Kutta time stepping scheme.

The constitutive equation for the extra stress (Eqn. (2.44)) is solved either using a simple backward Euler approximation (as in [76]),

$$De\left(\frac{T_{nn}(\mathbf{x}(t),t) - T_{nn}(\mathbf{x}(t-\triangle t),t-\triangle t)}{\triangle t}\right) + T_{nn}(\mathbf{x}(t),t) = \frac{1}{Re}\dot{\gamma}_{nn}(\mathbf{x}(t),t), \quad (2.59)$$

or a second-order trapezoidal approximation. Investigations have shown that results between the two discretisations are indistinguishable.
In phenomena such as bubble collapse, the velocity can increase rapidly in time. In order to capture the high speed dynamics, a variable time step is used. In particular, following Blake et al. [19], we choose

$$\Delta t = \frac{\Delta t_{max}}{\max[1 + (1/2)|\mathbf{u}|^2]}. \quad (2.60)$$

This choice ensures the time step is sufficiently small enough to capture any high speed dynamics. The value of Δt_{max} is taken to be 10^{-3} for the simulations undertaken.

At each time step, the points on the bubble surface are redistributed to ensure equal spacing with respect to arclength to prevent "bunching up" and the subsequent onset of instabilities. Such remeshing is standard procedure and is often required with Lagrangian methods.

2.4 Numerical Results and Discussion

2.4.1 Validation

Laplace Solver

To validate the Laplace solver, numerical results are compared with the analytical solution for a spherical void of radius 1, in an infinite domain with a potential $\phi = 1$ on the boundary. The exact solution is $\frac{\partial \phi}{\partial n} = -1$.

No of Segments	Linear	Splines
4	1.336×10^{-1}	1.232×10^{-3}
8	3.120×10^{-2}	7.070×10^{-5}
16	7.664×10^{-3}	4.630×10^{-6}
32	1.907×10^{-3}	5.530×10^{-7}
64	4.762×10^{-4}	3.921×10^{-7}

Table 2.1: Relative error of the normal velocity $\frac{\partial \phi}{\partial n}$ for the test case of a sphere of radius $R = 1$.

The comparison of the relative errors in the computed value of $\frac{\partial \phi}{\partial n}$ using linear surface segments and cubic splines is listed in Table 2.1. As can be seen, the use of cubic splines produces very accurate results - even at low mesh refinement. Note that the small decrease in the error from increasing the number of segments from 32 to 64, does not warrant the increase in computational time. For this reason, for the simulations undertaken in this study, 40 segments are usually used.

Inviscid Spherical Bubble Collapse

The full numerical code is compared with the analytical Rayleigh equation (2.8) for a spherical void collapsing in an infinite inviscid fluid. Setting $T_{nn} = 0$ in equation (2.27) gives the appropriate inviscid equation of motion, with which surface potential is updated

$$\frac{D\phi}{Dt} = 1 + \frac{1}{2}|\mathbf{u}|^2. \tag{2.61}$$

Figure 2.2 shows a plot of the solution of the Rayleigh equation (2.8). Figure 2.3 shows the relative error of the BEM code, and its variation with cavity radius.
As can be seen from Fig. 2.3, the relative error stays small until the very final stages of collapse. Instabilities in the radial velocity start to occur when $R \approx 5 \times 10^{-3}$. The

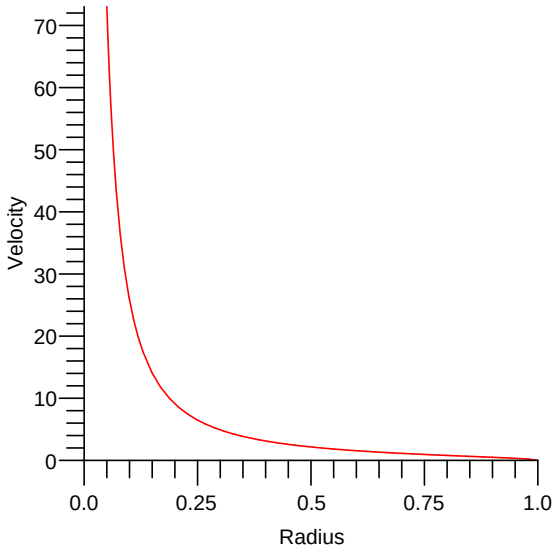

Figure 2.2: A plot of the solution of the Rayleigh equation.

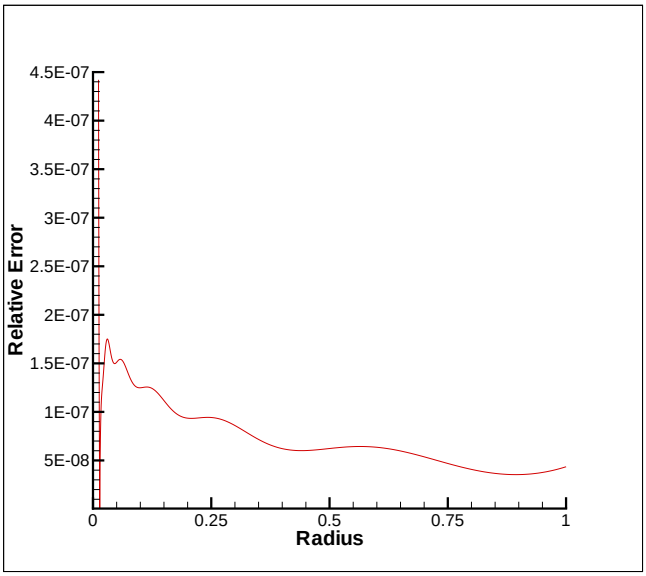

Figure 2.3: Relative error in the radial velocity of a spherical cavity in an inviscid fluid, varying with radius

collapse time at this point is $t_c = 0.914680$ (6sf); which is in excellent agreement with the analytical result (see Eqn. (2.9)).

Viscous Newtonian Spherical Bubble Collapse

The Newtonian bubble boundary element code is validated through comparison with the numerical solution of the Rayleigh-Plesset equation (Eqn. (2.7)). The non-linear ODE is solved using a 4th order Runge-Kutta scheme. Comparisons are made for Reynolds numbers $Re = 100$ (Fig. 2.4(a)), $Re = 20$ (Fig. 2.4(b)), and $Re = 10$ (Fig 2.4(c)). As can be seen the results are in good agreement.

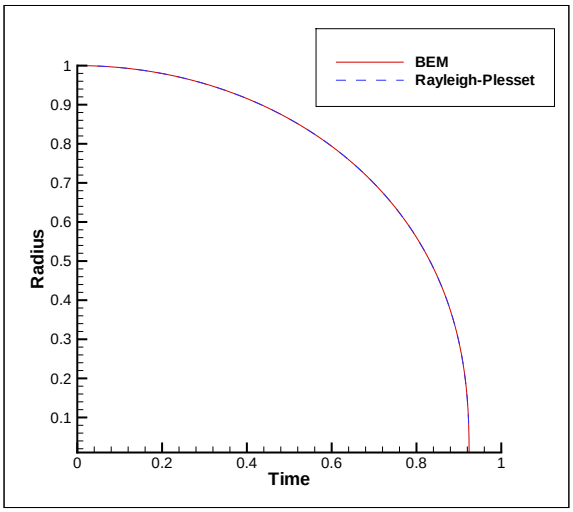

(a) $Re = 100$

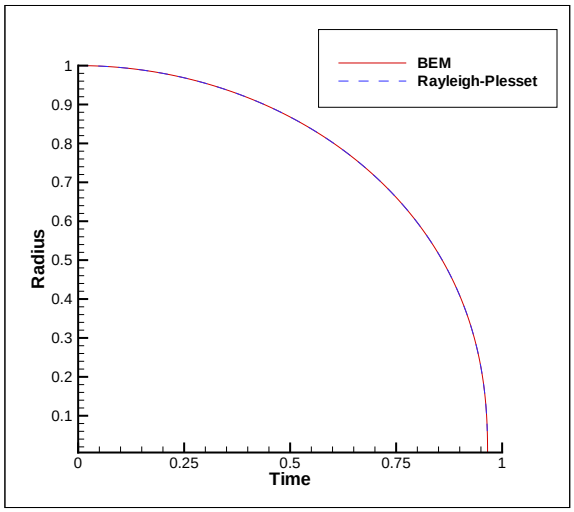

(b) $Re = 20$

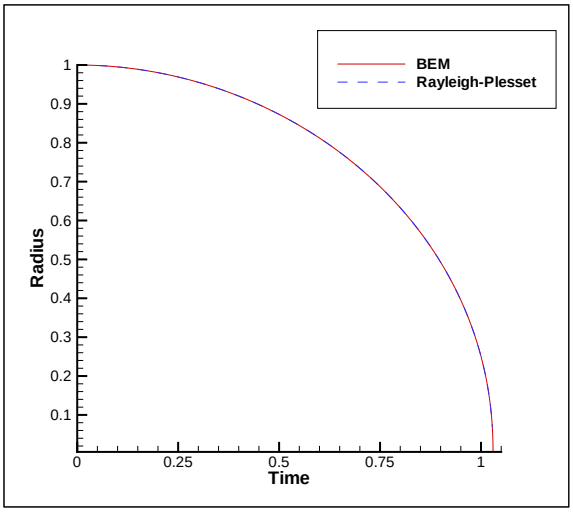

(c) $Re = 10$

Figure 2.4: Comparison of the BEM to the numerical solution of the Rayleigh-Plesset equation for a selection of Reynolds numbers.

2.4.2 Viscoelastic Dynamics

In this section, we investigate the influence of viscoelasticity on the dynamics of spherical bubble collapse and compare the predictions of the model with other studies in the literature. We begin by investigating the large Reynolds number case. Figure 2.5 displays the evolution of bubble radius for a range of De at $Re = 100$. It is evident that for such a large Reynolds number the dynamics do not differ greatly from the inviscid case. At $De = 0$, the solution obtained matches that of the Newtonian Rayleigh-Plesset equation. Increasing the Deborah number, leads to a decrease in the collapse time and the dynamics tend to those of the inviscid bubble as the increasing elastic effects negate the viscous damping effects - as reported in [148]. In fact at $De = 100$, the collapse time agrees with that for the inviscid bubble to 4 significant figures.

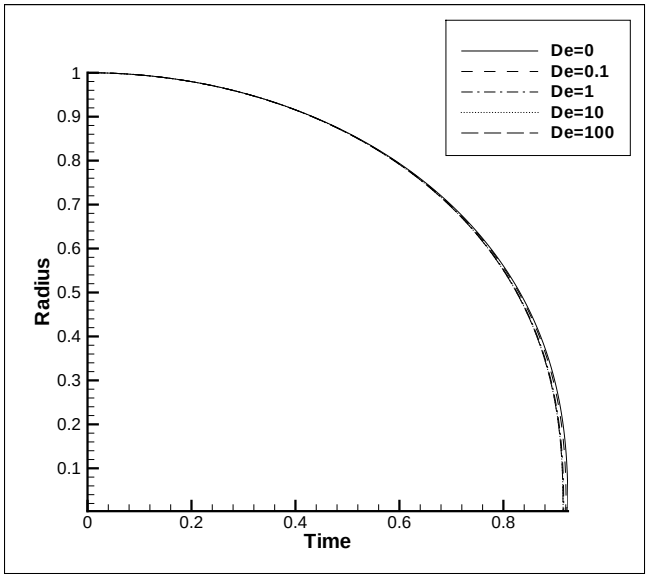

Figure 2.5: Variation of the radius of spherical bubble with time for different De. $Re = 100$.

When $Re = 10$ (Fig. 2.6) we see similar behaviour as before. When $De = 0$, the Newtonian result is obtained. Yet as the Deborah number is increased, the collapse time decreases, and the dynamics tend towards the inviscid case as elastic effects begin to negate the viscous effects. Mathematically, the reason for this can be easily seen from equation (2.44). We can see that the viscous term on the right hand side of (2.44) is already reasonably small given the choice of high Reynolds numbers. Increasing the Deborah number means that the derivative term is large, and so the other terms in the equation are negligible in comparison. With the zero initial extra stress condition, the

effective equation describing the extra stress is

$$\frac{D\mathbf{T}}{Dt} = 0, \qquad \mathbf{T}(0) = 0. \tag{2.62}$$

Therefore the extra stress is zero on the moving bubble surface throughout collapse and so the dynamics are identically inviscid.

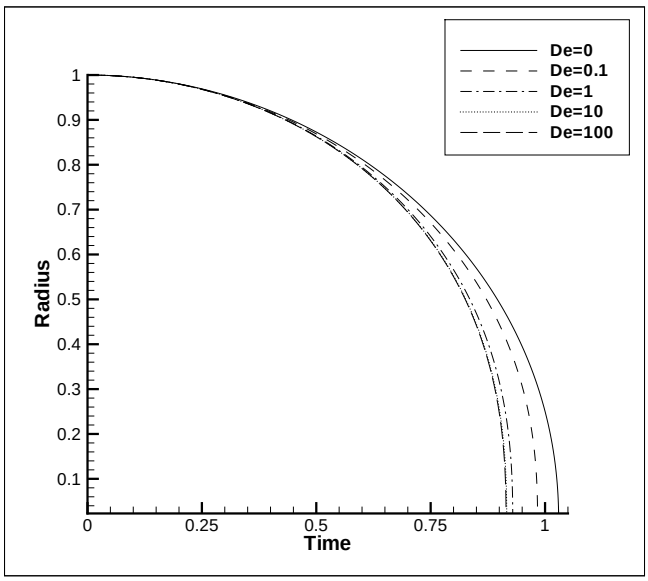

Figure 2.6: Variation of radius of spherical bubble with time for different De. $Re = 10$

More interesting results are seen when the Reynolds number is decreased further. Figure 2.7 shows the variation of bubble radius with time for $Re = 1$. For a small Deborah number we can see there is little effect on the dynamics since elastic effects are damped by the large viscous forces. By increasing the Deborah number to be of the order of the Reynolds number we see the damped oscillation of the bubble radius; the typical dynamic of bubbles in viscoelastic fluids, as seen in previous work such as Kim [78]. By increasing the Deborah number further, rebound does not occur and the dynamics resemble the Newtonian case. A similar effect at a large Deborah number was reported by Fogler and Goddard [54], and will be discussed in more detail shortly.
Figure 2.8 shows the effect of decreasing the Reynolds number further. As can be seen, oscillations are considerably more damped and require larger values of the Deborah number to be induced in the first instance. Yet still, if the Deborah number is large enough, the bubble will not rebound and dynamics similar to the Newtonian case result. Fig. 2.9 shows the effect of increasing De within the rebound limit, for a fixed Re. As reported in previous studies, the increase in elastic effects results in increasingly large

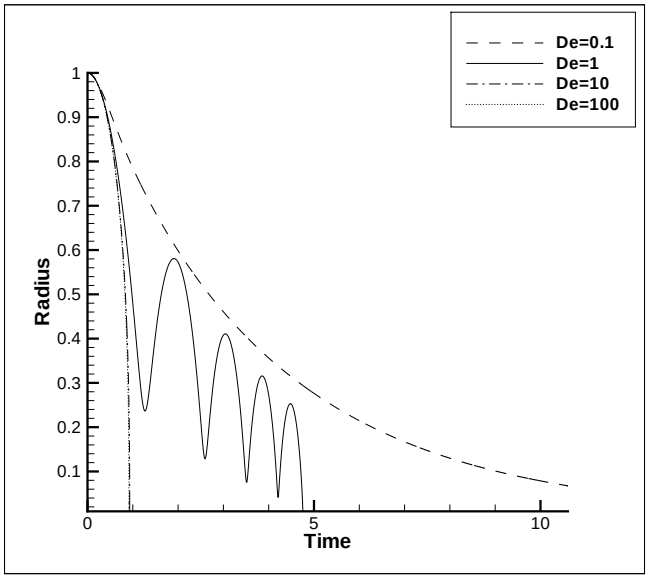

Figure 2.7: Variation of radius of spherical bubble with time for different De. $Re = 1$

oscillations and a decrease in their frequency (the bubble taking longer to rebound larger distances). As the bubble collapses, the frequency of oscillation then increases as the amplitude attenuates. Fig. 2.10 shows the effect of Re, while keeping De fixed. Again, we obtain the expected results of increasingly damped oscillations with decrease in Reynolds number (increase of viscous effects). With such a range of effects present in this phenomenon, it is clear that the ratio (or product) of the Deborah and Reynolds number is a crucial parameter in describing the dynamics.

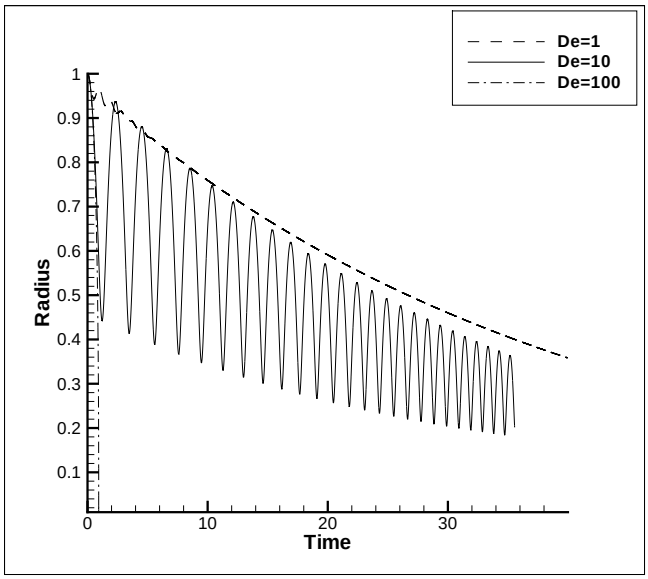

Figure 2.8: Variation of radius of spherical bubble with time for different De. $Re = 0.1$

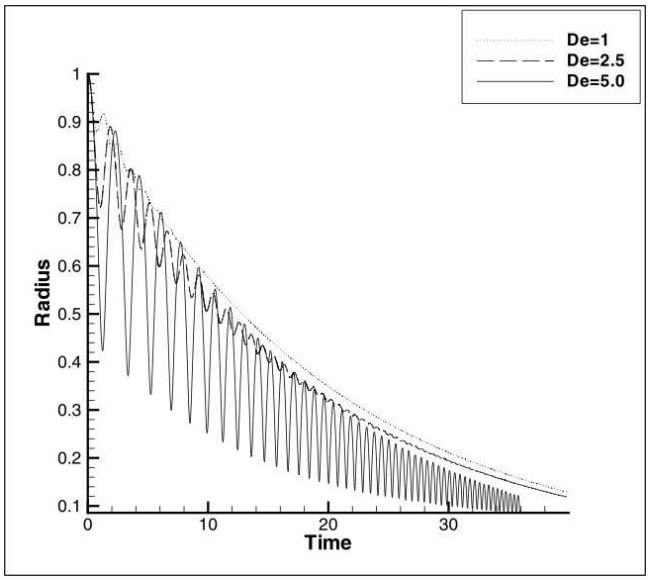

Figure 2.9: Variation of radius of spherical bubble with time for different De. $Re = 0.2$

To draw quantitative comparison with experimental results is difficult. The number of experimental papers in the literature is limited and, in most cases, they are restricted to the study of the collapse of cavities near rigid boundaries. Consequently, given the non-spherical nature of bubble dynamics near boundaries, to make meaningful comparisons with the spherical case studied here is not strictly valid. Despite this, some general observations made in experiments are relevant to the present study. Importantly, Chahine and Fruman [41] and Brujan et al. [34,37] note the inhibiting effect of polymer additives on bubble collapse. In essence, this effect is predicted using the numerical scheme presented here. The inclusion of elastic effects causes the oscillation in radius and inhibits the catastrophic bubble collapse seen in the Newtonian case.
Fig. 2.11 compares the results of Kim [78] with those of the present study for $Re = 0.5$ and $De = 0.5$. Kim [78] solves the full Rayleigh-Plesset equation for the upper convective Maxwell model. However, the qualitative similarity in the model predictions is evident. The amplitude and number of the oscillations are very similar, and the maximum difference in radius is approximately 10%.

Collapse Phenomena at Large Deborah Number

As already mentioned, the rebound limit at large Deborah number was reported also by Fogler and Goddard [54]. In the limit of very large Deborah numbers, a rebound condition on De and Re is derived analytically. Their condition states, that if

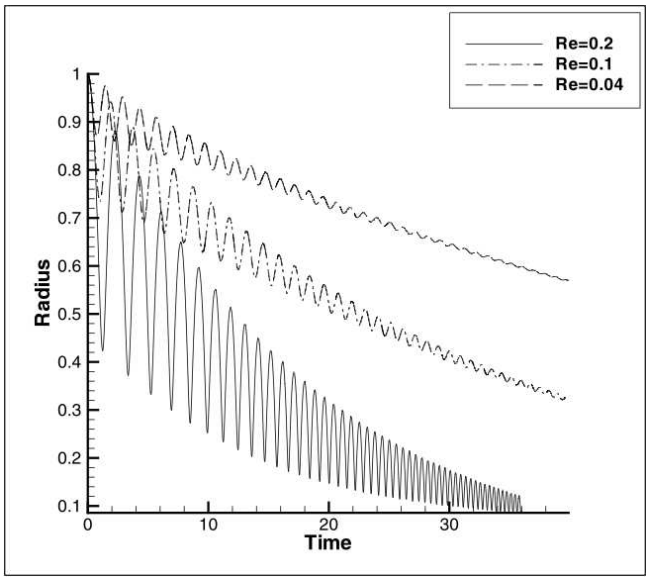

Figure 2.10: Variation of radius of spherical bubble with time for different Re. $De = 5$

$$DeRe > \frac{2\pi^2}{9}, \tag{2.63}$$

then collapse will occur without rebound. Vice versa, if

$$DeRe < \frac{2\pi^2}{9}, \tag{2.64}$$

then rebound will occur before collapse. The same phenomenon is apparent in the model under investigation in the present paper. The corresponding Rayleigh-Plesset equation relevant to our model is that with the viscoelastic effects present in the stress boundary condition at the bubble surface, viz.,

$$\rho(\ddot{R}R + \frac{3}{2}\dot{R}^2) = p_b - p_\infty - 4\int_0^t M(t-t')\left(\frac{\dot{R}(t')}{R(t')}\right)dt', \tag{2.65}$$

where $M(t) = (\mu/\lambda)\exp(-t/\lambda)$.
Consider the asymptotic case $\lambda \to \infty$. Since $\exp(-t/\lambda) \to 1$ as $\lambda \to \infty$ for finite t, equation (2.65) becomes

$$\rho(\ddot{R}R + \frac{3}{2}\dot{R}^2) = p_b - p_\infty - 4\frac{\mu}{\lambda}\ln\left(\frac{R}{R_0}\right) \tag{2.66}$$

in the limit $\lambda \to \infty$. Multiplying (2.66) by $2R^2$ and integrating over $[R_0, R]$ gives an expression for the kinetic energy viz.

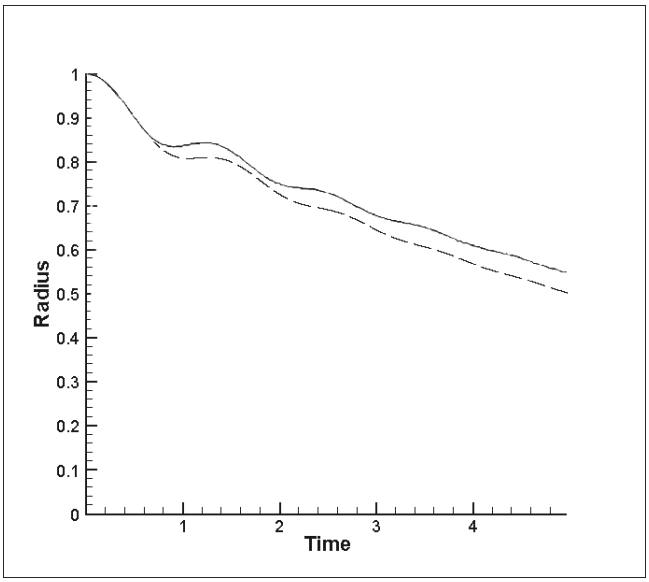

Figure 2.11: Variation of radius of spherical bubble with time for $Re = 0.5$, $De = 0.5$. The solid line shows the result of Kim [78], and the dashed line is that of the present study.

$$\rho \dot{R}^2 R^3 = \frac{2}{3}(p_\infty - p_b)(R_0^3 - R^3) - 8\frac{\mu}{\lambda}\int_{R_0}^{R} \ln\left(\frac{R}{R_0}\right) R^2 dR \tag{2.67}$$

The first term on the right-hand side is the work done by the pressure and the second is the elastic potential energy. If the kinetic energy is equated to zero, then the roots of the resulting equation will give the radii at which rebound occurs. Subsequent simplification and non-dimensionalisation yields the following energy function

$$f(R) = 4\ln(R)R^3 + \left(\frac{4}{3} - DeRe\right)(1 - R^3) = 0. \tag{2.68}$$

Considering the limit of rebound at $R = 0$, equation (2.68) yields,

$$DeRe = \frac{4}{3}. \tag{2.69}$$

Hence, for the bubble to collapse without rebound we require

$$DeRe > \frac{4}{3}, \tag{2.70}$$

and for collapse with rebound

$$DeRe < \frac{4}{3}. \tag{2.71}$$

Figure 2.13 shows the collapse with and without rebound, near to the $DeRe = 4/3$ limit.

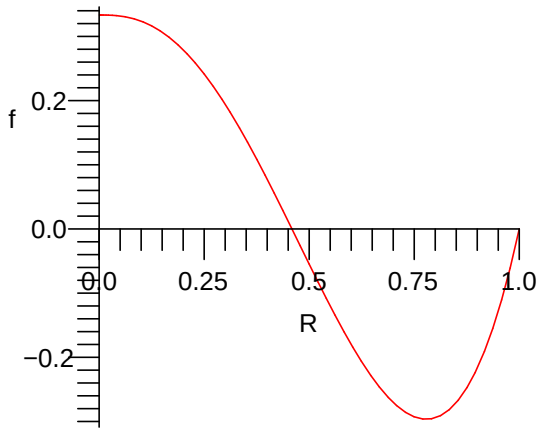

Figure 2.12: Plot of energy function $f(R)$; the roots of which indicate a zero kinetic energy.

A plot of energy function $f(R)$ for $DeRe = 1 < \frac{4}{3}$ is given in Fig. 2.12. Figure 2.14 shows the near elastic oscillations of the radius with time for a large Deborah number ($De = 100$, $Re = 0.01$) calculated using the BEM. From Fig. 2.14 we can see the first rebound radius is approximately 0.45804. The corresponding root of equation (2.68) (using a simple bisection method) is found to be 0.45892 (5 s.f.). This is a reasonably good agreement (the relative percentage error is approximately 0.2%) given the numerical method is unable to attain the analytical limit.

Jeffreys Fluid

With prior use of the viscous Newtonian and Maxwell models - extending the viscoelastic model to the Jeffreys fluid is straightforward. The Jeffreys constitutive equation is given by

$$\mathbf{T} + \lambda_1 \frac{D\mathbf{T}}{Dt} = \mu \left(\dot{\boldsymbol{\gamma}} + \lambda_2 \frac{D\dot{\boldsymbol{\gamma}}}{Dt} \right) \tag{2.72}$$

It can be shown, through the decomposition of the stress into solvent and polymeric

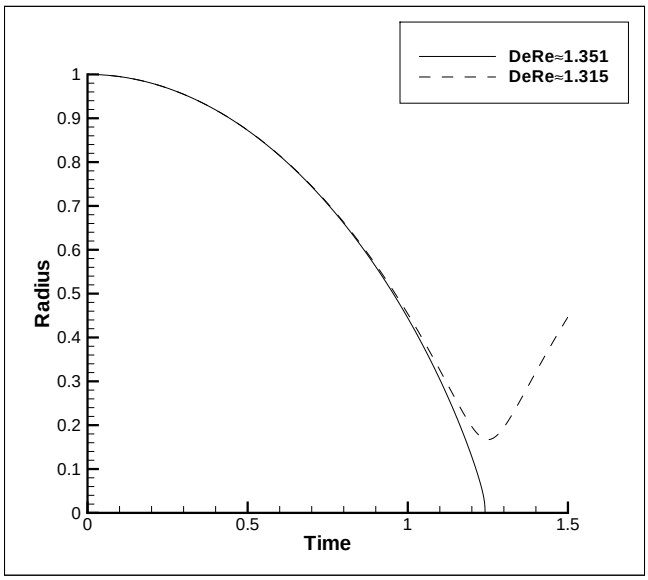

Figure 2.13: Variation of radius with time for $DeRe$ above and below the rebound limit $DeRe = 4/3 \approx 1.333$ ($De = 100$).

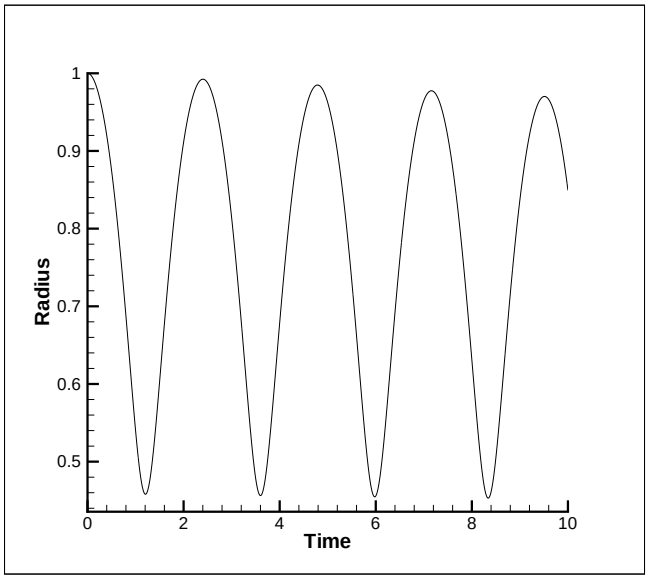

Figure 2.14: Near elastic oscillation of radius with time for $De = 100$, $Re = 0.01$)

contributions, that the Jeffreys model can be rewritten as,

$$\mathbf{T} = \mu_s \dot{\boldsymbol{\gamma}} + \boldsymbol{\tau}. \tag{2.73}$$

where $\boldsymbol{\tau}$ is given by the Maxwell constitutive equation

$$\boldsymbol{\tau} + \lambda_1 \frac{D\boldsymbol{\tau}}{Dt} = \mu_p \dot{\boldsymbol{\gamma}}, \tag{2.74}$$

and μ_s and μ_p are the solvent and polymeric viscosities, defined respectively as

$$\mu_s = \frac{\lambda_2}{\lambda_1}\mu, \tag{2.75}$$

$$\mu_p = \left(1 - \frac{\lambda_2}{\lambda_1}\right)\mu. \tag{2.76}$$

Re-casting the constitutive equation in the form of (2.73) - as the sum of a viscous and polymeric stress - allows the problem to be solved easily given that both contributions (Newtonian and Maxwellian) have been studied previously. Let the above constitutive equation be rewritten in dimensionless variables, with De and Re defined previously and $\beta = \mu_s/\mu$.

The results for the Jeffreys model are as expected. Figure 2.15 shows the evolution of bubble radius R for values of β as a fraction of the Reynolds number Re (equivalent to a varying solvent viscosity μ_s). The Deborah number here is $De = 10$ and a constant polymeric viscosity is assigned by setting $(1 - \beta)/Re = 10$. For $\beta = 0$, expectedly the Maxwell case is recovered and the results match those of Fig. 2.6 for $De = 10$. Increasing the solvent viscosity causes the oscillations to become increasingly damped. Indeed, increasing the solvent viscosity enough would damp oscillations until the Newtonian result is obtained as the polymeric part becomes small in comparison. Notably, the amplitude of the oscillations decrease but the period remains approximately constant as μ_s varies. This indicates that the relaxation time λ_1 is the controlling factor in determining the frequency of oscillation.

By setting $\beta = 1$ (equivalent to a zero polymeric viscosity), as expected (regardless of the value of De), one obtains the corresponding Newtonian dynamics with a Reynolds number Re (Fig. 2.16).

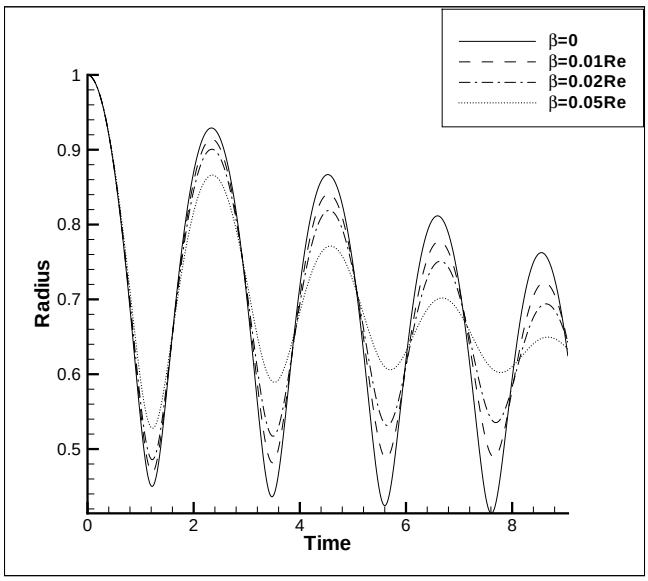

Figure 2.15: Variation of radius with time for a Jeffreys fluid, with $De = 10$

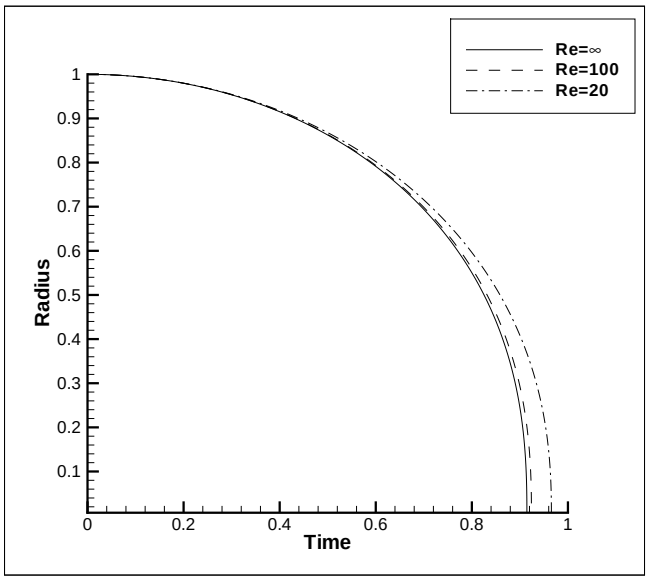

Figure 2.16: Variation of radius with time for a Jeffreys fluid, with $\lambda_1 = 10$ and μ_p=0 ($\beta = 1$).

The Generalised Maxwell Model

It should be mentioned that further extensions to the viscoelastic model can be easily made. The above models are limited to a single set of parameters. To fit experimental data, more parameters are often required [101]. It is for this reason that one can define a generalised or multi-mode model viz.,

$$\mathbf{T} = \sum_{k=1}^{N} \mathbf{T}_k, \tag{2.77}$$

where each $\mathbf{T}_k$ obeys its own constitutive equation:

$$\mathbf{T}_k + \lambda_k \frac{D\mathbf{T}_k}{Dt} = \mu_k \dot{\boldsymbol{\gamma}}, \quad k = 1, \ldots, N \tag{2.78}$$

The model then has a spectrum of relaxation times and viscosities which allow greater flexibility in fitting model predictions to experimental data. The convention is that $\lambda_1 > \lambda_2 > \cdots > \lambda_N$. Typically, $N = 3, 4$ or 5 in the representation (2.77) [101].
If necessary, one can select the parameters μ_k, λ_k with the following empiricisms [15]:

$$\mu_k = \mu_0 \frac{\lambda_k}{\sum_k \lambda_k}; \quad \lambda_k = \frac{\lambda_0}{k^\alpha}. \tag{2.79}$$

The Rouse molecular theory for dilute polymer solutions very nearly gives equations (2.79), with $\alpha = 2$. In a similar manner, the Doi-Edwards molecular theory for polymer melts suggests the following parameters [15]:

$$\mu_k = \mu_0 \frac{\lambda_k^2}{\sum_{k,odd} \lambda_k^2}; \quad \lambda_k = \frac{\lambda_0}{\pi^2 k^2}. \tag{2.80}$$

Taking a maximum of three terms for each model, Figure 2.17 shows the variation of bubble radius with time for the Rouse and Doi-Edwards theories.
It can be seen that, for the parameter set considered, the Rouse model exhibits a small oscillation in the radius, while the Doi-Edwards does not. This is because the λ_k associated with a given μ_k are smaller in the Doi-Edwards model. Consequently the elastic forces are not large enough to induce a rebound.

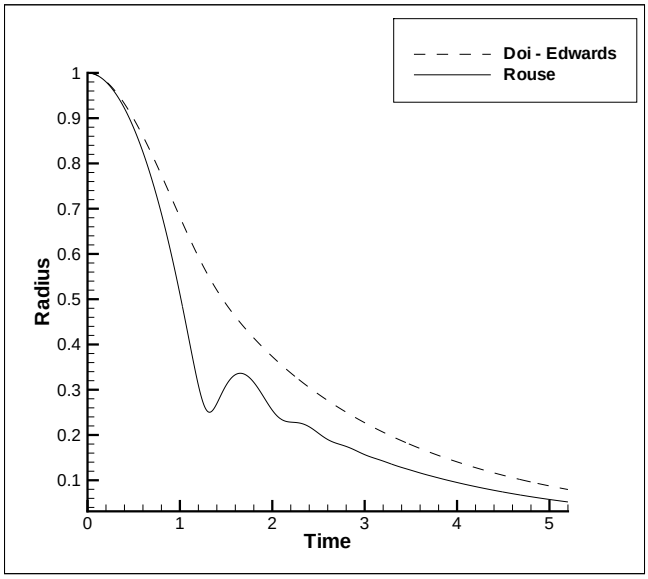

Figure 2.17: Variation of bubble radius with time for Rouse and Doi-Edwards like fluids, with $\lambda_0 = 0.5, \mu_0 = 0.5$.

2.5 Conclusions

The effect of viscoelasticity on spherical bubble dynamics has been studied for several different constitutive equations. A novel boundary element scheme has been developed, with the ultimate intention of gaining insights into non-spherical dynamics. Even though viscoelastic effects only appear through the normal stress condition on the free surface, we find the model predicts all the important phenomena seen in other studies. More specifically, the model predicts the damped oscillation of the bubble radius with time, the near elastic oscillations in the high Deborah number limit, and the no-rebound condition. Consequently, one can argue that it is the surface effects that primarily govern the bubble dynamics, in comparison to those viscoelastic effects within the bulk of the fluid. This is not surprising as, of course, the dynamics of the bubble are directly governed by its boundary with the fluid. Any internal viscous or elastic effects of the fluid on the bubble, are likely to be small compared to those directly experienced at the interface. On consideration of the Jeffreys constitutive relation in the model, we see the expected result of an increasingly damped radius with increasing solvent viscosity. Increasing the solvent viscosity, of course, has no effect on the relaxation time, and hence the period of oscillation for the model remains approximately constant. One can generalise the Maxwell model, allowing for a spectrum of relaxation times and viscosities to be prescribed. Empiricisms relating to Rouse and Doi-Edwards molecular

theories are used to prescribe the parameters. The Doi-Edwards model does not exhibit any oscillation in bubble radius. Only a slow decay of bubble radius with time is predicted. In comparison, the Rouse model predicts a small low amplitude rebound before being completely damped. This is in stark contrast to the more elastic behaviour predicted by the Maxwell and Jeffreys models.

Chapter 3

The Influence of Viscoelasticity on the Collapse of Bubbles Near a Rigid Boundary

3.1 Introduction

In this chapter, the mathematical model developed in Chapter 2 is extended in order to simulate the dynamics of a bubble near a rigid boundary. As mentioned in Chapter 1, when a bubble collapses near a rigid boundary, a high speed liquid jet can form and penetrate the bubble. This jet can either inflict damage directly by impacting upon the boundary, or indirectly by initiating the "splashing" effect which can release damaging pressure shock-waves. It was the experimental work of Benjamin and Ellis [9] that first observed these jets and postulated on their damage capability. The popularity of numerical simulation in subsequent decades meant that this otherwise intractable problem could be attacked with gusto.

Due to the high velocities seen in bubble collapse and jet formation, the common approach was to assume that the fluid was inviscid and the flow irrotational. Plesset and Chapman [119] undertook one of the first numerical studies, solving Laplace's equation using finite difference techniques. Blake et al. [19,20] then solved the same model problem using the more efficient and accurate boundary element method. The application of the boundary element method to this problem proved extremely fruitful and spawned a wide range of extensions to the model. These included cubic spline representation

of the boundary and the surface functions [46], the inclusion of non-condensible bubble contents [11], fully 3D calculations [167], the extension to toroidal dynamics [10], prediction of the splashing effect [21,151], the study of pulsating buoyant bubbles [38], bubbles bouncing off walls [40], explosion bubbles near structures [80], investigations into the effect of surface tension [171], and collapse near curved rigid boundaries [150].

Few studies of bubble collapse near rigid boundaries have considered anything other than an inviscid fluid. To the author's knowledge, the only theoretical studies of this phenomenon that include viscous effects are those of Popinet and Zaleski [121] and Kim et al. [79]. In both contributions, the full Navier-Stokes equations are solved numerically - the first uses a finite volume technique, while the second utilises a finite element approach with an ALE formulation. Both note the mitigating effect viscosity has on the jet dynamics - slowing the jet down and even preventing formation. Numerical studies of viscoelastic dynamics have numbered even less. In a recent paper, Brujan [32] notes the particularly slow pace of theoretical and numerical research into cavitation dynamics near a rigid wall in a viscoelastic fluid. Given the difficult nature of the problem and the success of the boundary element method, Brujan independently suggests the model developed in Chapter 2; employing a potential flow approximation with viscoelastic effects included at the bubble surface. In this chapter we present and discuss the predictions of this model for viscoelastic bubble collapse near a rigid boundary.
Section 3.2 summaries the aforementioned mathematical model and the extensions required to include the rigid boundary. In Section 3.3, the numerical results are presented and discussed, and conclusions are drawn in Section 3.4.

3.2 Mathematical Model and Governing Equations

As mentioned, it is known that experimentally cavitation collapse near a rigid boundary is, to a high degree of accuracy, an axisymmetric phenomena [19]. Hence, as in previous studies, we consider the axisymmetric problem geometry shown in Fig. 3.1. Initially, the bubble has radius R_0 and its centre is located at a distance h from a rigid wall.
We recall the key features of the model developed in Chapter 2. The ambient fluid is considered to be incompressible

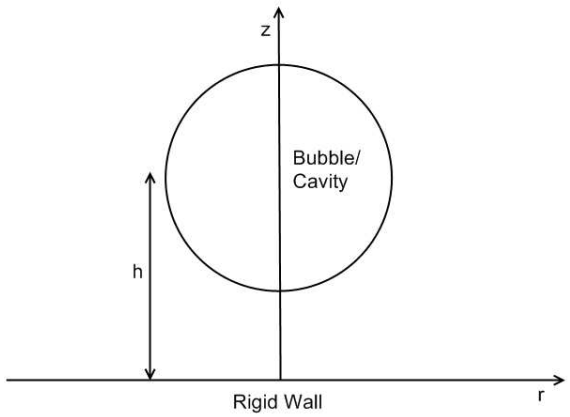

Figure 3.1: Schematic set up of bubble collapse near a wall problem.

$$\nabla \cdot \mathbf{u} = 0. \tag{3.1}$$

and the flow irrotational,

$$\nabla \times \mathbf{u} = 0. \tag{3.2}$$

Hence the velocity field of the fluid can be expressed as the gradient of some scalar potential function ϕ ($\mathbf{u} = \nabla\phi$), which satisfies Laplace's equation. By Green's theorem, Laplace's equation can be recast as integral over the bubble surface $\partial\Omega$ viz.,

$$c(\mathbf{p})\phi(\mathbf{p}) = \int_{\partial\Omega} \left(\frac{\partial\phi}{\partial n}(\mathbf{q}) G(\mathbf{p},\mathbf{q}) - \phi(\mathbf{q}) \frac{\partial G}{\partial n}(\mathbf{p},\mathbf{q}) \right) dS \tag{3.3}$$

where the constant $c(\mathbf{p})$ is given by

$$c(\mathbf{p}) = \begin{cases} 2\pi & \text{if } \mathbf{p} \in \partial\Omega, \\ 4\pi & \text{if } \mathbf{p} \in \Omega \backslash \partial\Omega \end{cases}$$

In contrast to the previous study of spherical dynamics, the bubble now resides near a rigid boundary positioned at $z = 0$. The boundary is represented by a no-penetration condition, viz.

$$\frac{\partial\phi}{\partial z} = 0, \qquad z = 0. \tag{3.4}$$

In order to satisfy equation (3.4), the Green's function, $G(\mathbf{p},\mathbf{q})$, is given by

$$G(\mathbf{p},\mathbf{q}) = \frac{1}{|\mathbf{p}-\mathbf{q}|} + \frac{1}{|\mathbf{p}'-\mathbf{q}|}. \tag{3.5}$$

This is the sum of two free space Green's functions, where $\mathbf{p}'$ is the reflected image of $\mathbf{p}$ in the rigid wall. The use of (3.5) means the boundary condition (3.4) automatically holds, so no integration over the expanse of the wall is necessary.

On the premise that viscous and viscoelastic effects are important only in the immediate proximity of the bubble surface, a generalised Bernoulli equation at the surface provides an equation of motion for the potential ϕ,

$$\frac{D\phi}{Dt} = 1 + \frac{1}{2}|\mathbf{u}|^2 - T_{nn}. \tag{3.6}$$

The normal-normal component of the extra stress T_{nn} is found from an appropriate constitutive equation. This study, for the most part, considers viscoelastic effects as described by the material Maxwell model

$$De\frac{DT_{nn}}{Dt} + T_{nn} = \frac{1}{Re}\dot{\gamma}_{nn}. \tag{3.7}$$

The Deborah number De and the Reynolds number Re are defined as previously, in equations (2.42) and (2.39) respectively.

Equation (3.3) is solved using collocation, with nodal points on the bubble surfaces and the potential ϕ interpolated using cubic splines. The discrete system is solved for the normal velocity using Gaussian elimination. The tangential velocity and higher derivatives of ϕ are found using generalised centred difference formulae found in [89]. A fourth-order Runge-Kutta scheme is then used to update the bubble surface and potential using (2.20) and (3.6) respectively. In the presence of viscoelasticity ($De \neq 0$), the constitutive equation is updated using an implicit second-order time stepping method.

Note that the transition to the toroidal phase of dynamics is not currently modelled in this study. The investigation into viscoelastic effects shows that, in the majority of cases, collapse into a toroidal bubble will not occur.

As in almost every study of cavitation dynamics using the boundary element method, (see [19, 20, 170], for example) instabilities can develop in the surface during computation. These are suppressed using the 5-point smoothing formula of Longuet-Higgins and Cokelet [97], which is implemented every 5-20 times steps as in Best and Kucera [11].

3.3 Numerical Results and Discussion

3.3.1 Validation

To validate the algorithm, the problem of inviscid growth and collapse of a bubble near a rigid horizontal wall is examined, allowing direct comparison with the results of Blake et al. [19]. Figure 3.2 shows the bubble wall profiles at different times for the growth and collapse of an initially small bubble ($R_0 = 0.1$), centred at a distance $h = 1.0$ from the boundary. The bubble profile shapes obtained agree well with those of Blake et al. [19] and Taib [146]. Figure 3.3 shows the jet velocities for a selection of heights. The maximum jet velocities obtained here are given by $v_{max} = 8.5$ for $h = 1.0$, $v_{max} = 10.8$ for $h = 1.5$, and $v_{max} = 15.4$ for $h = 2.0$. These compare well to the jet velocities obtained by Blake et al. [19], given respectively by $v_{max} = 8.6, 11.0, 16.1$. The difference in the values can be attributed to the surface discretisation used in each study. Blake et al. [19] use linear piecewise elements, while cubic splines are used here. As with previous investigations, we see a plateau in the jet velocity in the final stages of collapse for a cavity near to the wall. Also, we note that during the growth phase the transient behaviour of the jet velocity is independent of the initial distance h from the wall. The influence of h can only be seen in the final stages of collapse.

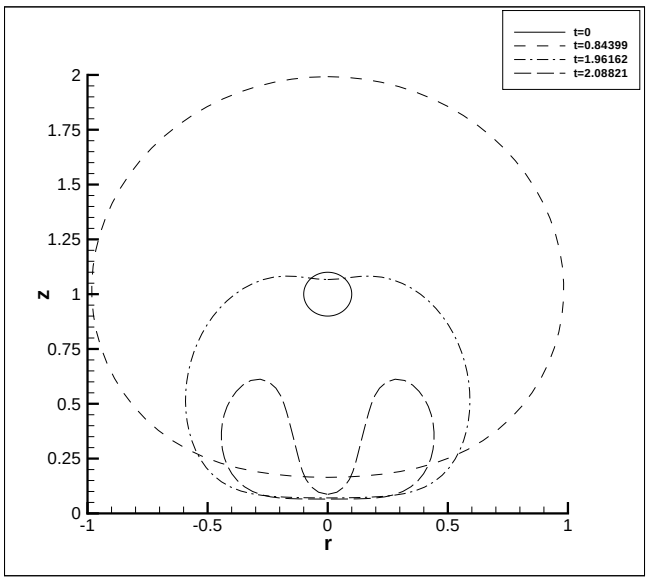

Figure 3.2: Bubble surface profiles at different stages of growth and collapse at an inception distance $h = 1.0$ from the boundary

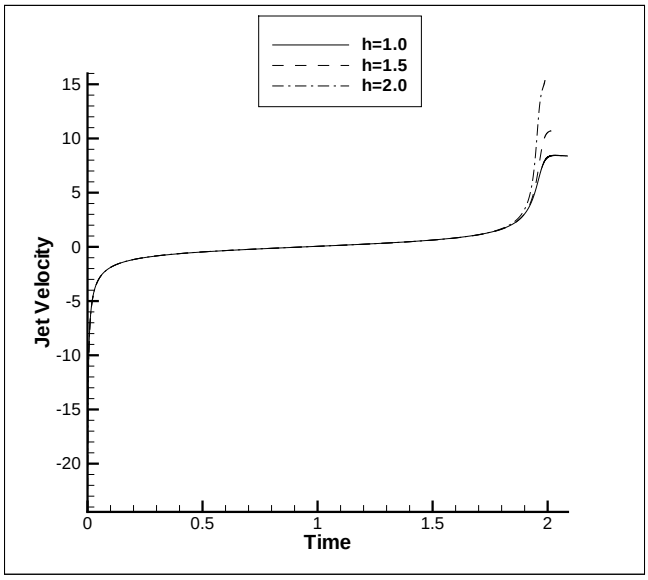

Figure 3.3: Jet velocities during growth and collapse of an inviscid bubble at varying initial distances from the rigid wall.

3.3.2 Newtonian Dynamics

In extending to the viscous Newtonian and non-Newtonian cases, only the collapse of a cavity near a wall is considered. This allows the simulations to run for longer in the more interesting phase of the dynamics. Simulations are carried out for a range of Reynolds and Deborah numbers at dimensionless distances $h = 1.1, 1.5, 2.0$ from the wall to the initial bubble centroid with $R_0 = 1$. The values of the Reynolds and Deborah numbers are chosen to demonstrate the dependence of dynamics on the material parameters.

Figure 3.4 shows a selection of profiles during the collapse of an inviscid bubble at a distance $h = 1.1$ from the wall.

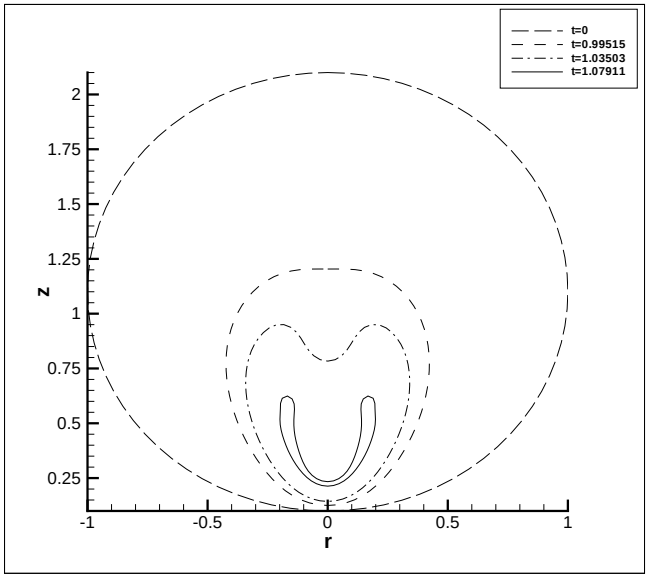

Figure 3.4: Bubble surface profiles at different stages of collapse at a distance $h = 1.1$, $Re = \infty$

It can be seen that close to the wall the bubble surface undergoes large deformation during collapse with a significantly pronounced jet forming in Fig. 3.4. For bubbles positioned further from the wall, collapse is less asymmetric with the liquid jet being less pronounced. Also, the lessened deformation means the final volume of the bubbles is smaller. The jet velocities associated with different h values can be seen in Fig. 3.5. The maximum jet velocities in each case are $v_{max} = 12.9, 16.9, 26.9$ for $h = 1.1, 1.5, 2.0$, respectively. It is generally true that closer to the wall the fluid velocities are smaller in magnitude. This is to be expected as the presence of a rigid boundary restricts

the flow of the fluid. Note that for $h = 1.1$ and $h = 1.5$ the jet tip plateaus in the final stages of collapse. As mentioned by Best and Kucera [11]; when the bubble collapses much of the fluid momentum manifests itself in the jet. Since only a finite amount of momentum can be transferred to the jet, it cannot continue to accelerate following the finite momentum transfer. Also, as a result of smaller velocities, the lifetime t_f of the bubble increases the closer it is to the wall; given in each case by $t_f = 1.079, 1.032, 1.004$, respectively. We define the bubble lifetime (or collapse time) as the time at which either the liquid jet impacts upon the bubble underside or the jet velocity displays near-singular behaviour.

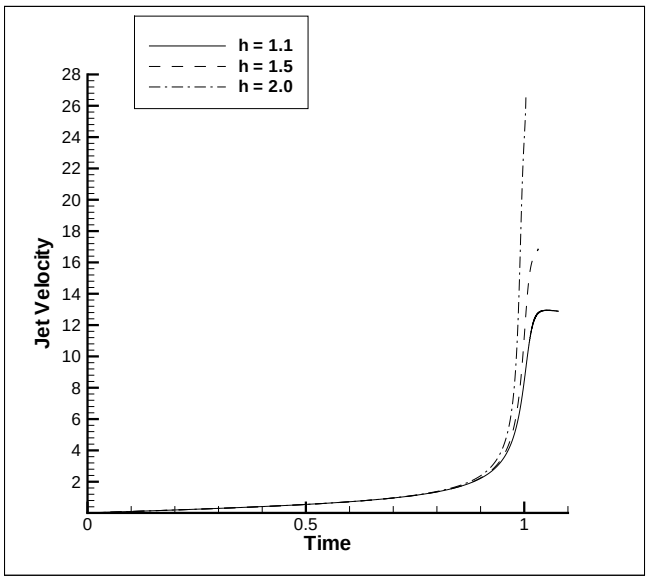

Figure 3.5: Jet velocities for the collapse of an inviscid bubble at different initial distances from a rigid wall.

We now look at the bubble dynamics following the inclusion of viscous effects. Figure 3.6 shows the influence of h on jet velocities for $Re = 100$. The maximum jet velocities in this case are $v_{max} = 13.1, 18.0, 30.1$ for $h = 1.1, 1.5, 2.0$, while the final collapse times t_f are given by $t_f = 1.089, 1.042, 1.013$. Despite there being little difference in the collapse times compared to the inviscid case, there is a marginal increase in the maximum jet velocity. This results from the bubble reaching a slightly smaller size before jet formation occurs. Consequently, surface velocities are larger - producing a slightly faster jet.

Figures 3.7-3.9 display bubble wall profiles for $Re = 20$. It is clear that increasing the viscosity has a more marked effect on the wall profiles and the dynamics. Fig. 3.7

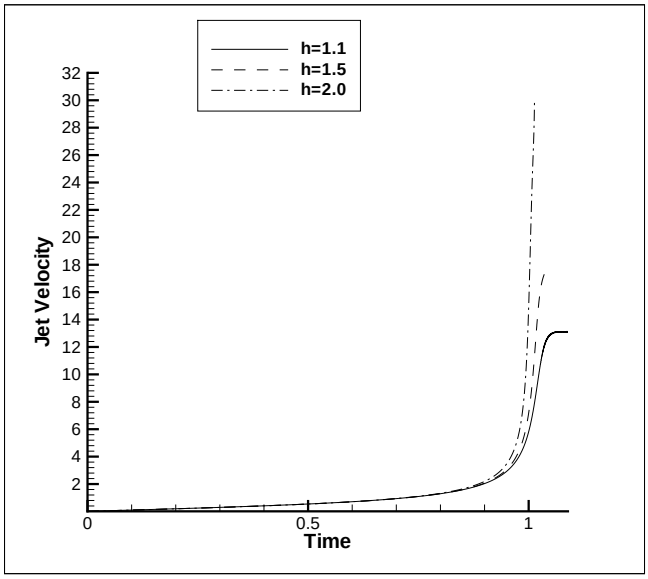

Figure 3.6: Jet velocities during collapse with $Re = 100$ for different initial distances from wall.

shows the wall profiles at $h = 1.1$. It can be seen that the formation of the liquid jet occurs much later in the collapse (when the cavity is substantially smaller) than in the inviscid case. The surface velocities are larger overall and while the jet penetrates, the bubble continues to collapse at a high speed. This results in the formation of an arrow-head bubble profile, as the underside comes up to meet the jet. The same mechanism explains the collapse behaviour shown in Figures 3.8 and 3.9, in which thin almost disc-like bubbles are produced. Note that the collapse times are also significantly longer than those obtained at higher Re with $t_f = 1.126, 1.083, 1.054$, for $h = 1.1, 1.5, 2.0$, respectively.

It is clear then that viscosity has a prohibitive effect on jet production, as reported in Popinet and Zaleski [121] and Kim et al. [79]. Perhaps the most important phenomena in Newtonian bubble dynamics, namely the complete suppression of the formation of the liquid jet, can be observed if viscous effects are increased further. Figures 3.10-3.12 show the bubble wall profiles for $Re = 10$. Note that in each case ($h = 1.1, 1.5, 2.0$) no jet forms on the top side of the bubble. Only in the very final stages, when the bubble is very small, does the top side of the surface dimple slightly but does not continue to produce a penetrating jet. Another interesting occurrence is the elongation and "cusping" on the underside of the bubble. The same phenomena is reported by Kim et al. [79] for moderate Reynolds numbers, in their finite element study of collapse of a Newtonian bubble near a rigid wall. This cusping results from the left and right

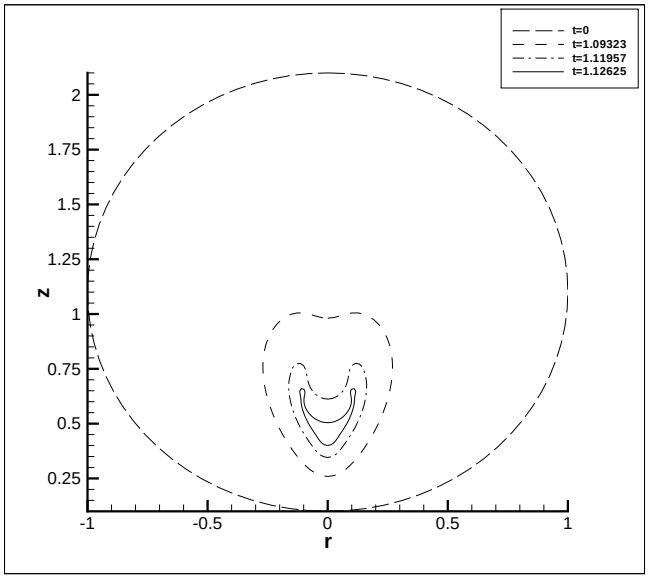

Figure 3.7: Bubble surface profiles at different stages of collapse at a distance $h = 1.1$, $Re = 20$

sides of the bubble surface moving slightly faster than the bubble underside. Evidently, viscous forces are more effective at inhibiting movement of the underside, due to the increased strain rates nearer the wall. Indeed, cusping is more pronounced closer to the wall (for $h = 1.1, 1.5$), where differences in velocity between the top and underside of the bubble are larger. Further from the wall ($h = 2.0$), as the velocity field is more uniform, the viscous forces inhibit almost uniformly, causing the bubble to remain very nearly spherical as it collapses.

As expected, collapse times are again longer, given the decrease in Reynolds number ($t_f = 1.183, 1.142, 1.115$ for $h = 1.1, 1.5, 2.0$ respectively). Also, as can be seen from Figure 3.14 the (jet) velocities become extremely large as the bubble is able to collapse to a very small size, without there ever being jet impact.

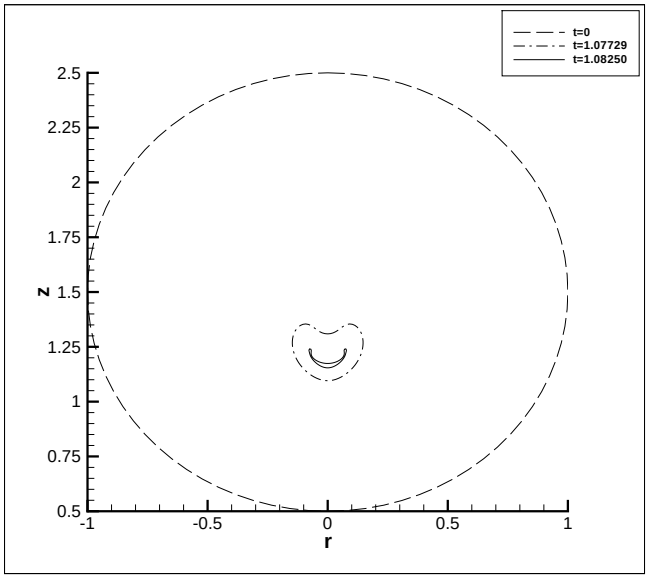

Figure 3.8: Bubble surface profiles at different stages of collapse at a distance $h = 1.5$, $Re = 20$

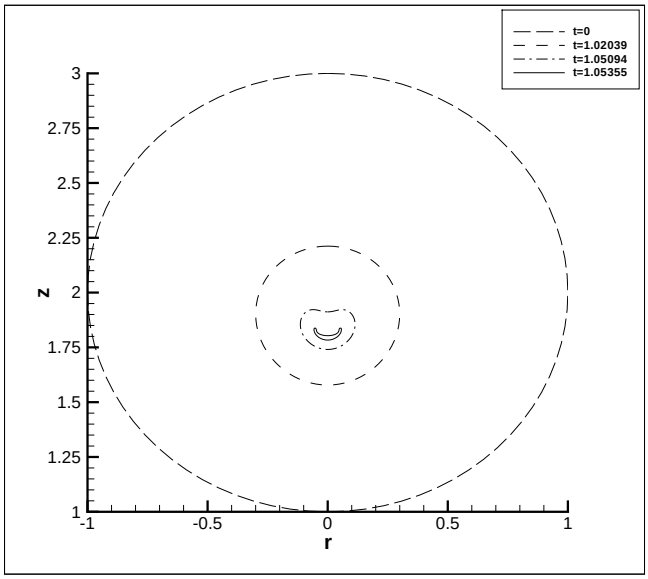

Figure 3.9: Bubble surface profiles at different stages of collapse at a distance $h = 2.0$, $Re = 20$

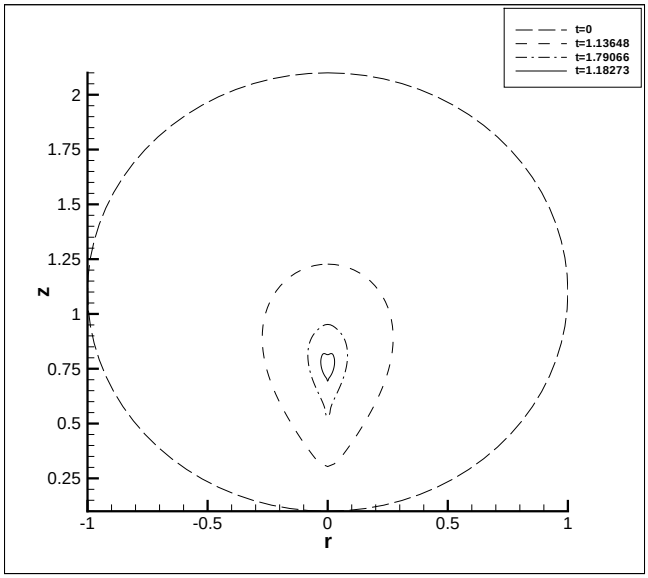

Figure 3.10: Bubble surface profiles at different stages of collapse at a distance $h = 1.1$, $Re = 10$

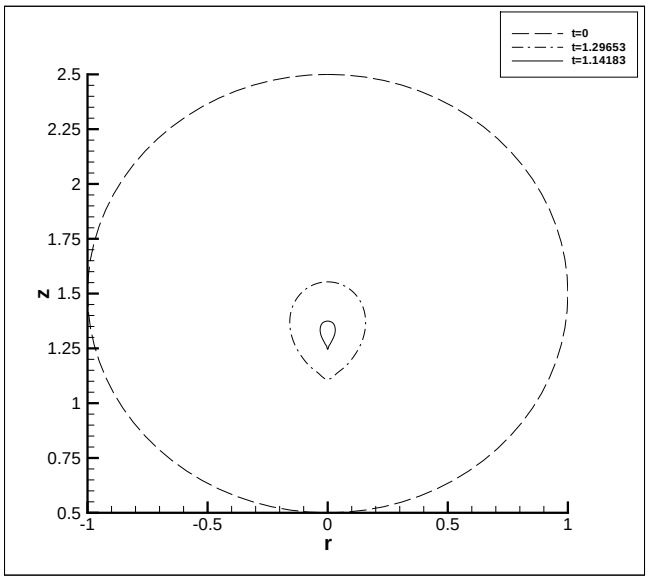

Figure 3.11: Bubble surface profiles at different stages of collapse at a distance $h = 1.5$, $Re = 10$

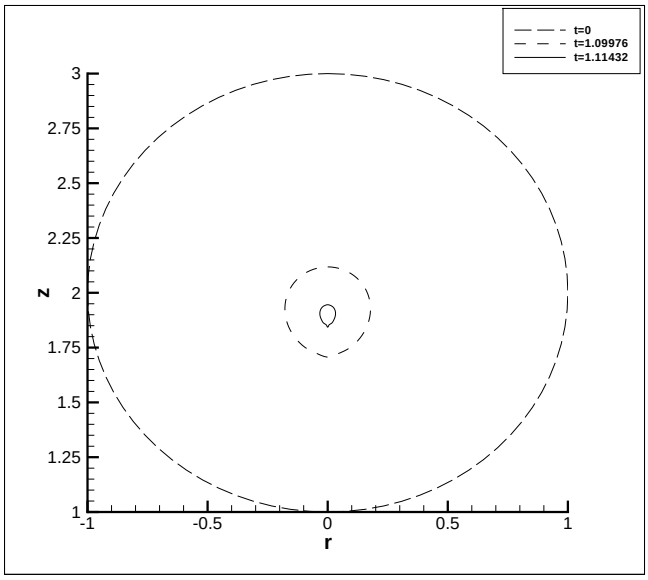

Figure 3.12: Bubble surface profiles at different stages of collapse at a distance $h = 2.0$, $Re = 10$

For ease of comparison, Figures 3.13 and 3.14 show the evolution of jet positions and jet velocities for various Reynolds numbers at a fixed distance, $h = 1.1$ from the wall. Here the jet position is defined as the axial co-ordinate on the top of the bubble (the North Pole); it is the position where the jet is expected to form. Clearly, at a given distance, a decrease in Reynolds number slows collapse and so extends the collapse time. Fig. 3.13 shows the jet positions at $h = 1.1$. Note that in the inviscid case, the jet position decreases sharply in the final stages of collapse. The profile then becomes smoother as one decreases Re. Similarly, studying the jet velocities at $h = 1.1$, at a given time the velocity decreases with the Reynolds number. Since the bubbles are able to attain smaller sizes with increasing viscosity, the collapse times are longer and the final velocities much larger. So much so, that for moderate Reynolds numbers, the jet velocity exhibits singular behaviour.

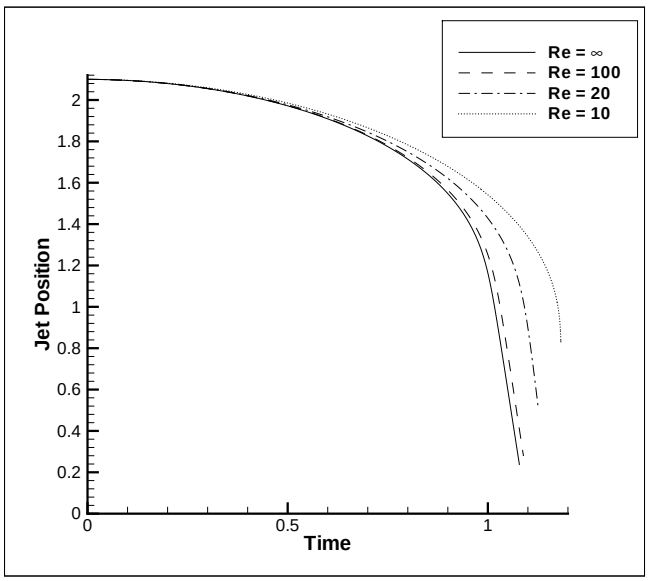

Figure 3.13: Position of jet point on z axis with time, at a distance of $h = 1.1$, with varying Re.

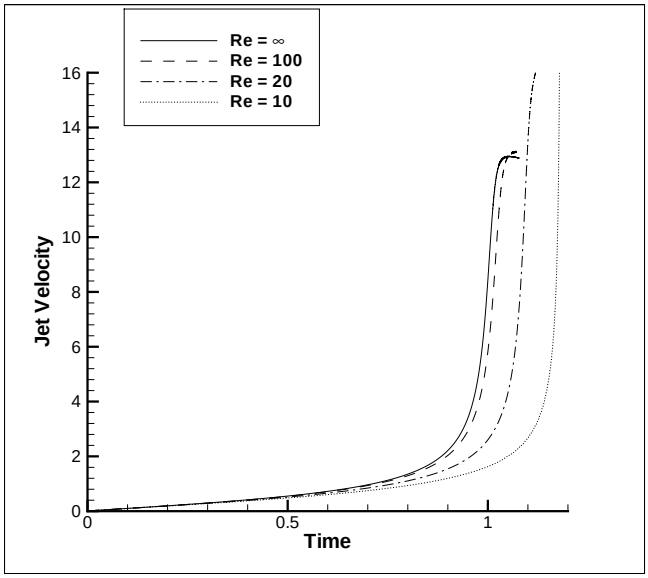

Figure 3.14: Jet velocities during collapse with varying Re. $h = 1.1$.

3.3.3 Viscoelastic Dynamics

The inclusion of elastic effects produces some very interesting dynamics, particularly when close to the rigid wall. As seen in spherical studies of viscoelastic cavitation dynamics e.g. [54], bubble oscillations occur during collapse. However, unlike the spherical case, the presence of the rigid wall induces an asymmetry in the oscillating bubble. As in the moderate Reynolds number Newtonian case, jet formation is completely suppressed in the viscoelastic case. Jet suppression has also been seen experimentally in viscoelastic fluids by Brujan et al. [37] and Chahine and Fruman [41]. Additionally, we observe cusping of varying degrees close to the wall, for some of the parameters studied.

Figure 3.15 shows bubble profiles for $Re = 1, De = 1, h = 1.1$. Due to the close proximity of the wall, the deformation in the underside is significant. The bubble rebounds due to elastic effects and during the second stage of collapse, a portion of the bubble underside meets on the central axis, and the computation breaks down. Of course, the presence of elasticity causes the bubble to rebound, and subsequently collapse times are significantly longer. Similarly, the velocities are reduced as the oscillating bubble does not have a chance to attain a large velocity before it rebounds.

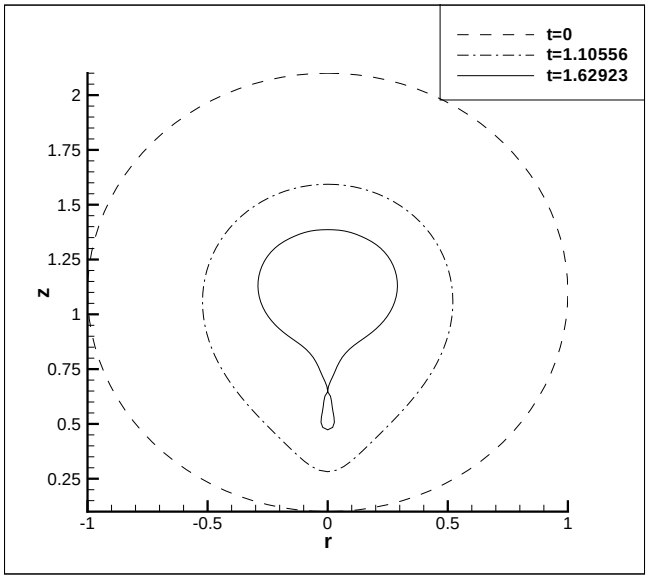

Figure 3.15: Bubble surface profiles at different stages of collapse at a distance $h = 1.1$, $Re = 1$, $De = 1$.

Figure 3.16 shows the variation of the jet position with time for different initial dis-

tances of the bubble from the wall. Note that the time at which the bubble first rebounds decreases with increasing distance from the wall. This is due to the lower velocity near the wall preventing the generation of sufficient elastic energy to balance the work done by the external pressure in compressing the bubble. From looking at the jet velocities in Fig. 3.17 one can see a plateau and small decrease in the jet velocity (for $h = 1.1$) at $t \approx 1.25$. Similar perturbations can be seen near the other peaks and troughs for $h = 1.5$ and also $h = 2.0$. This is an interesting occurrence, and is a consequence of the cusping and the subsequent out of phase oscillation of the top and bottom of the bubble. For example, as the bubble begins to collapse and then cusp, it seems the extra fluid drawn to the underside from the bulk of fluid around the bubble, causes the jet velocity to fall slightly. It then increases as fluid is replenished from elsewhere.

As the initial distance of the centre of the bubble from the wall increases, the perturbation in the jet velocity decreases. Also, we note that further from the wall, the lifetime of the bubble is longer: $t_f = 2.72$ and 3.59 for $h = 1.5$ and 2.0, respectively. This is due to the reduced deformation of the bubble further from the wall. Away from the wall, the flow around the bubble is not as irregular, and it takes longer for the bubble to deform into its self-destructive shape (as in Fig. 3.15).
Figures 3.18-3.20 show the jet velocities for different De at each of the studied distances from the wall. As in the spherical dynamics, a large enough De results in the bubble not rebounding, but instead resembling the Newtonian dynamics.

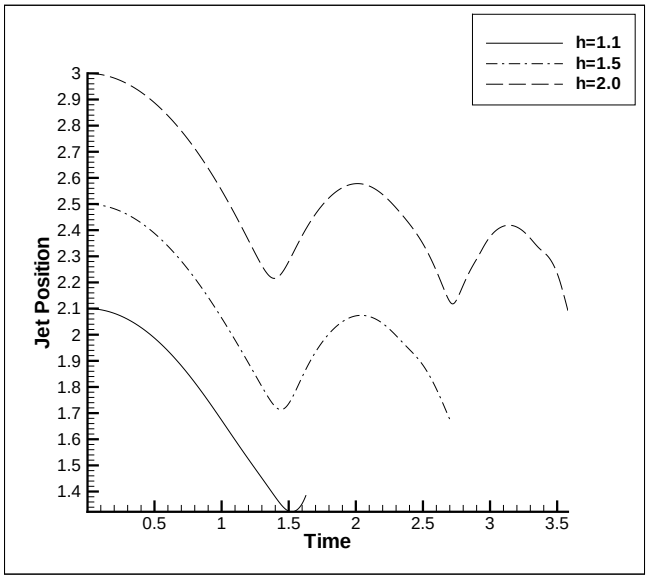

Figure 3.16: Position of jet point on z axis with time, $Re = 1$, $De = 1$, for varying height.

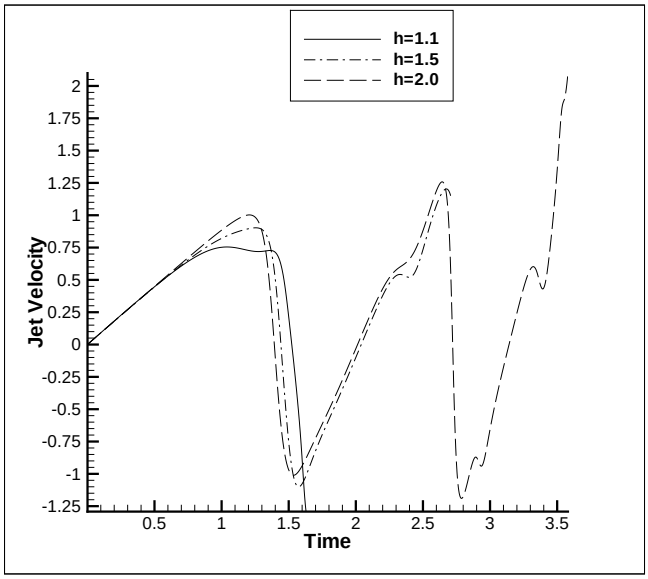

Figure 3.17: Jet velocities during collapse with varying height. $Re = 1$ and $De = 1$.

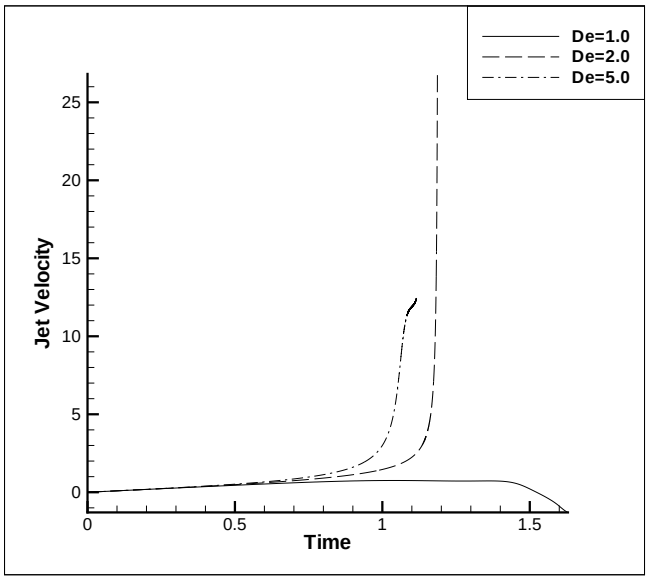

Figure 3.18: Jet velocities during collapse with varying De. $Re = 1$ and $h = 1.1$.

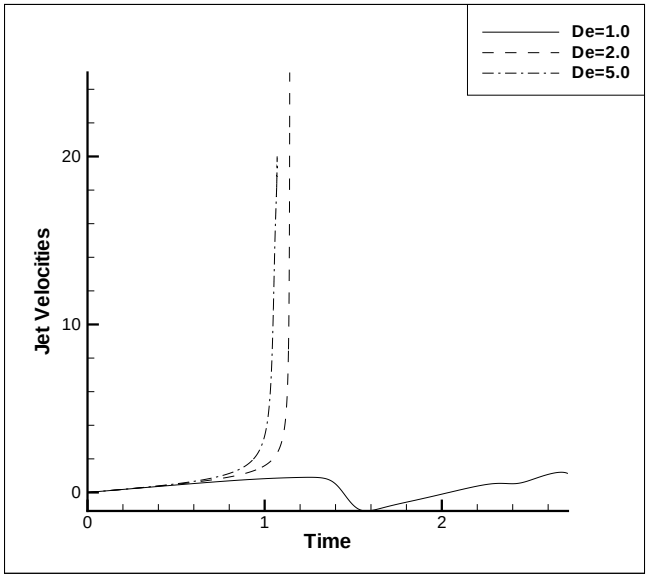

Figure 3.19: Jet velocities during collapse with varying De. $Re = 1$ and $h = 1.5$.

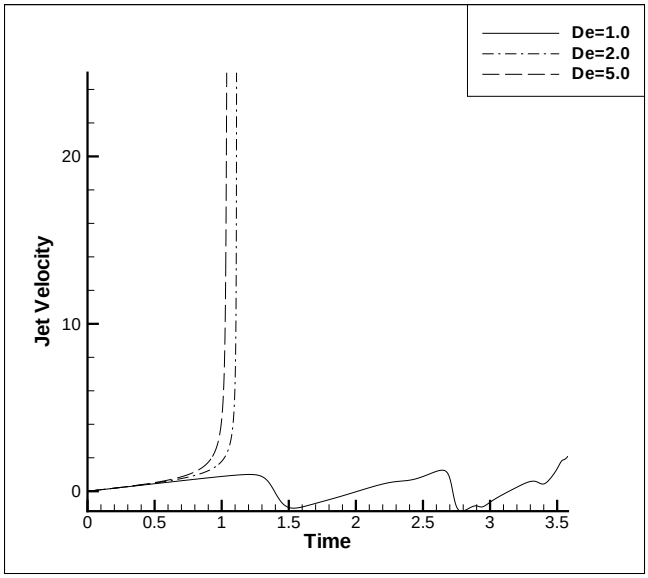

Figure 3.20: Jet velocities during collapse with varying De. $Re = 1$ and $h = 2.0$.

Figure 3.21 demonstrates the integrity of the solution with mesh refinement for the case $De = 1$, $Re = 1$ and $h = 1.5$. The differences in the jet velocity are negligible as the number of segments N is increased from $N = 40$ to $N = 100$.

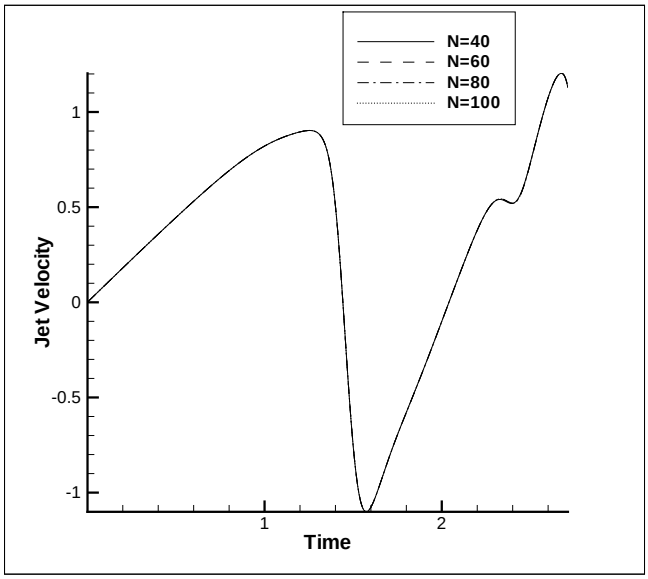

Figure 3.21: Jet velocity with different mesh refinements for $De = 1$, $Re = 1$, $h = 1.5$

Figure 3.22 shows the bubble profiles during collapse for $Re = 2.0$, $De = 0.5$. In a similar manner to Fig. 3.15, note the development of a sharp cusp on the bubble underside. However, despite being able to induce cusping, the reduced elastic effects are, in this case, unable to instigate bubble rebound.

Figure 3.23 shows the jet velocities for varying Reynolds numbers, with $De = 0.5$, $h = 1.1$. As expected, an increase in Reynolds number results in dynamics that increasingly resemble the inviscid case. The bubble changes from having a cusped underside with a rounded body (Fig. 3.22), to a shape with a pronounced jet formation (as previously observed in Fig. 3.4 for example).

Figures 3.24-3.26 show the bubble profiles for $Re = 0.2$ and $De = 5$ for $h = 1.1$, 1.5, and 2.0, respectively. Of course, one should be cautious of these lower Reynolds numbers which test the validity of the irrotational flow approximation. However, as mentioned, depending on the Deborah number, high velocity and hence high local Reynolds number flows are still permissible. Combined with the fact that vorticity generation is reduced on a free surface, these lower Reynolds numbers can still provide some important physical insights. As in the previous case, a cusping of the underside of the bubble occurs which is more pronounced for smaller values of h. At $h = 1.1$

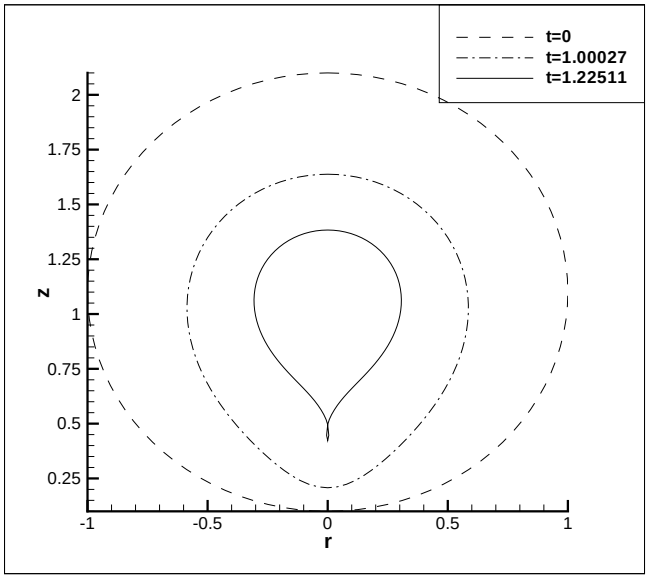

Figure 3.22: Bubble surface profiles at different stages of collapse at a distance $h = 1.1$, $Re = 2$, $De = 0.5$.

(Fig. 3.24) a sharp cusp develops in the final stages. Until then the deformation is not quite as extensive as that seen in the $Re = 1$, $De = 1$ case, due to the increased viscous effects. At $h = 1.5$ (Fig. 3.25) cusp formation becomes noticeably less pronounced, while at $h = 2.0$ (Fig. 3.26), deformation is further reduced with the bubble remaining nearly spherical.

Figure 3.27 shows the jet positions during the collapse, for different distances from the wall. It can be seen that, as in the $Re = 1, De = 1$ case, the time between oscillations decreases slightly (i.e. the frequency of oscillation increases) with increasing distance from the wall, though the amplitude of oscillation remains very similar with varying h. Also, perturbations in the gradient of the jet position are visible in the $h = 1.1$ case. Studying the jet velocities, these becomes more evident as significant perturbations appear in the velocity near its peaks and troughs (Fig 3.28). Figure 3.29 allows the comparison of jet positions and velocities at $h = 1.1$, and the corresponding perturbations, to be made more easily. Initially, as the underside cusps and rebounds, the top and underside of the bubble begin to oscillate slightly out of phase. This disrupts the uniformity of the flow around the bubble and creates the perturbations in the jet velocities. In particular a large jump occurs during the second rebound stage at about $t = 4.2$. This results from the underside rebounding before the top and throwing fluid out from the bubble vicinity; this then aids the top in rebounding, causing a sharp increase in rebound velocity. The oscillation of the velocity at the North and South pole

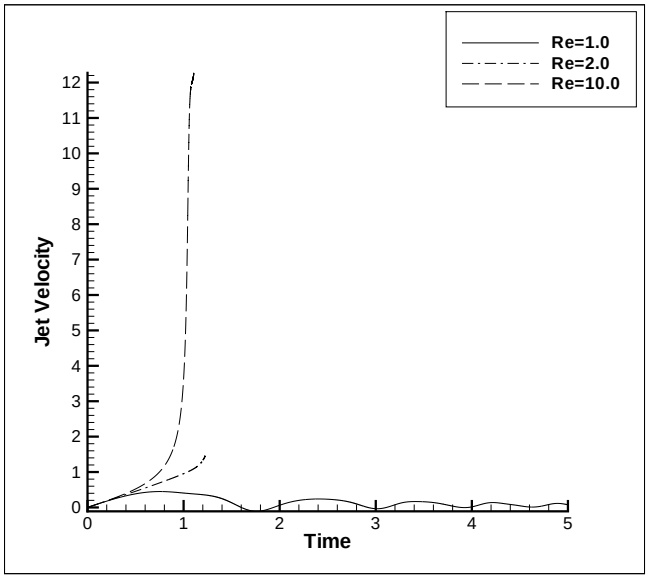

Figure 3.23: Jet velocities during collapse with varying Re. $De = 0.5$ and $h = 1.1$.

of the bubble are shown in Fig. 3.30. One can see a clear time lag between the time the top and the bottom of the bubble rebound (when the velocity is zero). From Fig. 3.28, we can see that for larger initial distances from the wall, the reduced deformation in the bubble shape means that this effect is less prominent.

Figures 3.31-3.33 show jet velocities at different distances for a selection of Deborah numbers, for $Re = 0.2$. For $h = 1.1$ the perturbations in the jet velocity at $De = 5.0$ can be significantly damped by decreasing De, as the viscous forces become more dominant. So much so, that for $De = 1.0$ the jet velocities tend toward to zero, indicating that the system is tending to a steady state. The effect of the damping can be seen at each distance h, and in fact at $h = 2.0$, the influence of the wall is suppressed to the extent that the velocity profile is almost indistinguishable from the spherical case.

The Effect of the Deformation Terms

In this section, we will briefly discuss the effect of the upper convected Maxwell (UCM) viscoelastic model on bubble dynamics. Namely by including the missing deformation terms in the material Maxwell model. Given the diagonal form of stress tensor on the shear-stress-free free surface, the normal-normal component of the extra stress, T_{nn}, is found from

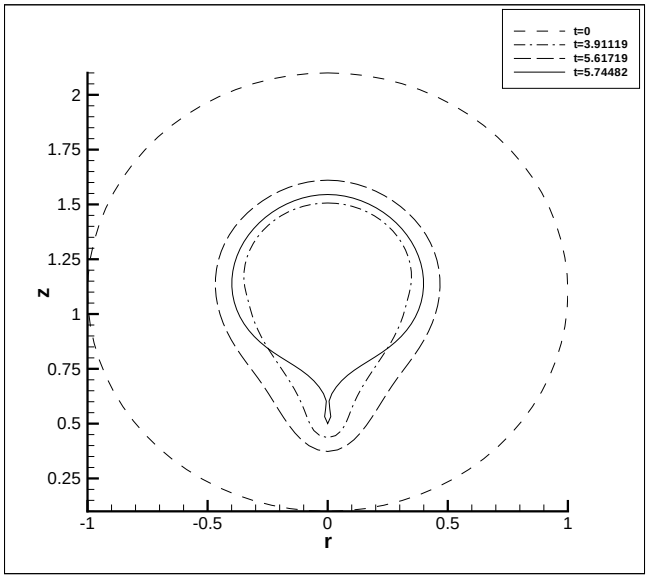

Figure 3.24: Bubble surface profiles at different stages of collapse at a distance $h = 1.1$, $Re = 0.2$, $De = 5$.

$$De\left(\frac{DT_{nn}}{Dt} - 2T_{nn}\dot{\gamma}_{nn}\right) + T_{nn} = \frac{1}{Re}\dot{\gamma}_{nn}. \tag{3.8}$$

Figure 3.34 shows the bubble profiles and jet velocity for $De = Re = 1$, $h = 1.1$, using the UCM model. Firstly, note that the primary characteristics associated with viscoelastic bubble collapse are still predicted; namely the oscillation of the bubble radius with time and the development of a cusped underside near the wall. Making more quantitative comparisons between the two models, we find that the dynamics predicted by the UCM model are more damped than those of the material model. Not only are the jet velocities (Fig. 3.34(b)) lower in amplitude, but deformation in the bubble is inhibited to the extent that the bubble no longer "pinches off", as in the material case (see Fig. 3.15). Consequently, the computation continues for longer with the bubble assuming a thin prolate tear-drop shape, with a longer, sharper cusp (Fig. 3.34(a)).

Such behaviour is not unexpected because, as can be seen from Eqn. (3.8), the additional deformation terms resemble the viscous rate of deformation term on the right-hand side. Hence one would anticipate that dynamics are not dissimilar to those observed when viscous effects are increased.

Figure 3.35 shows the bubble profiles and jet velocities when the initial distance of the bubble from the wall is increased to $h = 2.0$. The usual response to increasing distance

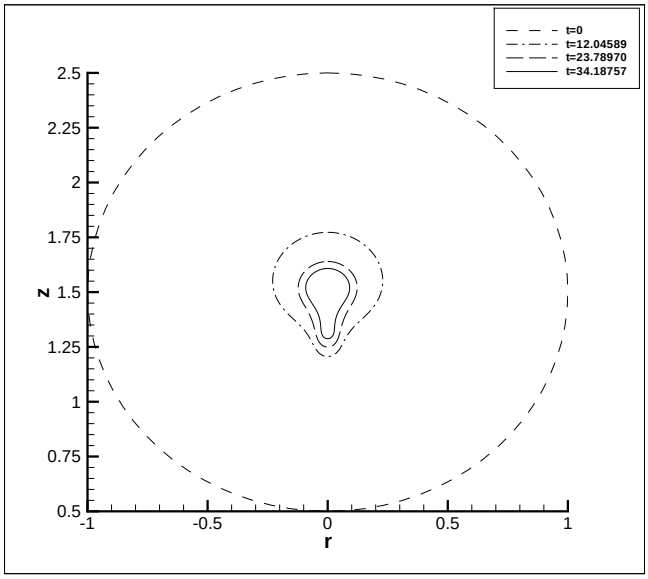

Figure 3.25: Bubble surface profiles at different stages of collapse at a distance $h = 1.5$, $Re = 0.2$, $De = 5$.

is observed. Firstly, deformation is reduced and the bubble remains close to spherical for most of its lifetime. Secondly, as a consequence of the reduced deformation, the jet velocity profile is more regular (see Fig. 3.35(b)) than in the $h = 1.1$ case (Fig. 3.34(b)). The perturbations in the velocity profile, that result from the unsynchronised oscillations of the bubble surface when close the wall, are no longer seen.

In summary, while the dynamics of the UCM and material models differ quantitatively, their behaviour and predictions are in general agreement and confirm the role of viscoelasticity on bubble collapse. The UCM model also predicts oscillatory bubble collapse, pronounced cusping, and perturbations to the jet velocity when near the wall.

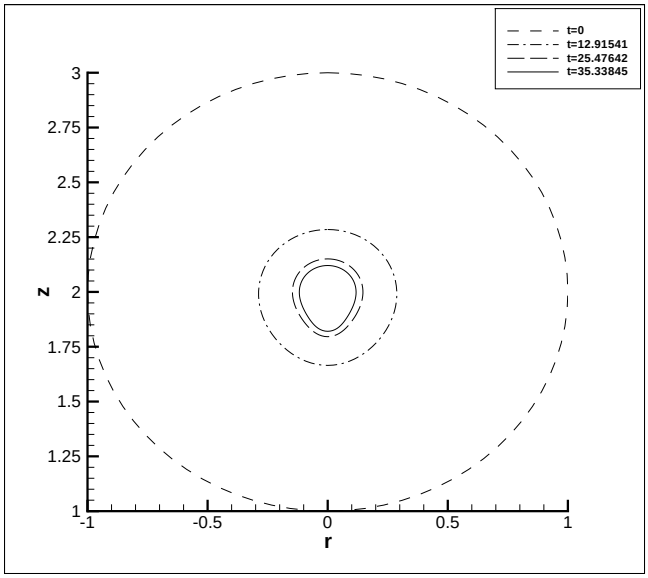

Figure 3.26: Bubble surface profiles at different stages of collapse at a distance $h = 2.0$, $Re = 0.2$, $De = 5$.

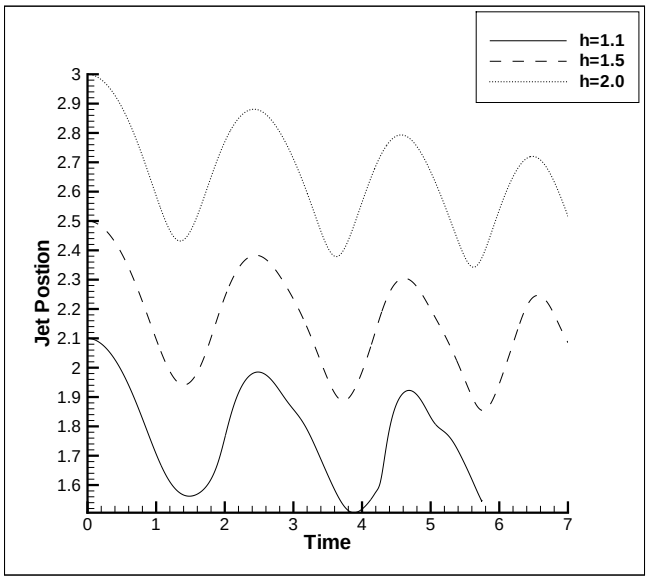

Figure 3.27: Position of jet point on z axis with time, $Re = 0.2$, $De = 5$, for varying height.

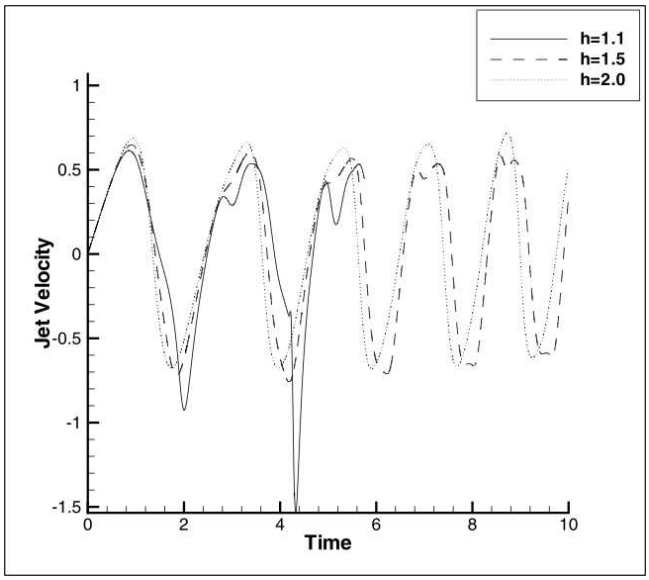

Figure 3.28: Jet velocities during collapse with varying height. $Re = 0.2$ and $De = 5$.

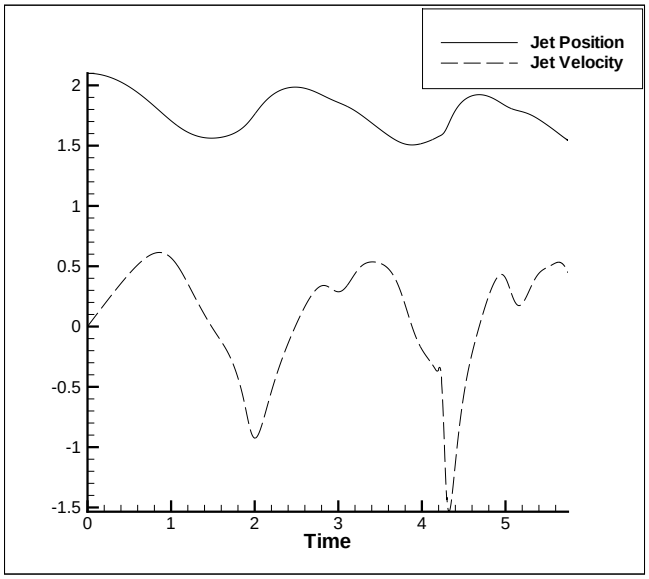

Figure 3.29: Comparison of jet positions and velocities, for $h = 1.1$, $Re = 0.2$ and $De = 5$.

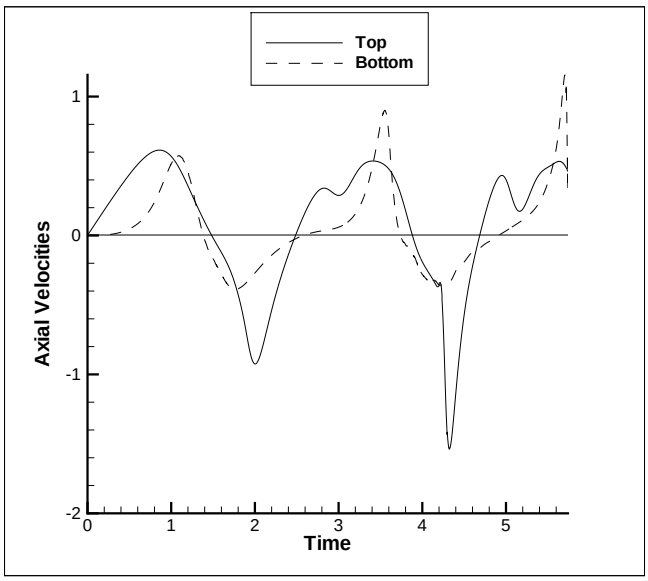

Figure 3.30: Comparison of North and South pole velocities, for $h = 1.1$, $Re = 0.2$ and $De = 5$.

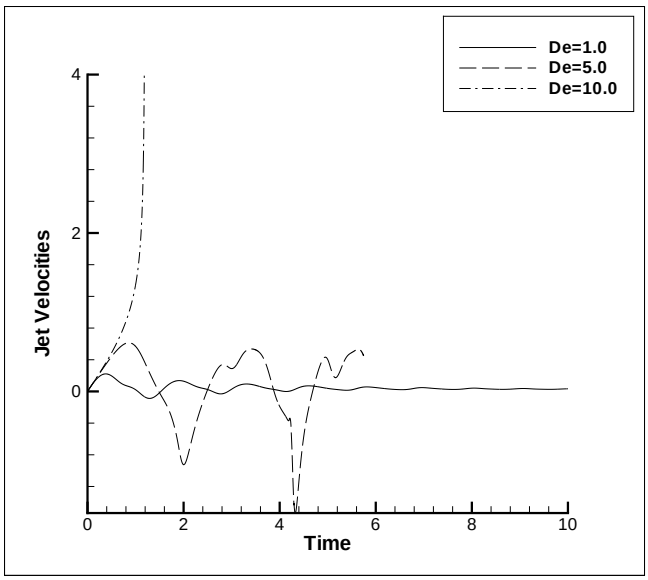

Figure 3.31: Jet velocities during collapse with varying De. $Re = 0.2$ and $h = 1.1$.

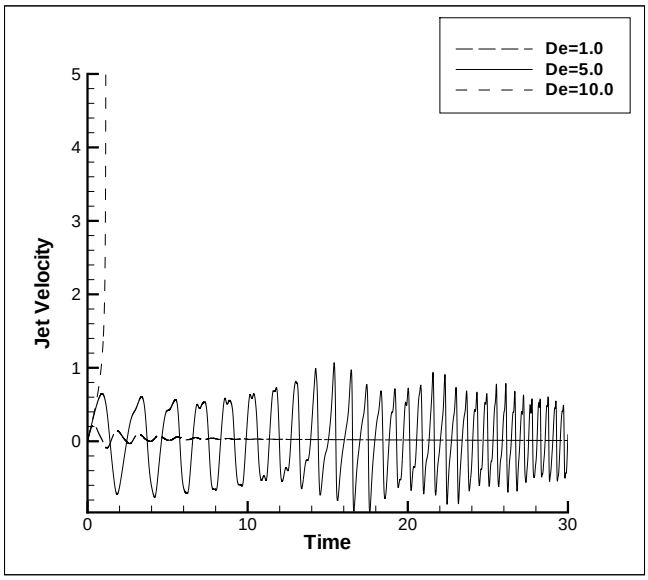

Figure 3.32: Jet velocities during collapse with varying De. $Re = 0.2$ and $h = 1.5$.

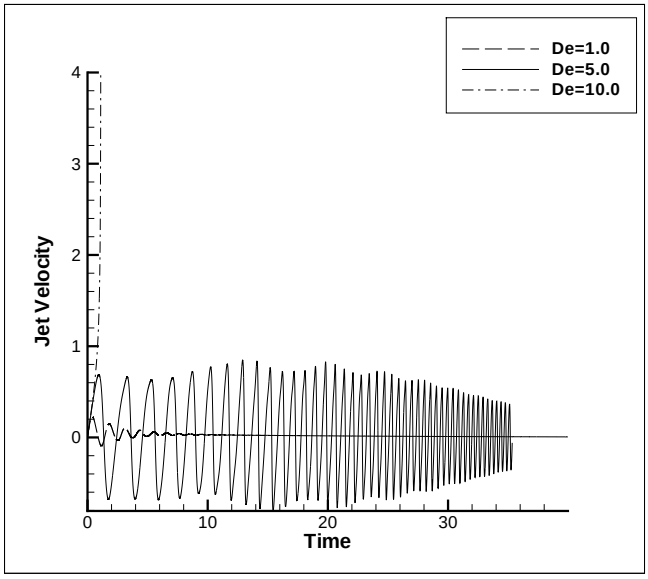

Figure 3.33: Jet velocities during collapse with varying De. $Re = 0.2$ and $h = 2.0$.

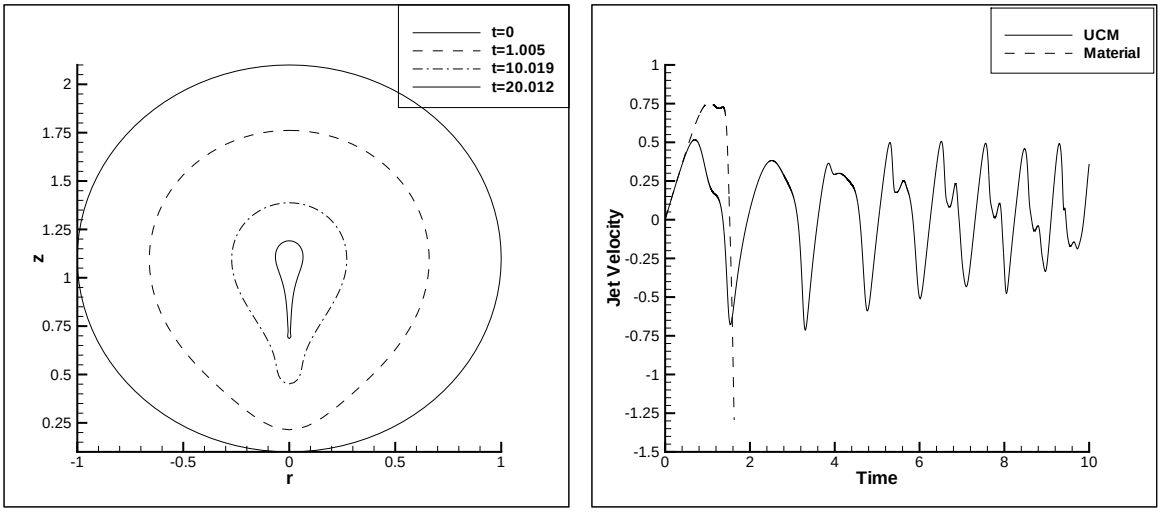

(a) Bubble surface profiles (b) Jet velocity

Figure 3.34: Bubble collapse near a wall using the UCM model. $De = Re = 1$, $h = 1.1$

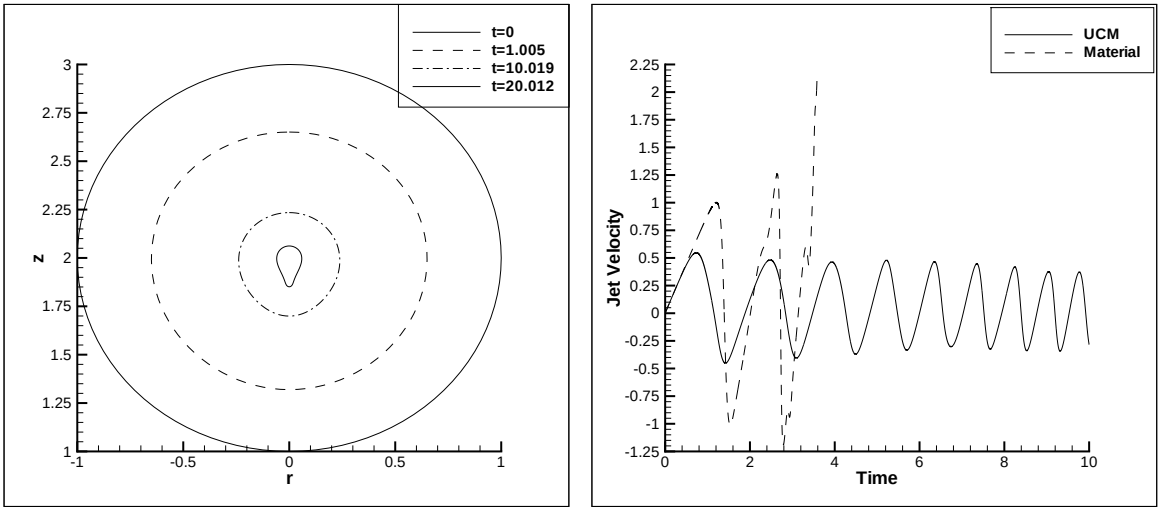

(a) Bubble surface profiles (b) Jet velocity

Figure 3.35: Bubble collapse near a wall using the UCM model. $De = Re = 1$, $h = 2$

3.3.4 The Pressure Field

The high pressures associated with bubble collapse are still considered to be a factor in phenomena such as cavitation damage. Therefore, it is important to study the pressure field surrounding the bubble and, interestingly, how this pressure field depends upon viscoelastic effects. The pressure field is calculated from the Bernoulli equation viz.,

$$p(\mathbf{x}) = -\rho\frac{\partial\phi}{\partial t} - \frac{\rho}{2}|\nabla\phi|^2 + p_\infty \tag{3.9}$$

The internal potentials ϕ are calculated at a selection of points using the boundary integral formula. Internal velocities can then be found using finite differences. To test the accuracy of the pressure contours produced, the spherical Rayleigh bubble in an infinite medium was initially considered. Figure 3.36 shows the pressure contour plots for a radius of $R \approx (1/20)R_0$. Rayleigh [126] states that the pressure just outside the bubble at this radius should be approximately $p = 1260$. The contour plot shows a good agreement with this calculation.

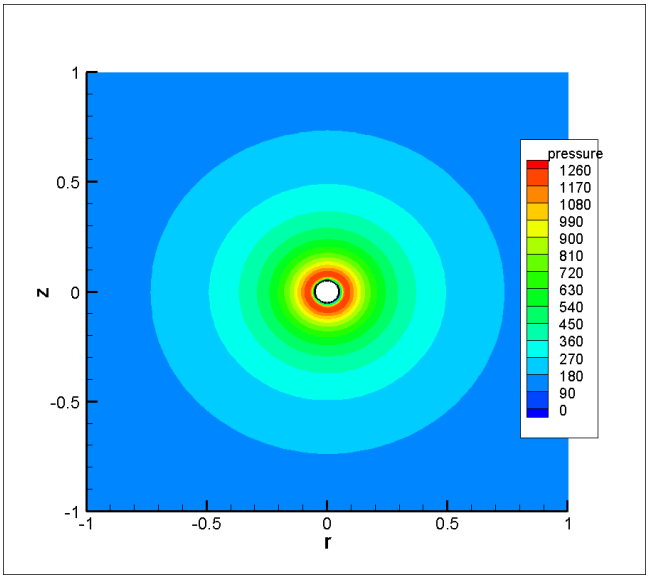

Figure 3.36: Pressure contours following the collapse of the Rayleigh bubble to a radius $R = \frac{1}{20}R_0$.

Considering the Newtonian case $Re = 10$, Figure 3.37 displays the pressure contours at distance $h = 1.1$ from the wall. The suppression of jet formation, and the resulting small bubble sizes attained mean that the pressures around the bubble are very large - of the order of those produced by the Rayleigh bubble. The high pressure regions

are indicative of regions of large accelerations and deformation. Expectedly therefore, we see a high pressure region on the top of the bubble (where the bulk of fluid is preferentially drawn) and on the underside of the bubble (where the cusping and high curvatures exist).

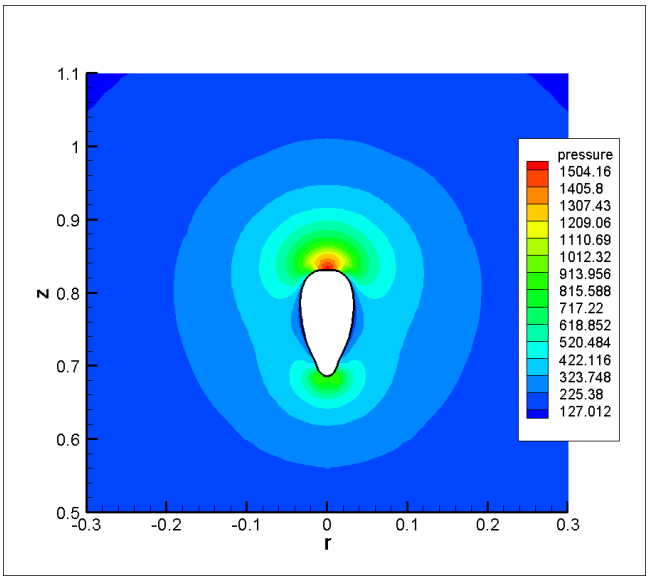

Figure 3.37: Pressure contours in the final stages of collapse, with $h = 1.1$, $Re = 10$, $De = 0$.

Pressure contours for $Re = 1, De = 1$ are displayed in Figures 3.38 and 3.39. The pressures are significantly smaller than the previous case as elastic effects prevent the catastrophic collapse and the associated high pressures. For $h = 1.1$ (Fig. 3.38) we see a high pressure region at the point of "pinch-off" - where the rate of surface deformation is the greatest.

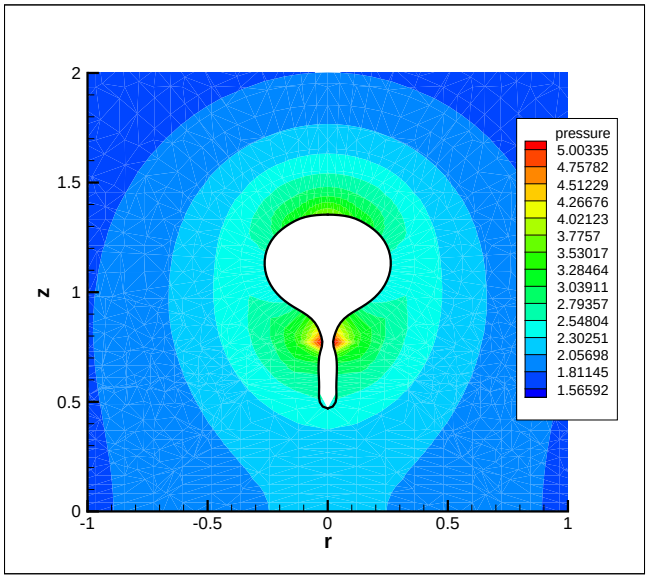

Figure 3.38: Pressure contours in the final stages of collapse ($t \approx 1.600$), with $h = 1.1$, $Re = 1$, $De = 1$.

At $h = 2.0$ (Fig. 3.39) the high pressure region is again found around the bubble underside, near the cusp. The larger curvatures in this region mean the surrounding pressures are slightly larger than in the $h = 1.1$ case. Figure 3.40 shows the maximum pressure in the field plotted with time. Note that close to the wall, there are perturbations in the maximum pressure much like those previously observed in the jet velocity profiles, indicative of the increased deformation in the bubble near the wall. The variation in the maximum pressure then becomes more regular as the distance from the wall is increased and bubble deformation is decreased.

Figure 3.41 shows the pressure contours for $Re = 0.2, De = 5$ at a distance $h = 1.1$. A higher pressure region at the cusp is noticeable as before. Again the pressures remain small in comparison to the Newtonian case, as the rebounding bubble prevents the build up of large pressures. Fig. 3.42 shows the maximum pressure variation with time. As in the $De = 1$, $Re = 1$ case, we see perturbations in the pressure close to the wall, which diminish with increasing distance. Also, the further the bubble is from the

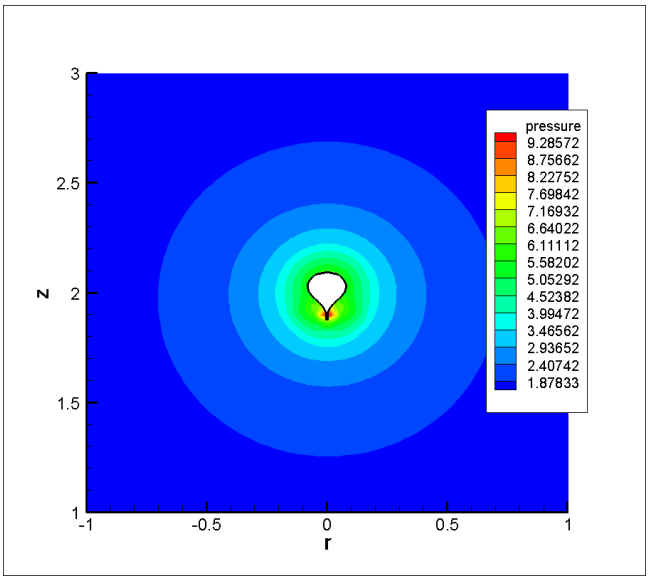

Figure 3.39: Pressure contours in the final stages of collapse ($t \approx 3.580$), with $h = 2.0$, $Re = 1$, $De = 1$.

wall, the decrease in deformation results in a slight decrease in the maximum pressure on average.

From the results presented in this section it is clear that viscoelasticity has a significant effect on the dynamics of bubbles near a rigid wall. Jet formation can be completely suppressed and entirely different dynamics can emerge. There are marked changes in bubble shape with varying distances from the wall. For example, close to the wall one can observe cusping in the bubble underside, while at greater distances, the bubble can remain near sphericity. Viscoelastic effects can prevent the catastrophic collapse observed in Newtonian fluids and the subsequent build up of large pressures. Given these results, it is clear that fluid rheology is the dominating factor in bubble dynamics, rather than the presence of a rigid boundary.

3.4 Conclusions

The effect of viscoelasticity on the dynamics of cavitation bubbles near boundaries has been studied. We validate the inviscid predictions with the literature and note the effect of viscosity in inhibiting jet formation and jet speed. For the values of Reynolds number and Deborah number necessary to induce oscillation, we find that during collapse near a wall the liquid jet will not form. Instead, the underside of the bubble can cusp and cause parts of the bubble surface to oscillate out of phase. The incoherent

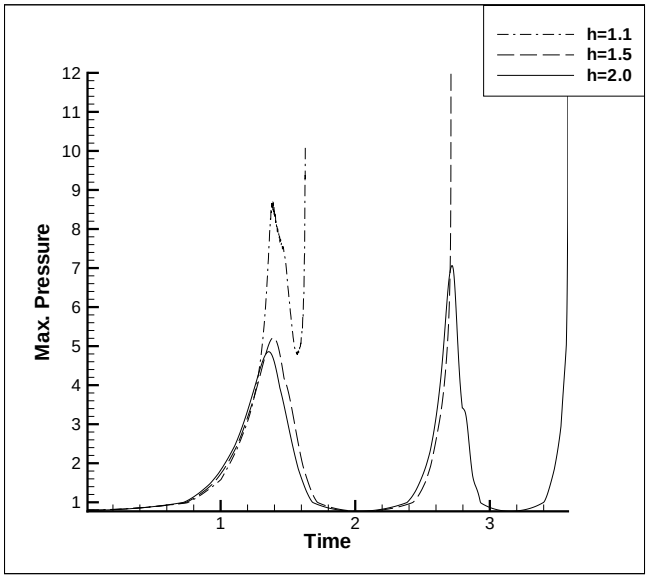

Figure 3.40: Maximum pressure with time at different heights $Re = 1$, $De = 1$.

oscillations disrupt flow around the bubble causing perturbations in its position and velocity profiles. The cusping and perturbations are more noticeable closer to the wall, and less perceptible as one moves further away. Increasing viscous effects can prevent large deformations in bubble shape, regardless of distance from the rigid wall; and so reduce the incoherent oscillations and perturbations in the velocity. Viscoelastic effects can prevent the catastrophic collapse and the associated high pressures seen in the Newtonian cases. The bubbles oscillate near the wall for a significant period of time, without significant changes in volume. For some parameters, the results suggest that a steady state can be attained, as inertial forces become balanced by the elastic and viscous forces.

The implications of this investigation to cavitation damage are clear. The suppression of the liquid jet and the lower velocities and pressures suggest that viscoelasticity has a mitigating effect. Although this has been proposed experimentally by Williams et al. [165], this chapter is the first attempt to predict these effects using a mathematical model for bubble collapse in viscoelastic fluids. Provided the parameters are such that elastic rebound of the bubble can occur, velocities and pressures will not be as large as the inviscid case - and, consequently, one can postulate that cavitation damage will be less prominent.

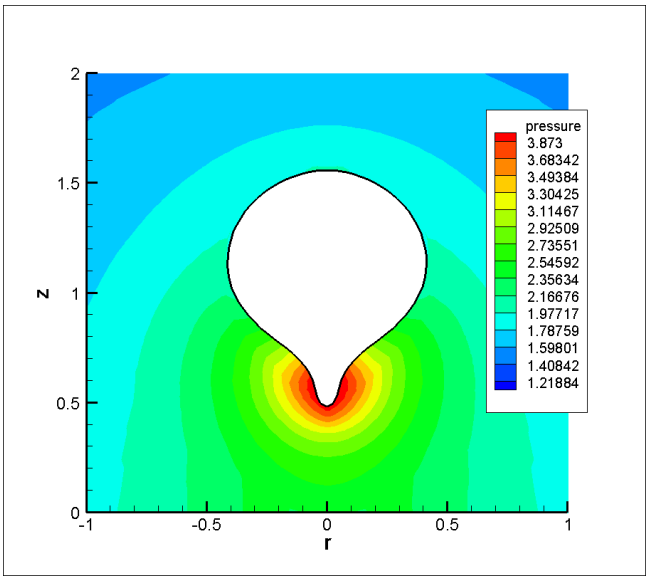

Figure 3.41: Pressure contours in the final stages of collapse ($t \approx 5.720$), with $h = 1.1$, $Re = 0.2$, $De = 5$.

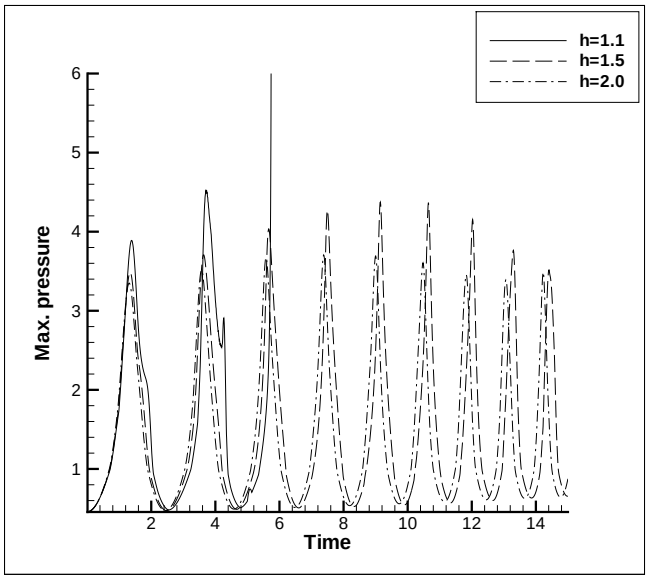

Figure 3.42: Variation of maximum pressure with time at different heights: $Re = 0.2$, $De = 5$.

Chapter 4

The Effect of Viscoelasticity on the Dynamics of Two Gas Bubbles Near a Rigid Boundary

4.1 Introduction

In reality, bubbles do not occur in isolation but in large numbers or bubble clouds. Given the importance of bubble dynamics in science, industry and medicine, and the implications to cavitation damage, a theoretical understanding of bubble-bubble interaction, as well as the bubble-boundary interaction, is extremely important. Also, in many practical situations, the ambient fluid is not ideal and fluid rheology plays a crucial role in the dynamics. Many important fluids (oils, lubricants, blood) are best modelled by non-Newtonian and viscoelastic constitutive equations. Multi-bubble dynamics have been studied numerically in the literature for some time. For example Bunner and Tryggvason [39] undertake a numerical study of the dynamics of bubbly flows, while Lu et al. [99] consider the effect of bubbles on wall drag in turbulent channels. The focus has tended towards studying the effect of bubbles on the fluid flow, and not on the near wall bubble dynamics and mechanisms of cavitation damage, such as jet formation. Blake et al. [16] use a boundary element technique to describe the growth and collapse of two cavitation bubbles near a rigid wall in an inviscid fluid. The resulting dynamics and jet formation show good agreement with experiment. Zhang and Zhang [172] consider the same problem, but include the effect of surface tension. They note that surface tension resists deformation in the cavity, as well as causing

faster collapse.

In this chapter, a numerical investigation is undertaken to determine the effect of viscoelasticity on multi-bubble dynamics near a rigid boundary. The boundary element method described in Chapter 2, which allows for the inclusion of viscoelastic effects, is extended to deal with multi-bubble geometries. However, in this chapter we only present results for the dynamics of *two* bubbles situated on an axis of symmetry near a wall.

4.2 Mathematical model

The fluid domain Ω surrounding the bubbles is assumed to be incompressible and the motion irrotational. It follows from the conservation of mass that there exists a velocity potential ϕ which satisfies Laplace's equation:

$$\nabla^2 \phi = 0, \tag{4.1}$$

in the region Ω. By Greens theorem, there exists an integral solution to (4.1), defined in terms of the boundary integral [113],

$$c(\mathbf{p})\phi(\mathbf{p}) = \sum_{i=1}^{N} \int_{\partial\Omega_i} \left(\frac{\partial \phi}{\partial n}(\mathbf{q}) G(\mathbf{p},\mathbf{q}) - \phi(\mathbf{q}) \frac{\partial G}{\partial n}(\mathbf{p},\mathbf{q}) \right) dS_i \tag{4.2}$$

where $\partial\Omega_i$ is the surface of bubble i, and the constant $c(\mathbf{p})$ is given by

$$c(\mathbf{p}) = \begin{cases} 2\pi & \text{if } \mathbf{p} \in \partial\Omega_i, \\ 4\pi & \text{if } \mathbf{p} \in \Omega \backslash \partial\Omega_i \end{cases}$$

In 3D, the appropriate Greens function $G(\mathbf{p},\mathbf{q})$ is given by

$$G(\mathbf{p},\mathbf{q}) = \frac{1}{|\mathbf{p}-\mathbf{q}|} + \frac{1}{|\mathbf{p}'-\mathbf{q}|}, \tag{4.3}$$

where $\mathbf{p}'$ is the image of $\mathbf{p}$ in the rigid boundary. Consequently the no penetration condition on the rigid boundary is immediately satisfied.
Given an initial potential ϕ_0 on the bubble surface $\partial\Omega_i$, the integral equation (4.2) can be solved numerically for the normal velocity to the surface $\frac{\partial \phi}{\partial n}$. The tangential velocity $\frac{\partial \phi}{\partial s}$ can be calculated given the potential ϕ_0, and the surface geometry $\partial\Omega_i$. Hence the

velocity on the surface is completely described. The fluid particles with position vector $\mathbf{x}$ initially on the surface $\partial\Omega_i$ will remain there. Consequently, the surface can be updated in a Lagrangian manner according to

$$\frac{D\mathbf{x}}{Dt} = \nabla\phi, \quad \mathbf{x} \in \partial\Omega_i. \tag{4.4}$$

A generalised Bernoulli equation provides an equation of motion from which the potential ϕ can also be updated in a Lagrangian manner

$$\rho\frac{D\phi}{Dt} = \frac{\rho}{2}|\mathbf{u}|^2 - T_{nn} + p_\infty - p_b. \tag{4.5}$$

Here T_{nn} is the normal normal component of the extra-stress, p_∞ is the fluid pressure far from the bubbles, and p_b is the internal bubble pressure. The viscoelastic constitutive equation for T_{nn} is restricted to Maxwell type, and is given by

$$\lambda\frac{DT_{nn}}{Dt} + T_{nn} = \mu\dot{\gamma}_{nn}. \tag{4.6}$$

Note that setting $\lambda = 0$ recovers a Newtonian fluid of constant viscosity μ.

In contrast to the previous chapters, we include the bubble growth from an initially small spherical bubble, in addition to studying the bubble collapse. In the previous chapter, bubble growth near the wall does not significantly impact upon bubble shape, and the shape just before collapse was very nearly spherical. Here however, the presence of an additional bubble adds an extra perturbation to the flow. The two deformable bubble surfaces are unlikely to remain spherical during growth and so the initial shapes just before collapse are unlikely to be spherical. The shape prior to collapse is likely to play an important role in the subsequent dynamics.

Bubble growth is driven by the internal bubble pressure p_b which, as in many physical situations, results from the non-condensible gas content of the bubble. Assuming this gas to be ideal and adiabatic, the bubble pressure can be expressed as

$$p_b = p_0\left(\frac{V_0}{V}\right)^\gamma, \tag{4.7}$$

where V_0 is the initial bubble volume, and γ is the ratio of specific heats - in this case taken to be $\gamma = 1.25$.

As a consequence of also modelling bubble growth, the physical variables in the above equations are non-dimensionalised in a slightly different way to that described in Chap-

ter 2, viz.,

$$\begin{aligned} t^* &= \frac{t}{R_m}\left(\frac{p_\infty}{\rho}\right)^{1/2}, \\ p^* &= \frac{p}{p_\infty}, \\ \phi^* &= \frac{\phi}{R_m}\left(\frac{\rho}{p_\infty}\right)^{1/2}, \end{aligned} \tag{4.8}$$

where R_m is the maximum radius a single gas bubble would attain in an inviscid, infinite fluid domain. The subsequent non-dimensional equations are then given by (dropping asterisks)

$$\frac{D\phi}{Dt} = 1 + \frac{1}{2}|\mathbf{u}|^2 - T_{nn} - \epsilon\left(\frac{V_0}{V}\right)^\gamma, \tag{4.9}$$

where T_{nn} is found from

$$De\frac{DT_{nn}}{Dt} + T_{nn} = \frac{1}{Re}\dot{\gamma}_{nn}. \tag{4.10}$$

The dimensionless parameters for the problem (slightly different to the previous chapters) are defined viz.: the Deborah number,

$$De = \frac{\lambda}{R_m}\left(\frac{p_\infty}{\rho}\right)^{1/2}, \tag{4.11}$$

the Reynolds number,

$$Re = \frac{R_m(p_\infty\rho)^{1/2}}{\mu}, \tag{4.12}$$

and the bubble "strength"

$$\epsilon = \frac{p_0}{p_\infty}. \tag{4.13}$$

Initially, we consider two bubbles of small radii at rest. As mentioned, bubble growth is then driven by the internal compressed gas content. The initial conditions on the bubble surface are then $\phi(\mathbf{x}, 0) = 0$ and $T_{nn}(\mathbf{x}, 0) = 0$. The bubble strength of each bubble is taken to be $\epsilon = 100$ for all results in this study. Given this choice of ϵ we can find the initial bubble radius required for a single bubble in an infinite inviscid

fluid to expand to a maximum radius of $R_m = 1$. This then ensures a consistent non-dimensionalisation. To find the initial radius R_0, the following variation of the Rayleigh-Plesset equation is solved numerically,

$$\frac{\epsilon}{\gamma - 1}\left(R_0^{3\gamma} - R_0^3\right) = -1 + R_0^3. \tag{4.14}$$

For the stated values of γ and ϵ, Equation (4.14) provides an initial radius of $R_0 \approx 0.149$.

Figure 4.1 details the initial configuration. In the interests of efficient nomenclature, the bubbles shall be referred to as B_1 and B_2, with B_1 always referring to the bubble closest to the wall. The heights h_1 and h_2 are the respective initial distances from the wall to each bubble centroid.

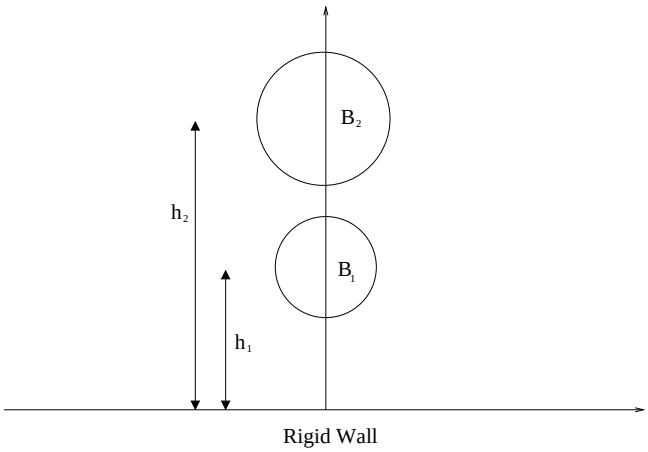

Figure 4.1: Schematic diagram detailing initial configuration.

Equation (4.2) is solved using collocation, with nodal points on the bubble surfaces and the potential ϕ interpolated using cubic splines. The discrete system is solved for the normal velocity using Gaussian elimination. The tangential velocity and higher derivatives of ϕ are found using generalised centred difference formulae found in [89]. A fourth-order Runge-Kutta scheme is then used to update the bubble surface and potential using (4.4) and (4.9), respectively. In the presence of viscoelasticity ($De \neq 0$), the constitutive equation is updated using an implicit second-order time stepping method. The nodal points on the bubble surfaces are redistributed with respect to arclength at each time step and, as is necessary with such boundary integral schemes,

smoothing is periodically used to prevent the onset of numerical instability.

4.3 Numerical Results

4.3.1 Validation

An initial validation of the multi-bubble code is to compare the dynamics of two identical bubbles in an infinite expanse of fluid, with that of a single bubble near a rigid wall. The formulations are mathematically identical, but differ slightly in computation. In the rigid wall case, the boundary conditions on the wall are imposed by the inclusion of a mirror image of the bubble on the other side of the wall. To do this a single image term is added to the Green's function in the single bubble integral (Eqn. 4.3).
To validate the two bubble case, this second (mirror) bubble is explicitly modelled with its surface being summed over and updated in time in the usual way. Figure 4.2 shows the near identical jet velocities obtained in both cases.

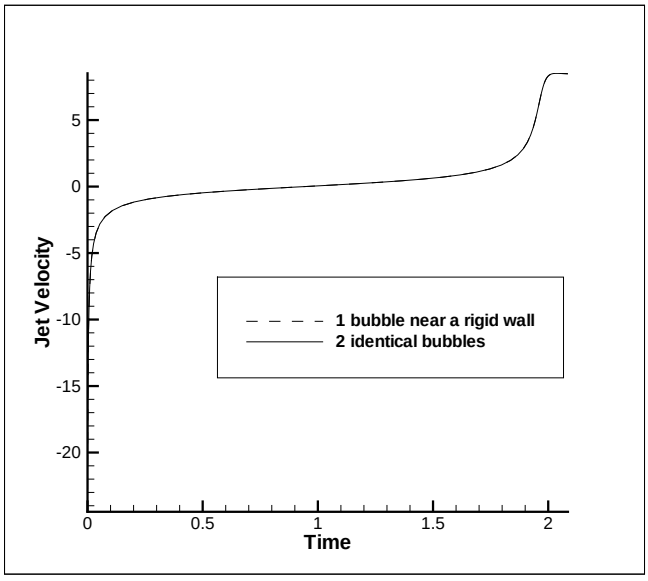

Figure 4.2: Jet velocities for a bubble near a rigid wall and one bubble near an identical bubble

To validate the code further, the results are compared with those of Blake et al. [16]. Their study concerns the interaction and dynamics of two inviscid bubbles near a rigid boundary.

In the paper of Blake et al. [16], the lengths are scaled with respect to the maximum equivalent bubble radius. To prescribe the correct initial potentials to give the maximum bubble radii observed in experiment, the following Newton-Raphson iterative scheme is used,

$$\phi_i^{k+1} = \phi_i^k - [J^{-1}]^k (R_i - R_i^k), \tag{4.15}$$

where J is the Jacobian matrix element and is calculated using finite differences. Here R_i is the desired maximum radius of bubble i. It typically takes 3-4 iterations to attain an error in R_i^k of less than 0.5%. Note that the choice of scaling here is such that if B_2 has the largest radius, then $R_2 = 1$ with $0 < R_1 \leq 1$, and vice versa.

Two cases are presented here in the interest of validation. Figure 4.3 shows the bubbles shapes during the collapse of two approximately equal-sized bubbles near a wall. The results indicate that the lower bubble perceives the upper bubble as an identical one, and consequently acts much like an image system, with the collapse of the upper bubble resembling that near a rigid wall. The lower bubble behaves as if it were between two rigid parallel plates, and so begins collapse from the side, producing the observed elongated shape. Identical profiles are observed in Fig. 9(a) of Blake et al. [16]. Figure 4.4 shows the centroid motion of each bubble in time - again showing excellent agreement with [16].

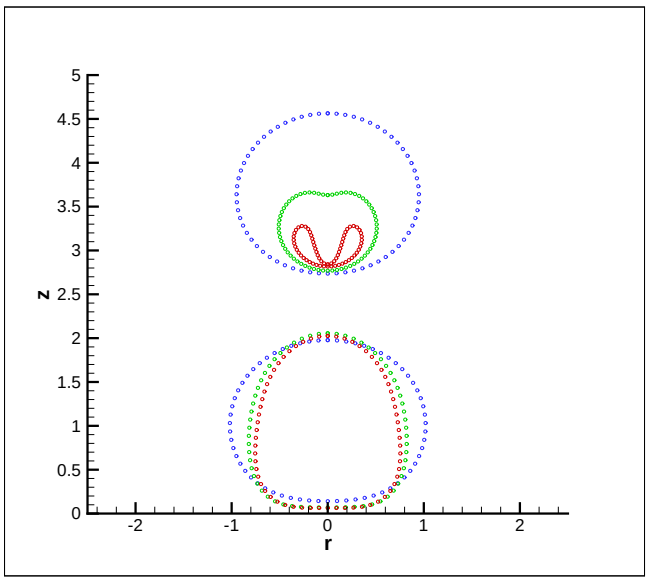

Figure 4.3: Bubble shapes of two approximately equal-sized bubbles near a rigid boundary. $h_2 = 0.99$, $h_1 = 3.60$, $R_1 = 0.94$. Different colours indicate different instances in time.

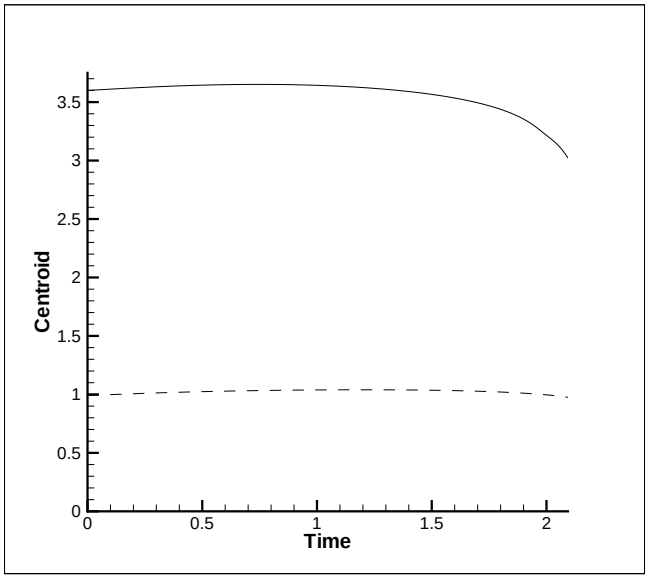

Figure 4.4: Evolution of bubble centroids. $h_2 = 0.99$, $h_1 = 3.60$, $R_1 = 0.94$

Figure 4.5 shows the bubble shapes for two different-sized bubbles near a rigid wall. The dynamics are markedly different. The growth near the rigid boundary causes the flattening of the underside of the lower bubble. During the collapse, the fluid flow parallel to the rigid boundary is far less restricted than that in the normal direction. Consequently, an annular jet penetrates the lower bubble, while the upper bubble displays a marked protrusion on its underside. Figure 4.6 shows the variation of the bubble centroid with time. Again, these results are in excellent agreement with those of Blake et al. [16].

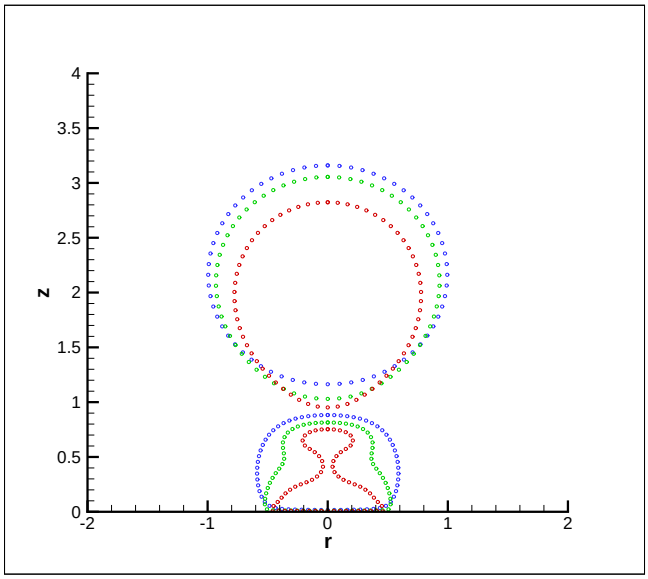

Figure 4.5: Bubble shapes of two different-sized bubbles near a rigid boundary. $h_2 = 0.47$, $h_1 = 2.17$, $R_2 = 0.57$. Different colours indicate different instances in time.

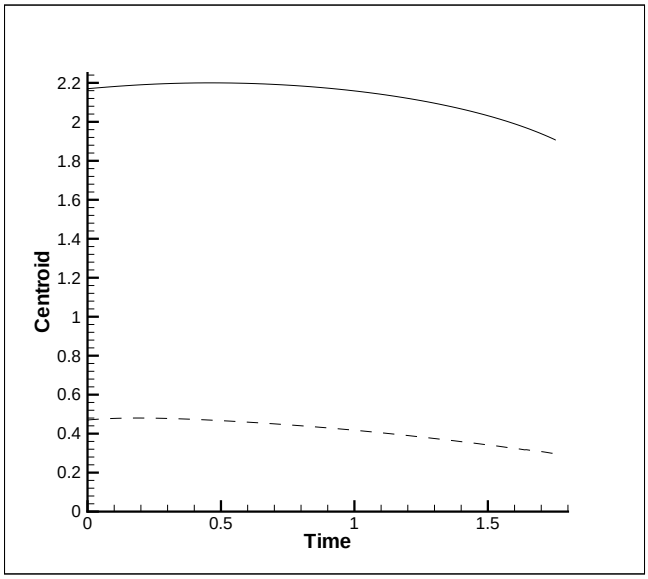

Figure 4.6: Evolution of bubble centroids. $h_2 = 0.47$, $h_1 = 2.17$, $R_2 = 0.57$.

4.3.2 The Growth and Collapse of Gas Bubbles near a Rigid Boundary

Equal-sized bubbles

In this section we present some numerical results showing the growth of two initially equal-sized gas bubbles. Firstly let us consider a fixed height configuration ($h_1 = 1.0$, $h_2 = 3.6$) and investigate the influence of fluid parameters. Figure 4.7 displays bubble profiles for the inviscid case ($De = 0$, $Re = \infty$). The profiles resemble closely those seen in Fig. 4.3 and so suggest that in this instance, the inclusion of non-condensible gas content has little effect on bubble dynamics. Figure 4.8 shows bubble profiles but with Newtonian effects included ($Re = 100$). Expectedly, given the high Reynolds number, the profiles resemble those for the inviscid case shown in Figures 4.7 and 4.3.

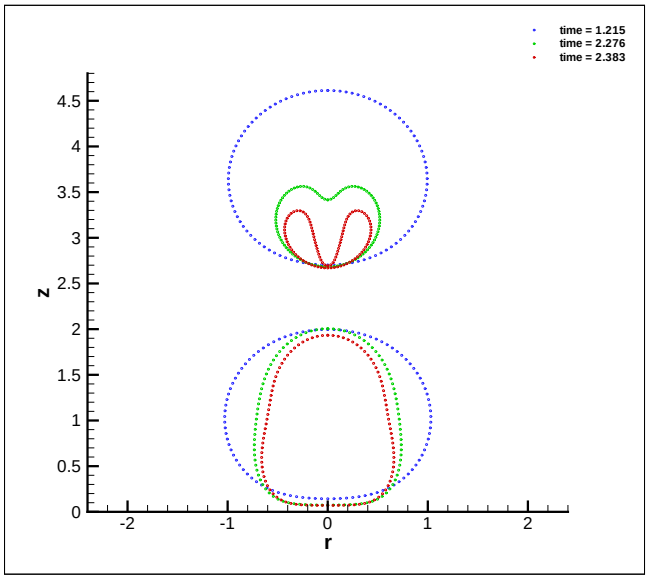

Figure 4.7: Bubble shapes for $De = 0$, $Re = \infty$, $h_1 = 1.0$, $h_2 = 3.6$. Different colours indicate different instances in time.

Figure 4.9(a) shows the North pole jet velocities of each bubble for $Re = 100$. One can plainly see the larger final velocity in B_2 that coincides with the liquid jet penetrating the bubble. The velocity vectors for the flow can then be seen in Fig. 4.9(b), and their notably larger values in the jet region. Additionally, the pressure contours show the creation of a high pressure region just above B_2. This is often seen in jet formation in single bubble dynamics near a wall, but here the maximum pressure is smaller due to the presence of B_1 and the associated restriction in fluid flow and acceleration.

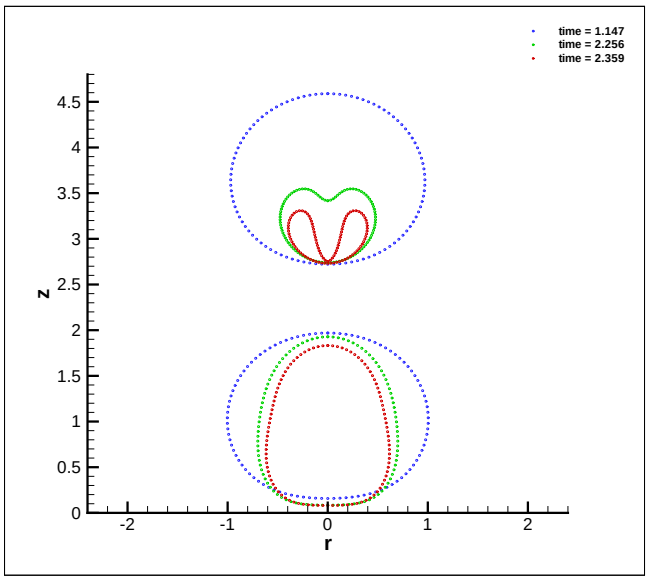

Figure 4.8: Bubble shapes for $De = 0$, $Re = 100$, $h_1 = 1.0$, $h_2 = 3.6$. Different colours indicate different instances in time.

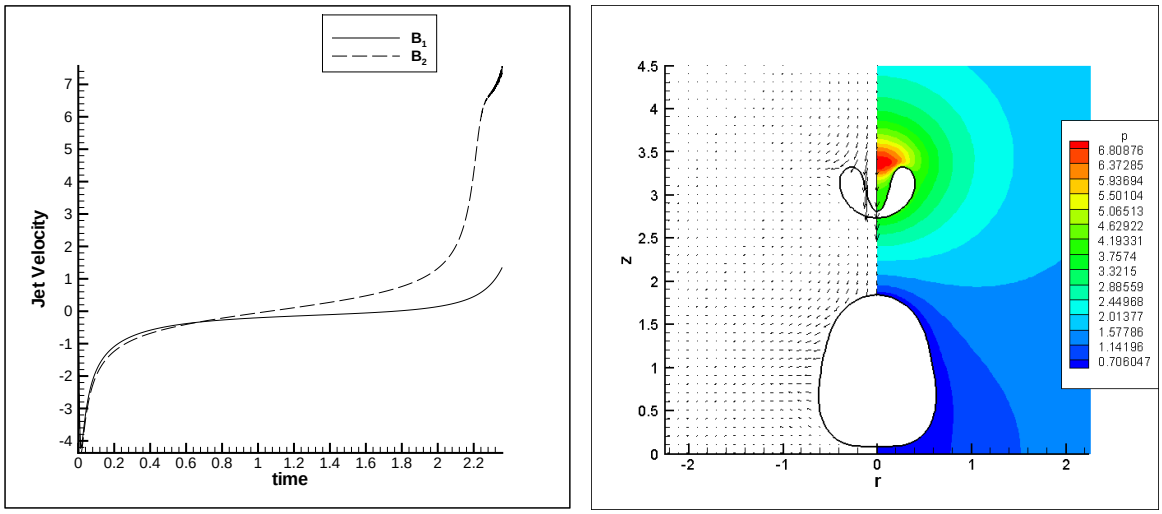

(a) North pole jet velocities.

(b) Velocity vector and pressure contour plots.

Figure 4.9: (a) North pole jet velocities, (b) velocity vector and pressure contour plots at $t \approx 2.3$ for $De = 0$, $Re = 100$, $h_1 = 1.0$, $h_2 = 3.6$

Figure 4.10 shows bubble profiles with the inclusion of viscoelastic effects for $De = 1$ and $Re = 2$. The dynamics are markedly different. A liquid jet penetrates B_1, while one only begins to form in B_2. This is almost the opposite occurrence to the previous cases where the jet would first penetrate B_2. In Fig 4.11(a) we see a large difference in the North pole jet velocities as the velocity rapidly grows in B_1, but in B_2 it becomes negative as the bubble begins to rebound. As we have seen in previous chapters, bubble rebound is a well-known characteristic of viscoelastic bubble dynamics. The above behaviour can be explained as follows: During the growth phase the viscous dissipation prevents either bubble from attaining as large a volume as the previous cases. Consequently, bubble interaction between the two is considerably less - the main influence of B_1 therefore is the wall. In wanting to revert to a prior state, elastic forces then encourage collapse in the early stages, but as inertia quickly increases, they can do little to inhibit collapse and jet formation in the final stages. In B_2 meanwhile, due to its distance from the wall, a jet does not fully form and the bubble collapses until a combination of the elastic stresses and gas content on the bubble cause the bubble to rebound.

As is typical with jet formation, in Fig. 4.11(b) we see a high pressure region develop above B_1, whereas around B_2, the pressure is considerably lower and more uniform.

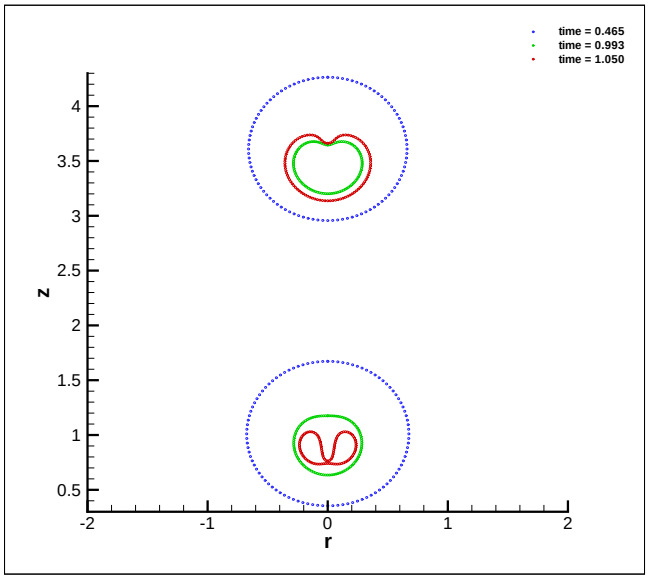

Figure 4.10: Bubble shapes for $De = 1$, $Re = 2$, $h_1 = 1.0$, $h_2 = 3.6$. Different colours indicate different instances in time.

In Figure 4.12 the Deborah number is increased to $De = 2.5$. We see that the general

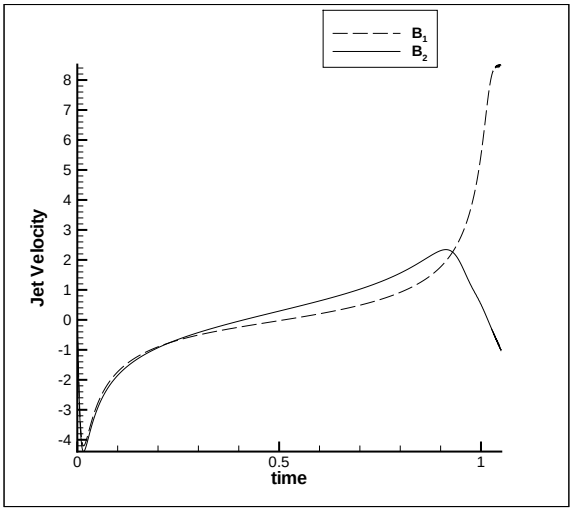

(a) North pole jet velocities.

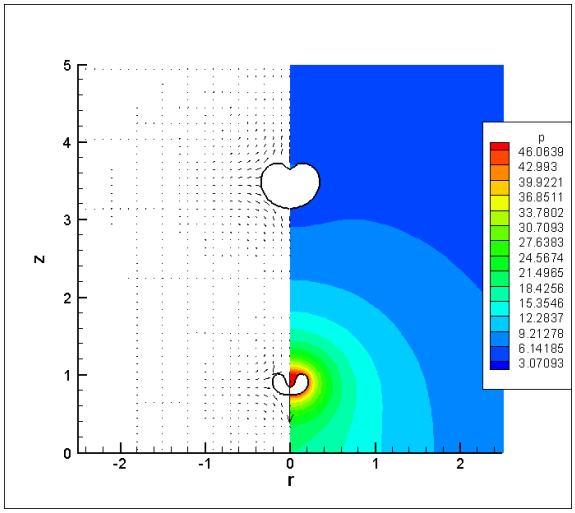

(b) Velocity vector and pressure contour plots at $t \approx 1.04$.

Figure 4.11: North pole jet velocities and velocity vector and pressure contour plots for $De = 1$, $Re = 2$, $h_1 = 1.0$, $h_2 = 3.6$

profile shape reverts back to dynamics similar the Newtonian cases - a jet forms first in B_2 but not in B_1. In this case though, note that B_1 is of a much smaller size than that attained in a Newtonian fluid. Thus the growth/collapse process occurs more quickly, with jet impact occurring at $t \approx 1.36$ in the viscoelastic case and $t \approx 2.36$ in the Newtonian ($Re = 100$). In the growth phase the larger elastic contribution counteracts viscous dissipation, consequently the bubbles grow to a slightly larger size than in the $De = 1$ case (but still smaller than the Newtonian), and so interaction between the bubbles is greater. The influence of B_2 on B_1 then inhibits jet formation in B_1 as in the Newtonian case. The high pressure region above B_2 (Fig. 4.13(b)) is also greater in magnitude than in the Newtonian case. This is most probably due to the increased freedom of the ambient fluid, as the influence of B_1 is reduced due to its smaller size. The jet velocities here (Fig. 4.13(a)) bear semblance to the Newtonian case (Fig. 4.9(a)) as contributions from the extra-stress are in the most part dwarfed by the high inertia during the growth and once again during collapse.

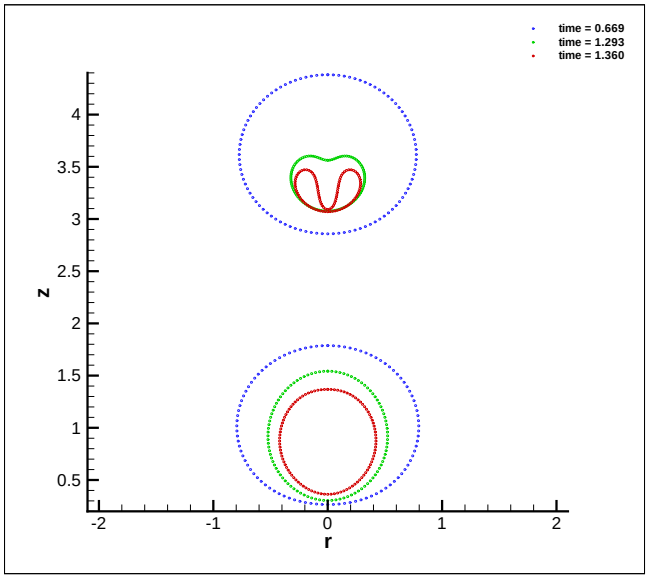

Figure 4.12: Bubble shapes for $De = 2.5$, $Re = 2$, $h_1 = 1.0$, $h_2 = 3.6$. Different colours indicate different instances in time.

Now let us consider the dynamics of equal-sized bubbles, with fixed fluid parameters $De = 1$, $Re = 2$, at varying height configurations. Figure 4.14 shows bubble profiles for $h_1 = 0.5$, $h_2 = 2.0$. Note the jet formation in B_1, but given the close proximity of B_2, B_2 itself deforms considerably into a heart-like shape. Evidently, the underside has deformed inwards towards the central axis as a result of the fluid flow forming the jet of B_1. Meanwhile, the influence of the wall and B_1 means that a jet also begins to form in B_2.

We see in Fig. 4.15, as B_2 is moved further away to a distance $h_2 = 4.0$, and the influence of B_1 and the wall decrease, deformation in B_2 is minimal and the profile remains mostly spherical. The primary influence of B_1 is again the wall, and we see collapse with jet formation in a manner very similar to Fig. 4.14.

The two bubbles are now moved away from the wall slightly, with $h_1 = 1.0$ and $h_2 = 2.5$, in the hope that bubble-bubble interaction becomes more evident. This is the case in Fig. 4.16, where the profile of B_2 resembles closely that in Fig. 4.14, but now B_1, being further from the wall, is more susceptible to the influence of B_2. This is evidenced by the inception of an upwards directed jet on the underside of B_1, as well as a fully formed downward jet from the topside (indicating that the wall is still the dominant influence).

If B_2 is moved further away to $h_2 = 4.5$, as in Fig. 4.17, we see that B_1 is almost entirely influenced by the wall, with the formation of a single downward jet during

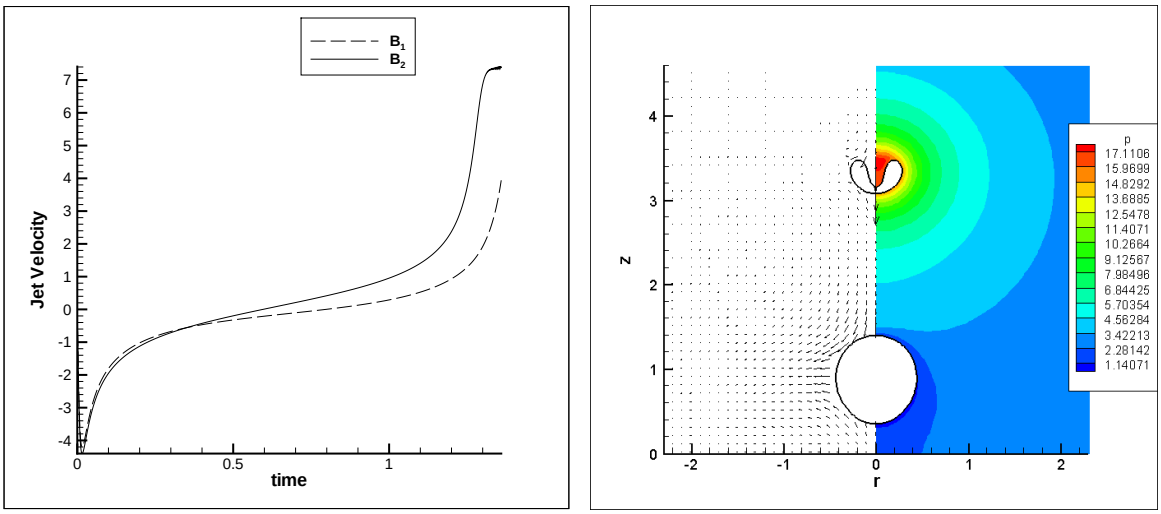

(a) North pole jet velocities.

(b) Velocity vector and pressure contour plots at $t \approx 1.35$

Figure 4.13: North pole jet velocities and velocity vector and pressure contour plots for $De = 2.5$, $Re = 2$, $h_1 = 1.0$, $h_2 = 3.6$

collapse. Meanwhile B_2, under little influence from the near wall dynamics, remains approximately spherical while oscillating due to the effect of the elastic stresses and gas content.

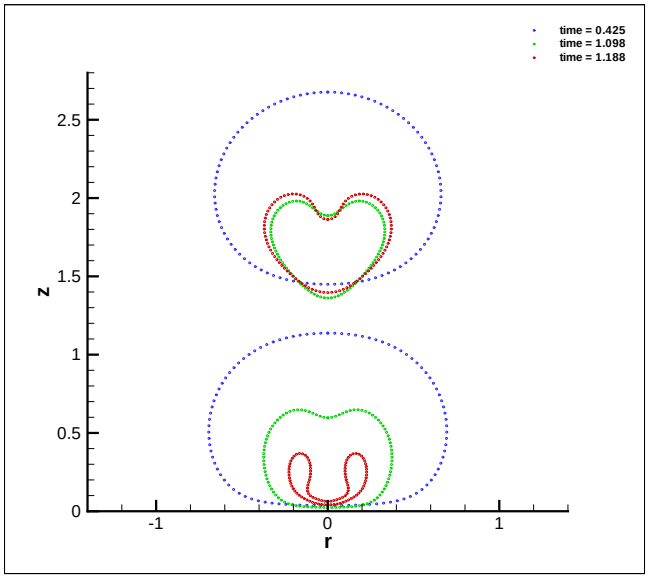

Figure 4.14: Bubble shapes for $De = 1$, $Re = 2$, $h_1 = 0.5$, $h_2 = 2.0$. Different colours indicate different instances in time.

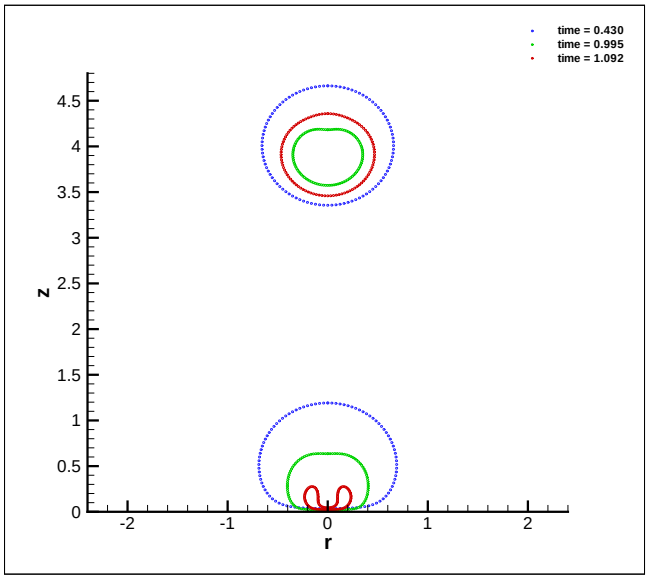

Figure 4.15: Bubble shapes for $De = 1$, $Re = 2$, $h_1 = 0.5$, $h_2 = 4.0$. Different colours indicate different instances in time.

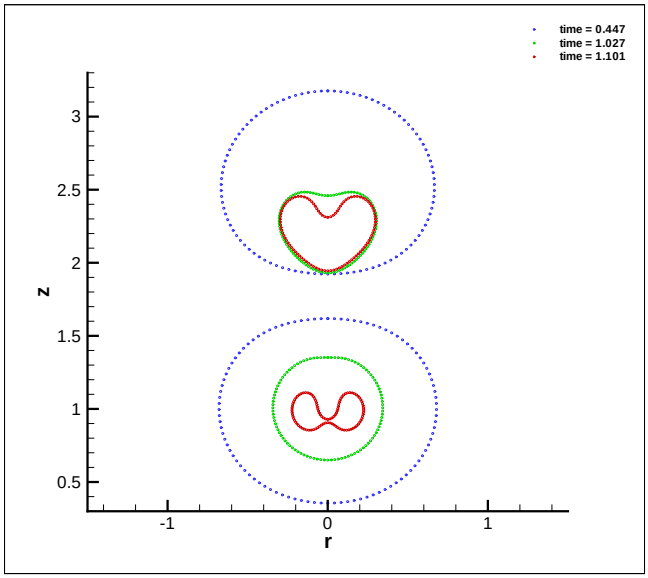

Figure 4.16: Bubble shapes for $De = 1$, $Re = 2$, $h_1 = 1.0$, $h_2 = 2.5$. Different colours indicate different instances in time.

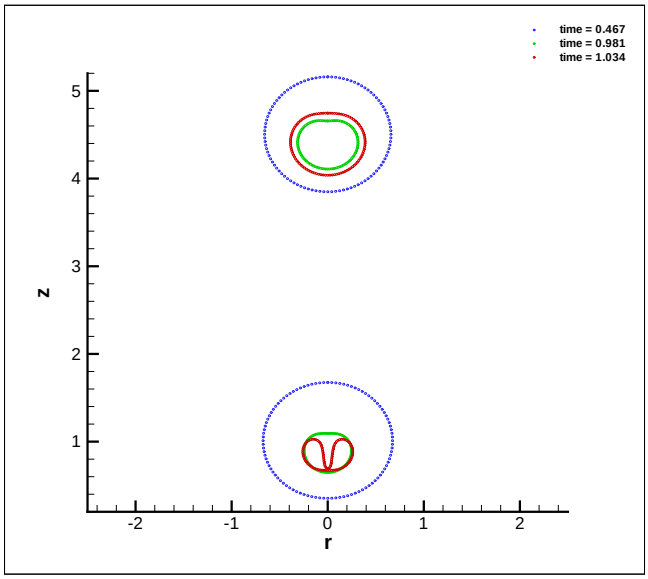

Figure 4.17: Bubble shapes for $De = 1$, $Re = 2$, $h_1 = 1.0$, $h_2 = 4.5$. Different colours indicate different instances in time.

Different-sized bubbles

We will now consider the dynamics of two initially different-sized bubbles. The initial radius of B_1, will always be half that of B_2. As previously, we consider a fixed height configuration and vary the fluid parameters at first. Then the influence of varying h_i for a fixed fluid will be studied.

Figure 4.18 shows bubble profiles for the inviscid case. The height configuration ($h_1 = 0.5$, $h_2 = 2.25$) is similar to Fig. 4.5. We see a similar annular jet penetrate the bubble from the side, but due to the presence of non-condensible gas content, the upper segment of B_1 then expands in volume. Consequently, this creates a much larger upper lobe than that seen in Fig. 4.5.

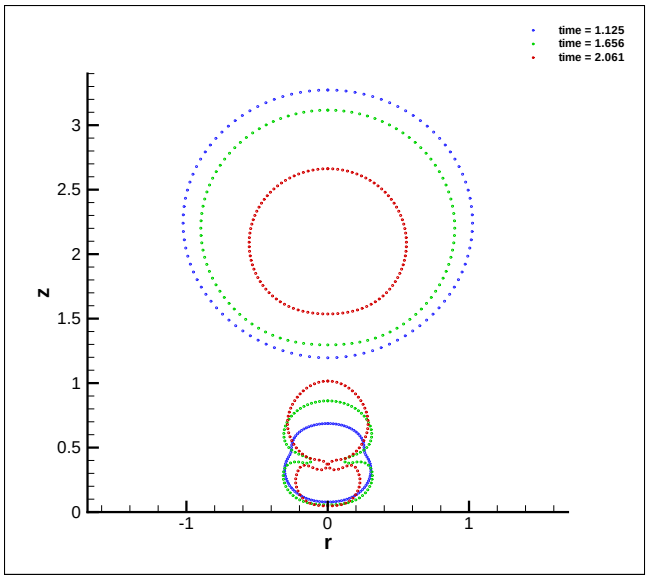

Figure 4.18: Bubble shapes for $De = 0$, $Re = \infty$, $h_1 = 0.5$, $h_2 = 2.25$. Different colours indicate different instances in time.

Figure 4.19(a) shows the North pole jet velocities, which remain small as no high speed axial jet forms. Similarly, the pressure contours remain small, with the highest pressure region developing above B_2, possibly anticipating jet formation.

Figure 4.20 shows the bubble profiles with the inclusion of Newtonian effects ($Re = 100$). In the equal bubble case there was little difference between the inviscid and Newtonian dynamics at $Re = 100$ (Figures 4.7 and 4.8). Here however, the dynamics between the two are drastically different. In B_1 there is no sideways annular jet - the bubble only becomes more prolate during collapse and in the final stage possible jet inception occurs on B_1's underside. In B_2 meanwhile, a downward jet (directed

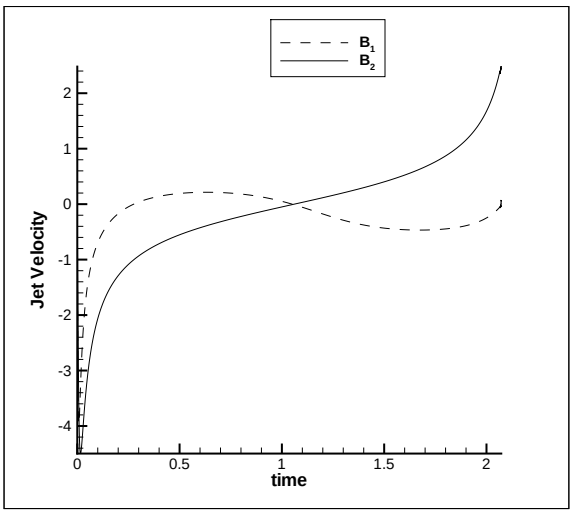

(a) North pole jet velocities.

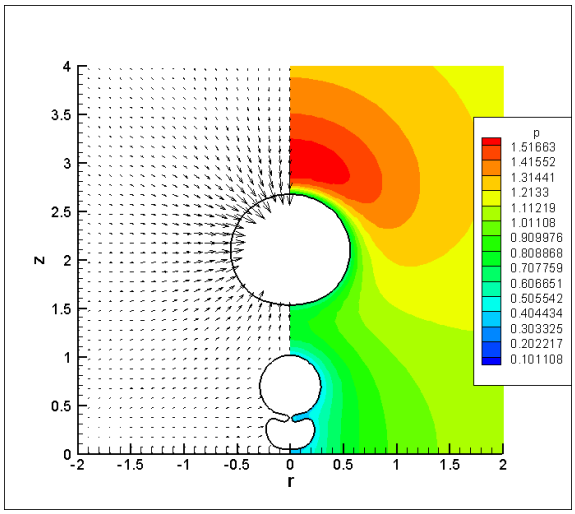

(b) Velocity vector and pressure contour plots at $t \approx 2.05$.

Figure 4.19: North pole jet velocities and velocity vector and pressure contour plots for $De = 0$, $Re = \infty$, $h_1 = 0.5$, $h_2 = 2.25$

towards the wall) forms during collapse. The reason for the drastic difference between the profiles in Figures 4.18 and 4.20 results from the inhibiting effect of viscosity on deformation. In Fig. 4.18, due to the presence of B_2 and the wall, fluid flows in from the sides to produce the annular penetrating jet. The width of this jet is thin, and velocities and curvatures - and consequently velocity gradients, will be high in this region. The presence of large velocity gradients mean that viscous effects will also be large and will act to inhibit fluid flow. As well as this, velocity gradients are larger in smaller bubbles. Hence the fact that B_1 was initially half the size of B_2, and so subject to larger viscous effects, is the crucial reason for such differing dynamics between the inviscid and $Re = 100$ case.

Figure 4.21(a) shows the jet velocity profiles. We see the significantly larger velocity of the liquid jet in B_2 which has been able to form due to the extended lifetime of B_1 (B_1 has not succumbed to the annular jet and split). As expected, the jet formation also coincides with a high pressure region above B_2 (Fig. 4.21(b)).

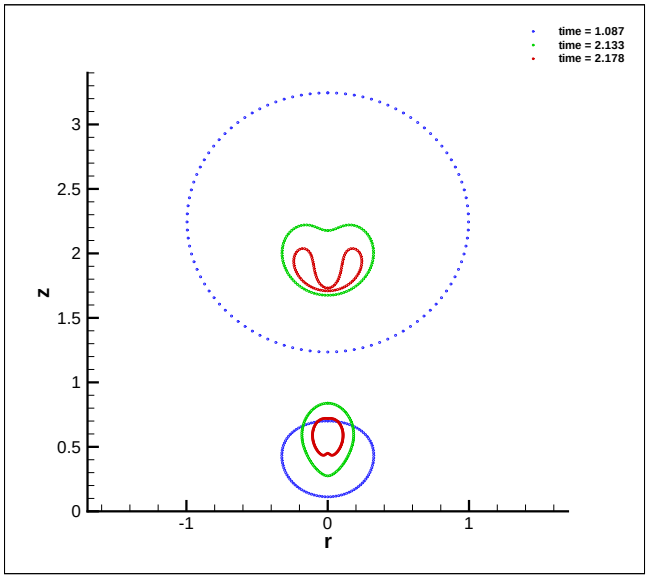

Figure 4.20: Bubble shapes for $De = 0$, $Re = 100$, $h_1 = 0.5$, $h_2 = 2.25$. Different colours indicate different instances in time.

Including viscoelastic effects ($De = 1$, $Re = 2$) we see in Fig. 4.22, as in the equal-sized case, the bubble behaviour switches; B_1 succumbs to jet penetration, while B_2 remains almost spherical. Here, however, we see no sign of jet inception in B_2 compared with Fig. 4.10, as the influence of B_1 is diminished due to its smaller size.

Figure 4.23(a) shows the jet velocity profiles. Note the small oscillation in B_1 before the velocity increases rapidly as the jet forms. Meanwhile in B_2, the jet velocity increases before it rapidly becomes negative as the bubble begins to rebound (again a result of elastic effects and bubble gas content). Here we also demonstrate the integrity of the numerical solution, by presenting the jet velocity profiles obtained with different mesh refinements. Increasing the number of elements N from 50 to 100 makes no visible difference to the results, and so setting $N = 50$ elements on each bubble surface is deemed sufficient. As is expected, the high pressure region now appears above B_1 in correspondence with the jet formation (Fig. 4.23(b)). The maximum pressure though is significantly lower here than the corresponding equal-size case (Fig. 4.11(b)), as B_1 is closer to the wall and so fluid flow is more restricted. This also explains why the final jet velocity in B_1 in this case is also slightly smaller comparatively.

Increasing the Deborah number to $De = 2.5$ (Fig. 4.24), we again note a considerable difference in dynamics. A jet now forms in B_2 as in the equal-size case, but we now also see jet formation in B_1. Figure 4.25(a) shows the similarity in the jet velocity profiles of each bubble, and the approximately equal final velocity. It seems that in this case

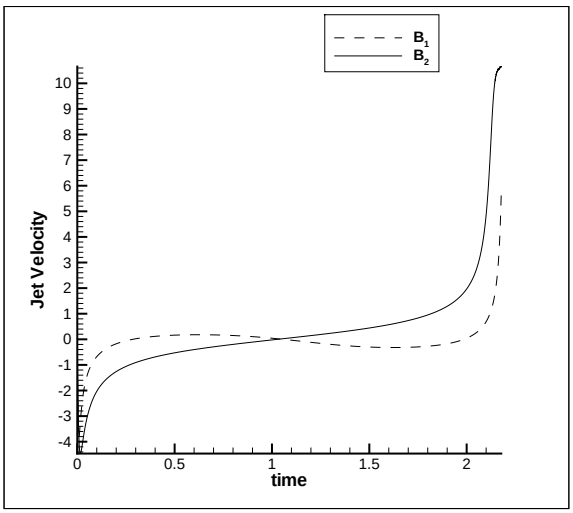

(a) North pole jet velocities.

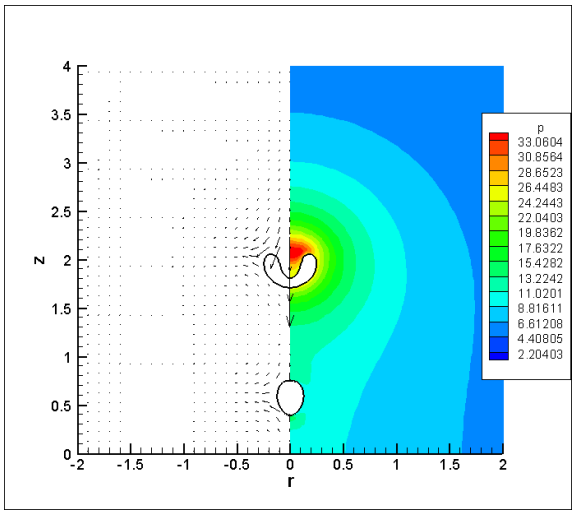

(b) Velocity vector and pressure contour plots at $t \approx 2.17$.

Figure 4.21: North pole jet velocities and velocity vector and pressure contour plots for $De = 0$, $Re = 100$, $h_1 = 0.5$, $h_2 = 2.25$

the increased elastic effects have counteracted the viscous effects to allow both bubbles to grow to a slightly larger size. Consequently, B_2 is large enough to be influenced by B_1 and the wall (and so a jet forms), but it is not so large as to negate the effect of the wall on B_1 and prevent jet formation there. Hence high speed jets form in both bubbles. As we see jet formation in the two bubbles we see a high pressure region develop above each of them (Fig. 4.25(b)). The maximum pressure although resides above B_2 where fluid flow is less restricted.

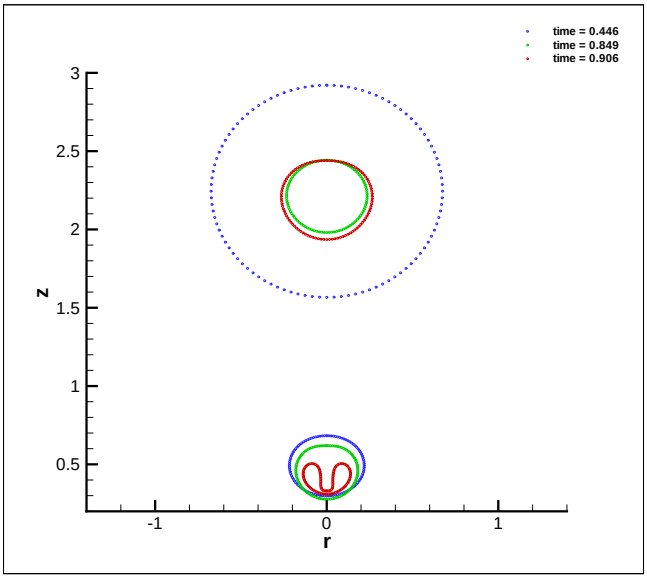

Figure 4.22: Bubble shapes for $De = 1$, $Re = 2$, $h_1 = 0.5$, $h_2 = 2.25$. Different colours indicate different instances in time.

We shall now fix the fluid parameters ($De = 1$, $Re = 2$) and study dynamics for different height configurations. For $h_1 = 0.5$ and $h_2 = 1.5$ (Fig. 4.26) the wall effects dominate and we see the formation of a liquid jet in B_1 and, due to the close proximity of B_2, jet inception also begins to take place on B_2's topside.

Moving B_2 away from the wall to $h_2 = 3.0$ (Fig. 4.27), as expected we see that B_1 is still dominated by the presence of the wall, while B_2 - now under little external influence, remains near sphericity, undergoing oscillatory collapse.

Figure 4.28 shows jet velocities in B_1 as B_2 is moved further away (as h_2 is increased). We see that with increasing h_2, the final jet velocity also increases, as fluid flow around B_1 becomes less restricted. To accompany this, the oscillations in B_1 also increase in magnitude with increasing h_2. The pressure fields behave similarly with increasing h_2 (Fig. 4.29). For B_2 close to B_1, the pressure around B_1 is small compared to that around B_2 (Fig. 4.29(a)). As h_2 is increased the maximum pressure now occurs above B_1 (Fig. 4.29(b)) and then continues to increase with increasing h_2 (Fig. 4.29(c)), as fluid motion becomes increasingly less restricted.

In Figure 4.30 the bubbles are moved away from the wall slightly with $h_1 = 1.0$, $h_2 = 2.0$. It is clear that bubble-bubble interaction plays a greater role than previously. The collapse of B_1 results in the formation of an annular axial liquid jet, which penetrates B_1 to leave an axial bubble "spike". Similar bubble shapes are seen in bubbles collapsing next to infinitely long free surfaces which include viscoelastic (see Chapter 5) and

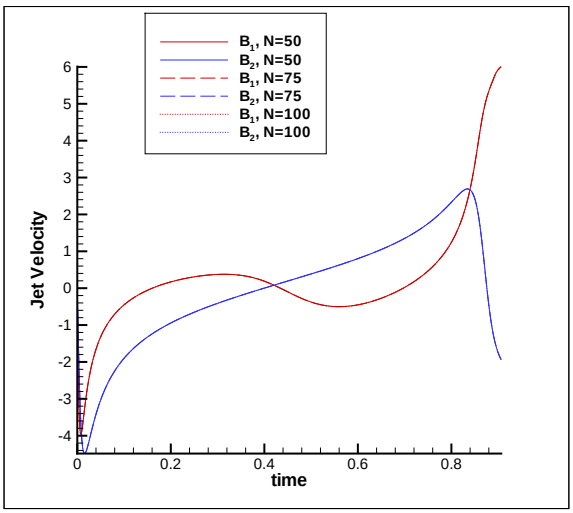

(a) North pole jet velocities for different mesh refinement.

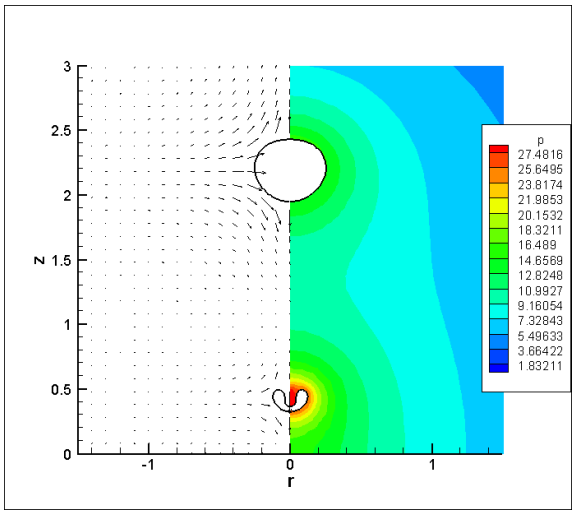

(b) Velocity vector and pressure contour plots at $t \approx 0.9$.

Figure 4.23: North pole jet velocities and velocity vector and pressure contour plots for $De = 1$, $Re = 2$, $h_1 = 0.5$, $h_2 = 2.25$

elastic effects [81]. This suggests the smaller bubble B_1, sees B_2 almost as an infinite free surface and in fact B_2 has become the dominant influence over B_1, instead of the wall.

Predictably, as B_2 moved further away (Fig. 4.31), its influence on B_1 is less compared to the wall, and the usual jet formation in B_1 results. Expectedly, B_2 remains very nearly spherical.

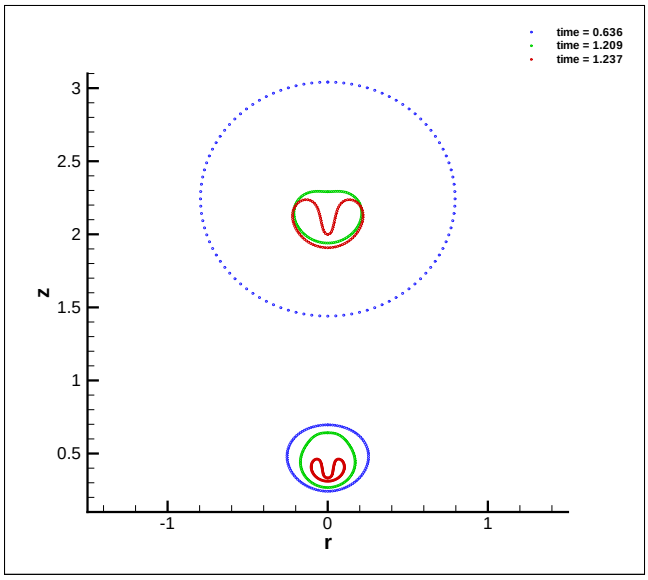

Figure 4.24: Bubble shapes for $De = 2.5$, $Re = 2$, $h_1 = 0.5$, $h_2 = 2.25$. Different colours indicate different instances in time.

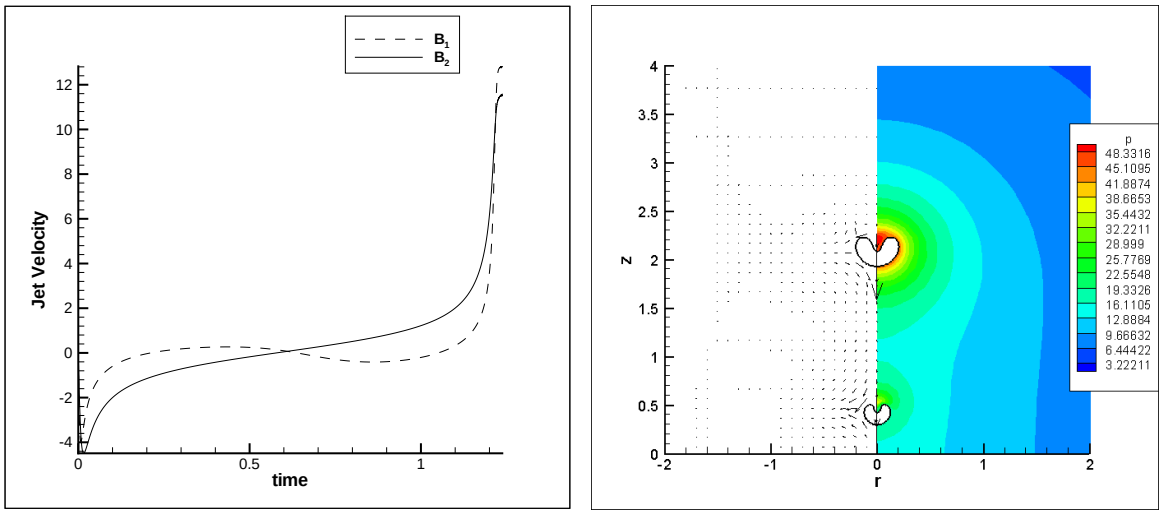

(a) North pole jet velocities.

(b) Velocity vector and pressure contour plots at $t \approx 1.23$.

Figure 4.25: North pole jet velocities and velocity vector and pressure contour plots for $De = 2.5$, $Re = 2$, $h_1 = 0.5$, $h_2 = 2.25$

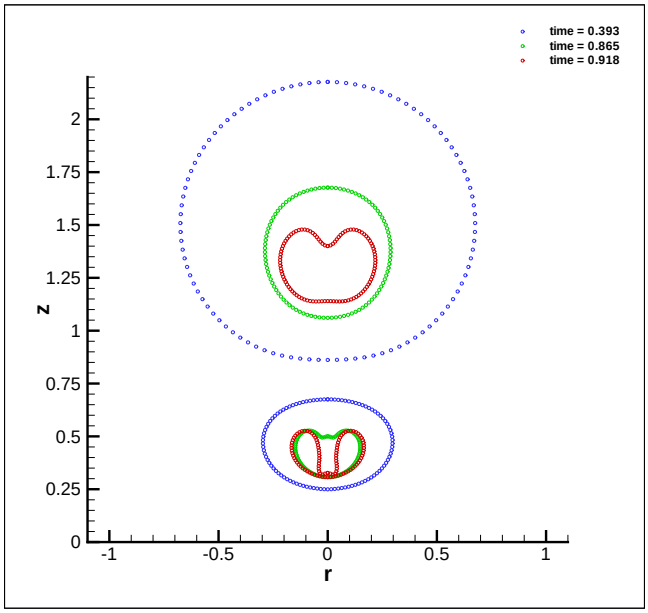

Figure 4.26: Bubble shapes for $De = 1$, $Re = 2$, $h_1 = 0.5$, $h_2 = 1.5$. Different colours indicate different instances in time.

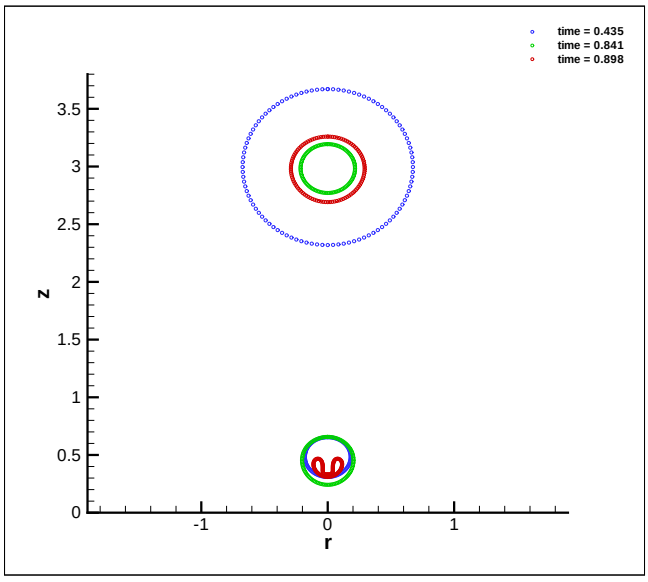

Figure 4.27: Bubble shapes for $De = 1$, $Re = 2$, $h_1 = 0.5$, $h_2 = 3.0$. Different colours indicate different instances in time.

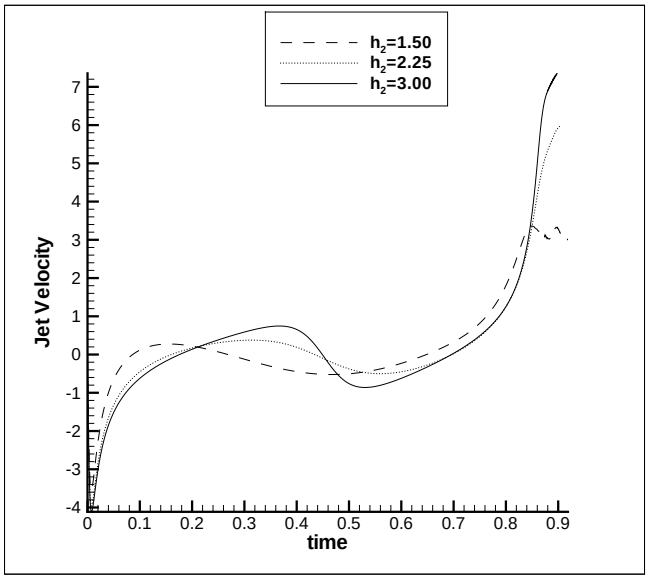

Figure 4.28: Jet velocities in B_1 at $h_1 = 0.5$, for varying h_2 ($De = 1$, $Re = 2$).

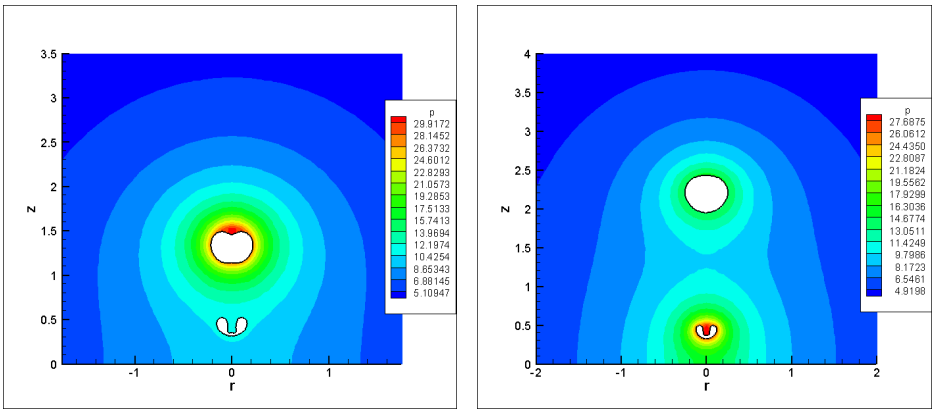

(a) $h_2 = 1.5$ (b) $h_2 = 2.25$

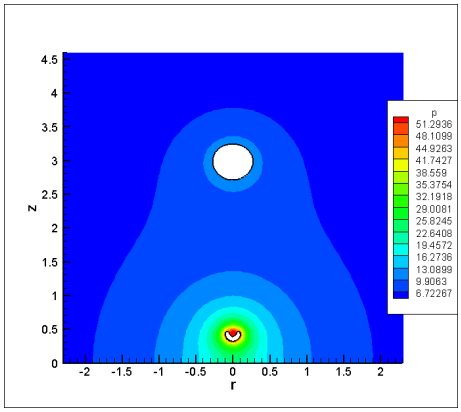

(c) $h_2 = 3.0$

Figure 4.29: Pressure contour plots for varying h_2 with $De = 1$, $Re = 2$, $h_1 = 0.5$

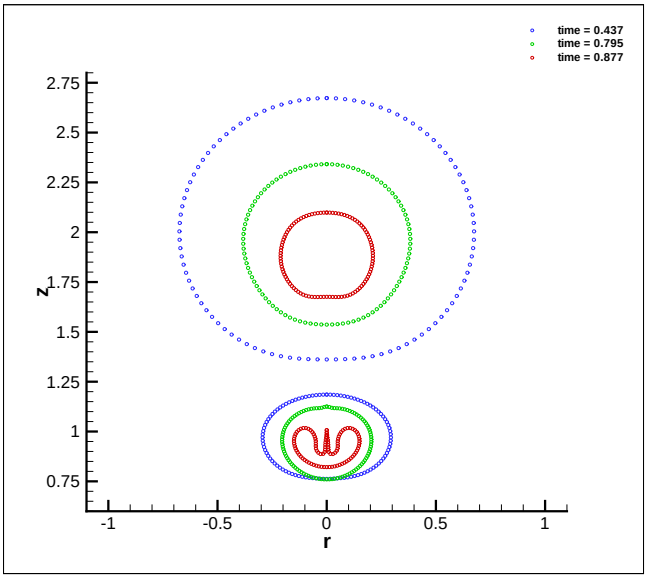

Figure 4.30: Bubble shapes for $De = 1$, $Re = 2$, $h_1 = 1.0$, $h_2 = 2.0$. Different colours indicate different instances in time.

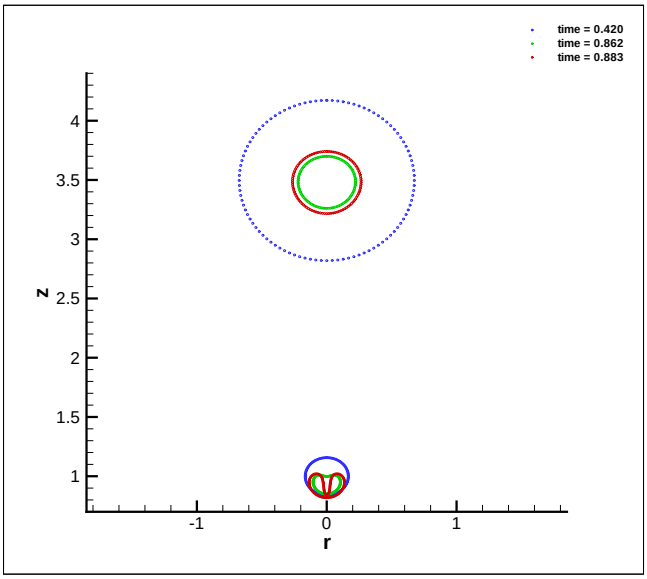

Figure 4.31: Bubble shapes for $De = 1$, $Re = 2$, $h_1 = 1.0$, $h_2 = 3.5$. Different colours indicate different instances in time.

4.4 Conclusion

The dynamics of two bubbles near a rigid boundary are both interesting and varied, and are made more so with the inclusion of viscoelastic effects. The dynamics are strongly dependent on initial bubble size, the distance between the bubbles and the wall, and on the fluid parameters. Table 4.1 summarises the behaviour observed in this study.

	Equal-sized	Different-sized
Inviscid	B_1: Large, prolate B_2: Jet formation	B_1: Annular side jet B_2: Large, near-spherical
Newtonian	B_1: Large, prolate B_2: Jet formation	B_1: Jet formation B_2: Possible jet inception
Viscoelastic (moderate De)	B_1: Jet formation B_2: Possible jet inception	B_1: Jet formation B_2: Jet inception
Viscoelastic (larger De)	B_1: Small, near-spherical B_2: Jet formation	B_1: Jet formation B_2: Jet formation

Table 4.1: Summarising observed bubble behaviour for different bubble sizes and fluid parameters

Bubble-bubble interaction clearly plays an important role, but does not necessarily dominate when including viscoelasticity. Jets readily form in certain situations in viscoelastic fluids (a sign of greater wall influence) but not in the corresponding Newtonian case (suggesting bubble-bubble interaction dominates). This may provide some explanation for the ambiguity present in the experimental works which directly measure cavitation damage in viscoelastic fluids. Ashworth and Procter [4] and Shima et al. [139] find an increased incidence and rate of cavitation damage in dilute polymer solutions, while other studies e.g. Brujan et al. [33] note a decrease in cavitation damage. The fact that jet formation is so subtly dependent on bubble size, distances from the wall and each other, and the fluid parameters, means that it is reasonable to expect that instances of cavitation damage will be high for some viscoelastic fluids and low for others, and will depend crucially on neighbouring bubbles. Given that these bubbles can exist in "clouds" where they number thousands, to attempt to control or model bubble interaction, and the subsequent influence on cavitation damage, is nearly impossible. The ideal theoretical situation studied here, and the range of behaviours observed, merely highlights the complex situation that exists in nature. Evidently, more experimental and theoretical research on multi-bubble dynamics and the role of

viscoelasticity is required. Obvious extensions to the current theory include the development of a fully 3D system that allows for multi-bubble dynamics which are not restricted to the axis of symmetry.

Chapter 5

The Effect of Viscoelasticity on the Dynamics of Gas Bubbles Near Free Surfaces

5.1 Introduction

The study of bubble dynamics near a free surface has received considerable attention for a number of years. Since World War II, the problem has been studied extensively given the application to underwater explosions. More recently however, the interaction of cavitation bubbles with such deformable boundaries has become of great importance to the medical field, particularly with the advent of ultrasound and laser techniques. The creation of bubbles within the body plays a crucial role in shock lithotripsy [42], drug delivery [166], and tissue and cell damage [85].

One of the first numerical studies of a bubble near a free surface was undertaken by Dommermuth and Yue [46]. Under the assumptions of incompressibility and irrotationality, the boundary element method was used to calculate, amongst other free surface problems, the growth and collapse of a cavity near a free surface. This work was extended by Blake et al. [20], who used the same techniques to specifically study bubble collapse near a free surface in more detail. Their results showed good agreement with the experimental work of Blake and Gibson [17], and highlighted the formation of a free surface liquid jet and a liquid jet which penetrates the bubble. Depending on the magnitude of buoyancy forces the bubble will either migrate away (small buoyancy

forces) or towards the boundary with the bubble jet directed away or toward the free surface, respectively.

Given the success of the boundary element method in free surface studies, research using such techniques continued. Boulton-Stone and Blake [26] used the BEM to investigate the *bursting* of gas bubbles near a free surface, and the subsequent free surface jet. The motivation behind the study being the cell damage observed in bioreactors as a result of such bursting bubbles. The study also included viscous effects at the bubble surface. This study was extended by Boulton-Stone [25] to include the presence of surfactants on the bubble surface, where it was found that surface dilatational viscosity can slow and even prevent the formation of the liquid jet. The bursting bubble problem was also investigated by Georgescu et al. [60] who, using a similar boundary element scheme, included the drop ejection from the formed liquid jet. Viscous effects were included solely through the normal stress balance and their results showed good agreement with experiment.

Simultaneously, improvements were made to techniques in studying the collapse of bubbles near free surfaces. Wang et al. [161] used a nonlinear distribution of nodes on the free and bubble surface which allowed for greater surface deformations and closer bubble-surface proximities which were unattainable in [20]. This work was then extended in [160] to include non-condensible gas content of the bubble and also the evolution of the bubble into toroidal form following jet impact. Similarly Robinson et al. [132] undertook a numerical and experimental investigation into one and two bubble dynamics near a free surface. Using a non-linear node distribution and cubic splines in their BEM scheme, they were able to reproduce the sharp free surface spikes and bubble centroid motions observed in their experiments. The work of Pearson et al. [114] then extended this work to include the transition of the bubble into toroidal form.

While the aforementioned work was concerned with bubble interaction with free surfaces, biological application motivated study in the theoretically similar, but more general, bubble interaction with fluid/fluid interfaces. The aim being to better model the fluid difference across tissue boundaries and cell membranes. Klaseboer and Khoo [81] used the boundary element method to describe bubble dynamics near an interface of

two fluids of different densities. In the limit of the density of the external fluid tending to zero, the free surface situation mentioned above is reached. Conversely, if this density was to approach infinity, the bubble dynamics mirror those near a rigid boundary. Consequently a liquid jet within the bubble could be directed away or toward the interface, depending on the density ratio of the two fluids. Given that biological fluids exhibit elastic properties, Klaseboer and Khoo [82] extended their previous work to model bubble dynamics (in an inviscid fluid), near an elastic fluid. The elasticity of the second fluid being modelled through a pressure term at the fluid-fluid interface. A wide range of bubble shapes were observed, including the usual liquid jetting but also mushroom-like bubble shapes and bubble splitting. Good agreement was found with the experimental work of Brujan et al. [35, 36], who investigated the comparable situation of the dynamics of laser induced cavitation bubbles in water near a polyacrylamide gel. A similar study by Turangan et al. [155] proceeded to investigate experimentally and numerically, the bubble dynamics near an elastic membrane. They noted that bubble shapes closely resemble those near elastic boundaries, despite the different boundary physics.

This chapter investigates the effect of viscoelasticity on bubble dynamics near a free surface. While the Newtonian dynamics have been well documented, the influence of viscoelasticity on bubble and free surface dynamics has not. The experimental literature is also sparse, but for the work of Williams et al. [165], on liquid free surface jets formed by bubbles in non-Newtonian fluids. They note that jet production is markedly suppressed in elastic fluids than in their Newtonian counterparts. We shall comment on these results in relation to the numerical ones to be presented here. Also, given the semblance with the aforementioned work on bubbles near elastic boundaries, appropriate comparisons will be made.

5.2 Mathematical model

The fluid in domain Ω is assumed to be incompressible and the fluid motion irrotational. It follows from the conservation of mass that there exists a velocity potential ϕ which satisfies Laplace's equation:

$$\nabla^2 \phi = 0, \tag{5.1}$$

in the region Ω. By Greens theorem, there exists an integral solution to (5.1), defined in terms of the boundary integral [113],

$$c(\mathbf{p})\phi(\mathbf{p}) = \int_{\partial\Omega} \left(\frac{\partial\phi}{\partial n}(\mathbf{q}) G(\mathbf{p},\mathbf{q}) - \phi(\mathbf{q}) \frac{\partial G}{\partial n}(\mathbf{p},\mathbf{q}) \right) dS \tag{5.2}$$

where $\partial\Omega = \partial\Sigma \cup \partial B$ is the boundary of the fluid domain and $\partial\Sigma$ and ∂B are the boundaries of the free surface and the bubble respectively. The constant $c(\mathbf{p})$ is given by

$$c(\mathbf{p}) = \begin{cases} 2\pi & \text{if } \mathbf{p} \in \partial\Omega, \\ 4\pi & \text{if } \mathbf{p} \in \Omega \backslash \partial\Omega \end{cases}$$

In 3D, the appropriate Greens function $G(\mathbf{p},\mathbf{q})$ is given by

$$G(\mathbf{p},\mathbf{q}) = \frac{1}{|\mathbf{p}-\mathbf{q}|} \tag{5.3}$$

Given an initial potential ϕ_0 on the fluid surface $\partial\Omega$, the integral equation (5.2) can be solved numerically for the normal velocity to the surface $\frac{\partial\phi}{\partial n}$. The tangential velocity $\frac{\partial\phi}{\partial s}$ can be calculated given the potential ϕ_0, and the surface geometry $\partial\Omega$. Hence the velocity on the surface is completely described. The fluid particles with position vector $\mathbf{x}$ initially on the surface $\partial\Omega$ will remain there. Consequently, the surface can be updated in a Lagrangian manner according to

$$\frac{D\mathbf{x}}{Dt} = \nabla\phi, \quad \mathbf{x} \in \partial\Omega. \tag{5.4}$$

As previously, a generalised Bernoulli equation provides an equation of motion from which the potential ϕ can also be updated in a Lagrangian manner. This equation takes a slightly different form on the free and bubble surfaces. The normal fluid stresses are balanced by the internal bubble pressure p_b on the bubble surface ∂B and by the hydrostatic pressure p_∞ on the free surface $\partial\Sigma$. Hence we have

$$\rho\frac{D\phi}{Dt} = \frac{\rho}{2}|\mathbf{u}|^2 - T_{nn} + p_\infty - p_b \quad \text{on } \partial B, \tag{5.5}$$

and

$$\rho\frac{D\phi}{Dt} = \frac{\rho}{2}|\mathbf{u}|^2 - T_{nn} \quad \text{on } \partial\Sigma. \tag{5.6}$$

For the same reasons as the previous chapter, bubble growth as well as bubble collapse is modelled. The internal bubble pressure p_b results from the ideal and adiabatic gas

content of the bubble, described by equation (4.7). The governing equations are non-dimensionalised in an identical manner to the previous chapter (see equations (4.8)), to give,

$$\frac{D\phi}{Dt} = 1 + \frac{1}{2}|\mathbf{u}|^2 - T_{nn} - \epsilon\left(\frac{V_0}{V}\right)^{\gamma} \quad \text{on } \partial B, \tag{5.7}$$

and

$$\frac{D\phi}{Dt} = \frac{1}{2}|\mathbf{u}|^2 - T_{nn} \quad \text{on } \partial\Sigma, \tag{5.8}$$

where T_{nn} is found from

$$De\frac{DT_{nn}}{Dt} + T_{nn} = \frac{1}{Re}\dot{\gamma}_{nn}. \tag{5.9}$$

Equation (5.2) is solved using collocation, with nodal points on $\partial\Omega$ and the potential ϕ interpolated using cubic splines (which are parameterised with respect to arclength s). The free surface $\partial\Sigma$ requires special consideration. As in [114] the free surface is partitioned into an analytic portion in the far field, and treated numerically within the vicinity of the bubble. It can be argued that in the far field leading order behaviour is like that of a dipole with the velocity decaying like $O(|r|^{-3})$. Consequently the quantities z, ϕ and ψ are taken to be of the form

$$f(r,t) = \left(\frac{r_{max}}{r}\right)^3 f(r_{max},t) \quad \text{if } |r| > r_{max}. \tag{5.10}$$

r_{max} denotes the last point of the numerical portion of $\partial\Sigma$. As in [161] we take $r_{max} = 10R_m$ (ten maximum bubble radii). Consequently, equation (5.10) forces the cubic spline interpolants to be clamped at the far-field end of the free surface, by enforcing the following

$$\frac{dr}{ds} = \frac{1}{D}, \tag{5.11}$$

$$\frac{dz}{ds} = -\frac{3z}{Dr}, \tag{5.12}$$

$$\frac{d\phi}{ds} = -\frac{3\phi}{Dr}, \tag{5.13}$$

with $D = (1 + (3z/r)^2)^{1/2}$.

The subsequent discretisation of (5.2) gives

$$c(\mathbf{p}_i)\phi_i + \sum_{s=1}^{2}\sum_{j=1}^{N_s} A_{ij}^s + P_i = \sum_{s=1}^{2}\sum_{j=1}^{N_s}(B_{ij}^s\psi_j^s + C_{ij}^s\psi_{j+1}^s) + L_i\psi_{N_1+1}^1, \tag{5.14}$$

where i varies over all the collocation points on $\partial\Omega$, $i = 1, ..., N_T$, where $N_T = N_1 + 1 + N_2 + 1$ is the total number of points on $\partial\Omega$. Subscript label 1 refers to the free surface, and label 2 to that of the bubble. P_i and L_i represent the integration over the analytic portion of the free surface.

The discrete system is solved for the normal velocity ψ using Gaussian elimination. The tangential velocity and higher derivatives of ϕ are calculated using the spline interpolation. A fourth-order Runge-Kutta scheme is then used to update the bubble surface and potential from equations (5.4), (5.5) and (5.6). In the presence of viscoelasticity ($De \neq 0$), the constitutive equation is updated using an implicit second-order time stepping method.

As in [114], the nodal points on the bubble surface are redistributed equally with respect to arclength at each time step. On the free surface, the redistribution is enacted using the following function

$$s_i = \frac{s_{max}}{2}\left(\frac{i-1}{N_1}\right)^{1.1}\left(1 + \frac{1}{(N_1 - i + 2)^2}\right) \tag{5.15}$$

for $i = 2, ..., (N_1 + 1)$. The above redistribution function ensures a high density of nodes near the axis of symmetry allowing the formation of any free surface jets to be captured accurately.

As is necessary with such boundary integral schemes, smoothing is periodically used to prevent the onset of numerical instability. Smoothing needs only to be applied to the bubble surface given the employment of (5.15) on the free surface. To preform the smoothing, as in [114] a scheme based on the fourth-order diffusion-like equation is used

$$\frac{\partial f}{\partial t} = -\alpha'\frac{\partial^4 f}{\partial s^4}, \tag{5.16}$$

which damps high order modes, but leaves lower order modes virtually unchanged. Here f is the function to be smoothed and α' is a diffusive constant. Solution of (5.16) using an Euler scheme for the time derivative and a centred difference scheme for the spatial derivative yields the following applicable formula

$$\bar{f}_j = f_j - \alpha(f_{j-2} - 4f_{j-1} + 6f_j - 4f_{j+1} + f_{j+2}). \tag{5.17}$$

$\bar{f}$ is the smoothed function and α is a smoothing parameter. The presence of this parameter means one has more freedom in choosing to what degree smoothing is applied (other than how frequently). A choice of $\alpha = 1/16$ gives the previously used smoothing formula of Longuet-Higgins and Cokelet [97]. In practice one can smooth sufficiently for a value of $\alpha < 1/16$, regardless of bubble distance from the free surface. In most situations this formula is applied every ten time steps.

Initially, we consider a single gas bubble of small radius at rest a distance h from an unperturbed free surface $z = 0$. A schematic diagram of the set up is given in Fig. 5.1. Bubble growth is then driven by the internal compressed gas content. The initial conditions on the bubble and free surface are then $\phi(\mathbf{x}, 0) = 0$ and $T_{nn}(\mathbf{x}, 0) = 0$. The bubble strength is taken to be $\epsilon = 100$ for all results in this study. As in the previous chapter, to ensure a consistent non-dimensionalisation, this choice of ϵ requires an initial radius of $R_0 \approx 0.149$.

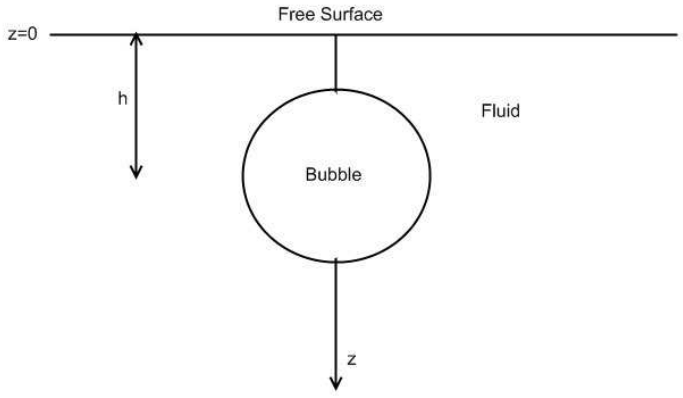

Figure 5.1: Schematic diagram of initial set up.

5.3 Numerical Results

5.3.1 Validation

The free surface boundary element formulation is now validated through comparison with the free surface results of Wang et al. [161] for an inviscid bubble. The bubble is assumed to have zero gas content and is prescribed an initial velocity through an initial potential given by

$$\phi_0 = -A \cdot R_0 \left(\frac{2}{3} \left(\left(\frac{R_m}{R_0} \right)^3 - 1 \right) \right)^{0.5}, \tag{5.18}$$

where

$$A = 1 - \frac{1}{\sqrt{(z+h)^2 + r^2}} \tag{5.19}$$

Equation (5.18) is like that for the potential of an inviscid spherical bubble in an infinite fluid, as used in [19], but for the inclusion of parameter A (Equation (5.19)), which accommodates the presence of the free surface.

Fig. 5.2 shows the bubble/free surface profiles for a distance of $h = 0.5$ from the unperturbed free surface. The bubble and free surface shapes show very good agreement. The maximum height reached by the free surface jet is $z_{max} \approx 2.8$ - as predicted by Wang et al. [161].
Fig. 5.3 shows the bubble/free surface profiles for $h = 1.0$. Again, there is excellent agreement. The bubble and free surface shapes are identical to those in [161] with the free surface jet reaching the same maximum height, $z_{max} \approx 0.85$.
Fig. 5.4 presents the variation of the bubble centroid with time for different distances h. Once again, the results show excellent agreement with those of Wang et al. [161].

5.3.2 Newtonian Dynamics

Now, we present results for the growth and collapse of a gas bubble near a free surface, and investigate the influence of viscous effects. Fig. 5.5 shows the bubble/free surface profiles for $h = 0.5$ in the inviscid case. The profile shapes resemble closely those of previous results, where instead the bubble was prescribed an initial velocity with zero gas content. A tall thin, free surface jet forms, while a thin jet penetrates the bubble,

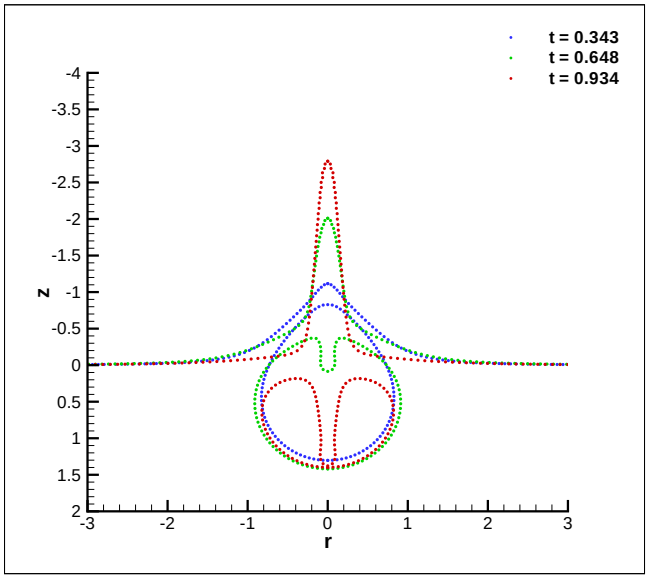

Figure 5.2: Bubble and free surface shapes for $h = 0.5$. Different colours indicate different instances in time.

directed in the opposite direction.

Figure 5.6 shows a three dimensional visualisation of Fig. 5.5, the instant before bubble jet impact. The tall, thin free surface jet, in relation to the bubble size and shape, can be fully appreciated.

If viscous effects are included with $Re = 50$, we see the small effects of viscous dissipation playing a part in the dynamics. Figure 5.7 shows the bubble/free surface profiles for $Re = 50$, $h = 0.5$. Most notably, the free surface jet now attains a smaller height ($z_{max} \approx 2.2$) than in the inviscid case ($z_{max} \approx 2.5$). Kinetic energy that would be provided by the growing gas bubble to the free surface jet, is reduced as a result of the energy lost to viscous dissipation in both the bubble and free surface. We also note the formation of a slightly thinner sharper jet being formed in the bubble as a result of the viscous effects. Increasingly thinner jets with decreasing Reynolds number were noted by Popinet and Zaleski [121] in their study on the effect of viscosity on bubble collapse near a rigid wall. This results from viscosity inhibiting fluid flow into the jet, creating a less voluminous jet, with a subsequently sharper tip.

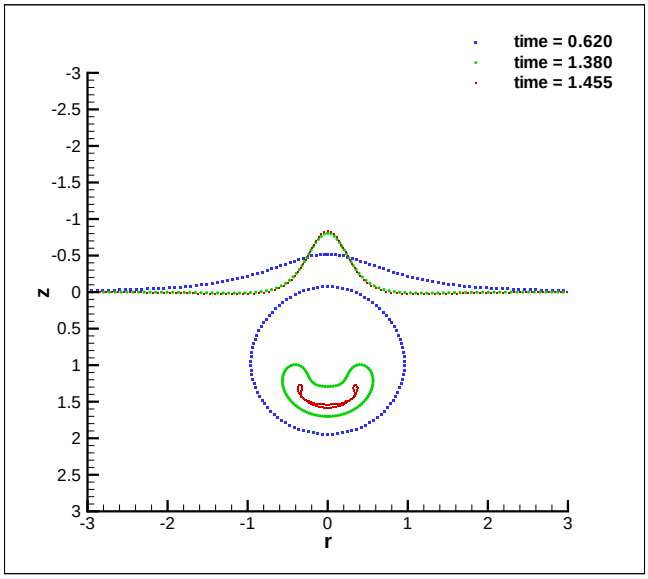

Figure 5.3: Bubble and free surface shapes for $h = 1.0$. Different colours indicate different instances in time.

Figure 5.8 displays bubble/free surface profiles for an inviscid bubble at $h = 1.0$. In being further from the free surface, the interaction between it and the bubble is less than the $h = 0.5$ case. The free surface jet is much smaller and broader, attaining a maximum height of $z_{max} \approx 0.8$. Similarly, the bubble jet forms and grows wider during collapse, causing the bubble to assume a more bowl-like shape in the final stages.
Figure 5.9 shows bubble/free surface profile shapes following the inclusion of viscous effects ($Re = 50$). We note a similar occurrence to the $h = 0.5$ case - namely, a shorter free surface jet ($z_{max} = 0.6$), and a slightly thinner bubble jet. But again, in general appearance, the form and shape of the bubble are still similar to the inviscid case.

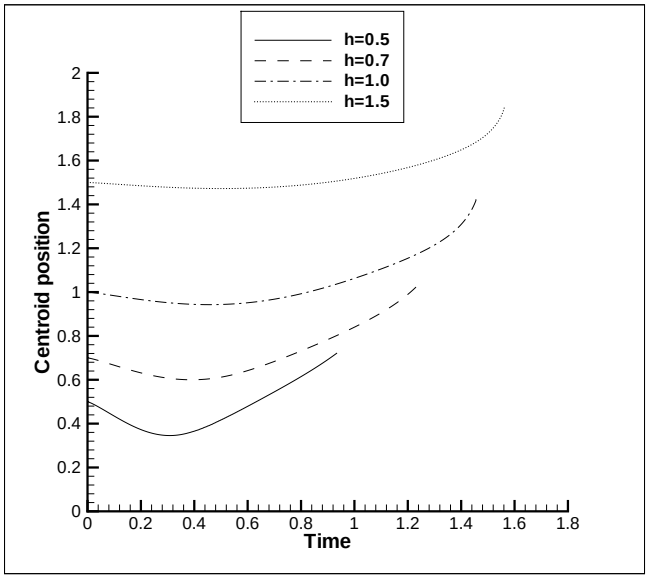

Figure 5.4: Bubble centroid positions for a range of values of h

Figure 5.10 shows the pressure contours and velocity vector plot in the final stages of collapse for the inviscid $h = 0.5$ case. Notable aspects are the high pressure region above and below the bubble and free surface jet respectively; a point of focus as fluid is drawn in to form either jet. The velocity vectors then highlight the significant velocities in both of the liquid jets, directed in opposite directions.

Figure 5.11 shows the pressure contours/velocity vectors for an inviscid bubble a distance $h = 1.0$ from the unperturbed free surface. A high pressure region is observed above the bubble jet where fluid acceleration is greatest. The maximum magnitude of the pressure is higher here ($p_{max} \approx 12.3$) than in the $h = 0.5$ case ($p_{max} \approx 2.0$), as a greater volume and mass of fluid is focused into the bubble jet region, with a comparative increase in fluid momentum.

Figure 5.12 shows the pressure contour/velocity vectors at $h = 1.0$ for $Re = 50$. The general form of the fields is similar to the inviscid case, but expectedly, the high pressure region is slightly smaller in magnitude as fluid flow is inhibited slightly by the effects of viscous dissipation.

Figure 5.13 displays the free surface jet height varying with time, for different h and Re. As we have seen, the distance of the bubble from the free surface is the dominant factor in determining jet height. Jets are taller and thinner for bubbles closer to a free surface than for bubbles further away. The effect of viscosity, though small in comparison, is also evident. Increasing viscous effects results in decreased jet heights

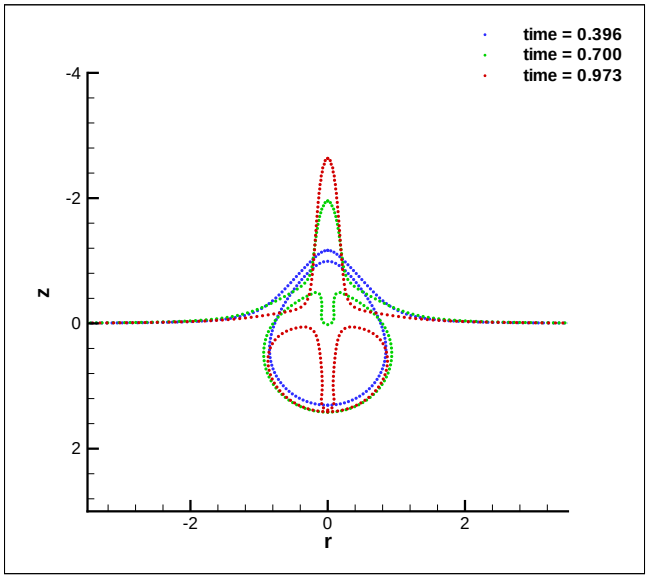

Figure 5.5: Bubble and free surface shapes for an inviscid fluid at $h = 0.5$. Different colours indicate different instances in time.

as the kinetic energy that would be used in the formation of these jets is lost through viscous dissipation.

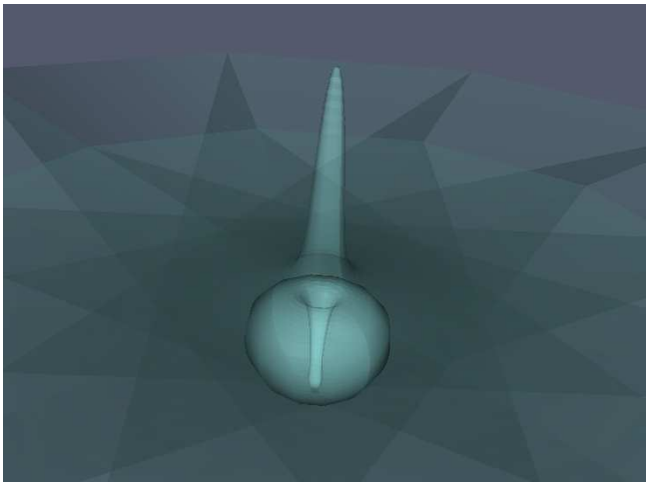

Figure 5.6: 3D visualisation of Fig. 5.5

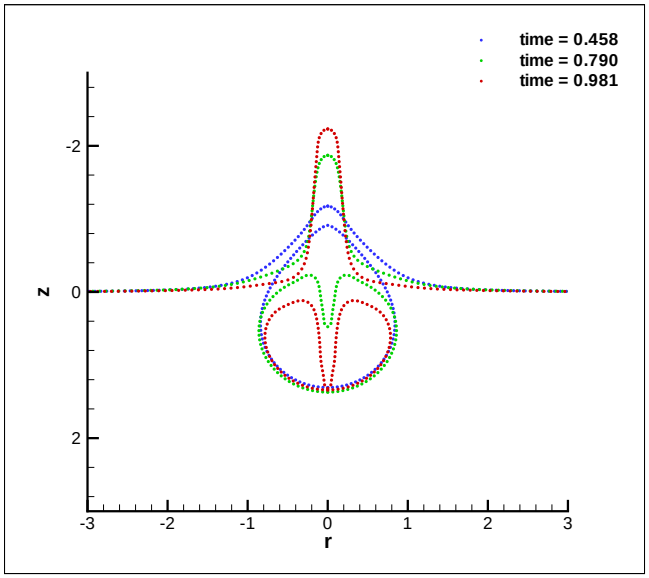

Figure 5.7: Bubble and free surface shapes with $Re = 50$ at $h = 0.5$. Different colours indicate different instances in time.

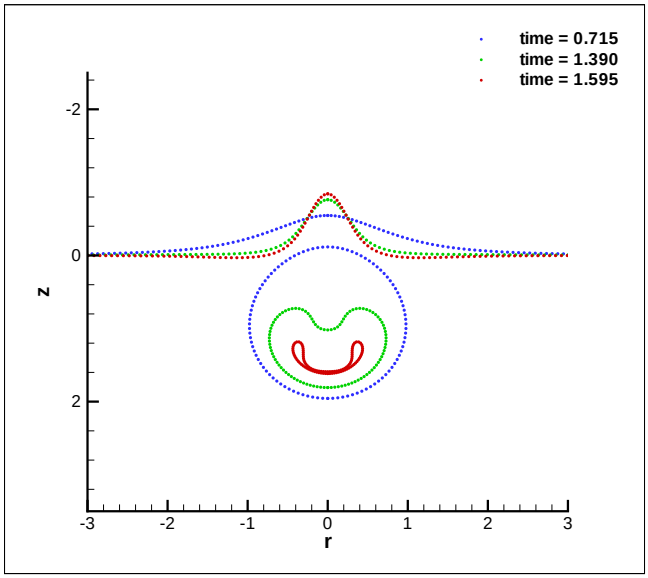

Figure 5.8: Bubble and free surface shapes for an inviscid fluid at $h = 1.0$. Different colours indicate different instances in time.

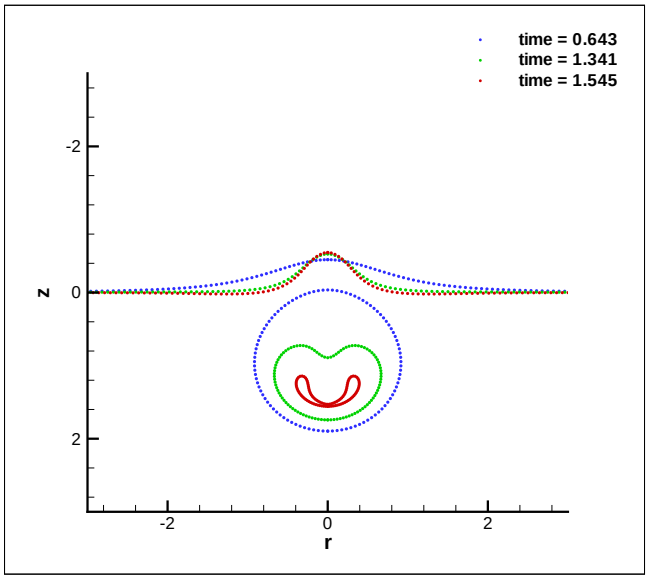

Figure 5.9: Bubble and free surface shapes with $Re = 50$ at $h = 1.0$. Different colours indicate different instances in time.

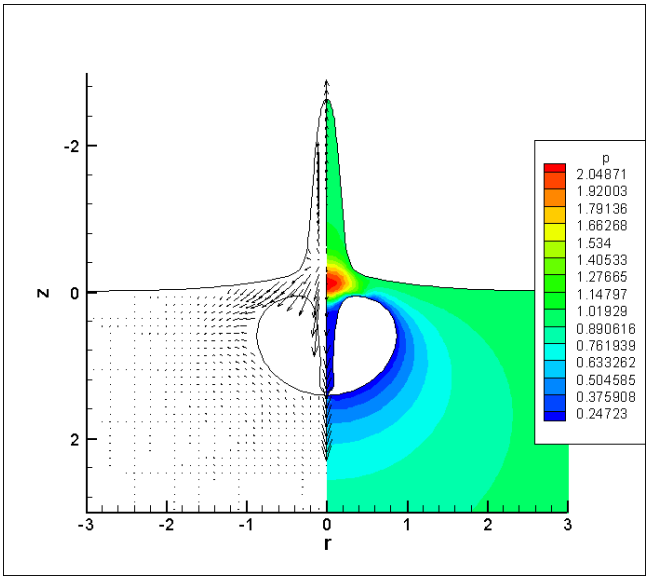

Figure 5.10: Pressure contours and velocity vectors at $t = 0.973$ for an inviscid fluid ($h = 0.5$).

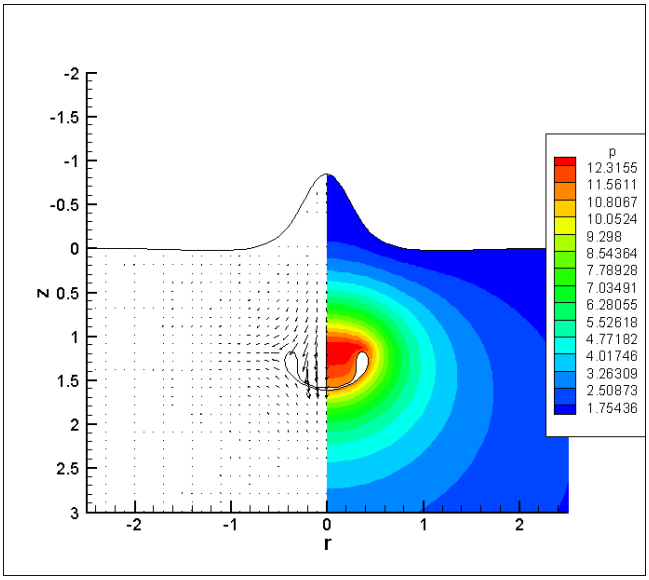

Figure 5.11: Pressure contours and velocity vectors at $t = 1.595$ for an inviscid fluid ($h = 1.0$).

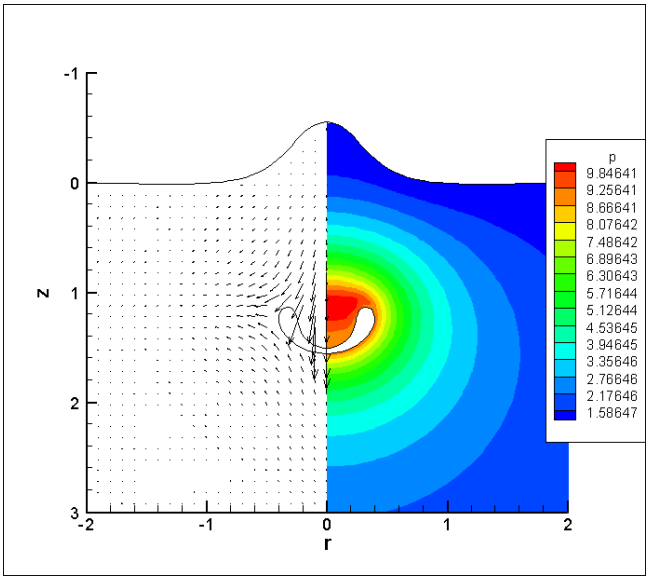

Figure 5.12: Pressure contours and velocity vectors at $t = 1.545$ with $Re = 50$ ($h = 1.0$).

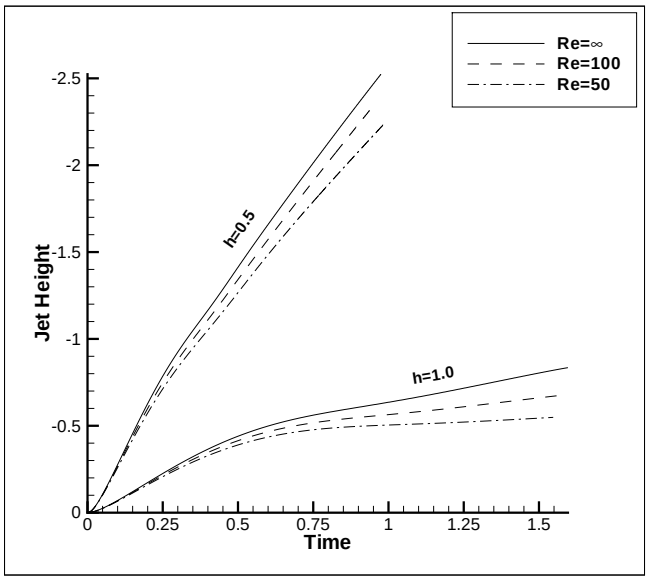

Figure 5.13: Jet height varying with time for different Reynolds number at $h = 0.5$ and $h = 1.0$.

5.3.3 Viscoelastic Dynamics

With the inclusion of viscoelastic effects we see a marked change in the dynamics. Figure 5.14 shows the bubble and free surface profiles for $De = 1.0$, $Re = 1.0$, $h = 0.5$. Interestingly, the usual axial jet does not form. Instead we see the formation of an annular, ring-like jet which is centred on the axis of symmetry. This produces an "upsidedown mushroom" like bubble shape, with a sharp stem. Similar bubble shapes are seen by Klaseboer and Khoo [82] and Turangan et al. [155] following bubble collapse near an elastic surface and membrane. The similarities between these studies will be discussed in more detail in Section 5.3.4.

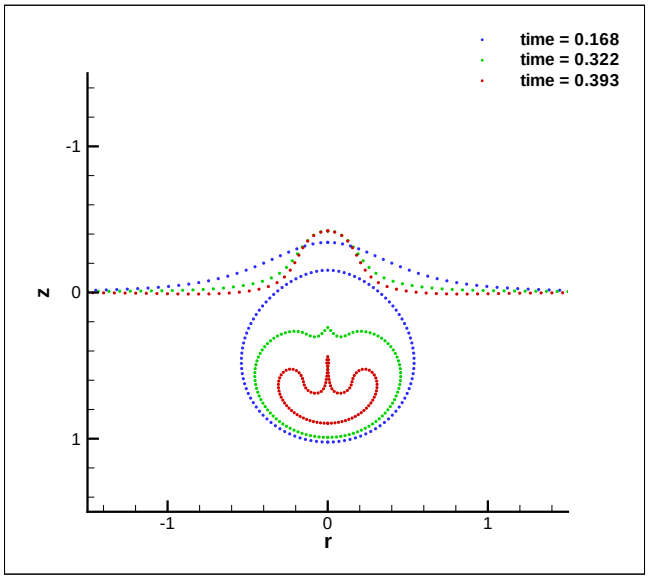

Figure 5.14: Bubble and free surface shapes with $De = 1$, $Re = 1$ at $h = 0.5$. Different colours indicate different instances in time.

To ensure that a sufficient mesh refinement is used in obtaining these results, Fig. 5.15 shows the jet velocity on the free surface with different mesh refinements on the bubble and free surface. From this it can be seen that $N_f = 75$ and $N_b = 50$ provides a sufficiently refined mesh, and is consequently used in obtaining the following results. Also, to ensure that the distance to which the numerical portion of the free surface extends is large enough, Fig 5.16 displays the free surface jet velocity at $r_{max} = 10$ and 20 for different mesh refinements. For the mesh with $N_b = N_f = 75$, increasing r_{max} to 20, creates a discrepancy in the results as increasing the length of the free surface causes the mesh to become under-refined. If the mesh refinement is then increased, the results match those of the $r_{max} = 10$, $N_b = N_f = 75$ case well. This suggests that

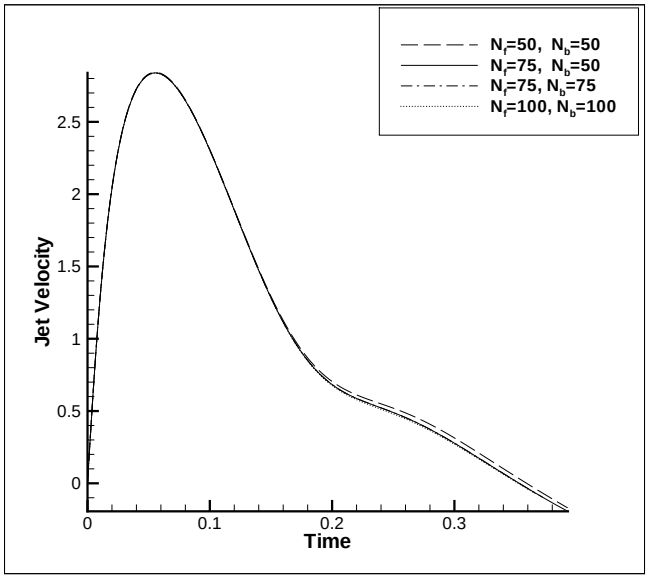

Figure 5.15: Free surface jet velocity for $De = 1$, $Re = 1$, with mesh refinement

$r_{max} = 10$ is indeed sufficiently long enough to describe the numerical portion of the free surface.

If the Deborah number is decreased to $De = 0.5$, we observe a bubble shape similar to that for $De = 1$ (Fig. 5.14). Here though, the annular jet which forms, continues to travel through to the opposite side of the bubble. Also, during collapse, the bubble begins to expand as a result of the internal gas content and the effect of the elastic stresses. This helps to create the small ringed jet, with a thin bubble "stem" and a large surrounding body. Given that viscous dissipation effects are more dominant now, the height reached by the free surface is significantly less ($z_{max} \approx 0.2$) than that reached in the $De = 1.0$ case ($z_{max} \approx 0.4$).

Figure 5.18 shows a 3D visualisation of the final stage of collapse for $De = 0.5$, $Re = 1.0$. The annular jet, having penetrated the top of the bubble about the thin axial stem, can be seen clearly.

Now if the Deborah number is increased to $De = 2.5$ (Fig. 5.19), we see a reversion in the dynamics. Instead of an annular ring jet, an axial jet, much like those seen in the Newtonian case, forms. Although, this jet is considerably larger and the jet tip broader and flatter than its Newtonian counterparts. The increase in Deborah number means that viscous effects are suppressed by the increasing elastic effects. Consequently, the effect of viscous dissipation is less and the bubble is able to expand to a larger volume and interact and deform with the free surface. With viscous effects reduced,

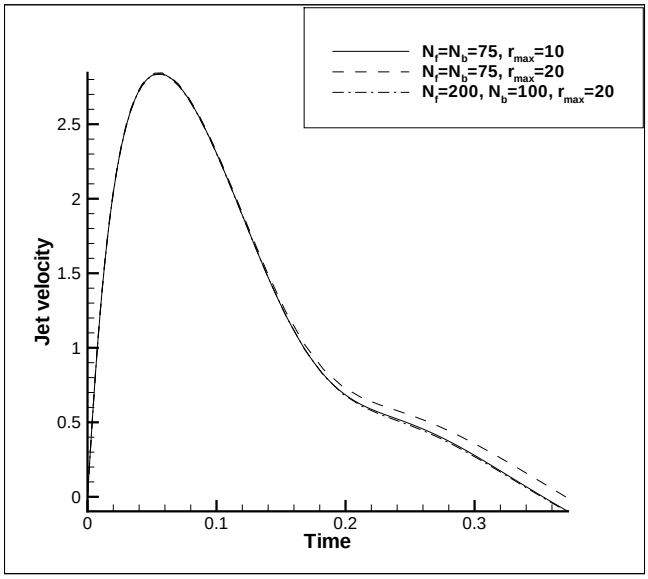

Figure 5.16: Free surface jet velocity for $De = 1$, $Re = 1$, with varying mesh refinement and r_{max} values.

the bubble now succumbs to more dominant inertia terms and the usual axial jet forms and penetrates the bubble. In addition, the free surface jet produced is significantly taller ($z_{max} \approx 1.0$), but still less than half the size of its inviscid Newtonian counterpart (Fig. 5.5) - emphasising that viscosity still plays a considerable role.

The effect of varying Deborah number can be readily seen in Figures 5.20 and 5.21. As the Deborah number is increased, so do the jet velocity and height on the free surface. For $De = 0.5$ viscous dissipation plays a more important role and consequently the free surface jet velocity and free surface height are smaller, as energy is dissipated into the fluid. Also, note the rebound in the jet velocity at $t \approx 0.3$, describing the re-expansion of the bubble due to elastic and internal gas effects. By increasing the Deborah number one increases the effect of elasticity, but also inertia, as viscous effects are offset. Subsequently, the velocity of the jet and the height reached by the jet increase.

Similar behaviour is observed with the bubble. Figure 5.22 shows the variation of the bubble centroid position with time. Evidently, the mobility of the bubble's centre of mass increases with Deborah number. Reduced viscous dissipation results in the bubble being able to move more freely along the axis of symmetry.

Figures 5.23 and 5.24 display the pressure contours and velocity vectors for the above parameters.

For Deborah number $De = 2.5$ (Fig. 5.23), we see a pressure field much like that

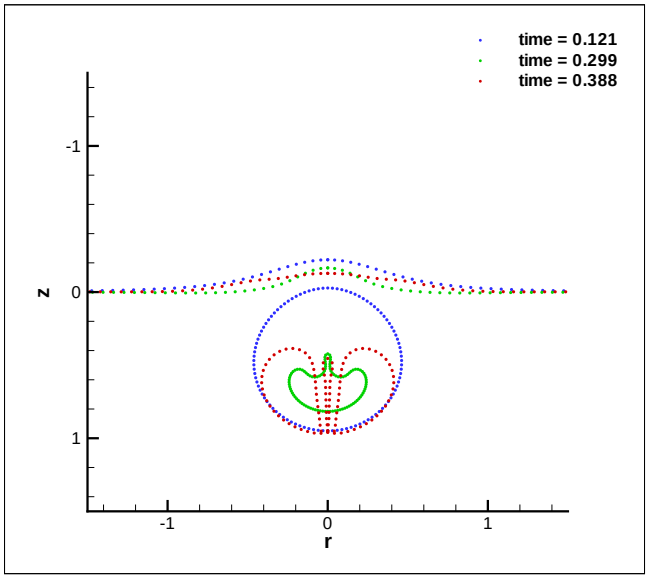

Figure 5.17: Bubble and free surface shapes with $De = 0.5$, $Re = 1.0$ at $h = 0.5$. Different colours indicate different instances in time.

observed in the Newtonian case, with the formation of the axial jet accompanied by the corresponding high pressure region between the bubble and free surface. The maximum pressure here is larger than the corresponding Newtonian case, given the greater volume/mass of fluid focused into the larger, voluminous bubble jet.

Fig. 5.24 displays corresponding results for $De = 1.0$, $Re = 1.0$, $h = 0.5$. Expectedly, a high pressure region occurs in the vicinity of the bubble - specifically along the thin, sharp "stem" that is produced during collapse. This is a consequence of the extremely high curvatures near the tip of this stem and the subsequent large normal stresses. Note the larger velocities *around* the axis of symmetry, forming the annular ring jet.

For a Deborah number of $De = 0.5$ (Fig. 5.25), we see the high pressure region form at the tip of the annular jet that penetrates and impacts upon the opposite side of the bubble. The maximum value of this pressure is significantly less than the $De = 1.0$ case as the surface curvatures in this region are smaller, and the increased effect of viscous dissipation acts to suppress the high pressures. Note the negative pressure around the outer body of bubble, indicating the expansion of this outer segment, due to the expansion of the internal gas content and elastic stresses.

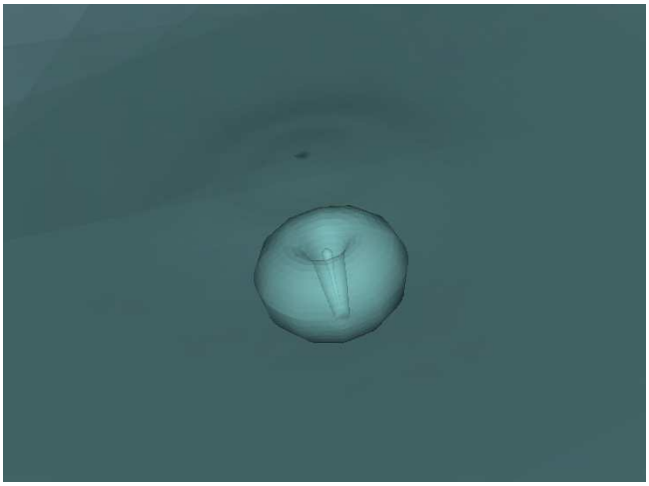

Figure 5.18: 3D visualisation of Fig. 5.17.

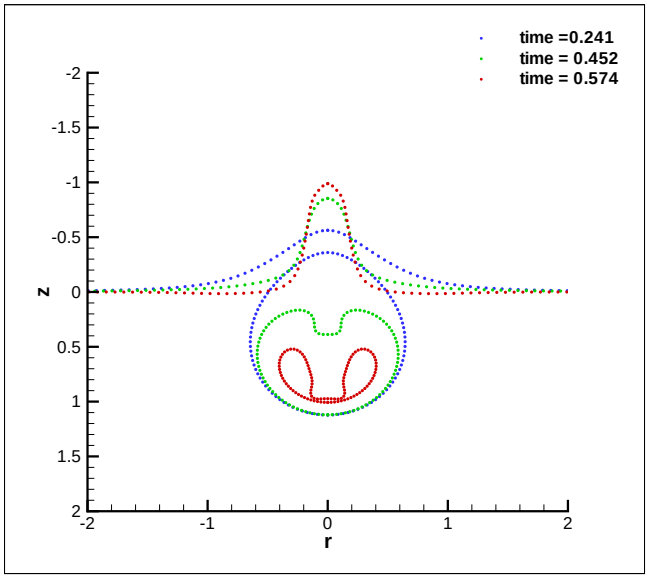

Figure 5.19: Bubble and free surface shapes with $De = 2.5$, $Re = 1.0$ at $h = 0.5$. Different colours indicate different instances in time.

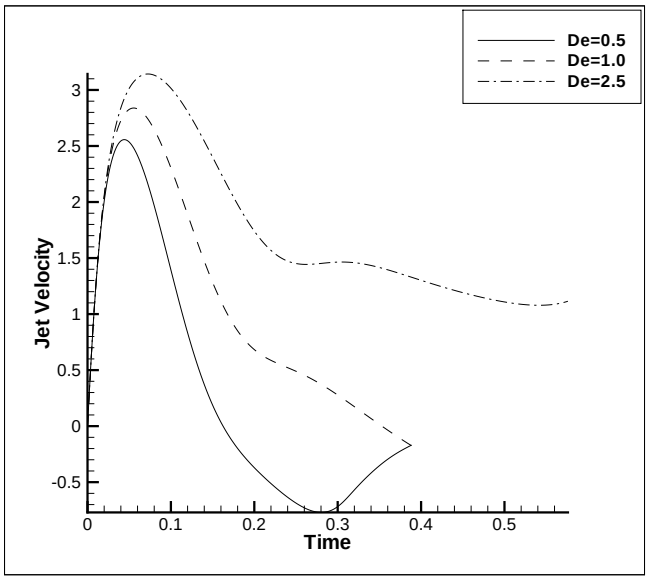

Figure 5.20: Free surface jet velocity for $h = 0.5$ with different De.

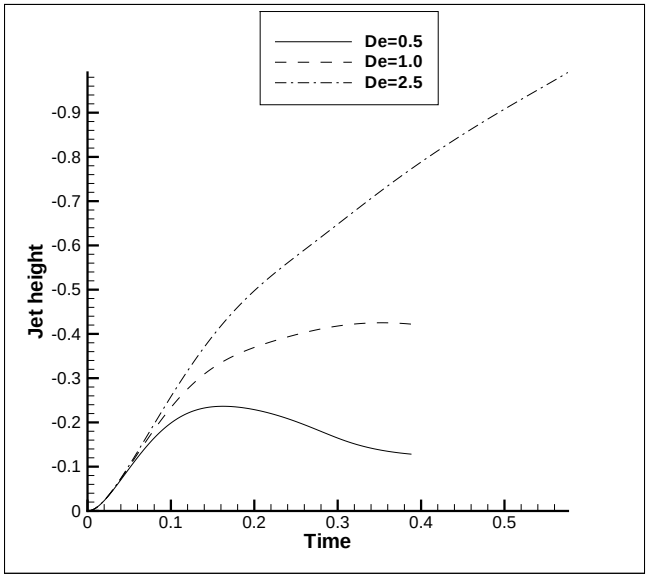

Figure 5.21: Free surface jet height for $h = 0.5$ with different De.

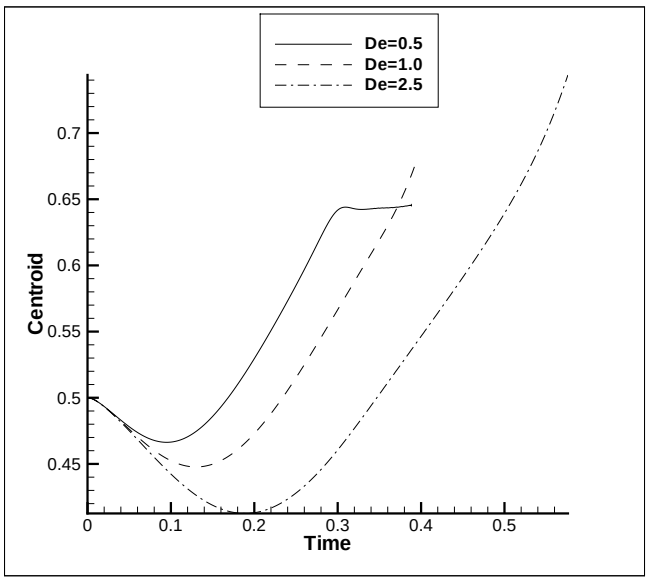

Figure 5.22: Bubble centroid position for $h = 0.5$ with different De.

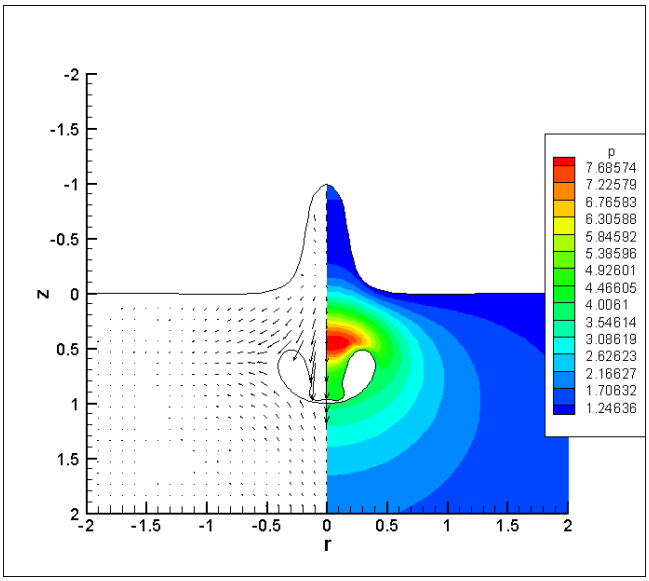

Figure 5.23: Pressure contours and velocity vectors at $t = 0.574$ with $De = 2.5$, $Re = 1.0$ ($h = 0.5$).

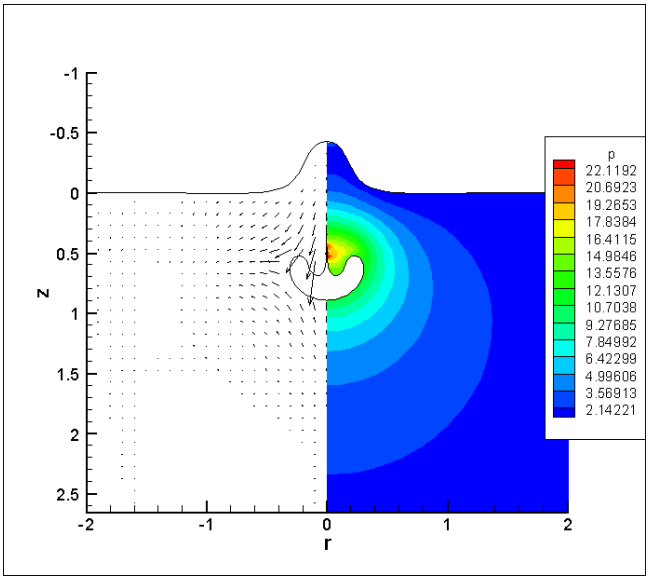

Figure 5.24: Pressure contours and velocity vectors at $t = 0.393$ with $De = 1.0$, $Re = 1.0$ ($h = 0.5$).

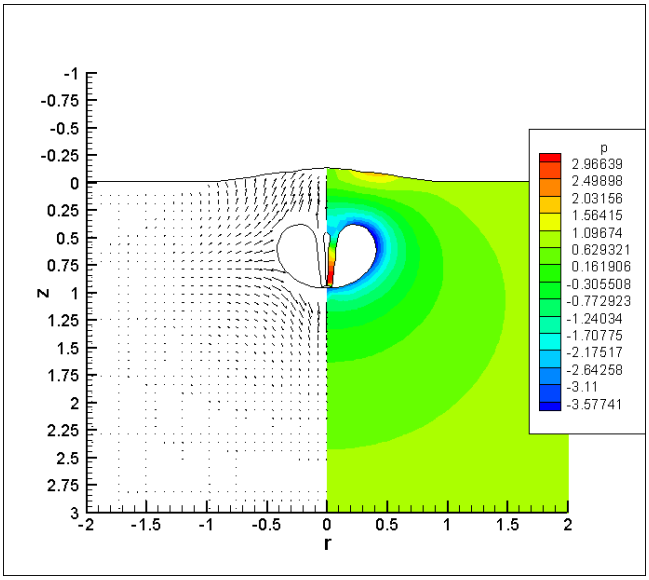

Figure 5.25: Pressure contours and velocity vectors at $t = 0.388$ with $De = 0.5$, $Re = 1.0$ ($h = 0.5$).

We shall now briefly comment on the dynamics when the bubble is positioned further away from the free surface at an initial distance $h = 0.75$. Figure 5.26 shows the bubble and free surface profiles for $De = 1.0$ and $Re = 1.0$, $h = 0.75$. Interestingly, the annular jet that was seen in the $h = 0.5$ case is no longer seen for $h = 0.75$. The bubble expands and causes slight deformation in the free surface, then during collapse the top of the bubble flattens before an axial liquid jet penetrates the bubble and impacts upon the underside. Indentations in the flattened bubble surface at $t = 0.435$ indicate the possibility of an annular jet forming, before the irresistible action of the axial jet.

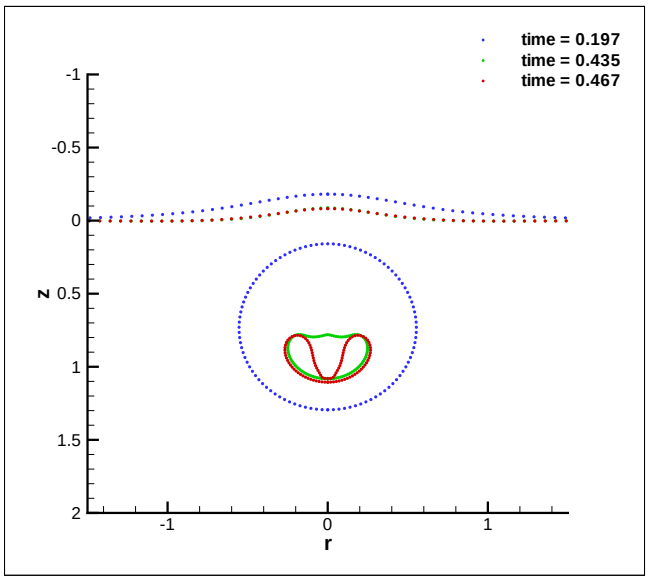

Figure 5.26: Bubble and free surface shapes with $De = 1.0$, $Re = 1.0$ at $h = 0.75$. Different colours indicate different instances in time.

Figure 5.27 shows the bubble and free surface profiles when the Deborah number is decreased to $De = 0.5$. As before, viscous forces become more dominant, and inertia plays a smaller role. Consequently the elastic effects become more discernible from the inertial. During growth, the bubble undergoes minimal deformation, and perturbs the free surface only slightly. The collapse is then characterised by the oscillation of the bubble surface with time. Such oscillation being due to the action of the compressed gas content and the elastic stresses. No jet of any kind forms, and the deformation in the bubble throughout its oscillation is small.

This oscillation can be seen readily in the graphs of the free surface jet velocity (Fig. 5.28) and jet height (Fig. 5.29). For $De = 1.0$ there is a single oscillation in the free surface, despite there being no oscillations in the bubble. For $De = 0.5$ there are several oscillation during the growth phase and collapse phase, but with the jet velocity

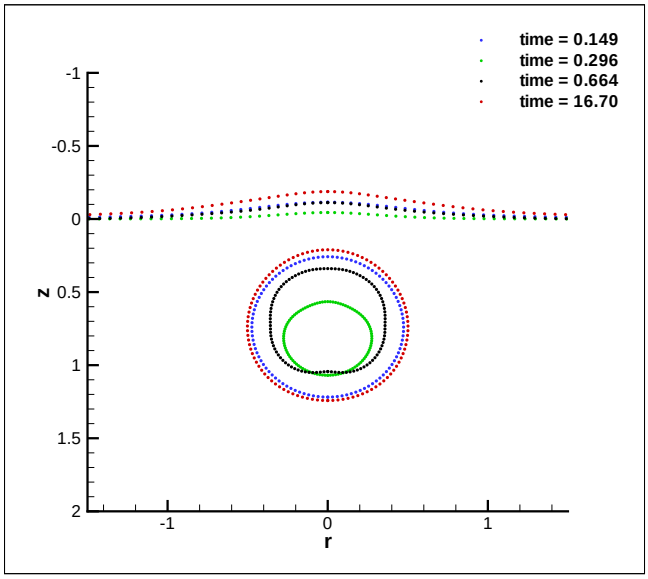

Figure 5.27: Bubble and free surface shapes with $De = 0.5$, $Re = 1.0$ at $h = 0.75$. Different colours indicate different instances in time.

or height never reaching as large a value as seen for $De = 1.0$, due to the increased effect of viscous dissipation.

Similarly, the plot of centroid position with time (Fig. 5.30) highlights the difference in the oscillatory nature of the dynamics. The $De = 1.0$ case resembles the centroid profiles observed previously, while $De = 0.5$ displays a marked difference as the bubble centre of mass undergoes a large oscillation first, before subsequent smaller oscillations.

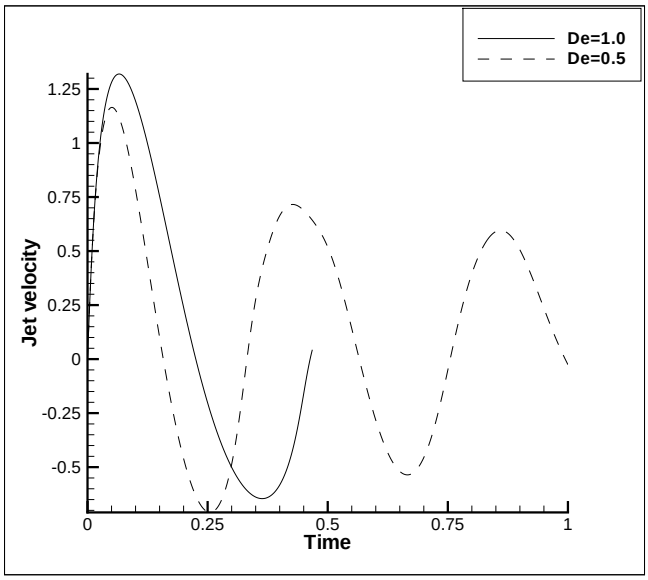

Figure 5.28: Free surface jet velocity for $h = 0.75$ with different De.

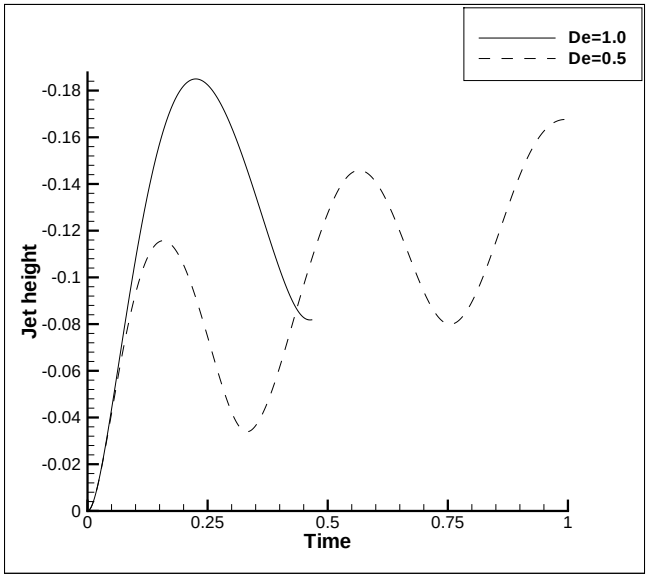

Figure 5.29: Free surface jet height for $h = 0.75$ with different De.

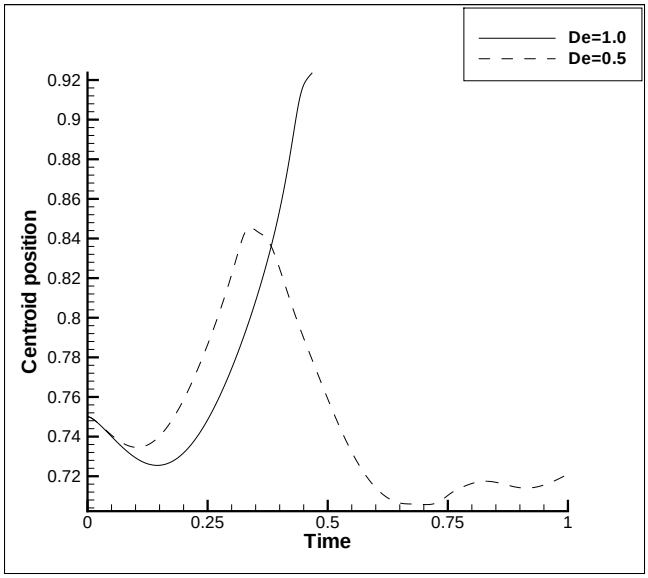

Figure 5.30: Bubble centroid position for $h = 0.75$ with different De.

The initial position of the bubble from the free surface is now increased to $h = 1.0$. Figure 5.31 shows the bubble and free surface profiles for $De = 1.0$, $Re = 1.0$, $h = 1.0$. Expectedly, the deformation in the free surface is less as the influence of the bubble decreases with increasing distance. No discernible free surface jet forms. As in the previous case when $h = 0.75$, there is no annular jet, but an axial one which penetrates the bubble, while the bulk of the bubble expands due to the gas content and elasticity.

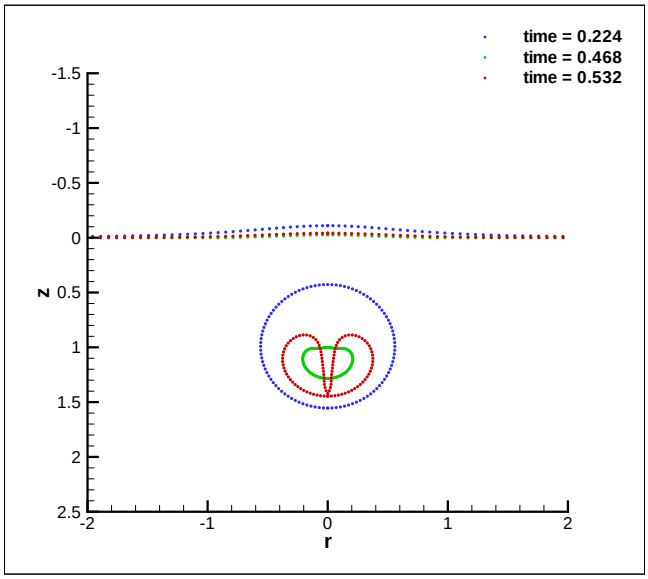

Figure 5.31: Bubble and free surface shapes with $De = 1.0$, $Re = 1.0$ at $h = 1.0$. Different colours indicate different instances in time.

If the Deborah number is decreased to $De = 0.5$ (Fig. 5.32), as in the $h = 0.75$ case, the effects of inertia are suppressed by the viscous effects, so jet formation is prevented and the elastic effects become more apparent. The bubble oscillates as it grows and collapses, and given the increased distance of the bubble from the free surface the bubble remains very nearly spherical throughout its lifetime, with minimal deformation in the free surface.

Figures 5.33 and 5.34 display the free surface jet velocity and jet height, respectively. The oscillation in the free surface for both $De = 1.0$ and $De = 0.5$ is evident. Given the reduced effects of viscous dissipation, the maximum velocity and height of the free surface jet is larger in the $De = 1.0$ case. Whereas the computation stops following jet impact for $De = 1.0$, the near-spherical oscillations for $De = 0.5$ are able to continue. Figure 5.35 shows the variation of the bubble centroid positions with time. The plots resemble those of the $h = 0.75$ case, with the bubble migrating from the boundary when $De = 1.0$ (as also seen in the Newtonian case). But when $De = 0.5$, the bubble

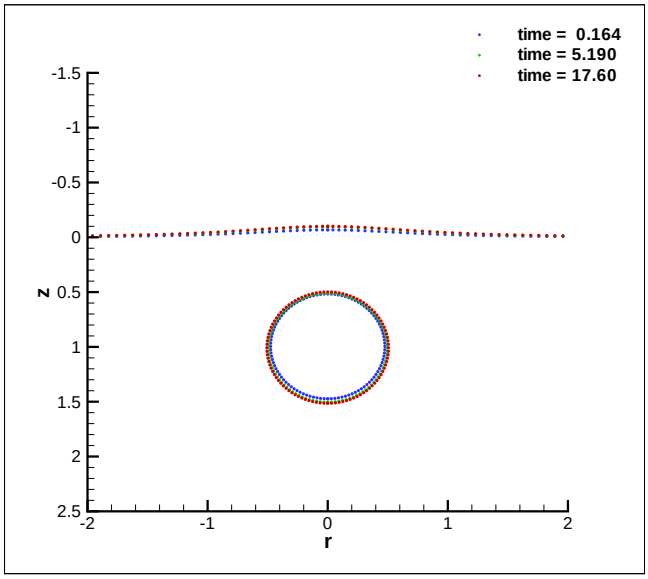

Figure 5.32: Bubble and free surface shapes with $De = 0.5$, $Re = 1.0$ at $h = 1.0$. Different colours indicate different instances in time.

centroid undergoes low amplitude oscillations near its initial position.

As alluded to, the bubble and free surface will continue to oscillate until an apparent steady state is reached. In fact such a situation occurs for $h = 0.75, De = 0.5, Re = 1.0$ also, but we just discuss the results for the $h = 1.0$ case here. Figure 5.36 shows the bubble centroid, free surface jet height and jet velocity over a larger time interval for the parameters $De = 0.5, Re = 1.0, h = 1.0$. The arrival at a steady state is clear as beyond $t \approx 8.0$ each measure reaches a constant value, with the jet velocity very nearly zero.

Considering the pressure contours and velocity vectors, Fig. 5.37 plots an instant in time just before jet impact for $De = 1.0$. In contrast to the pressure fields usually seen for axial jets, the high pressure region occurs within the jet, with a maximum at the jet tip. This is a result of the high curvatures present in the sharp jet tip and the subsequently large normal stresses.

For the $De = 0.5$ case, the apparent arrival at a steady state is confirmed. The pressure throughout the fluid is approximately $p \approx 1.0$, namely hydrostatic pressure. With little variation from the hydrostatic pressure the fluid must be near stationary, with the gas pressure inside the bubble and the atmospheric pressure beyond the free surface, balanced exactly by the fluid pressure.

Note that steady states were also observed for the collapse of viscoelastic cavities near

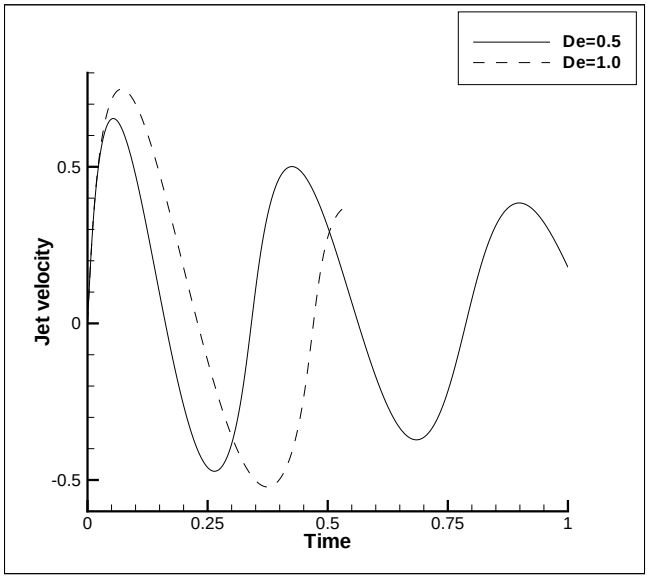

Figure 5.33: Free surface jet velocity for $h = 1.0$ with different De.

rigid boundaries in Chapter 3 and suggests that this is a consistent phenomenon in viscoelastic bubble dynamics.

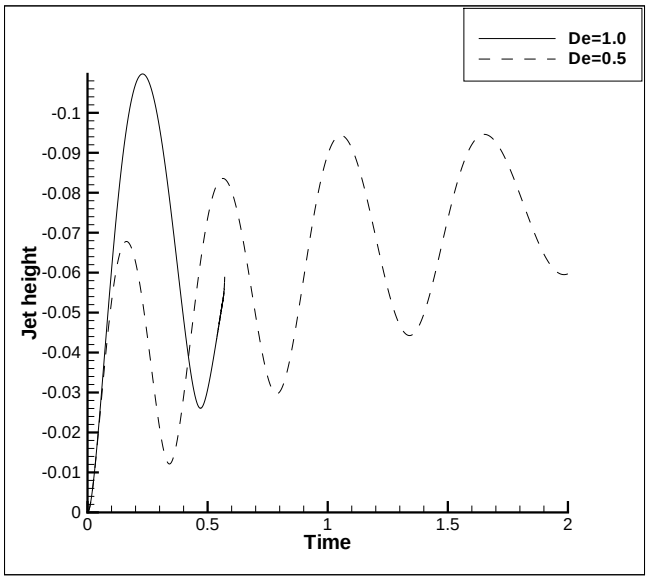

Figure 5.34: Free surface jet height for $h = 1.0$ with different De.

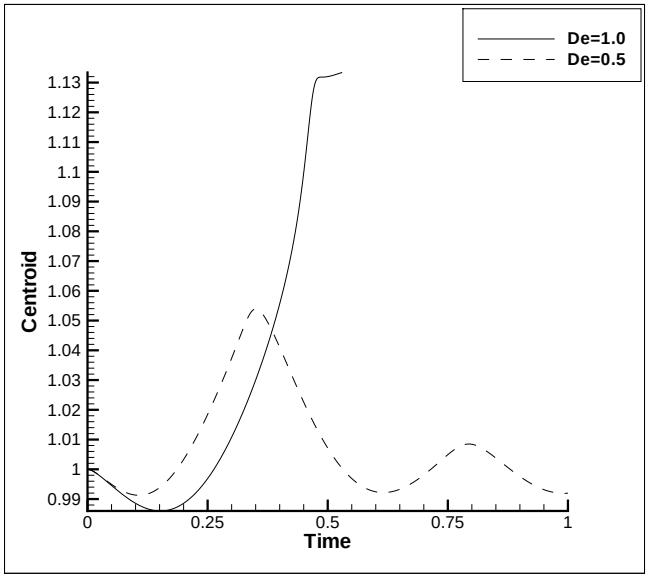

Figure 5.35: Bubble centroid position for $h = 1.0$ with different De.

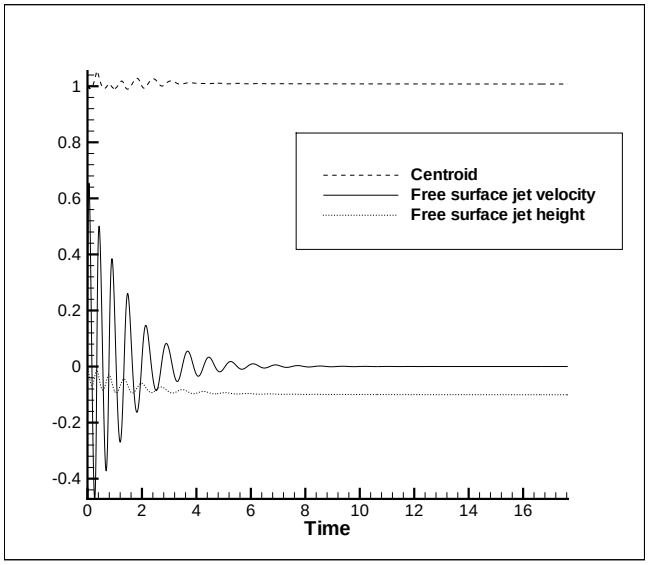

Figure 5.36: Bubble centroid position, free surface jet position and free surface velocity for $h = 1.0$, $De = 0.5$, $Re = 1.0$.

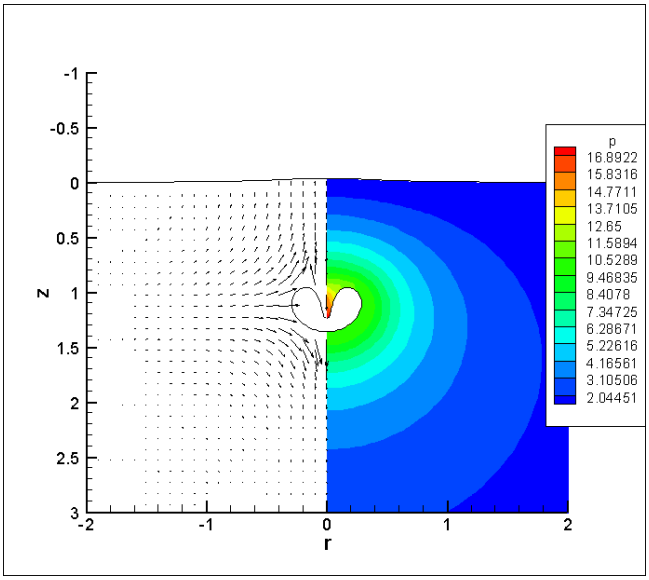

Figure 5.37: Pressure contours and velocity vectors at $t = 0.532$ with $De = 1.0$, $Re = 1.0$ ($h = 1.0$).

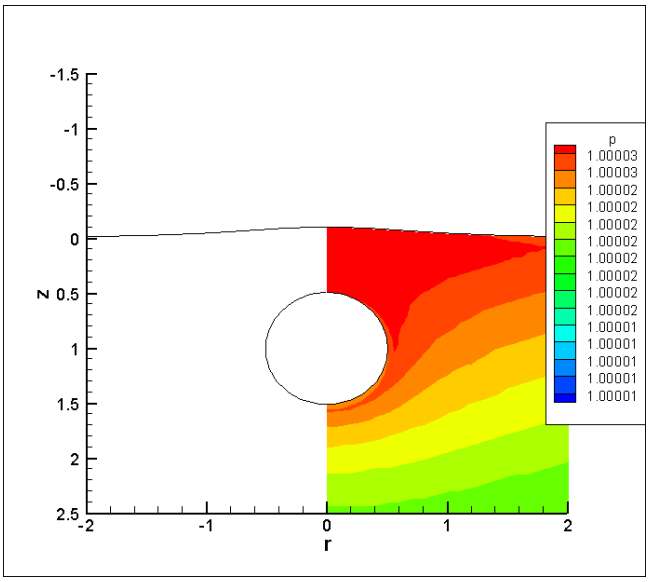

Figure 5.38: Pressure contours and velocity vectors at $t = 17.6$ with $De = 0.5$, $Re = 1.0$ ($h = 1.0$).

5.3.4 Comparison with bubbles near elastic boundaries

As mentioned in Section 5.3.3, the mushroom-like bubble shapes produced in the current work are similar to those produced when a bubble collapses near an elastic medium or membrane. Figure 5.39(a) presents the results of [82] (Fig. 3) which show a bubble collapsing near an elastic medium. The density ratio between the two fluids is 0.967, and the elasticity coefficient is 0.799. The experimental images below (Fig. 5.39(b)) are those of Brujan et al. [35] for a bubble near a PAA/ 85% water sample. The results show good agreement until the very final stages.

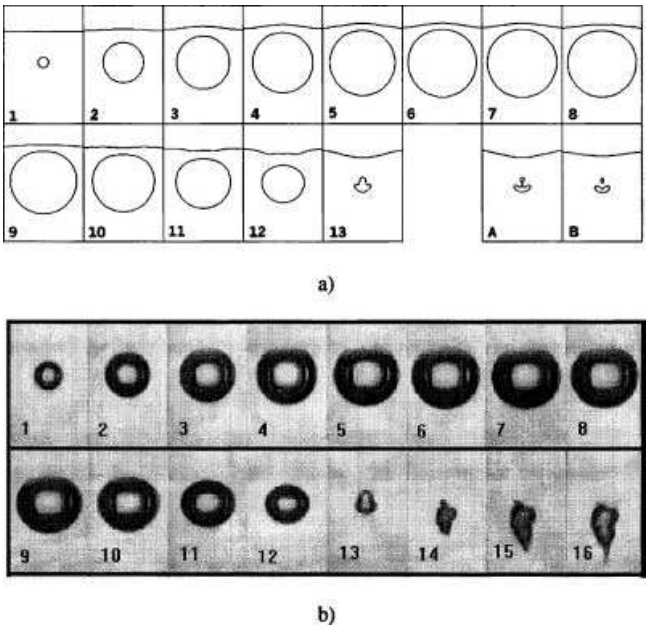

Figure 5.39: Bubble collapse near an elastic medium[2].

Note the similarity in the bubble shapes of Fig. 5.39(a), Frame A, to that of Fig. 5.14 for example. The studies of Klaseboer and Khoo [82] and Turangan et al. [155] note that such shapes are not produced when elasticity is not present in the external medium. In concurrence with the Newtonian studies presented here, no such shapes are observed. The current work seems to confirm the role of elasticity in the formation of such mushroom shaped bubbles in close proximity to (visco)elastic surfaces. The presence of the free surface is the crucial factor, for if the bubble is positioned further from the free surface, as seen in Fig. 5.27, the mushroom shape does not form, despite the presence of viscoelasticity. Interestingly, such mushroom shapes were observed in the study of

[2]Reprinted with permission from E. Klaseboer and B. C. Khoo, An oscillating bubble near an elastic material, Journal of Applied Physics, 2004, Vol. 96, 5808. Copyright 2004, American Institute of Physics.

two bubble dynamics near a wall in Chapter 4. For two bubbles positioned a moderate distance from the wall, the lower smaller bubble forms into a mushroom-like shape, under the influence the upper, larger bubble. Evidently, the smaller bubble views the larger bubble as an approximation to an infinite free surface, and subsequently, exhibits similar dynamics. As described in Klaseboer and Khoo [82], the reason for the formation of these shapes is the introduction of a perturbation in the bubble surface, by the neighbouring free surface. Deformations resulting from the elastic responses of the free surface exert a force on the neighbouring bubble, introducing perturbations in its surface. In [82], depending on parameters, these perturbations can travel along the whole length of the bubble, or only a short distance before the bubble collapses, producing different shapes. In the current work, the perturbations do not seem to travel far from the north-pole of the bubble before fluid inertia causes bubble collapse, and creates the observed annular jets and thin-stemmed mushrooms with voluminous bodies. Figure 5.40 highlights the formation of this perturbation graphically. Without a doubt it is the effect of viscous dissipation that dampens the propagation of these perturbations along the bubble surface, in comparison to [82], where no dissipative mechanisms are present.

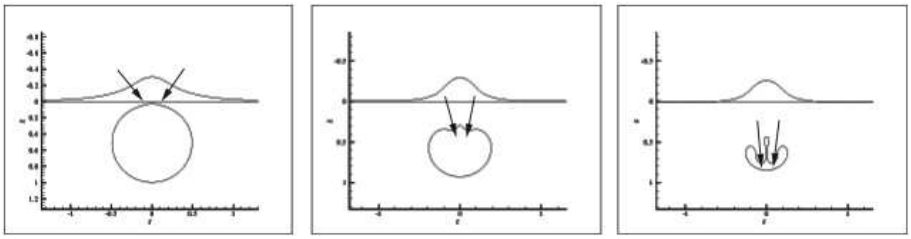

Figure 5.40: The instigation of a perturbation in the bubble surface by the free surface, resulting in annular jet formation.

5.3.5 Comment on comparison with experimental work of Williams et al. [165]

Williams et al. [165] performed an experimental study of the liquid jets formed in free surfaces by bubble collapse in viscoelastic fluids. The study utilises the novel experimental technique described in [164] in creating the free surface jets. A gas bubble created in a cylindrical column of viscoelastic fluid rises through the column to a free surface, coming to rest directly beneath it. The liquid column is then subject to dynamic tension causing cavitation bubbles to form. The collapse of these cavitation bubbles creates a shockwave which then drives the collapse of the gas bubble near the free surface, creating the free surface jet. Figure 5.41 shows the gas bubble near the free surface, and the subsequent jet produced by bubble collapse. The experimental technique in fact approximates in vivo situations where multiple cavities are formed, and the interaction of shocks with bubbles play an important part in cavitation damage.

Although modelling this situation using the BEM is possible, considerable extensions to the theory are necessary. A pressure pulse can be introduced into the scheme as in the work of Klaseboer et al. [83]. Their BEM results compare well to other compressible numerical methods in studying bubble collapse in an infinite medium due to shock waves, despite their theory being incompressible.

The pressure pulse incident on the gas bubble is assumed to have the simplest possible form (that of a square waveform, see Fig. 5.42), with amplitude P_s, velocity U_s, and width W_s. A schematic depiction is given in Fig. 5.43. The propagation of the pulse is then included by setting the hydrostatic pressure p_∞ in Equation (5.5) to the pressure of the pulse when the pulse passes through the region of space in question, while p_∞ is set to a reference pressure P_{ref} everywhere else. Mathematically,

$$p_\infty = \begin{cases} P_{\text{ref}} & \text{if } z < z_0 + tU_s - W_s \\ P_s & \text{if } z_0 + tU_s - W_s < z < z_0 + tU_s \\ P_{\text{ref}} & \text{if } z > z_0 + tU_s \end{cases}$$

The variables are non-dimensionalised as in Section 5.2 but with respect to the refer-

[3]Reprinted from the Journal of non-Newtonian Fluid Mechanics, Vol. 76, P. R. Williams and P. M. Williams and S. W. J. Brown, A study of liquid jets formed by bubble collapse under shock waves in elastic and Newtonian liquids, 307-325, Copyright (1998), with permission from Elsevier.

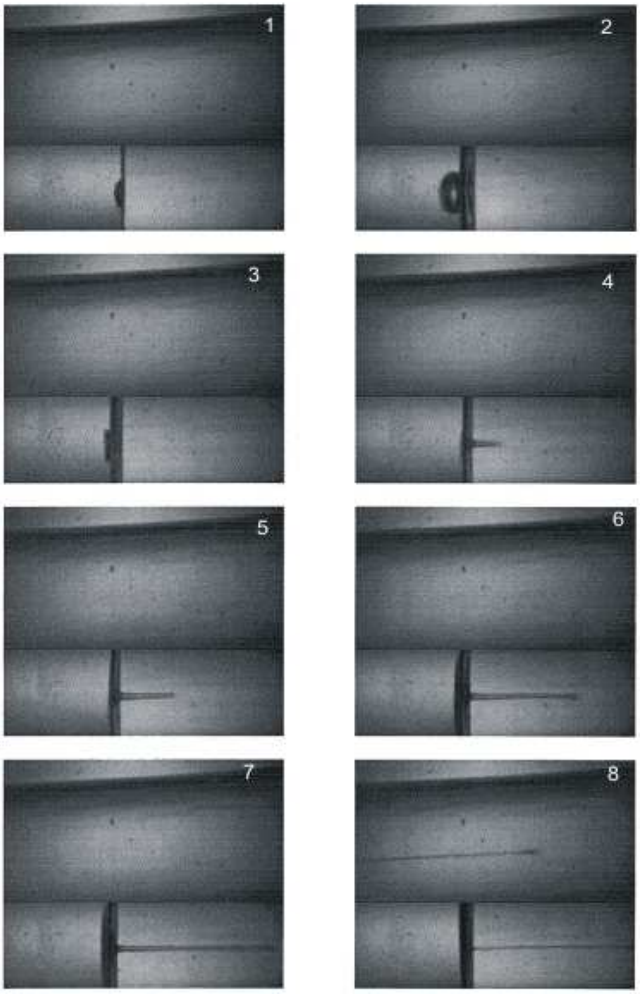

Figure 5.41: Jet formation in Newtonian silicon oil, with a shear viscosity of 0.18Pa·s.[3]

ence pressure, P_{ref}, instead of hydrostatic pressure p_∞. The reference pressure P_{ref} is taken to be atmospheric pressure, $P_{\text{ref}} = 1 \times 10^5\text{Pa}$. To attempt to model the phenomena observed in experiment, we place an initially spherical bubble near a free surface at $h = 1.5$, before initiating its collapse by subjecting it to the shockwave defined above. The simulation starts at the instant the shockwave strikes the bubble, hence $z_0 = 2.5$. From the pressure record provided by Williams et al. [165], the amplitude of the shockwave is $P_s \approx 1.3 \times 10^7\text{Pa}$, while the speed of the shock is of the order of $U_s \sim 400\text{ms}^{-1}$. Scaling with respect to the reference pressure, maximum bubble radius (approximately 2.5mm), and assuming the fluid density $\rho \approx 1000\text{kgm}^{-3}$, the non-dimensional parameters are, $P'_{\text{ref}} = 1$, $P'_s = 130$, and $U'_s = 40$. The shock width is taken to be $W'_s = 100$.

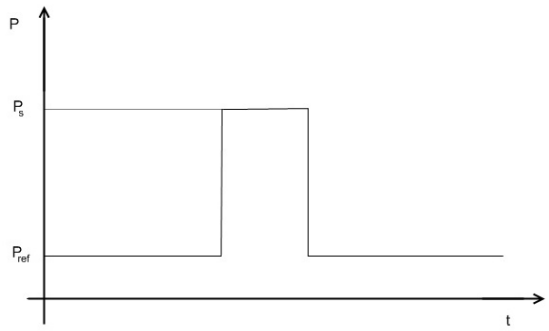

Figure 5.42: Form of pressure pulse

The fluid used in the experiment of Fig. 5.41 was Newtonian with a shear viscosity of $\mu = 0.18$Pa·s. By Equation (4.12), the corresponding Reynolds number is approximately $Re = 140$. Hence assuming the fluid to be inviscid is a viable approximation, certainly for illustrative purposes. Figure 5.44 shows the computed bubble and free surface profiles during collapse.

The top left image details the initial configuration, with the incident shockwave represented by the red horizontal line. The shockwave then initiates collapse, and as it passes through the bubble, a liquid jet begins to form. The jet begins to penetrate the bubble, travelling in the direction of the shockwave - the opposite direction to the jets observed in Section 5.3.2. These results are promising, closely resembling the transition from frame 2 to frame 3 of Fig. 5.41. That is, the moment before the arrival of the shockwave (frame 2) and the thin flattened bubble produced before the formation of the free surface jet (frame 3). In the experiment, the liquid jet then completely penetrates the bubble, passing through to the free surface to create a thin free surface jet (frames 4-8) - much like those seen in Section 5.3.2. Meanwhile, the newly formed toroidal bubble continues to collapse. In the current study however, the theory has yet to be extended to include the evolution to a toroidal geometry. This is a necessity in order to model the high speed jet fully penetrating the bubble and creating that observed in the free surface. The most popular methodology in modelling toroidal dynamics was introduced by Best [10]. Considering the dynamics immediately prior to and after jet impact, Best derived the following integral equation appropriate for the

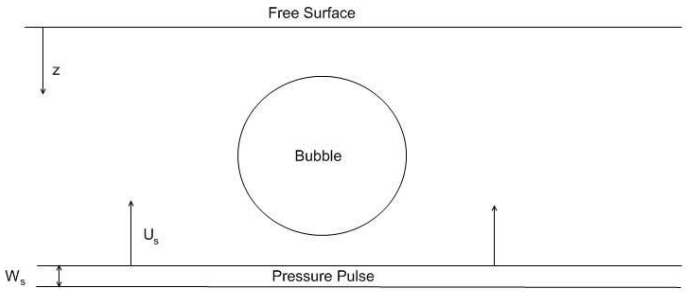

Figure 5.43: Schematic diagram of pulse, bubble, and free surface

doubly-connected toroidal geometry,

$$c(\mathbf{p})\phi(\mathbf{p}) = \int_{\partial\Omega} \left(\frac{\partial\phi}{\partial n}(\mathbf{q}) G(\mathbf{p},\mathbf{q}) - \phi(\mathbf{q}) \frac{\partial G}{\partial n}(\mathbf{p},\mathbf{q}) \right) dS - \Delta\phi \int_T \frac{\partial G}{\partial n}(\mathbf{p},\mathbf{q})\, dS, \quad (5.20)$$

where T denotes the surface over which jet impact takes place. This surface is retained throughout the simulation, acting as an imaginary link across the centre of the toroidal bubble in order to restore the singly-connected geometry. The quantity $\Delta\phi$ is the jump in potential across T and is equal to the circulation set up in the flow following jet impact. This extension to a toroidal geometry and the study of post-penetration dynamics is reserved for future work.

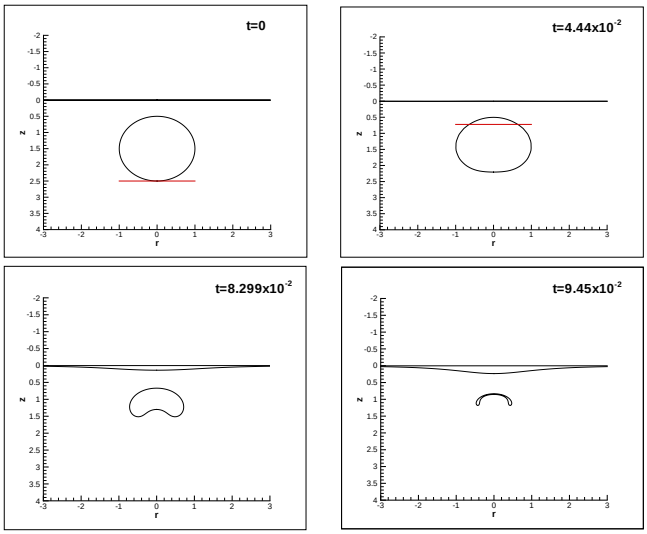

Figure 5.44: Bubble collapse under a shockwave, near a free surface, in a Newtonian inviscid fluid

5.4 Conclusions

This chapter has investigated the effect of viscoelasticity on the dynamics of gas bubbles near free surfaces. The phenomenon is most befitting to biological applications and has implications for cell damage and drug delivery to name only two. Besides this, the work gives a greater understanding of the role of viscoelasticity in bubble dynamics in general. A range of dynamics is seen to occur, with a subtle dependence on the Deborah number, Reynolds number and the initial distance of the bubble from the free surface. In the presence of viscoelasticity, the motion of free surface jets can be significantly retarded compared to the Newtonian cases, and the bubbles take a wide range of shapes. Provided inertial forces are not too large, the usual axial jet observed in many instances in the Newtonian dynamics, is no longer seen. Instead, an annular, ring like jet forms and can penetrate the bubble to produce mushroom-like shapes. Similar shapes are observed in bubbles collapsing near purely elastic boundaries, and are due to perturbations in the bubble surface resulting from the elastic responses of the free surface. This study acts to confirm the role of elasticity in producing such shapes. But the proximity of the free surface is crucial, for if the bubble is moved further away from the free surface, little interaction takes place and the bubble collapses in a near-spherical, oscillatory manner, before reaching some steady state. Given that no high speed jets form in the bubble or free surface, the implications for cavitation/cell damage can clearly be mitigatory. But the role of elasticity is not generally inhibitive, for it is the *balance* between inertial, viscous and elastic effects that determines dynamics. Increasing elastic effects can abate viscous effects to the extent that in fact inertia dominates dynamics, so that at higher Deborah number, a reversion to Newtonian-like dynamics occurs, with the formation of an axial bubble jet. The observed dynamics, though veracious in exhibiting viscoelastic behaviour, is of course constitutive model dependent. The simple material Maxwell model has been used here, and so future work will entail further studies on the same situations but with other compatible viscoelastic models.

Brief comparisons with the experimental work of Williams et al. [165] have also been made. The model was extended to include the propagation of shock waves and shock-induced bubble collapse. The results are promising in the early stages, but to recreate the observed free surface jets, the theory needs to be extended to include evolution to a toroidal geometry, to allow the liquid jet to fully penetrate the bubble and form

the free surface jet. Future work will include this extension to the theory, allowing full comparisons to be made.

Chapter 6

The Effect of Viscoelasticity on a Rising Gas Bubble

6.1 Introduction

The study of the motion of air bubbles in liquids has received much attention for many years due to its fundamental and practical importance. The rise of bubbles in Newtonian fluids has been studied intensively both theoretically and experimentally. The dynamics of rising Newtonian bubbles depends primarily on the effects of surface tension and the Reynolds number. When surface tension effects are dominant the bubble can remain spherical during ascension. Similarly at very small Reynolds numbers, deformation is small and the bubble remains spherical. In the limit of negligible inertia, Stokes approximation for a translating rigid sphere [141] provides a reasonable approximation to the flow and the drag on the bubble [29]. This approximation was extended independently by Hadamard [62] and Rybzynski [136], who considered a fluid sphere which allowed for slip and a zero shear stress on the bubble surface. Levich [88] and Moore [106] employed a viscous potential flow approximation, and their drag prediction is in better agreement with experiments in cases where inertia is not negligible. As its size increases, the bubble deviates from its spherical shape. At progressively larger volumes the bubble evolves into a prolate ellipsoid with an increasingly flattened underside until, at negligible surface tension effects, a spherical cap bubble can form [163]. There are many numerical studies examining the deviation from the spherical shape seen in Newtonian fluids. The work of Boulton-Stone [24, 27] and Robinson et al. [131] use the boundary element method to study the deformation in rising gas

bubbles in an inviscid fluid for the 3D axisymmetric and 2D cases, respectively. Their numerical simulation studies reproduce many of the bubble shapes observed in experiment. Similarly, Pozrikidis [122] uses a boundary element method to study the oscillations in rising bubbles for the fully 3D problem, noting that rising bubbles oscillate at higher frequencies than stationary bubbles. Miksis et al. [105] use a boundary element method to study the bubble shapes produced in a steady-state viscous potential flow. Again, their results bear a strong resemblance to experimental observations and empirical results. Non-BEM studies include that of Pillapakkam and Singh [116], who use a level set finite element method, and similarly Sussman et al. [144] who use a level set method but with finite differences. Ryskin and Leal [137] solve a steady-state reformulated Navier-Stokes equation to determine terminal bubble shapes, while Tryggvason et al. [154] use a front tracking scheme combined with a finite volume method, in modelling rising bubbles and associated phenomena. Each of these studies captures many of the essential features observed experimentally for the Newtonian rising bubble.

Unsurprisingly, the characteristics of a rising viscoelastic bubble differ drastically from the Newtonian case. Subsequently, the interesting dynamics associated with viscoelastic fluids has spurred a plethora of experimental studies, although comparatively few theoretical and numerical ones. At low Reynolds numbers one still observes near spherical rise as viscous effects dominate and inhibit deformation. However, larger bubbles form more prolate ellipsoidal shapes with the underside becoming increasingly drawn out. As explained by Bird et al. [15], this results from an additional tension along the streamlines, squeezing the bubble at the equator. Beyond a certain critical volume, a cusp can then form at the trailing end [118]. Accompanying the change in shape from fully concave to cusped can be a large increase in the terminal rise velocity. Given the small change in volume over which this transition takes place, it effectively represents a discontinuity [72]. One of the first studies of this velocity jump was undertaken by Astarita and Apuzzo [6] who attributed it to a transition from a Stokes to Hadamard regime. Subsequent studies have proposed other reasons such as drag reduction [95], the presence of surface active agents [133] combined with surface tension forces [134], and the appearance of a negative wake [66] in the flow behind the rising bubble. The negative wake behind a rising gas bubble in a non-Newtonian elastic liquid is a typical occurrence, first observed by Hassager [65]. It is a non-Newtonian phenomenon but not unique to gas bubbles, having also been observed behind spheres settling in viscoelastic

liquids [3, 63]. Although there have been several studies of the flow field around the rising bubble (e.g. Funfschilling and Li [58]), a full explanation of the appearance of the negative wake behind bubbles is not yet available. Herrera-Velarde et al. [66] find that the negative wake only appears at bubble sizes above the critical volume. But as pointed out by Kemiha et al. [73], the deformation in the surface (cusping) at the critical volume cannot fully explain the origin of the wake, given that it is also seen behind settling rigid spheres. They conclude that the viscoelastic properties of the fluid must be responsible.

Numerical studies are fewer in number than their experimental counterparts. Wagner et al. [159] and Frank and Li [55] use 2D Lattice Boltzmann methods to study the problem, using Maxwell type constitutive equations for the ambient fluid. Both are able to predict the observed cusp, with the latter also predicting the formation of the negative wake. However, the velocity jump discontinuity is not observed in either of these studies. Málaga and Rallison [102] undertake an axisymmetric boundary element study of the problem, under the assumption of Stokes flow in a FENE fluid. Once again, despite reproducing a small cusp at the trailing end, no jump discontinuity was observed. The numerical technique which seems to have borne most fruit is that of Pillapakkam et al. [117]. They make use of a 3D level-set finite element method to solve the full equations of motion with an Oldroyd B constitutive equation. Not only do they observe a cusp and the negative wake, but also the velocity jump discontinuity. As in Herrera-Velarde et al. [66], they attribute the principal cause of the jump to the negative wake.

The above review highlights the complex and fascinating dynamics observed in rising bubbles in viscoelastic fluids. Furthermore, it emphasises that little is still known about the three characteristic phenomena - the formation of the cusp, the jump discontinuity, the negative wake, and crucially, their relationship to one another. The variety of explanations given in the experimental literature, and the sparsity of numerical results means there is much work still to be done in gaining a full understanding of the dynamics. In this chapter we use a modification of the theory presented in chapter 2 to attempt to describe the dynamics of a gas bubble rising in a viscoelastic fluid. The choice assumptions allow crucial insights into the dynamics that could not be made in experiments, allowing us to vindicate theories proposed in previous experimental and

numerical works.

6.2 Mathematical Model and Governing Equations

As in previous numerical studies (for example [24, 102, 131]), we consider the rise of a constant volume gas bubble. This is also consistent with experimental observations [118] and, in effect, means that the change in hydrostatic pressure as the bubble rises is small compared to the ambient fluid pressure. The bubble rises under the action of buoyancy forces, and is subject to viscoelastic effects as it ascends. As outlined in chapter 2, the fluid surrounding the bubble is assumed to be incompressible and irrotational, with viscoelastic effects appearing in the normal stress balance on the bubble surface. Consequently, the conservation of mass is described by Laplace's equation

$$\nabla^2 \phi = 0, \tag{6.1}$$

while the potential is governed by the following irrotational equation of motion

$$\rho \frac{D\phi}{Dt} = \frac{\rho}{2}|\mathbf{u}|^2 + p_\infty - p + \rho g z, \tag{6.2}$$

where $\mathbf{u}$ is the fluid velocity and ρ the fluid density. Note the additional buoyancy term due to the inclusion of the gravity body force, where g is the acceleration due to gravity and z is the vertical displacement from some reference height.

At any instant in time, the fluid pressure p is related to the bubble pressure $p_b(t)$ and viscoelastic effects, through the normal stress balance

$$p = p_b(t) - \sigma\kappa + T_{nn}, \tag{6.3}$$

where σ is the surface tension, κ is the curvature, and T_{nn} is the normal-normal component of the extra stress.

We assume the bubble is initially spherical and that it starts at rest, centred at $z = 0$. The reference pressure p_∞ is defined such that $p = p_\infty$ at $z = 0$, and thus the initial normal stress balance gives

$$p_\infty = p_b(0) - \frac{\sigma}{R_0}. \tag{6.4}$$

(Noting that $T_{nn} = 0$ since the fluid is at rest). Substituting equations (6.4) and (6.3)

in equation (6.2) gives the following equation of motion, in terms of bubble pressure term $\Delta p_b(t) = p_b(t) - p_b(0)$

$$\rho \frac{D\phi}{Dt} = \frac{\rho}{2}|\mathbf{u}|^2 + \Delta p_b - T_{nn} + \sigma\left(\kappa - \frac{1}{R_0}\right) + \rho g z, \tag{6.5}$$

with the rheological properties governed by the Maxwell constitutive equation viz.,

$$\lambda \frac{DT_{nn}}{Dt} + T_{nn} = \mu \dot{\gamma}_{nn}, \tag{6.6}$$

where λ is the relaxation time and μ is the shear viscosity. Meanwhile, the solution of Eq. (6.1) can be expressed in the usual integral form,

$$c(\mathbf{p})\phi(\mathbf{p}) = \int_{\partial\Omega} \left(\frac{\partial \phi}{\partial n}(\mathbf{q}) G(\mathbf{p}, \mathbf{q}) - \phi(\mathbf{q}) \frac{\partial G}{\partial n}(\mathbf{p}, \mathbf{q}) \right) dS \tag{6.7}$$

where $\partial\Omega$ is the boundary of the bubble in fluid domain Ω, and the constant $c(\mathbf{p})$ is given by

$$c(\mathbf{p}) = \begin{cases} 2\pi & \text{if } \mathbf{p} \in \partial\Omega, \\ 4\pi & \text{if } \mathbf{p} \in \Omega \backslash \partial\Omega \end{cases}$$

Spatial variables are non-dimensionalised with respect to the initial bubble radius R_0, while time, pressure and the potential are scaled, respectively, according to

$$t^* = \frac{t}{(R_0/g)^{1/2}}, \tag{6.8}$$

$$p^* = \frac{p}{\rho g R_0}, \tag{6.9}$$

$$\phi^* = \frac{\phi}{(R_0^3 g)^{1/2}}. \tag{6.10}$$

The subsequent non-dimensionalised governing equations are (dropping asterixes),

$$\frac{D\phi}{Dt} = \frac{1}{2}|\mathbf{u}|^2 + \Delta p_b - T_{nn} + \frac{4}{E\ddot{o}}(\kappa - 1) + z, \tag{6.11}$$

and

$$De \frac{DT_{nn}}{Dt} + T_{nn} = \frac{1}{Re} \dot{\gamma}_{nn}, \tag{6.12}$$

with the conservation of mass given as in Eqn. (6.7). The non-dimensional parameters are the Deborah number,

$$De = \frac{\lambda g^{1/2}}{R_0^{1/2}}, \tag{6.13}$$

the Reynolds number,

$$Re = \frac{\rho g^{1/2} R_0^{3/2}}{\mu} \tag{6.14}$$

and the Eötvös number,

$$E\ddot{o} = \frac{4\rho g R_0^2}{\sigma}. \tag{6.15}$$

The Eötvös (or Bond) number can be described as a ratio between the buoyancy and surface tension forces.

As mentioned, experimental observation shows that rising gas bubbles in Newtonian and viscoelastic fluids remain very nearly constant in volume. Therefore, during bubble ascension, the internal bubble pressure $p_b(t)$ must vary in accordance with the changing external hydrostatic pressure. This provides an additional unknown with an additional equation provided by the volume constraint. The equation of motion (Eq. (6.11)) and the conservation of mass (Eq. (6.7)) now need to be recast to remove dependence on the unknown pressure term Δp_b. Define a new potential φ, such that

$$\varphi = \phi + k(t), \tag{6.16}$$

where

$$k(t) = \int_0^t (p_b(t) - p_b(0))\, dt. \tag{6.17}$$

Crucially, the fluid velocity is independent of this definition since $\nabla k(t) = \mathbf{0}$ and so $\mathbf{u} = \nabla\varphi = \nabla\phi$. Consequently, substituting Eq. (6.16) into the equation of motion (Eq. (6.11)) results in

$$\frac{D\varphi}{Dt} = \frac{1}{2}|\mathbf{u}|^2 - T_{nn} + \frac{4}{E\ddot{o}}(\kappa - 1) + z. \tag{6.18}$$

In particular, note that $T_{nn}(\varphi) = T_{nn}(\phi)$ as we start from an initial zero extra stress and $\dot{\gamma}_{nn} = \frac{\partial^2\phi}{\partial n^2} = \frac{\partial^2\varphi}{\partial n^2}$. Equation (6.18) is essentially the same as Eq. (6.11) but for the absence of the internal bubble pressure term Δp_b.

Secondly, substituting Eq. (6.16) into Eq. (6.7) gives,

$$c(\mathbf{p})\varphi = 4\pi k + \int_{\partial\Omega} \left(\frac{\partial \varphi}{\partial n} G - \varphi \frac{\partial G}{\partial n} \right) dS. \tag{6.19}$$

The first term on the right hand side derives from the property that $c = \int \frac{\partial G}{\partial n}\, dS = 2\pi$ on the bubble boundary.

To determine $k(t)$ one requires an additional equation provided by the volume constraint. If the volume of the bubble is to remain constant, then the net flux of fluid into the bubble surface must be zero. Therefore,

$$\int_{S_b} \frac{\partial \varphi}{\partial n}\, dS = 0. \tag{6.20}$$

Equivalently, for a constant volume bubble, the divergence of the velocity $\mathbf{u}^*$ of some hypothetical fluid within V_b must be zero. Hence, by the divergence theorem of Gauss

$$0 = \int_{V_b} \nabla \cdot \mathbf{u}^*\, dV = \int_{S_b} \mathbf{u}^* \cdot \mathbf{n}^*\, dS = -\int_{S_b} \frac{\partial \varphi}{\partial n}\, dS, \tag{6.21}$$

and we arrive at Eq. (6.20).
Given a potential φ, Eqns (6.19) and (6.20) can be solved simultaneously to obtain the normal velocity $\frac{\partial \varphi}{\partial n}$ and the pressure integral $k(t)$. Subsequently, the potential can be updated using Eq. (6.18), and the motion of the bubble tracked, in the usual Lagrangian manner.

6.3 Numerical Solution of Governing Equations

Many of the phenomena in bubble dynamics, such as spherical collapse and jet formation near a boundary, are seen to be axisymmetric [19]. Rising bubbles in viscoelastic fluids are also known to maintain axisymmetry over the jump inclusive volume ranges [118]. Consequently, as in the numerical study of Málaga and Rallison [102], we assume axisymmetry about the direction of motion. The problem is then effectively reduced from 3D to 2D, as the third dimension is treated analytically.

The boundary (the bubble surface) $\partial\Omega$ is discretised into N segments, characterised

by the nodes s_i, $1 \leq i \leq N+1$, with nodes 1 and $N+1$ lying on the axis of symmetry on the top and bottom of the bubble, respectively. The surface variables $r(s)$ and $z(s)$ and the potential $\varphi(s)$, are represented by cubic splines so that

$$q_i(s) = q_{i0} + q_{i1}(s - s_i) + q_{i2}(s - s_i)^2 + q_{i3}(s - s_i)^3, \tag{6.22}$$

for $s_i \leq s \leq s_{i+1}$, $i = 1, .., N$. The normal derivative of the potential $\frac{\partial \varphi}{\partial n}$ is represented linearly with respect to arclength.

Subsequent discretisation of the integral conservation of mass (Eq. (6.19)) and the volume constraint (Eq. (6.20)) results in the following linear system for k and the normal velocities (ψ_i) at each nodal point,

$$c(\mathbf{p}_i)\varphi_i + \sum_{j=1}^{N} A_{ij} = 4\pi k + \sum_{j=1}^{N}(B_{ij}\psi_j + C_{ij}\psi_{j+1}), \tag{6.23}$$

$$\sum_{j=1}^{N}(D_j\psi_j + E_j\psi_{j+1}) = 0. \tag{6.24}$$

The coefficients in Eqs. (6.23) and (6.24) are given by

$$\begin{aligned}
A_{ij} &= \int_{s_j}^{s_{j+1}} \varphi_j(s)\alpha_i(s)\, ds, \\
B_{ij} &= \int_{s_j}^{s_{j+1}} \frac{(s_{j+1} - s)}{\Delta s_j}\beta_i(s)\, ds, \\
C_{ij} &= \int_{s_j}^{s_{j+1}} \frac{(s - s_j)}{\Delta s_j}\beta_i(s)\, ds, \\
D_j &= \int_{s_j}^{s_{j+1}} \frac{(s_{j+1} - s)}{\Delta s_j} r(s)\, ds, \\
E_j &= \int_{s_j}^{s_{j+1}} \frac{(s - s_j)}{\Delta s_j} r(s)\, ds,
\end{aligned} \tag{6.25}$$

where α_i and β_i denote the analytical azimuthal integrations viz.,

$$\alpha_i(s) = \int_0^{2\pi} \frac{\partial G}{\partial n}(\mathbf{p}_i, s) r(s)\, d\theta, \tag{6.26}$$

$$\beta_i(s) = \int_0^{2\pi} G(\mathbf{p}_i, s) r(s)\, d\theta. \tag{6.27}$$

The integrals in (6.25) are approximated using a 10-point Gaussian quadrature rule while Gaussian elimination is used to solve the linear system (Eq. (6.23) and (6.24)). After solving the system for the normal velocity, the tangential velocity and higher derivatives of φ are found using a high-order finite difference approximation on non-uniform grids [89]. With the velocity now fully described on $\partial\Omega$, the bubble surface is advected in a Lagrangian manner while the potential and extra stress are updated using Eqs. (6.18) and (6.12), respectively. A fourth-order Runge Kutta method is used in updating the surface and the potential, with a second-order trapezoidal rule employed for the extra stress.

6.4 Rising Bubbles in a Newtonian Fluid

In this section we present the numerical results obtained in studying the rise of a gas bubble in a Newtonian fluid, and investigate the influence of the Reynolds and Eötvös numbers on the rise dynamics and terminal bubble shape. Figure 6.1 shows the bubble profile for $Re = \infty$ and a high Eötvös number, $E\ddot{o} = 106$ (near negligible surface tension), at different points during the bubble ascent. The bubble shapes are identical to those obtained in the boundary element study of Boulton-Stone [24] and the level-set approach detailed by Sussman et al. [144]. Here inertia and buoyancy dominate, creating a fluid jet that forms on the underside of the bubble and then travels upward, in the direction of bubble motion, before impacting on the upper surface. If the theory allowed for toroidal geometries, a toroidal vortex ring bubble would then form, as modelled by Lundgren and Mansour [100].

Figure 6.2 shows the rising bubble profiles following a decrease in the Eötvös number to $E\ddot{o} = 6.6$. Once again the bubble profiles agree well with those of Boulton-Stone [24]. As the jet forms, surface tension forces act to prevent deformation, creating a much broader jet with an increasingly thin outer rim. Surface tension forces then act to retract this outer rim, causing the bubble to pinch off the outer lobe (see final frame) creating a second thin ring bubble.

Figure 6.3 shows the bubble profiles for $E\ddot{o} = 2.4$. The effects of surface tension are such that no distinguishable liquid jet forms. The upward action of the buoyancy force

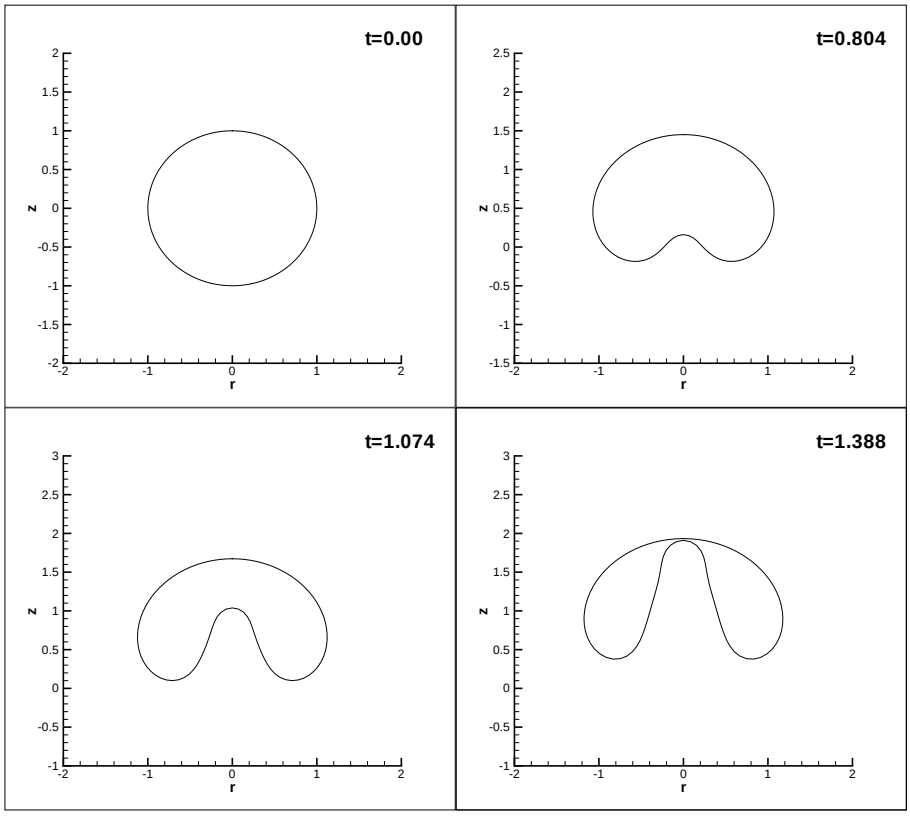

Figure 6.1: Bubble profiles at select times during ascent for $Re = \infty$ and $E\ddot{o} = 106$.

combined with the retractive effect of surface tension causes the bubble to evolve into a thin disk-like shape. Eventually the bubble thickness decreases to the point where upper and lower surfaces meet, allowing a possible transformation into a toroidal shape. Again, these results agree closely with those of Boulton-Stone [24].

Figure 6.4 shows the evolution of bubble profiles for two Eötvös numbers, $E\ddot{o} = 106$ and $E\ddot{o} = 2.4$, following the inclusion of viscous effects with $Re = 50$. Clearly the Reynolds number is still rather large and consequently there is no great difference in the terminal bubble shapes. However, the presence of viscosity has still had a noticeable effect on the transient dynamics. In particular, the time at which the final (non-toroidal) bubble shape occurs, has increased in both cases. This increase is substantial for $E\ddot{o} = 2.4$, with $t_f \approx 6.7$ for $Re = \infty$, but $t_f \approx 14.5$ for $Re = 50$. Subsequently, the final height reached is significantly larger, with $h_{max} \approx 9.4$ for $Re = \infty$ and $h_{max} \approx 21.8$ for $Re = 50$. Evidently viscosity is acting in the usual manner - inhibiting the fluid flow and bubble deformation. Consequently, bubbles undergo deformation at a slower rate and so exist (in their initial singly-connected form) for longer.

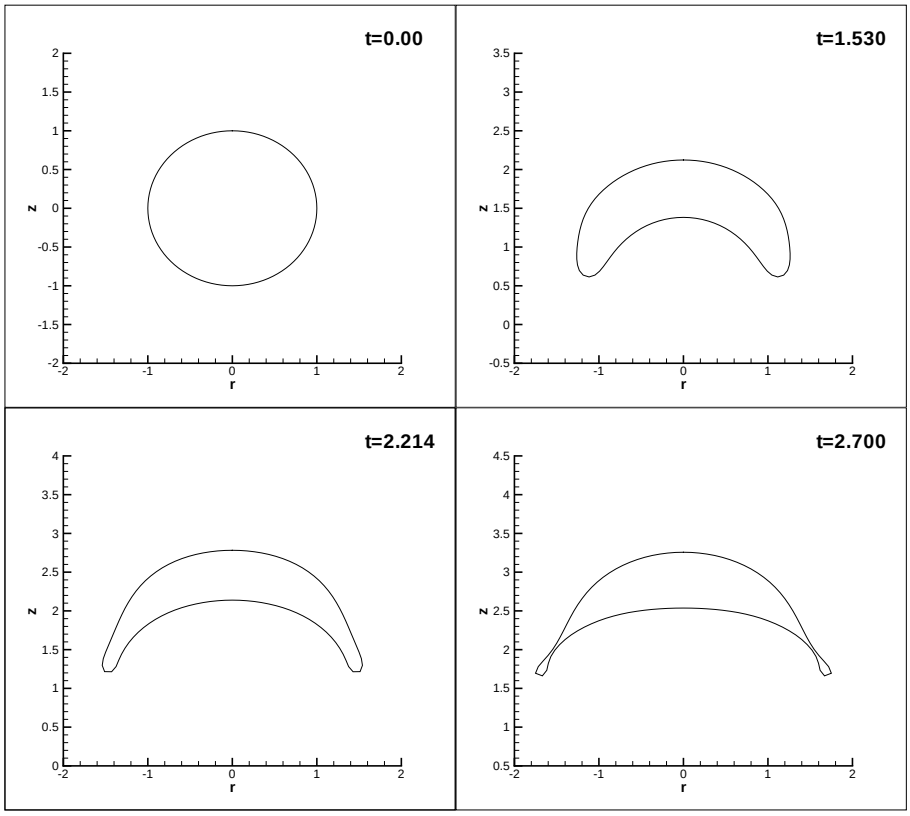

Figure 6.2: Bubble profiles at select times during ascent for $Re = \infty$ and $E\ddot{o} = 6.6$.

In the interests of conciseness, Figure 6.5 displays the final or steady state bubble shapes for a selection of Reynolds and Eötvös numbers. One can clearly see the wide range of bubble shapes produced, exemplifying the combined inhibitive role viscosity and surface tension have in preventing jet formation and bubble deformation. At $E\ddot{o} = 106$, the final bubble shapes are nearly identical for all chosen values of the Reynolds number. Decreasing the Eötvös number to $E\ddot{o} = 6.6$, at high Reynolds number we see the skirted bubbles discussed previously, whereas at moderate Reynolds number $Re \leq 20$, steady state bubble shapes are achieved. A curved thin disk forms for $Re = 20$, while a fatter perturbed ellipsoid is produced for $Re = 10$. In fact, for $Re \leq 20$ and $E\ddot{o} \leq 6.6$ all the bubbles attain a steady state, with the profiles resembling those seen by Sussman and Smereka [145] and Ryskin and Leal [137] at comparable Reynolds and Weber numbers (an alternative dimensionless parameter for the surface tension). At the lower Eötvös and Reynolds numbers the combined resistance to deformation means that the steady state shapes are very nearly ellipsoidal, a comparatively small deviation from the original spherical shape.

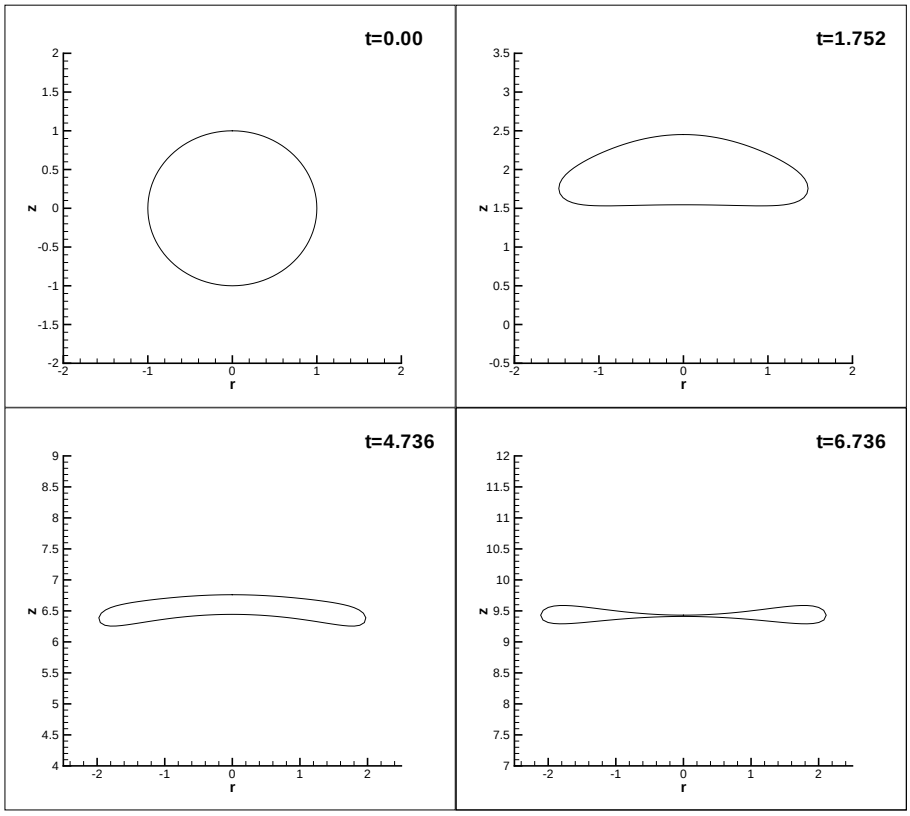

Figure 6.3: Bubble profiles at select times during ascent for $Re = \infty$ and $E\ddot{o} = 2.4$.

Figures 6.6-6.8 show the rise velocity of the bubble with time, at each Eötvös number and Reynolds number. The rise velocity U is defined in the following way,

$$U = \frac{\int_s u_z \, ds}{s_{max}}. \tag{6.28}$$

Essentially, this is an average of the z-component of velocity over the arc-length of the bubble surface. Figure 6.6 shows the variation of U with time for $E\ddot{o} = 106$ at a selection of Reynolds numbers. The bubbles exist for a comparatively short time ($t_f < 2.5$) in their singly-connected state, and expectedly, a decreasing Reynolds number results in a reduced rise velocity, but an increase in lifetime as deformation is slowed.

Figure 6.7 shows the rise velocity when $E\ddot{o} = 6.6$. The rise velocities in this case are slightly smaller in magnitude compared to the corresponding $E\ddot{o} = 106$. This is a consequence of the more oblate shape assumed and the absence of a distinguishable liquid jet due to the increase in surface tension. Once again, at like times, decreasing the Reynolds number is accompanied by a decrease in the rise velocity, but notably for

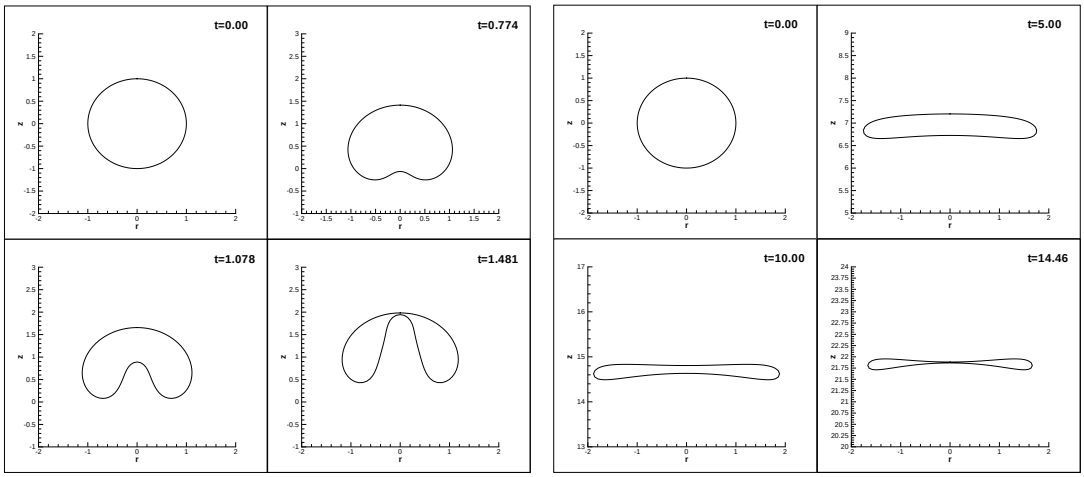

(a) $E\ddot{o} = 106$ (b) $E\ddot{o} = 2.4$

Figure 6.4: Bubble profiles at select times during ascent for $Re = 50$.

Reynolds numbers $Re = 10, 20$ the rise velocity attains a constant value as the rising bubbles reach their steady state terminal velocity U_T. For $Re = 20$, $U_T \approx 0.73$, while for $Re = 10$, $U_T \approx 0.52$.

Figure 6.8 displays the rise velocity for $E\ddot{o} = 2.4$. As before, for like times, decreasing Reynolds number results in a decrease in rise velocity. Again, for $Re = 20$ and $Re = 10$ the bubble attains a steady state, with the rise velocity tending to its terminal value. For $Re = 20$, $U_T \approx 0.96$, while for $Re = 10$, $U_T \approx 0.50$. For $Re = 10$, the terminal rise velocity is approximately equal ($U_T \approx 0.5$) for both $E\ddot{o} = 6.6$ and $E\ddot{o} = 2.4$. For $Re = 20$ however, the difference is more significant with $U_T = 0.73$ and 0.96 for $E\ddot{o} = 6.6$ and 2.4, respectively. This difference can be explained by the differing drag on the bubbles, resulting from their different shapes - itself a consequence of the different surface tensions. At $E\ddot{o} = 6.6$, the bubble is noticeably thinner, and has a larger surface area exposed to the flow direction. Thus the drag is larger and so its terminal velocity smaller, regardless of the fluid rheology. It seems that for $Re = 10$, the difference in shape between $E\ddot{o} = 6.6$ and $E\ddot{o} = 2.4$ is not significant enough to produce a significant change in drag.

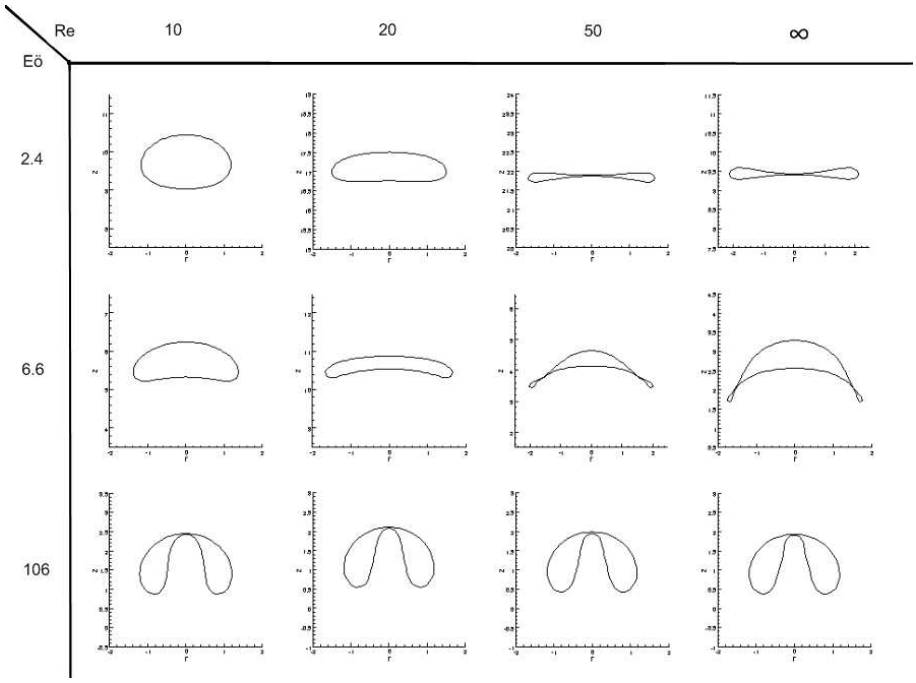

Figure 6.5: The terminal bubble shapes for different values of the Reynolds and Eötvös number.

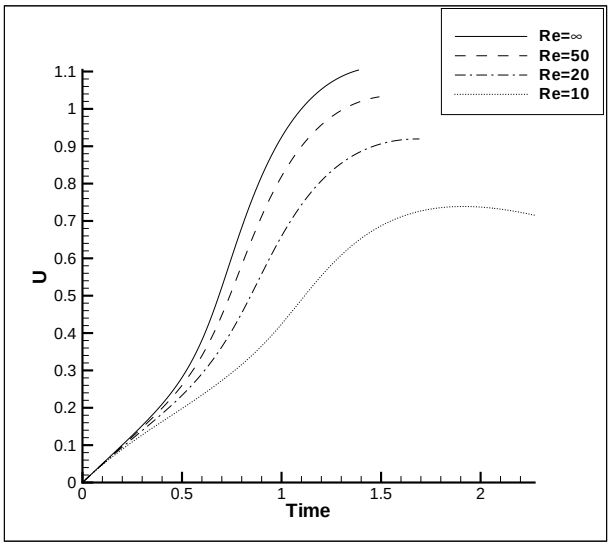

Figure 6.6: Evolution of the rise velocity for a selection of Reynolds numbers with $E\ddot{o} = 106$.

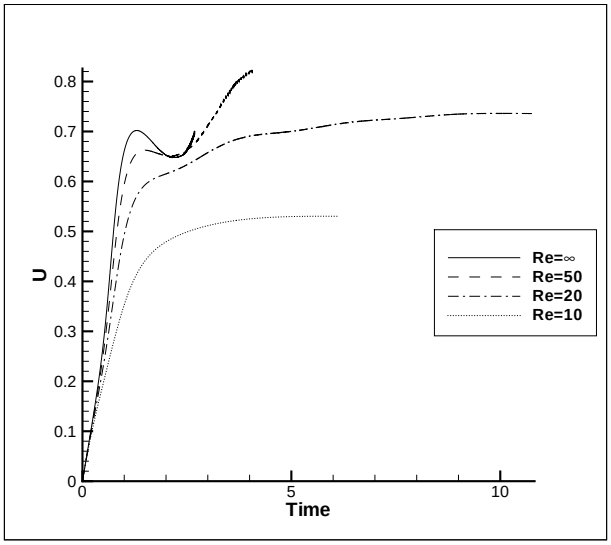

Figure 6.7: Evolution of the rise velocity for a selection of Reynolds numbers with $E\ddot{o} = 6.6$.

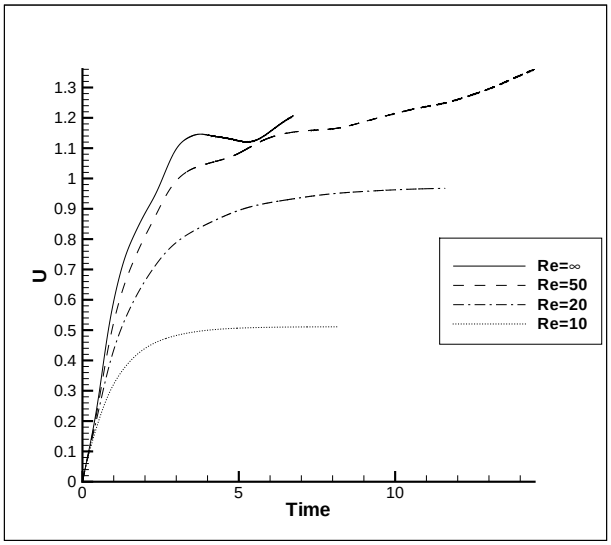

Figure 6.8: Evolution of the rise velocity for a selection of Reynolds numbers with $E\ddot{o} = 2.4$.

6.5 Rising Bubbles in Viscoelastic Fluids

6.5.1 The Rise of a Near-Spherical Gas Bubble

The rise of a spherical gas bubble in a Newtonian fluid under the effect of gravity has been well documented. Analytical approximations to the drag on the bubble can be found by approximating the form of the ambient flow. The three main flow approximations yield the Stokes, Hadamard-Rybczynski, and Levich drag, with the former two giving a better experimental agreement when inertia is negligible, and the lattermost otherwise. Each equation for the drag is of the same form (to leading order), namely $D = A\pi R\mu U_T$, for some dimensionless constant A. Balancing the drag with the displaced fluid weight allows one to derive an expression for the terminal rise velocity U_T of the bubble, viz.

$$A\pi R\mu U_T = \frac{4}{3}\pi R^3 \Delta\rho g \Rightarrow U_T = Le\frac{\Delta\rho g R^2}{\mu}, \tag{6.29}$$

where Le is Levich number and takes the following values depending on the drag approximation

$$Le = \begin{cases} \frac{2}{9} & \text{(Stokes)} \\ \frac{1}{3} & \text{(Hadamard)} \\ \frac{1}{9} & \text{(Levich)} \end{cases}$$

The numerical results of Brabston [28] show that the rise velocity is in fact bounded below and above by the Levich and Stokes approximations, respectively. The increased complexity of viscoelastic constitutive equations means that equivalent expressions for viscoelastic fluids are intractable for all but for the simplest cases. Joseph and Liao [72], in their study of viscoelastic potential flow consider a rising spherical bubble in second order and linear Maxwell fluids. In both cases the drag equals the Levich drag at steady state, with no dependence on elastic parameters. This is a surprising result, and as reported by Astarita [5], is not seen in experiments. In fact, in the moderate Reynolds number regime, the observed Levich number is much less (about 50%) than the Newtonian $Le = 1/9$, with $Le \approx 0.05$. Astarita uses an order-of-magnitude dimensional analysis to gain some insight into the motion of spherical bubbles in Maxwell fluids. The approach is applicable to more general Maxwell models, like the material Maxwell model used here. As such we adopt a similar analysis in an attempt to confirm the

behaviour observed numerically.

The terminal velocity is found from equating the drag to the displaced fluid weight, or equivalently balancing the rate of dissipation in the flow,

$$E_D = \int_V \mathbf{T} : \nabla \mathbf{u} \, dV, \tag{6.30}$$

with the rate of positional energy loss

$$E_P = \frac{4}{3}\pi \Delta \rho g R^3 U_T. \tag{6.31}$$

If rates of strain are taken to be of order U_T/R, and the derivatives of $\mathbf{T}$ of order $[T]U_T/R$, then a dimensional analysis of the Maxwell constitutive equation gives,

$$[T] + \left[\lambda \frac{U_T}{R} T\right] + \left[\mu \frac{U_T}{R}\right] = 0. \tag{6.32}$$

The square brackets indicate the appearance of one or more terms, the order of magnitude of which is given within the brackets. The order of magnitude of the stress is thus

$$[T] = f(We) \cdot \frac{\mu U_T}{R}, \tag{6.33}$$

where f is some function of the Weissenberg number, which is defined as

$$We = \lambda \frac{U_T}{R}. \tag{6.34}$$

Substituting Eq. (6.33) into Eq. (6.30), yields the leading order energy dissipation rate

$$E_D = f(We) \mu R U_T^2. \tag{6.35}$$

Equating this with the positional energy (Eq. (6.31)) one obtains a leading order equation for the terminal rise velocity

$$U_T = f(We) \frac{\rho g R^2}{\mu}. \tag{6.36}$$

Note that this is of the same form as Eq. (6.29) - suggesting that in the case of a Maxwell fluid, the Levich number will be some function of the Weissenberg number

(We), or without loss of generality, the Deborah number (De). Namely,

$$Le = f(De). \tag{6.37}$$

Thus, for a fixed Deborah number, the terminal rise velocity of a spherical bubble in a Maxwell fluid behaves as in a Newtonian fluid (to leading order). Non-dimensionalising Eq. (6.36) yields the following expression in terms of Reynolds number Re,

$$U_T = LeRe. \tag{6.38}$$

Thus, for a fixed Deborah number, the terminal rise velocity U_T should still vary linearly with the Reynolds number Re (over not too large a range). Figure 6.9 displays the numerically obtained rise velocity for different Reynolds numbers, at fixed $De = 0.1$. The Reynolds numbers are restricted to a range in which the sphericity of the bubble is near-preserved. Unlike the analytical studies, this is not explicitly enforced. The relationship is clearly linear, supporting the theoretical argument presented above.

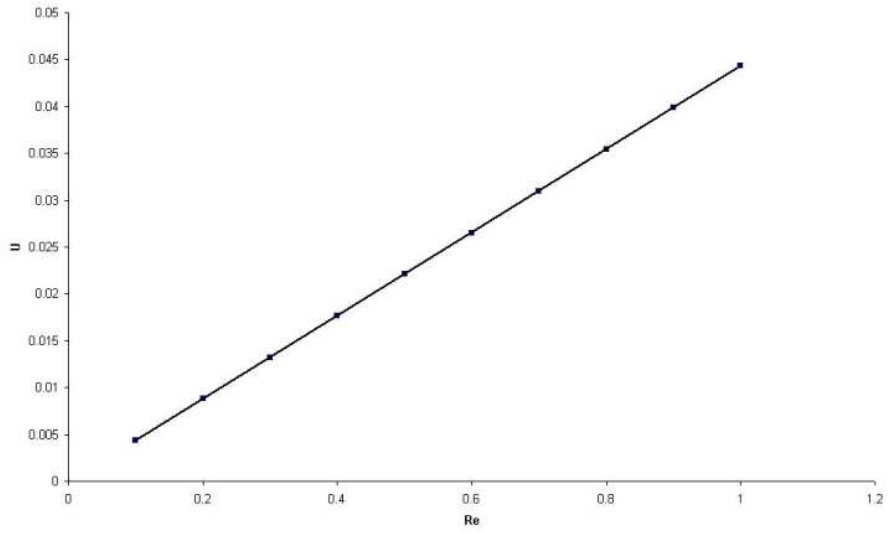

Figure 6.9: Variation of terminal rise velocity with Reynolds number in a Maxwell fluid. The equation of the linear fit to the data is $U_T = 0.044Re$.

6.5.2 The Rise of a Non-Spherical Gas Bubble

As described in the introduction, the rise of a bubble in a viscoelastic fluid is characterised by three distinct phenomena: (i) the formation of a cusp at the trailing end of the bubble, (ii) an apparent discontinuity in the steady state velocity as a function of bubble volume, and (iii) the presence of a negative wake in the region of the trailing edge. As discussed, the relation between each of these phenomena is still a matter for debate.

Figure 6.10 shows snapshots of the bubble profile during ascension for a viscoelastic fluid with $De = 0.93$ and $Re = 1.18$. As the bubble rises it begins to assume a more prolate shape before the underside becomes drawn out, eventually forming a trailing edge cusp as seen in the final frame.

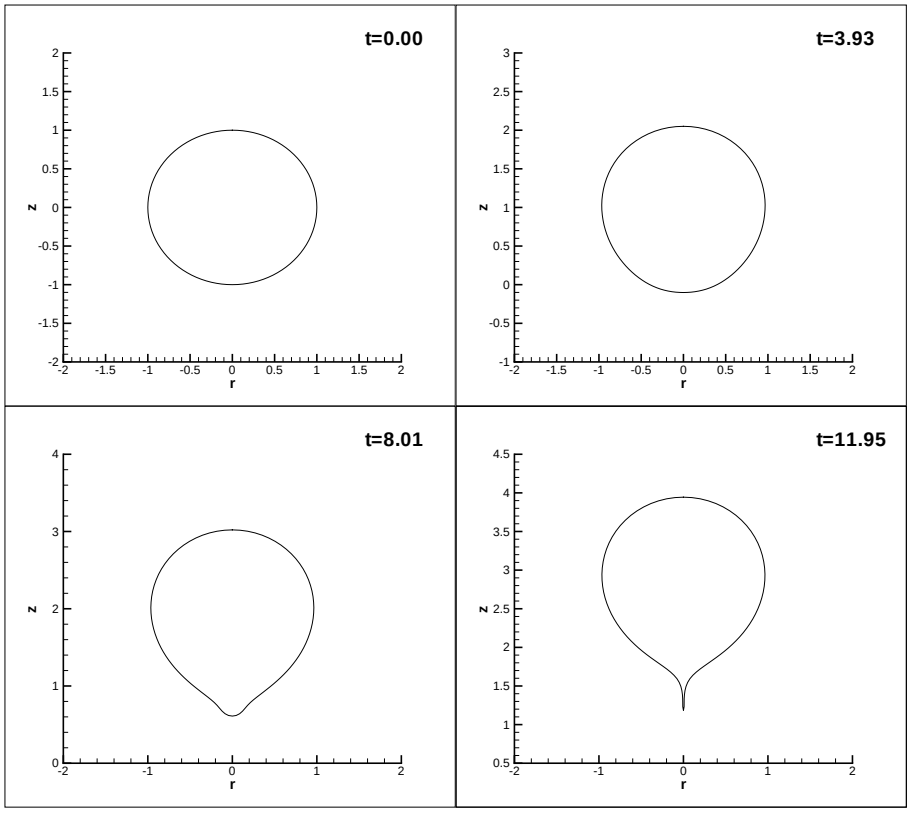

Figure 6.10: Bubble profiles at select times during ascent for $De = 0.93$, $Re = 1.18$

The bubble shape observed in the final frame of Figure 6.10 is typical of that seen in experiments (see, for example, Astarita and Apuzzo [6]). In Figure 6.11 one can see the particularly striking resemblance of the numerical profile to the picture found in Wagner et al. [159] of a bubble rising through liquid soap.

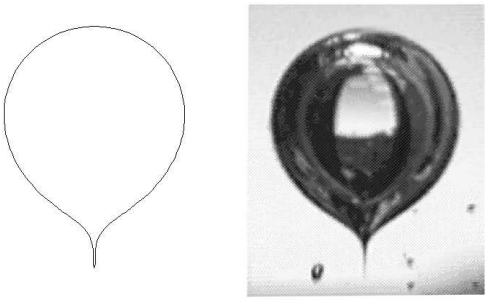

Figure 6.11: Comparison of numerical bubble profile (left) with the experimental image of a bubble rising in liquid soap (right)[4]

Similar cusp-like shapes are reproduced in other numerical studies, but to the knowledge of the authors, no numerical study has reproduced such a sharp interface. Full domain numerical studies such as the level-set finite element studies of Pillapakkam et al. [116, 117] and the lattice Boltzmann studies of Wagner et al. [159] and Frank and Li [55], produce visibly rounded tips. It seems that factors such as the mollified density change over the fluid interface by the level-set method and the computational restrictions in mesh refinement in both schemes, results in an under resolved cusp. The boundary element method provides a truly discontinuous pressure/density interface, and allows for an easy re-distribution of nodes and refinement in the vicinity of the cusp, without costly domain calculations. Such benefits apply to the boundary element scheme of Málaga and Rallison [102], but it seems the lack of a sharp elongated cusp in their work results from the neglect of inertia in their model and the associated reduction in deformation.

Liu et al. [95] find from their experiments that the 2D-cusps formed by rising bubbles adopt a universal asymptotic form of $z = a|r|^{2/3}$. Although the cusps here are axisymmetric, not 2D, it is interesting to see if they can fit a similar analytical expression. Figure 6.12 shows a close up of the cusp formed for $De = 0.934$, $Re = 1.180$. Using the method of least squares, the curve $z = 1.01|r|^{0.381}$ (shown in red) is found to give a fit with a residual mean square of 1.46×10^{-3}. This suggests that perhaps more general

[4]Reprinted from Computer Physics Communications, Vol. 129, A. J. Wagner, L. Giraud and C. E. Scott, Simulation of a cusped bubble rising in a viscoelastic fluid with a new numerical method, 227-232, Copyright (2000), with permission from Elsevier.

cusps can be described by analytical expressions of the form $z = a|r|^n$, certainly to leading order. Note that $n < 1$ in order that the surface be convex.

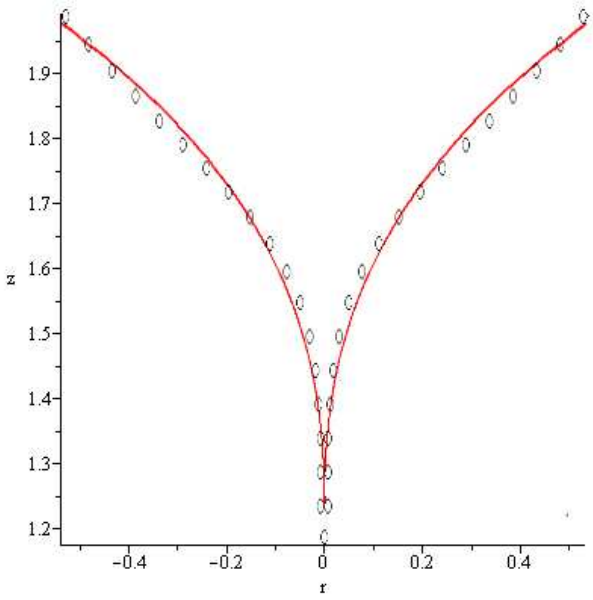

Figure 6.12: The numerical cusp (circles) from Fig. 6.10 and the associated least squares fit (red line).

The variation in bubble volume is an important focus of experiment studies, especially due to the velocity jump discontinuity that takes place once the bubble exceeds a certain critical volume. Figure 6.13 displays the terminal bubble profiles of a rising bubble at increasing volumes. The fluid has fixed material parameters but given the change in volume, the relevant Reynolds and Deborah number are given within each frame. The transition in shape for $Re = 0.21$ to $Re = 1.18$, is qualitatively very similar to the transition in bubble shape seen experimentally when increasing volume. See for example Pilz and Brenn [118] or Soto et al. [140]. At the lower Reynolds numbers, $Re = 0.21, 0.30$, viscous effects dominate and inhibit deformation so terminal bubble shapes deviate little from sphericity. At $Re = 0.42$ the viscous effects abate slightly, and elastic effects play a more significant role as the bubble becomes more prolate with evidence of a more pointed underside. Between $Re = 0.42$ and $Re = 0.50$ the shape undergoes a marked change from a wholly convex interface to the underside now displaying a concave portion with an accompanying pseudo-cusp. By increasing the volume further, the increased effect of elasticity causes this pseudo-cusp to sharpen and lengthen, culminating in the terminal cusped bubble shape observed for $Re = 1.18$,

$De = 0.93$. The shapes beyond this (those outside of the red box) do not seem to reach a steady state. The shapes shown are those before the computation undergoes numerical difficulties. Yet, once again one can see there is a general transition in bubble shape. A cusp no longer forms and instead a liquid jet seems to form on the bubble underside, as in the Newtonian case studied in Section 6.4. Evidently the increase in volume is such that viscous and elastic effects are subdued by the increasing effect of buoyancy and inertia. Subsequent bubbles have increasingly larger jets, with the shape tending from a prolate to a more oblate form. At $Re = 6.67$, $De = 0.53$ viscous and elastic effects have diminished to the extent that the profile resembles that of the inviscid Newtonian case with negligible surface tension, as seen in Fig. 6.5.

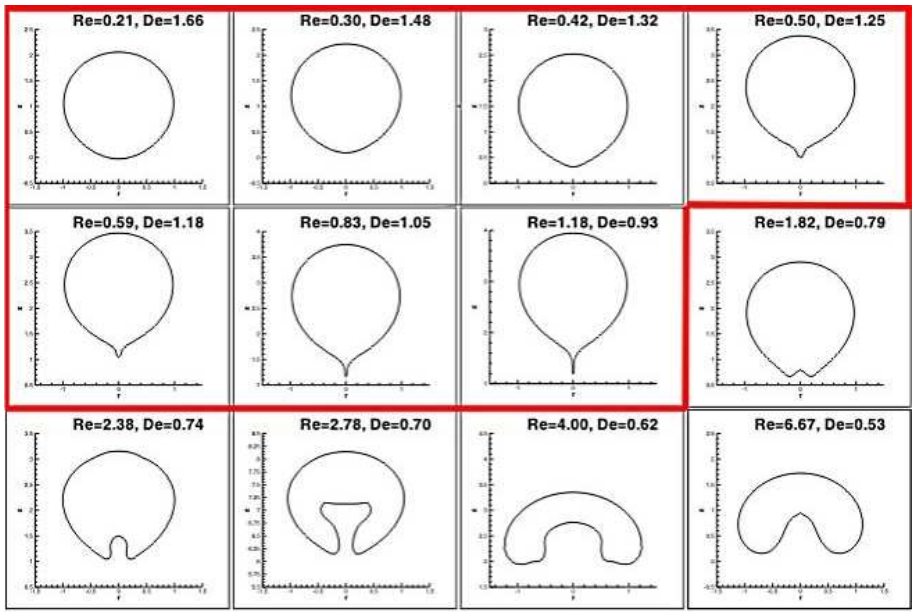

Figure 6.13: Final profiles of rising bubbles of different volumes in a viscoelastic fluid. Steady state bubble shapes reside within the red box.

Figures 6.14-6.17 display the transient rise velocity with time for a selection of the above profiles. Figure 6.14 shows the rise velocity for $Re = 0.21$, $De = 1.66$. The damped oscillation in the velocity, a characteristic of so many viscoelastic phenomena, is the most notable feature. The impulse provided by the buoyancy force initialises the repeated over and undershoots in the velocity, which decay in magnitude until U reaches a steady-state value of $U_T \approx 0.01$. Oscillations in the rise velocity are also seen by Pillapakkam et al. [117] in their study of a bubble rising in an Oldroyd B fluid. Generally, their oscillations number less but this is consistent with the increased

viscous properties of the Oldroyd model over the more elastic Maxwell model used here.

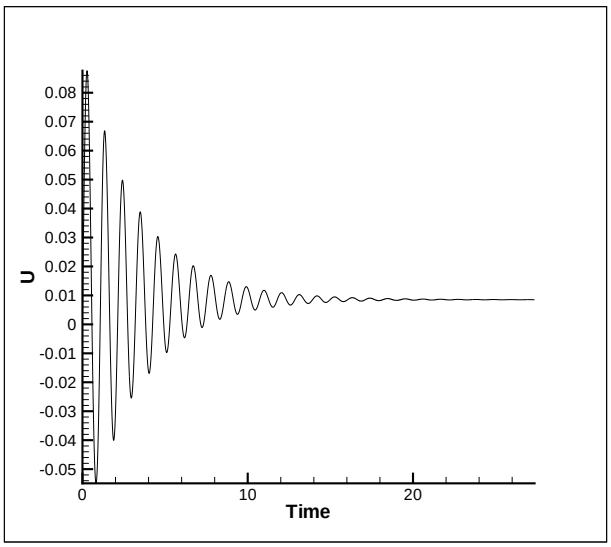

Figure 6.14: Variation of rise velocity U with time for $Re = 0.21$, $De = 1.66$.

Figure 6.15 shows the rise velocity with time for $Re = 0.5$, $De = 1.25$. The increased volume and Reynolds number means that buoyancy plays a more prominent role. Consequently the maximum and terminal rise velocities are larger, with $U_T \approx 0.02$. Also, the frequency of the oscillations is markedly reduced.

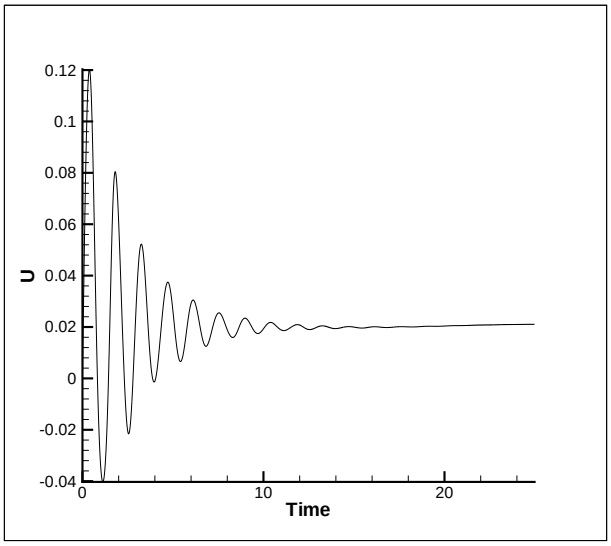

Figure 6.15: Variation of rise velocity U with time for $Re = 0.5$, $De = 1.25$.

The trend continues when the volume is increased further with $Re = 1.18$ and $De = 0.93$ (Fig. 6.16). The increased buoyancy force results in a larger maximum and

terminal velocity ($U_T \approx 0.05$). Once again, the frequency of the oscillations is also reduced but the oscillations themselves seem less structured and coherent. This can be explained by the increased irregularity in the bubble shape, caused by the formation of the cusp as the bubble rises.

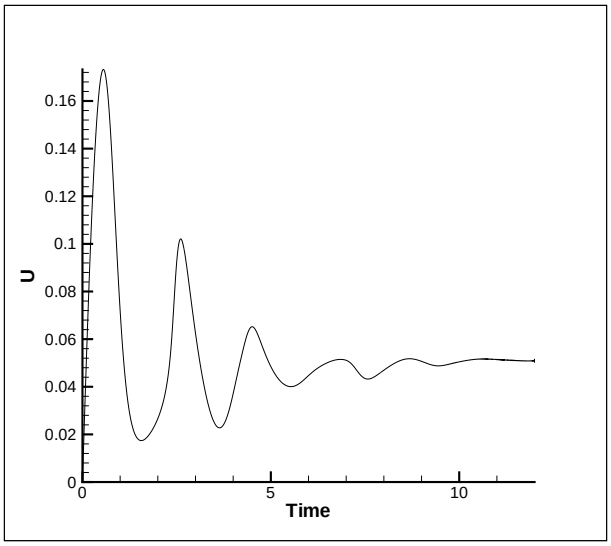

Figure 6.16: Variation of rise velocity U with time for $Re = 1.18$ and $De = 0.93$.

Figure 6.17 shows the variation of rise velocity with time for some of the larger bubble volumes. Expectedly, oscillations no longer occur due to the decrease in viscous and elastic effects over the increased strength of buoyancy forces. By the same means the rise velocity continues to increase with volume, but as mentioned, does not necessarily tend to a steady state (as has also been observed with Newtonian dynamics). Unsurprisingly, in increasing the Reynolds number to $Re = 6.67$, the behaviour of the transient rise velocity begins to bear semblance to the Newtonian rise velocity profile (Fig. 6.6).

Studying the terminal rise velocity of a rising bubble in a viscoelastic fluid for a range of bubble volumes, experimentalists can observe a single large jump in the magnitude of the velocity over a small change in volume. This change is such that it effectively resembles a discontinuity. The size of the jump varies from study to study and, of course, depends on the ambient fluid, but can range from a two to ten fold increase in the rise velocity [95, 117]. As mentioned in the introduction, the reason for this jump is still debatable. Furthermore, its relationship to cusping and the negative wake is not fully understood. Astarita and Apuzzo [6] attributed the jump to a change in the

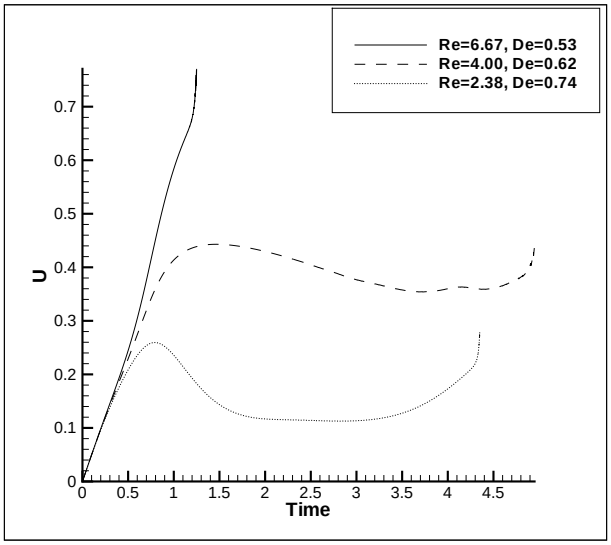

Figure 6.17: Variation of rise velocity U with time for a selection of Reynolds and Deborah numbers.

bubble dynamics from the Stokes to Hadamard regime. Later studies recognised that the jump takes place at a critical volume where the bubble underside first becomes convex and starts to cusp. Liu et al. [95] suggest that the jump is due to the reduction in drag caused by the cusped bubble shape. Rodrigue et al. attributed the jump to the presence of surface active agents (such as polymer molecules) [133] combined with surface tension forces [134]. Herrera-Velarde et al. [66] conclude that the jump is due to the appearance of the negative wake, which they found only appears for bubbles larger than the critical volume. Soto et al. [140] report that the jump is the direct result of the appearance of (measurable) elastic stresses, which causes the change in shape and so a drag reduction which causes the jump (as in [95]). They then form a dimensionless group comparing elastic to capillary forces to determine a jump condition for the liquids tested. Similarly, Pilz and Brenn [118] derive empirical relations for the critical bubble volume. They then postulate that the jump discontinuity is due to the relaxation of polymer chains, with the change in conformation being accompanied by forces which push the bubble upwards.

Figure 6.18 displays plots of the terminal rise velocity U_T with increasing bubble volume V. We find no discernible velocity jump as one increases bubble volume. The inserted bubble profiles indicate approximately the point where the cusp first forms, which according to experiment should be the point at which the discontinuity appears. The results have been repeated for a range of viscosities, relaxation times and surface

tensions, without any indication of the rise velocity jump being present.

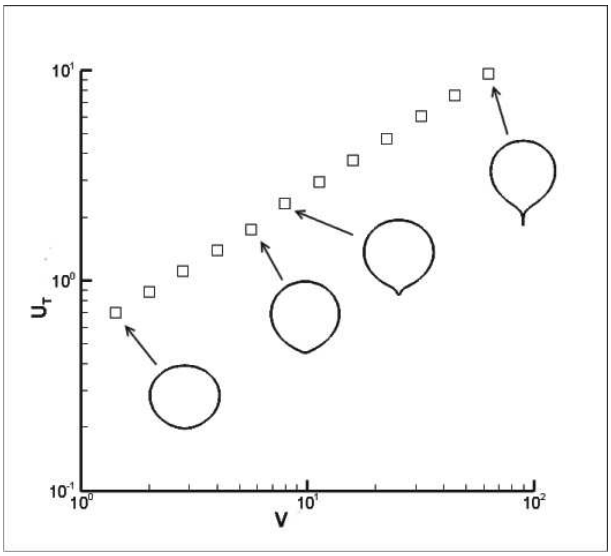

Figure 6.18: Terminal rise velocity for different bubble volumes. Noteworthy bubble shapes are indicated at particular bubble volumes.

By not predicting the jump discontinuity, important insights can still be gained in understanding this phenomenon. Firstly, the cusping of the bubble surface can be predicted, but given that this change in shape does not result in a significant increase in velocity, it suggests that the decrease in drag due to the cusping is not the reason for the jump (the affirmative was suggested by Liu et al. [95] and Soto et al. [140]). Also, the proposition of Rodrigue et al. [133, 134] that the discontinuity is a surface phenomenon is unlikely. They claim that the presence of surface active agents, such as polymer molecules or surfactants, can cause the jump. The action of polymer molecules and the surface physics on the bubble is modelled here (all be it simply) through the normal stress balance and the Maxwell constitutive law (in effect assuming molecules are infinitely extendable dumbbells in a negligible viscosity Newtonian solvent). The results suggest that the presence of the molecules produces the observed change in shape and cusping, but does not create any additional forces that would cause the jump in velocity. The cause of the jump therefore, must lie within the ambient fluid.
In particular, there is one occurrence in the dynamics of a rising bubble that the current method certainly cannot predict - the negative wake. The imposition of an irrotational flow around the bubble suppresses the formation of the rotational flow that comprises the vortex ring seen in the wake. Figure 6.19 displays the velocity vectors in the field

around the cusped bubble for $Re = 1.18$ and $De = 0.93$. Expectedly, there is no evidence of a negative wake in the region behind the rising bubble.

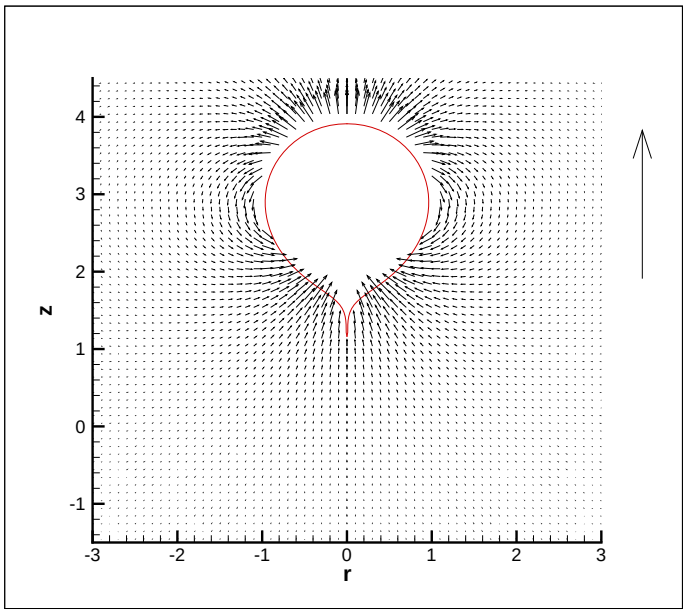

Figure 6.19: Velocity field in the fluid around the rise bubble. The velocity in the wake of the bubble is everywhere directed upwards, i.e. there is no negative wake.

The absence of both the jump discontinuity and the negative wake corroborates the experimental findings of Herrera-Velarde [66] who concluded that the negative wake was the main reason for the jump discontinuity. This is supported by the numerical study of Pillapakkam et al. [117] which, to the author's knowledge, is the only numerical study that can predict the jump. As in [66] they find the formation of a negative wake once the bubble begins to cusp. They note that the additional surface tension force created by the cusp is not significant enough to explain the large jump observed (the effect of surface tension will be discussed further in the next section). Also the bubble shape does not change drastically with increasing concentration parameter, but the magnitude of the jump and the negative wake do - indicating that the jump depends more importantly on changes in the external flow than on bubble shape and drag effects. They provide the following explanation for the negative wake creating the jump. Consider a box-shaped control volume surrounding the rising bubble, as in Fig 6.20. In the steady state the sum of the net momentum through sidewalls BC and DA must be zero (else there would be sideways movement). In a Newtonian fluid the velocity through the surfaces AB and CD is always directed upwards. The net momentum flux

through these surfaces is then determined by the difference in the velocity magnitudes, and should be positive given the bubble is rising upwards, i.e. $M_{net} = M_{CD} - M_{AB} > 0$. In a viscoelastic fluid with a negative wake, the velocity through bottom surface AB is pointed downwards and consequently, the net momentum flux is guaranteed to be positive and will be larger than if there was no negative wake, i.e. $M_{net} = M_{CD} + M_{AB}$. This results in an additional thrust in the upward direction. It can be thought of in a similar way to the jet engine, with thrust provided by the expulsion of gas in the opposite direction (Newton's third law). In this case the oppositely directed flow (the negative wake) is formed purely as a consequence of the viscoelasticity of the fluid.

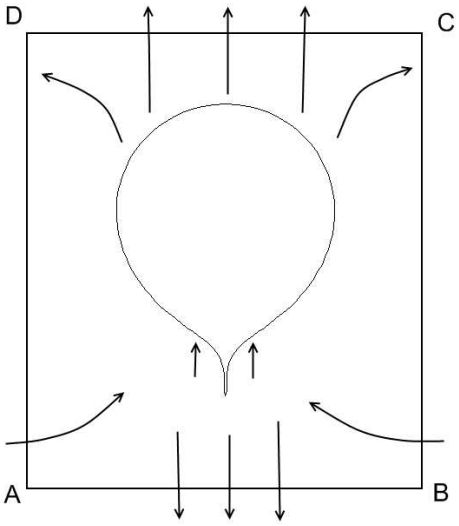

Figure 6.20: Indication of direction of velocities in rising bubble with negative wake, resulting in an additional upward thrust.

6.5.3 The Effect of Surface Tension

In this section we briefly discuss the effect of surface tension on the rising viscoelastic bubble. From Section 6.4 on the Newtonian rising bubble it is clear the surface tension plays an important role in determining bubble shape and subsequently drag and terminal rise velocity. Figure 6.21 shows the terminal bubble shapes for a selection of Eötvös numbers, with $Re = 1.18$ and $De = 0.93$. For zero surface tension ($E\ddot{o} = \infty$) we see the case presented previously, with the sharp cusp formed on the bubble underside. For $E\ddot{o} = 53$ there is a clear difference in profiles, with surface tension forces acting to smooth out the sharp cusp and prevent high curvature deformations. The shape

is still representative of a pseudo-cusp, with a region of convexity on the underside and so in experiment one would still expect to see this beyond the jump discontinuity. The rightmost figure has the largest surface tension with $E\ddot{o} = 6.6$. The prevention of deformation is such that no evidence of cusping occurs and the shape is near-spherical but still visibly prolate in form. Consequently, we would expect such a shape to form at a volume smaller than that at the jump discontinuity.

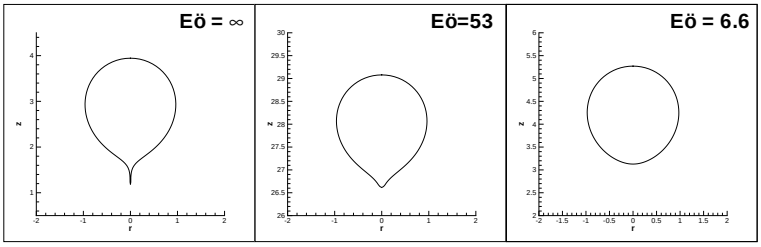

Figure 6.21: Terminal bubble profiles at varying Eötvös numbers, with $Re = 1.18$ and $De = 0.93$.

Figure 6.22 displays the transient rise velocities of the rising bubble for the different Eötvös numbers. Despite large variations in surface tension, the effect on the rise velocity is minimal. The plots for $E\ddot{o} = \infty$ and $E\ddot{o} = 53$ follow each other closely, while that for $E\ddot{o} = 6.6$, despite exhibiting high frequency oscillations, still follows the general trend on the larger scale. The high frequency oscillations are interesting and describe the fast, localised low amplitude oscillations in the bubble surface as the whole bubble rises with a viscoelastic, oscillatory, overall velocity. An analogous response to the increase in surface tension can be found in a stretched elastic band. Under increasing tension, oscillations are higher in frequency and smaller in amplitude. Notably the terminal velocities are very nearly equal, with the rise speed for $E\ddot{o} = \infty$ being only slightly larger. Evidently, the rise velocity has little dependence on the surface tension for the viscoelastic rising bubble. This then supports the claim made by Pillapakkam et al. [117] that the effect of surface tension is not significant enough to explain the jump discontinuity. Additionally, given that both the pre- and post-jump bubble shapes have approximately the same terminal rise velocity, this again shows that drag reduction due to cusping is negligible and cannot be responsible for the velocity jump.

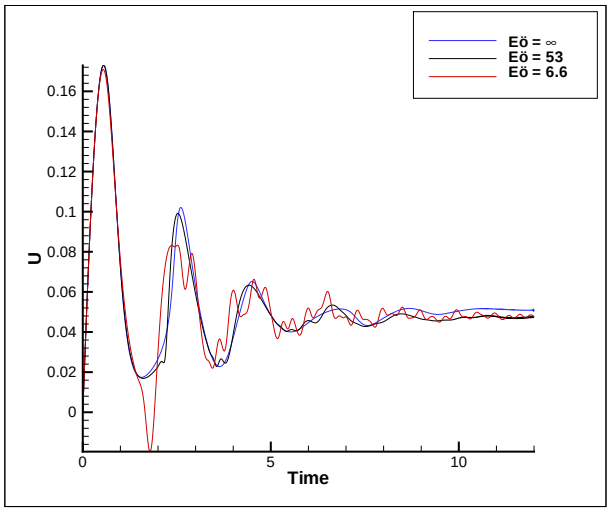

Figure 6.22: Rise velocity with time for a selection of Eötvös numbers with $Re = 1.18$ and $De = 0.93$

6.5.4 The Effect of the Deformation Terms

It is interesting to note the effect of the deformation terms, which would otherwise appear in the Upper Convected Maxwell model, on dynamics. While it can be expected, given the above discussion, that they will have no effect on the jump discontinuity, they are likely to play a measurable role in forming the bubble shape. Figure 6.23(a) shows the steady state bubble shape for the same material parameters as studied previously. The volume is such that the Reynolds number is $Re = 1.18$ and the Deborah number $De = 0.93$. Comparing this to the corresponding case for the material Maxwell model (Fig. 6.10), we see that on including the deformation terms, the bubble is much more stretched and elongated with a longer trailing-end cusp. By reducing the Deborah number to $De = 0.47$ (Figure 6.23(b)), the length of the cusp decreases and there is a greater degree of concavity in the bubble's underside.

6.6 Conclusions

In this chapter, the dynamics of a rising gas bubble under the influence of viscous and viscoelastic effects are studied. The bubble is assumed to be constant in volume, rising through an incompressible fluid under an irrotational flow. Viscous and viscoelastic effects act directly on the bubble through the normal stress boundary condition. Results for the Newtonian rising bubble show good agreement with previous studies and steady state bubble shapes qualitatively match full domain solutions. In the viscoelastic case,

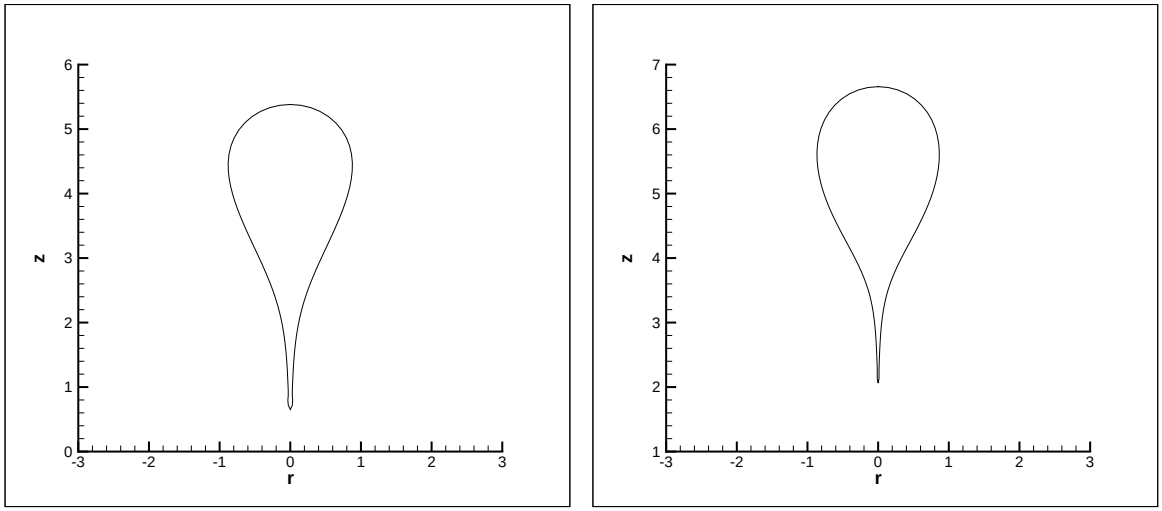

(a) $Re = 1.18$, $De = 0.93$ (b) $Re = 1.18$, $De = 0.47$

Figure 6.23: Steady state bubble shapes for the Upper Convected Maxwell (UCM) constitutive equation.

the results predict the bubble's prolate shape and the formation of the trailing end cusp. The method allows for high curvatures and deformations and so can capture the sharpness of the cusp to a higher degree than seen in other numerical schemes. Furthermore, the cusped bubble profile bears a good qualitative agreement to experimental observations. The imposition of an irrotational flow prevents the formation of the negative wake, allowing insights into the mechanisms of the velocity jump discontinuity that cannot be ascertained experimentally. Proposed reasons for the velocity jump include drag reduction due to cusping [95], the action of surface forces [133] and the negative wake [66]. Here, we include the appropriate surface effects and inertia terms and observe cusping, but detect no velocity jump discontinuity. This suggests that the negative wake is primarily responsible for its occurrence, corroborating previous experimental and numerical findings [66, 117].

Chapter 7

The Prediction of Bubble Dynamics using a Spectral Element Marker Particle Method

7.1 Introduction

In this chapter we return to the problem of bubble collapse near a rigid wall, in a viscoelastic fluid. In Chapter 3 a simplified model was devised and solved using the boundary element method. The model assumed that viscoelastic effects were confined to thin layers near the surface, and that the ambient fluid was irrotational. Predictions include the ability of viscoelasticity to the prevent jet formation, and to form cusps in the underside of the bubble when near the wall. Despite the insight gained by employing the above model, the potential flow approximation does preclude an exacting account of the role of viscoelasticity, as mentioned in Chapter 1.

Hence, in this chapter, the aim is to solve the full governing equations over the whole fluid domain. This is done not only to gain further insight into the role of viscoelasticity, but also to validate the predictions of the boundary element study. While the boundary element method fell squarely within the Lagrangian class of multiphase numerical methods, in this chapter a mainly Eulerian approach will be employed. It is a one-field model [124], so a single set of governing equations will be used in describing the both the fluid (gas) comprising the bubble and ambient liquid. Fluid properties, such as viscosity, then vary appropriately within each phase. For example, the density

and viscosity in the region describing the bubble should be less than the ambient fluid. The *compressible* governing equations must be solved given the requirement for the bubble to change volume during collapse.

The multiphase description is provided by the marker particle method. The marker particle (MP) method of Rider and Kothe [128] bears a semblance to both the volume of fluid and MAC method. In a similar manner to VOF, a colour function C is updated using the usual advection equation. However, instead of directly tracking volume, massless marker particles are tracked. Each particle is assigned a particular "colour" depending upon the phase in which it resides. Since a particle of fluid will remain of that fluid type (assuming no change in phase), a particle will keep its colour indefinitely. Within fluid-fluid interface regions, where two (or more) differently coloured sets of marker particles reside, a weighted average is taken of the surrounding particles to determine an interpolated colour at the point in question. To accurately describe the different phases, the whole computational domain is filled with a high density of these marker particles, with each being updated to a new position every time step. An obvious disadvantage compared to VOF methods is the additional computational cost in tracking such a large number of particles. The main advantages include the ease of implementation, the trivial extension to compressible flows, and the minimal numerical diffusion of the colour function over time. Furthermore, the method retains the VOF's ability to deal with large deformations and topology changes automatically.

Traditionally, the marker particle method has been combined with finite difference schemes and with a high degree of success. However, in prescribing velocities to particles from the grid, a low order interpolation is typically used. This can be a significant source of error and can produce a velocity field which is not divergence free (for the incompressible case) [12]. Also finite difference grids can be restrictive in the sense that mesh refinement around regions of interest, and so improved efficiency, can be tricky. Discretising non-rectangular domains is also a particularly cumbersome task. To overcome these shortfalls, we present a new numerical scheme where we combine the marker particle method with the spectral element method (SEM). The SEM will solve the compressible governing equations, while the marker particle method provides the overlying multiphase description. The spectral element method is, in essence, a high-order finite element method and so is more adept at discretising irregular domains

and selective mesh refinement. Additionally, the marker particles can be prescribed a very accurate velocity by using high-order polynomial approximations on each element.

In Section 7.2 we will present the mathematical model and governing equations. Section 7.3 will then provide details on the combined spectral element and marker particle method. Within Section 7.4 we validate the numerical method with the available literature before presenting results obtained for bubble collapse near a wall in a viscoelastic fluid.

7.2 The Mathematical Model and Governing Equations

Consider a bubble of initial density ρ_1, surrounded by fluid of initial density ρ_2 (all subsequent variables with index 1 shall refer those associated with the bubble, while those labelled 2, with the ambient fluid). A schematic depiction of this is given in Fig. 7.1. As mentioned in the introduction, a "one field" model is utilised in describing the two phases. Here a single set of governing equations is solved with the different phases possessing different material parameters such as viscosity and relaxation time. Therefore, in solving the governing equations one must note that these material parameters are required to vary as one moves from one phase into the next (but they can be constant within each phase).

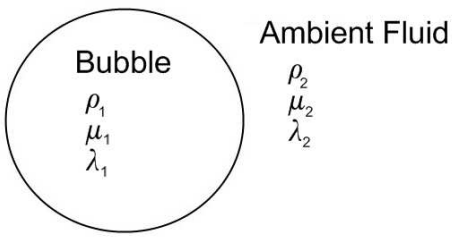

Figure 7.1: Schematic of bubble and ambient fluid, each with different densities and material properties.

In general, the equations governing fluid motion are the mathematical statements of conservation of momentum

$$\rho \frac{D\mathbf{u}}{Dt} = -\nabla p + \nabla \cdot \mathbf{S}, \tag{7.1}$$

and conservation of mass

$$\frac{D\rho}{Dt} + \rho \nabla \cdot \mathbf{u} = 0. \tag{7.2}$$

In modelling bubble dynamics, particularly growth or collapse, one needs to account for the change in volume of the bubble and so any fluid which may reside within must be modelled as compressible. In utilising a "one field" model, where the bubble content as well as the ambient fluid is described, the full conservation of mass equation needs to be retained. Consequently, to complete the system of governing equations, a thermodynamic equation of state needs to be prescribed. The choice of an appropriate equation of state is itself a non-trivial task. Initially, we take the equation of state to be the ideal gas law viz.,

$$p = c^2 \rho, \tag{7.3}$$

where c is the speed of sound within the medium. Despite its simplicity, the model is a valid choice. Firstly, it can provide an accurate thermodynamic description for the bubble's gaseous contents. Secondly, by adopting a variable speed of sound, one can use an increased value within the ambient fluid to attain near-incompressibility. Furthermore, it is well known that the compressibility of the ambient fluid plays an important role in bubble collapse, particularly during the final stages [29]. Such a model enables the role of compressibility to be easily investigated.

7.2.1 Rheological Equations of State for Compressible Fluids

A Compressible Newtonian fluid

The constitutive equation, or rheological equation of state, for a compressible Newtonian fluid is well known. A Newtonian fluid is defined by the extra stress $\mathbf{S}$ being proportional to the velocity gradient, namely

$$S_{ij} = A_{ijkl} \frac{\partial u_k}{\partial x_l}, \tag{7.4}$$

where A_{ijkl} is a fourth-order isotropic tensor, detailing the material properties. *Any*

fourth-order isotropic tensor can be written as a combination of Kronecker delta functions viz.,

$$A_{ijkl} = \eta_1 \delta_{ik}\delta_{jl} + \eta_2 \delta_{ij}\delta_{kl} + \eta_3 \delta_{il}\delta_{jk}, \tag{7.5}$$

for scalar constants η_1, η_2, η_3. The symmetry of the Cauchy stress tensor implies symmetry of the extra stress S_{ij}, and so A_{ijkl} is symmetric with respect to i and j. Consequently, from Equation (7.5), $\eta_1 = \eta_3$ and so the extra stress becomes,

$$S_{ij} = \eta_1 \left(\frac{\partial u_i}{\partial x_j} + \frac{\partial u_j}{\partial x_i} \right) + \eta_2 \left(\frac{\partial u_k}{\partial x_k} \right) \delta_{ij}, \tag{7.6}$$

or, in vector notation,

$$\mathbf{S} = \eta_1 (\nabla \mathbf{u} + \nabla \mathbf{u}^T) + \eta_2 (\nabla \cdot \mathbf{u}) \mathbf{I}. \tag{7.7}$$

This is the most general constitutive equation for a Newtonian fluid, having imposed no restrictions on compressibility or on the scalars $\eta_{1,2}$. Here η_1 is named the (dynamic) shear viscosity coefficient while η_2 is the dilatational viscosity coefficient. Commonly, one abides by Stokes' Hypothesis and sets the bulk viscosity κ, defined $\kappa = \left(\frac{2}{3}\eta_1 + \eta_2\right)$, to zero [49]. Consequently the pressure p in Equation (7.1) becomes equivalent to a mean mechanical pressure p^* since

$$p^* := -\frac{1}{3}\sigma_{ii} = p - \left(\frac{2}{3}\eta_1 + \eta_2 \right) (\nabla \cdot \mathbf{u}) = p. \tag{7.8}$$

By assuming $\left(\frac{2}{3}\eta_1 + \eta_2\right) = 0$, the extra stress $\mathbf{S}$ is now trace free i.e. $S_{ii} = 0$.

We must emphasise that generally $p \neq p^*$, and so care must be exercised in applying the correct pressure to the thermodynamic equation of state. As reiterated by both Oldroyd [110] and Truesdell [153], it is p not p^* that should be used. Generally, the Cauchy stress is always split into a part that does work which is recoverable $p\delta_{ij}$ and a part which is always dissipative, S_{ij}. However, (in the Newtonian case) Stokes' hypothesis (equivalently $S_{ii} = 0$, $p = p^*$) means that there is no energy dissipation due to a change of volume within the fluid, and so all changes in volume are thermodynamically recoverable. Although it may provide a good approximation in some cases, such an assumption is clearly unphysical. In fact, the Stokes hypothesis has been debated for many years, see for example Truesdell [152]. Even Stokes himself had doubts over its

validity [149]. It is a moot point for incompressible fluids since the contestable term vanishes since $\nabla \cdot \mathbf{u} = 0$. Within this work Stokes' hypothesis is not adopted, and the more general form of the compressible Newtonian extra stress (Equation (7.7)) is retained.

Compressible Maxwell/Oldroyd type models

Satisfied in the choice of a constitutive equation for a compressible Newtonian fluid, the question remains as to what form non-Newtonian compressible constitutive equations assume. The answer is not entirely straightforward and there has been much inconsistency in compressible viscoelastic models in the literature, particularly in those of Maxwell/Oldroyd type, which of course is an essential first port of call in compiling compressible viscoelastic models. In the incompressible case, the Oldroyd B constitutive equation is

$$\mathbf{S} + \lambda_1 \overset{\triangledown}{\mathbf{S}} = \eta_0 \left(\dot{\boldsymbol{\gamma}} + \lambda_2 \overset{\triangledown}{\dot{\boldsymbol{\gamma}}} \right), \tag{7.9}$$

where $\dot{\boldsymbol{\gamma}} = (\nabla \mathbf{u} + \nabla \mathbf{u}^T)$ is the usual rate of strain tensor.
This can then be recast in terms of solvent and polymeric contributions viz.,

$$\mathbf{S} = \eta_s \dot{\boldsymbol{\gamma}} + \boldsymbol{\tau}, \tag{7.10}$$

with

$$\boldsymbol{\tau} + \lambda_1 \overset{\triangledown}{\boldsymbol{\tau}} = \eta_p \dot{\boldsymbol{\gamma}}. \tag{7.11}$$

Here η_s and η_p are the solvent and polymeric viscosities, respectively, defined by

$$\eta_s = \tfrac{\lambda_2}{\lambda_1} \eta_0, \quad \eta_p = \left(1 - \tfrac{\lambda_2}{\lambda_1} \right) \eta_0. \tag{7.12}$$

Note that $\eta_0 = \eta_s + \eta_p$.

Keshtiban et al. [74], in extending this model to study compressible viscoelastic contraction flows, include the appropriate compressible term in the rate of deformation as in Equation (7.7). This is the only compressible term present in their model. A slightly different model is used by Matušů-Nečasová et al. [104] who include compress-

ible effects only in the solvent contribution to the stress, leaving the polymeric part in its incompressible form. Edwards and Beris [48] show that if one includes compressibility in the kinetic theory derivation of the Oldroyd B model, an additional term of the form $\nabla \cdot \mathbf{uS}$, appears in the convected derivative. However, they do not include a compressible term in the rate of deformation. Sureshkumar [143] undertakes a stability analysis of a compressible UCM fluid. The compressible term of Edwards and Beris [48] is incorporated while the term $\eta_2(\nabla \cdot \mathbf{u})\mathbf{I}$ from Eq. (7.7) is added as a forcing term to the momentum equation. It is not included as part of the constitutive equation.

The above discussion highlights the rather eclectic range of compressible viscoelastic models in the literature. With the aforementioned studies in mind, the aim is to construct a compressible Oldroyd constitutive model which is as general as possible. One must firstly include the additional compressible terms that appear in the convected derivative (as derived by Edwards and Beris [48]). Secondly, as these models originate from simple relations between stress and the rate of strain, if the rate of strain (Eq. (7.7)) contains compressible components then these should appear within the constitutive equation in the usual way (as in [74]), and not as detached forcing terms (as in [143]). Finally, one should ensure that the model is consistent in the appropriate limits. For example, if $\lambda_2 = 0$, one should attain a compressible UCM fluid. Then if $\lambda_1 = 0$, a compressible Newtonian fluid, as described by Equation (7.7), should result. Furthermore, in the incompressible limit, compressible terms should vanish and the familiar incompressible Oldroyd B constitutive equation (Eq. (7.9)) should remain. Consequently, the following compressible Oldroyd B constitutive equation is proposed:

$$\mathbf{S} = \eta_1^s(\nabla\mathbf{u} + \nabla\mathbf{u}^T) + \eta_2^s(\nabla \cdot \mathbf{u})\mathbf{I} + \boldsymbol{\tau} \tag{7.13}$$

with

$$\boldsymbol{\tau} + \lambda_1 \left(\overset{\nabla}{\boldsymbol{\tau}} + (\nabla \cdot \mathbf{u})\boldsymbol{\tau} \right) = \eta_1^p(\nabla\mathbf{u} + \nabla\mathbf{u}^T) + \eta_2^p(\nabla \cdot \mathbf{u})\mathbf{I} \tag{7.14}$$

where superscripts s and p indicate solvent and polymeric viscosities respectively. The above form is general in the respect that it contains all known compressible terms and retains them in the UCM and Newtonian limits.

Compressibility is an important property and in general should be compatible with any

rheological constitutive equation. Consequently, we will briefly discuss the extension of other popular rheological models to compressible fluids.

Compressible Generalised Newtonian models

One of the earliest empiricisms in attempting to describe non-Newtonian effects observed in rheometry, was to extend the Newtonian model by assuming some dependence of viscosity on the scalar invariants of the rate of strain tensor. Hence the constitutive equation becomes

$$\mathbf{S} = \eta(I, II, III)\dot{\boldsymbol{\gamma}}, \tag{7.15}$$

where the viscosity η is some function of the scalar invariants I, II, III, defined by,

$$I = \sum_i \dot{\gamma}_{ii}, \tag{7.16}$$

$$II = \sum_{i,j} \dot{\gamma}_{ij}\dot{\gamma}_{ij}, \tag{7.17}$$

$$III = \sum_{i,j,k} \dot{\gamma}_{ij}\dot{\gamma}_{jk}\dot{\gamma}_{ki}. \tag{7.18}$$

The standard assumptions are then that the fluid is incompressible (in which case $I = 0$), and that the flow is shearing or very near shearing (as for simple shear $III = 0$). The viscosity can then be expressed as a function of the magnitude of the rate of strain, or the strain rate $\dot{\gamma}$, defined viz.,

$$\dot{\gamma} = \sqrt{\frac{1}{2}II}. \tag{7.19}$$

Despite the assumptions of shear flow in this empiricism, the model is frequently applied to more complicated flows and can be a successful description, particularly in flows with large shear components [15]. Then under the assumption of a such a model providing a good description of the flow, the contribution of compressibility becomes moot since, for a shearing flow, the divergence of the velocity field is zero - despite the fluid being compressible. Hence, assuming a dominant shear component to remove dependence on III in Equation (7.15), automatically removes a dependence on I, without making any assumptions on the fluids compressibility. Consequently, in the application of generalised Newtonian models to compressible flows, given the assump-

tions inherently made, one can argue that the current models for viscosity (such as the Carreau-Yasuda or Power-Law models) provide a sufficient description. Such is the approach of Taliadorou et al. [147], in their study of a compressible Herschel-Bulkley fluid, with the incompressible expression for the viscosity being retained.

Compressible Order Fluids

In wishing to construct a constitutive equation that describes small departures from Newtonian behaviour, the extra stress can be expressed as a series expansion of increasing powers of the rate of strain tensor $\dot{\boldsymbol{\gamma}}$ and of its (convected) derivatives (a "retarded motion" expansion) [15]. Retaining only the second order terms results in the constitutive equation for the second-order fluid, which for an incompressible fluid is

$$\mathbf{S} = \alpha_1 \dot{\boldsymbol{\gamma}} + \alpha_2 \overset{\triangledown}{\dot{\boldsymbol{\gamma}}} + \alpha_{11}(\dot{\boldsymbol{\gamma}} \cdot \dot{\boldsymbol{\gamma}}) + \alpha_{1:1}(\dot{\boldsymbol{\gamma}} : \dot{\boldsymbol{\gamma}})\mathbf{I}. \tag{7.20}$$

Prud'homme and Bird [125], in their study of the dilatational properties of suspensions of gas bubbles, discuss the generalisation of a second order constitutive model to a compressible fluid. They note that, in analogy to the derivation of the incompressible model, a compressible second order fluid would contain all possible combinations of $\dot{\boldsymbol{\gamma}}$ and $\nabla \cdot \mathbf{u}$ which yield tensors that are quadratic in velocity. Of course an identical approach allows generalisation to N^{th} order fluids. Hence, the constitutive equation for a compressible second order fluid will take the form,

$$\begin{aligned} \mathbf{S} \;=\; & \alpha_1 \dot{\boldsymbol{\gamma}} + \beta_1(\nabla \cdot \mathbf{u})\mathbf{I} + (\alpha_2 \dot{\boldsymbol{\gamma}} + \overset{\triangledown}{\beta_2}(\nabla \cdot \mathbf{u})\mathbf{I}) \\ & + \alpha_{11}\dot{\boldsymbol{\gamma}} \cdot \dot{\boldsymbol{\gamma}} + \beta_{11}(\nabla \cdot \mathbf{u})\dot{\boldsymbol{\gamma}} + (\alpha_{1:1}(\dot{\boldsymbol{\gamma}} : \dot{\boldsymbol{\gamma}}) + \beta_{1:1}(\nabla \cdot \mathbf{u})^2)\mathbf{I}. \end{aligned} \tag{7.21}$$

The scalars α_i, β_i are retarded motion expansion coefficients. Note that by retaining only the first order term, the constitutive equation is that of a compressible Newtonian fluid, with the shear viscosity given by α_1 and the dilatational viscosity by β_1.

In this chapter, the focus will be on rheological models of the Maxwell and Oldroyd type, with the other models reserved for future work.

7.2.2 Non-dimensionalisation of the Governing Equations

Velocities are non-dimensionalised with respect to some reference velocity U. In the benchmark problem of planar Poiseuille flow, U corresponds to the centreline steady-state velocity, while in bubble dynamic problems, U is some reference speed of sound. Distances are scaled with respect to the channel width, or in bubble dynamics problems, the initial bubble radius R. Similarly, the density is scaled with respect to initial fluid density or initial bubble density ρ_b. Hence pressures and stresses are scaled with respect to $\rho_b U^2$, with non-dimensional viscosities η^* scaled thus

$$\eta^* = \frac{\eta}{\rho_b U R}. \tag{7.22}$$

A Reynolds number can be defined as $Re = 1/\eta^*$, but it is perhaps more beneficial to continue to refer to non-dimensional viscosities given the several viscous parameters present in compressible models. In the case of viscoelastic flows, one has the usual dimensionless parameter for the relaxation time, the Weissenberg number,

$$We = \frac{\lambda_1 U}{R}. \tag{7.23}$$

Therefore, dropping asterixes, the non-dimensional governing equations for a compressible Oldroyd B fluid are the equation of motion,

$$\rho \frac{D\mathbf{u}}{Dt} = -\nabla p + \nabla \cdot \mathbf{S}, \tag{7.24}$$

the conservation of mass,

$$\frac{D\rho}{Dt} + \rho \nabla \cdot \mathbf{u} = 0, \tag{7.25}$$

the thermodynamic equation of state,

$$p = c^2 \rho, \tag{7.26}$$

and finally, the constitutive equation,

$$\mathbf{S} = \eta_1^s (\nabla \mathbf{u} + \nabla \mathbf{u}^T) + \eta_2^s (\nabla \cdot \mathbf{u}) \mathbf{I} + \boldsymbol{\tau}, \tag{7.27}$$

where the polymeric stress $\boldsymbol{\tau}$ is given by

$$\boldsymbol{\tau} + We\left(\overset{\nabla}{\boldsymbol{\tau}} + (\nabla \cdot \mathbf{u})\boldsymbol{\tau}\right) = \eta_1^p(\nabla\mathbf{u} + \nabla\mathbf{u}^T) + \eta_2^p(\nabla \cdot \mathbf{u})\mathbf{I}. \tag{7.28}$$

7.2.3 The Log-Density Formulation of the Governing Equations

As in Bollada and Phillips [22], we note that the dynamic viscosities $\eta_{1,2}$ vary linearly with density, such that

$$\eta_1 = \mu\rho, \qquad \eta_2 = \nu\rho, \tag{7.29}$$

for some kinematic viscosities μ and ν.
Defining a log density viz.

$$q := \ln\rho, \tag{7.30}$$

the conservation of mass and momentum can be rewritten in the following forms,

$$\frac{D\mathbf{u}}{Dt} = -\frac{dp}{d\rho}\nabla q + \nabla \cdot \mathbf{T} + \nabla q \cdot \mathbf{T} \tag{7.31}$$

and

$$\frac{Dq}{Dt} + \nabla \cdot \mathbf{u} = 0, \tag{7.32}$$

where $\mathbf{T}$ is a kinematic extra stress defined such that $\mathbf{S} = \rho\mathbf{T}$. Note that for the ideal gas equation of state (7.3), $\frac{dp}{d\rho} = c^2$ (for a constant speed of sound with respect to density).

The constitutive equation for the kinematic extra stress follows directly from Equation (7.13), to give

$$\mathbf{T} = \mu_s(\nabla\mathbf{u} + \nabla\mathbf{u}^T) + \nu_s(\nabla \cdot \mathbf{u})\mathbf{I} + \mathbf{P}, \tag{7.33}$$

where μ_s, ν_s are solvent kinematic viscosities and $\mathbf{P}$ is the kinematic polymeric stress (with $\boldsymbol{\tau} = \rho\mathbf{P}$).

Similarly, one can determine the constitutive equation for $\mathbf{P}$, given that $\boldsymbol{\tau} = \rho\mathbf{P}$ satisfies

the original polymeric constitutive equation (7.14) viz.,

$$We\overset{\triangledown}{(\rho\mathbf{P})} + We(\rho\mathbf{P})(\nabla\cdot\mathbf{u}) + (\rho\mathbf{P}) = \rho\mu_p(\nabla\mathbf{u} + \nabla\mathbf{u}^T) + \rho\nu_p(\nabla\cdot\mathbf{u})\mathbf{I}. \tag{7.34}$$

Making use of the definition of the upper-convected derivative on scalars,

$$\overset{\triangledown}{\rho} = \frac{D\rho}{Dt}, \tag{7.35}$$

and the conservation of mass (7.2), the compressible term of Edwards and Beris [48] vanishes to give

$$We\overset{\triangledown}{\mathbf{P}} + \mathbf{P} = \mu_p(\nabla\mathbf{u} + \nabla\mathbf{u}^T) + \nu_p(\nabla\cdot\mathbf{u})\mathbf{I}. \tag{7.36}$$

Although the compressible term of Edwards and Beris [48] does not appear explicitly in the recast form of the polymeric constitutive equation, it is, of course, present implicitly through the implementation of the log-density formulation.

So finally, the set of reformulated, non-dimensional governing equations to be solved are,
the equation of motion (conservation of momentum),

$$\frac{D\mathbf{u}}{Dt} = -c^2\nabla q + \nabla\cdot\mathbf{T} + \nabla q\cdot\mathbf{T}, \tag{7.37}$$

the conservation of mass,

$$\frac{Dq}{Dt} + \nabla\cdot\mathbf{u} = 0, \tag{7.38}$$

and the constitutive equation,

$$\mathbf{T} = \mathbf{T}_s + \mathbf{P}, \tag{7.39}$$

where the polymeric stress $\mathbf{P}$ is found from,

$$We\overset{\triangledown}{\mathbf{P}} + \mathbf{P} = \mathbf{T}_p. \tag{7.40}$$

Here, $\mathbf{T}_s$ denotes the solvent stress

$$\mathbf{T}_s = \mu_s(\nabla\mathbf{u} + \nabla\mathbf{u}^T) + \nu_s(\nabla\cdot\mathbf{u})\mathbf{I}, \tag{7.41}$$

and $\mathbf{T}_p$ the corresponding rate of deformation contribution to the polymeric stress,

$$\mathbf{T}_p = \mu_p(\nabla \mathbf{u} + \nabla \mathbf{u}^T) + \nu_p(\nabla \cdot \mathbf{u})\mathbf{I}. \tag{7.42}$$

Note that henceforth, in referring to density and stress, we in actuality mean the log density and kinematic stress, given the simple relation between these quantities and their log form.

7.3 Numerical Solution of the Governing Equations

7.3.1 Time discretisation

As in Bollada and Phillips [22, 23] we employ a semi-Lagrangian treatment of the material derivative in the momentum equation. In discretising the constitutive equation we will investigate two different approaches. A 1st order semi-Lagrangian scheme which is semi-implicit with respect to the stress, and a 2nd order Eulerian scheme which is explicit with respect to the stress. We first provide details of the semi-Lagrangian treatment of the material derivative.

Semi-Lagrangian Treatment of the Material Derivative

A first order Lagrangian approximation to the material derivative is,

$$\frac{D\mathbf{u}}{Dt} \approx \frac{\mathbf{u}^{n+1}(\mathbf{x}^{n+1}) - \mathbf{u}^n(\mathbf{x}^n)}{\Delta t} = f(\mathbf{u}^{n+1}), \tag{7.43}$$

where $\mathbf{x}^n$ denotes the position of a fluid particle at time t^n that is at the point $\mathbf{x}^{n+1}$ at time t^{n+1}. The function f is the right hand side of the equation of motion (7.37). Given $\mathbf{u}^n$, we wish to solve Equation (7.43) implicitly for $\mathbf{u}^{n+1}$ at each nodal point (note that by construction $\mathbf{x}^{n+1}$ lies upon a nodal point). Hence, in order to approximate the material derivative, one needs the previous position $\mathbf{x}^n$ of the fluid particle that moves onto the node with velocity $\mathbf{u}^{n+1}$. This is illustrated in Fig. 7.2. We solve for $\mathbf{u}^{n+1}$ iteratively, and give details of the scheme below.

1. Firstly provide an initial approximation $\mathbf{u}_0^{n+1}$ to $\mathbf{u}^{n+1}(\mathbf{x}_i)$ at a nodal point $\mathbf{x}_i$, namely $\mathbf{u}^n(\mathbf{x}_i)$

2. Then use $\mathbf{u}_0^{n+1}$ to approximate previous position of particle $\mathbf{x}_0^n$, using

$$\mathbf{x}_0^n = \mathbf{x}_i - \mathbf{u}_0^{n+1}\Delta t.$$

Then $\mathbf{u}^n(\mathbf{x}_0^n)$ is calculated (as $\mathbf{u}^n$ is known everywhere).

3. Set $m = 1$

4. The next approximation to $\mathbf{u}^{n+1}(\mathbf{x}_i)$ can then be found by solving the equation of motion,

$$\frac{\mathbf{u}_m^{n+1}(\mathbf{x}_i) - \mathbf{u}^n(\mathbf{x}_{m-1}^n)}{\Delta t} = f(\mathbf{u}_m^{n+1}).$$

5. An improved approximation to the previous particle position $\mathbf{x}_m^n$ is now found using the mid point approximation

$$\mathbf{x}_m^n = \mathbf{x}_i - \frac{\Delta t}{2}(\mathbf{u}_m^{n+1}(\mathbf{x}_i) + \mathbf{u}^n(\mathbf{x}_{m-1}^n)). \tag{7.44}$$

The velocity at this new particle position is then $\mathbf{u}^n(\mathbf{x}_m^n)$.

6. If $\max_S |\mathbf{u}^n(\mathbf{x}_m^n) - \mathbf{u}^n(\mathbf{x}_{m-1}^n)| < \epsilon$ then we have converged upon the previous particle position $\mathbf{x}_m^n$ and its velocity. Hence the material derivative is correctly approximated, and so we can set $\mathbf{u}^{n+1}(\mathbf{x}_i) = \mathbf{u}_m^{n+1}(\mathbf{x}_i)$ to obtain the converged velocity at node i, time step $n+1$. The computation can then proceed to the next time step.

7. Else, if $\max_S |\mathbf{u}^n(\mathbf{x}_m^n) - \mathbf{u}^n(\mathbf{x}_{m-1}^n)| \geq \epsilon$ then set $m := m + 1$ and return to step 4.

Here ϵ is some small tolerance (typically $\epsilon = 1 \times 10^{-6}$). Having converged upon the previous position $\mathbf{x}^n$ of the fluid particle at node i, the material derivative of other quantities such as density q can be found directly from the approximation,

$$\frac{Dq}{Dt} \approx \frac{q^{n+1}(\mathbf{x}_i) - q^n(\mathbf{x}^n)}{\Delta t}. \tag{7.45}$$

Discretisation of the Polymeric Stress

Two discretisations of the polymeric stress are investigated. Firstly we present the second-order scheme as used in van Os and Phillips [157] and Fiétier and Deville

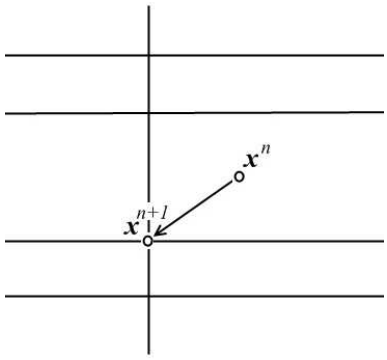

Figure 7.2: Movement of fluid particle at $\mathbf{x}^n$ at time n on to GLL node at time $n+1$. The position $\mathbf{x}^n$ and the velocity at the GLL node at time $n+1$ are determined iteratively.

[52]. The material derivative is approximated using a second order backward difference formula viz.,

$$\frac{D\mathbf{P}}{Dt} = \frac{\partial \mathbf{P}}{\partial t} + \mathbf{u}\cdot\nabla\mathbf{P} \approx \frac{3\mathbf{P}^{n+1} - 4\mathbf{P}^n + \mathbf{P}^{n-1}}{2\triangle t} + 2\mathbf{u}^n\cdot\nabla\mathbf{P}^n - \mathbf{u}^{n-1}\cdot\nabla\mathbf{P}^{n-1}. \quad (7.46)$$

The deformation terms, labelled thus $\mathbf{F} = (\nabla\mathbf{u})\mathbf{P} + \mathbf{P}(\nabla\mathbf{u})^T$, are then approximated using a second order extrapolation scheme

$$\mathbf{F}^{n+1} \approx 2\mathbf{F}^n - \mathbf{F}^{n-1}. \quad (7.47)$$

The rate of deformation terms $\mathbf{T}_p$ (and the solvent stress $\mathbf{T}_s$) are treated implicitly. The semi-discrete polymeric constitutive equation is therefore

$$(1 + \frac{3We}{2\triangle t})\mathbf{P}^{n+1} - \mathbf{T}_p^{n+1} = \lambda\mathbf{B}^n, \quad (7.48)$$

where $\mathbf{B}^n$ is given by

$$\mathbf{B}^n = \frac{1}{2\triangle t}(4\mathbf{P}^n - \mathbf{P}^{n-1}) - (2\mathbf{u}^n\cdot\nabla\mathbf{P}^n - \mathbf{u}^{n-1}\cdot\nabla\mathbf{P}^{n-1}) + (2\mathbf{F}^n - \mathbf{F}^{n-1}). \quad (7.49)$$

The second scheme to be investigated incorporates the semi-Lagrangian treatment already being used in the conservation of momentum. The material derivative of the stress is approximated using an identical first order Lagrangian description,

$$\frac{D\mathbf{P}}{Dt} \approx \frac{\mathbf{P}^{n+1}(\mathbf{x}_i) - \mathbf{P}^n(\mathbf{x}^n)}{\Delta t}, \tag{7.50}$$

where $\mathbf{x}^n$ is the previous particle position, already found iteratively from the process described in subsection 7.3.1. The remaining terms, the deformation terms $\mathbf{F}$ and rate of deformation are treated semi-implicitly to yield the following semi-discrete equation,

$$\left(1 + \frac{We}{\Delta t}\right)\mathbf{P}^{n+1} - We\left((\nabla\mathbf{u}^{n+1})\mathbf{P}^n + \mathbf{P}^n(\nabla\mathbf{u}^{n+1})^T\right) - \mathbf{T}_p^{n+1} = \frac{We}{\Delta t}\mathbf{P}^n(\mathbf{x}^n). \tag{7.51}$$

Note that it is indeed possible to implement a fully implicit equation with respect to both $\mathbf{P}$ and $\mathbf{u}$ by replacing $\mathbf{P}^n$ by $\mathbf{P}^{n+1}$ in the deformation terms. However, as will be explained shortly, to do so would result in a significant increase in computation time.

To summarise, the time discretised governing equations to be solved using the spectral element method are:

The equation of motion,

$$\frac{\mathbf{u}^{n+1} - \mathbf{u}^n}{\Delta t} = -c^2\nabla q^{n+1} + \nabla\cdot\mathbf{T}^{n+1} + \nabla q^{n+1}\cdot\mathbf{T}^{n+1}. \tag{7.52}$$

The conservation of mass,

$$\frac{q^{n+1} - q^n}{\Delta t} + \nabla\cdot\mathbf{u}^{n+1} = 0. \tag{7.53}$$

The constitutive equation,

$$\mathbf{T}^{n+1} = \mathbf{T}_s^{n+1} + \mathbf{P}^{n+1} = \mu_s(\nabla\mathbf{u}^{n+1} + (\nabla\mathbf{u}^{n+1})^T) + \nu_s(\nabla\cdot\mathbf{u}^{n+1})\mathbf{I} + \mathbf{P}^{n+1}. \tag{7.54}$$

The polymeric stress $\mathbf{P}^{n+1}$ is found either from the second order scheme (henceforth called scheme A),

$$\left(1 + \frac{3We}{2\triangle t}\right)\mathbf{P}^{n+1} - \mathbf{T}_p^{n+1} = We\mathbf{B}^n, \tag{7.55}$$

where $\mathbf{B}^n$ is given in Equation (7.49), or from the first order Lagrangian scheme (scheme B),

$$\left(1+\frac{We}{\Delta t}\right)\mathbf{P}^{n+1} - We\left((\nabla\mathbf{u}^{n+1})\mathbf{P}^{n} + \mathbf{P}^{n}(\nabla\mathbf{u}^{n+1})^{T}\right) - \mathbf{T}_{p}^{n+1} = \frac{We}{\Delta t}\mathbf{P}^{n}(\mathbf{x}^{n}). \quad (7.56)$$

7.3.2 The Spectral Element Method

The Weak Formulation

Let Ω represent the whole fluid domain, comprised of both the bubble and the ambient fluid. Let the boundary of this domain be $\partial\Omega$. In solving Equations (7.52)-(7.54) by the spectral element method, the weak form of said equations must first be derived. The dependent variables $\mathbf{u}$, q and stresses $\mathbf{T}_s$, $\mathbf{P}$, are chosen from the following function spaces,

$$\mathbf{u} \in V \subseteq [H^1(\Omega)]^2, \quad (7.57)$$

$$q \in Q = [H^1(\Omega)], \quad (7.58)$$

$$\mathbf{T}_s, \mathbf{P} \in R = [H^1(\Omega)]_s^4. \quad (7.59)$$

Here V is some subset of $[H^1(\Omega)]^2$ whose entries satisfy the desired velocity boundary conditions on $\partial\Omega$, while R is the space of symmetric 2×2 tensors whose components belong to $H^1(\Omega)$. Furthermore, we define the following test space for the velocity

$$V_0 = \{\mathbf{v} \in [H^1(\Omega)]^2, \mathbf{v} = 0 \text{ on } \partial\Omega\}. \quad (7.60)$$

Multiplying the strong form of the governing equations by the appropriate test function and then integrating, we arrive at the weak formulation:

Find $\mathbf{u} \in V$, $q \in P$, and $\mathbf{T}_s$, $\mathbf{P} \in R$ such that,

$$\int_\Omega \frac{\mathbf{u}-\mathbf{u}^n}{\Delta t}\cdot\mathbf{v} + \int_\Omega (\mathbf{T}_s+\mathbf{P}) : \nabla\mathbf{v} = c^2\int_\Omega q\nabla\cdot\mathbf{v} + \int_\Omega \nabla q\cdot(\mathbf{T}_s+\mathbf{P})\cdot\mathbf{v} \quad \forall\mathbf{v}\in V_0, \quad (7.61)$$

$$\int_\Omega \left(\frac{q-q^n}{\Delta t} + \nabla\cdot\mathbf{u}\right)p = 0 \quad \forall p \in Q, \quad (7.62)$$

$$\int_\Omega \mathbf{T}_s : \mathbf{W} - \int_\Omega \mu_s \nabla \mathbf{u} : (\mathbf{W} + \mathbf{W}^T) = \int_\Omega \nu_s (\nabla \cdot \mathbf{u}) \mathrm{tr}(\mathbf{W}) \quad \forall \mathbf{W} \in R, \tag{7.63}$$

Scheme A

$$\begin{aligned} \int_\Omega \left(1 + \frac{3We}{2\triangle t}\right) \mathbf{P} : \mathbf{W} &= \int_\Omega \mu_p \nabla \mathbf{u} : (\mathbf{W} + \mathbf{W}^T) \\ &+ \int_\Omega \nu_p (\nabla \cdot \mathbf{u}) \mathrm{tr}(\mathbf{W}) + \int_\Omega We \mathbf{B}^n : \mathbf{W} \quad \forall \mathbf{W} \in R, \end{aligned} \tag{7.64}$$

Scheme B

$$\begin{aligned} \int_\Omega \left(1 + \frac{We}{\triangle t}\right) \mathbf{P} : \mathbf{W} &= \int_\Omega \mu_p \nabla \mathbf{u} : (\mathbf{W} + \mathbf{W}^T) \\ &+ \int_\Omega \nu_p (\nabla \cdot \mathbf{u}) \mathrm{tr}(\mathbf{W}) \\ &+ \int_\Omega We((\nabla \mathbf{u})\mathbf{P}^n + \mathbf{P}^n (\nabla \mathbf{u})^T) : \mathbf{W} \\ &+ \int_\Omega \frac{We}{\Delta t} \mathbf{P}^n : \mathbf{W} \quad \forall \mathbf{W} \in R. \end{aligned} \tag{7.65}$$

Transfinite Mapping

The physical domain Ω is discretised into a number of non-overlapping, conforming, convex quadrilateral spectral elements labelled $\Omega_{\alpha,\beta}$. As in finite element methods, one has the freedom to design meshes suited to the problem geometry and to create highly resolved meshes near any regions of interest. Each spectral element is mapped onto the parent element $D = [-1, 1] \times [-1, 1]$ using the simple bilinear transfinite mapping,

$$\mathbf{x} = \frac{1}{4}(1-\xi)(1-\zeta)\mathbf{x}_1 + \frac{1}{4}(1+\xi)(1-\zeta)\mathbf{x}_2 + \frac{1}{4}(1+\xi)(1+\zeta)\mathbf{x}_3 + \frac{1}{4}(1-\xi)(1+\zeta)\mathbf{x}_4, \tag{7.66}$$

where $(\xi, \zeta) \in D$ corresponds to point $\mathbf{x} = (x(\xi, \zeta), y(\xi, \zeta)) \in \Omega_{\alpha,\beta}$, with the vertices of $\Omega_{\alpha,\beta}$ given by $\mathbf{x}_1, ..., \mathbf{x}_4$ (See Figure 7.3).

Spectral Approximation

The velocity, density and the stresses, are approximated on each element using Lagrangian interpolation through a select set of nodal points, called Gauss-Lobatto-

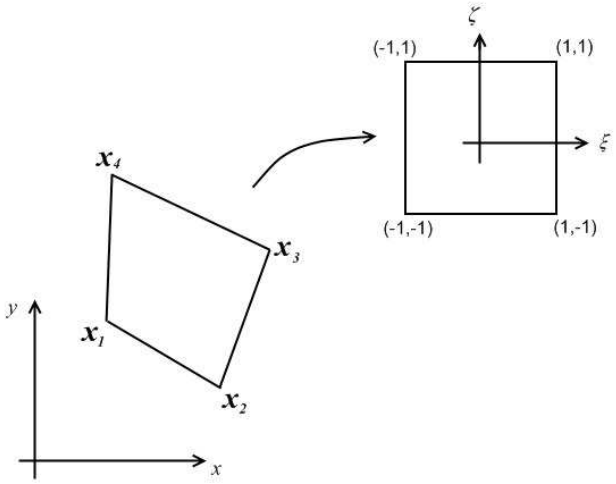

Figure 7.3: Illustration of mapping between quadrilateral spectral element and parent element.

Legendre (GLL) points. In one dimension, the $N+1$ GLL points are roots of the polynomial $(1-\xi^2)L'_N(\xi)$, where L_N is the Legendre polynomial of degree N. Consequently, the standard Lagrange interpolant

$$h_i(\xi) = \frac{\prod_{j=0,j\neq i}^{N}(\xi - \xi_j)}{\prod_{j=0,j\neq i}^{N}(\xi_i - \xi_j)}, \tag{7.67}$$

can be shown to take the form

$$h_i(\xi) = -\frac{(1-\xi^2)L'_N(\xi)}{N(N+1)L_N(\xi_i)(\xi - \xi_i)}, \tag{7.68}$$

with GLL points ξ_i, $0 \leq i \leq N$. Also, note that by the definition of the Lagrange interpolant,

$$h_i(\xi_j) = \delta_{ij}. \tag{7.69}$$

The Legendre polynomials are a subset of the polynomial eigenfunctions (Jacobi polynomials) of the singular Sturm-Liouville problem. This means that the expansion of a C^∞ function in terms of these eigenfunctions converges with spectral accuracy [112]. Hence, an expansion in terms of the Lagrange interpolants h_i (Equation (7.68)) ex-

hibits spectral properties, while also naturally lending itself to Gauss-Lobatto numerical quadrature.

In 2D, the GLL points form a $(N+1)^2$ grid within each element, interpolation over which yields the representation of the velocity component a over the parent element

$$u^a(\xi,\zeta) = \sum_{i=0}^{N}\sum_{j=0}^{N} u_{ij}^a h_i(\xi)h_j(\zeta), \tag{7.70}$$

where u_{ij}^a is the approximation to u^a at GLL nodal point (ξ_i, ζ_j).
Similarly, the stress components and density are represented as,

$$P^{ab}(\xi,\zeta) = \sum_{i=0}^{N}\sum_{j=0}^{N} P_{ij}^{ab} h_i(\xi)h_j(\zeta). \tag{7.71}$$

$$q(\xi,\zeta) = \sum_{i=0}^{N}\sum_{j=0}^{N} q_{ij} h_i(\xi)h_j(\zeta). \tag{7.72}$$

The Discrete Equations

The integrals in the weak form are calculated using the Gauss-Lobatto quadrature rule

$$\int_{-1}^{1}\int_{-1}^{1} f(\xi,\zeta)d\xi d\zeta \approx \sum_{i=0}^{N}\sum_{j=0}^{N} f(\xi_i,\zeta_j)\lambda_i\lambda_j \tag{7.73}$$

for GLL points (ξ_i, ζ_j) and weights λ_i. The approximation is exact when f is a polynomial of degree $2N-1$ or less in each of the independent variables. The discrete equations are obtained by inserting the variable expansions (Equations (7.70) - (7.72)), into the weak form (Equations (7.61) - (7.65)). By applying the above quadrature rule and the properties of the Lagrangian interpolant, substitution yields the following local arrays for each spectral element,

$$\bar{A}_{ijkl} = \int_D J(\xi,\zeta)h_i(\xi)h_j(\zeta)h_k(\xi)h_l(\zeta) = J_{ij}\lambda_i\lambda_j\delta_{ki}\delta_{lj}, \tag{7.74}$$

$$\bar{C}_{ijkl}^b = \int_D Z^{cb}(\xi,\zeta)h_i(\xi)h_j(\zeta)[h_k(\xi)h_l(\zeta)]_{,c} = \lambda_i\lambda_j Z_{ij}^{cb}\begin{cases} D_{ik}\delta_{lj}, & c=1 \\ \delta_{ki}D_{jl}, & c=2 \end{cases} \tag{7.75}$$

Here J is the Jacobian of the mapping (given by Equation (7.66)) from the spectral to the parent element , while Z^{cb} are the geometric factors associated with the mapping, defined

$$Z_{ij}^{cb} = \left(\frac{\partial \xi^c}{\partial x^b} J\right)(\xi_i, \zeta_j). \tag{7.76}$$

The matrix $\mathbf{D}$ with entries $D_{ij} = h_j'(\xi_i)$ is known as the Legendre pseudospectral differentiation matrix. Closed form expressions for the entries of $\mathbf{D}$ may be found using the properties of the Legendre polynomials

$$D_{ij} = \begin{cases} \dfrac{1}{(\xi_i - \xi_j)} \dfrac{L_N(\xi_i)}{L_N(\xi_j)}, & i \neq j, \\ 0, & 1 \leq i = j \leq N-1, \\ -\dfrac{N(N+1)}{4}, & i = j = 0, \\ \dfrac{N(N+1)}{4}, & i = j = N. \end{cases}$$

In effect, the matrix $\bar{A}_{ijkl}$ contains the weights and Jacobian of the spectral element mappings, while $\bar{C}_{ijkl}^b$ is the discretisation associated with the gradient operator. The global matrices A_{ijkl} and C_{ijkl}^b can be assembled from the local matrices, $\bar{A}_{ijkl}$ and $\bar{C}_{ijkl}^b$, using the following construction:

We define a matrix $\bar{\bar{L}}_{ijkl}$ with global indices $i, k \in [0, \hat{N}]$, $j, l \in [0, \hat{M}]$ thus,

$$\bar{\bar{L}}_{ijkl}^{\alpha\beta} = \begin{cases} \bar{L}_{ijkl}^{\alpha\beta} & \text{if } i, j, k, l \in [0, N] \\ 0 & \text{otherwise.} \end{cases}$$

Here $\hat{N}+1$ and $\hat{M}+1$ are the total number of GLL points (within domain Ω) in the x and y directions respectively.
The global matrix L_{ijkl} can then be assembled by summing over the contributing spectral elements, viz.,

$$L_{ijkl} = \sum_{\alpha=0}^{\hat{\alpha}} \sum_{\beta=0}^{\hat{\beta}} \bar{\bar{L}}_{i-\alpha N, j-\beta N, k-\alpha N, l-\beta N}^{\alpha\beta}. \tag{7.77}$$

Co-ordinates (α, β) label each spectral element, with $(\hat{\alpha}+1)$, $(\hat{\beta}+1)$ denoting the number of spectral elements in the x and y directions, respectively.

Consequently, in terms of the global arrays, the discretisation of the weak form yields the following set of discrete governing equations,
the conservation of momentum,

$$u^a_{ij}A_{ijkl} + \Delta t((T_s)^{ac}_{ij} + P^{ac}_{ij})C^c_{ijkl} = (u^n)^a_{ij}A_{ijkl} + \Delta t c^2 q_{ij}C^a_{ijkl} + \Delta t q_{ij}((T_s)^{ac}_{kl} + P^{ac}_{kl})C^c_{klij}, \tag{7.78}$$

the conservation of mass,

$$q_{ij}A_{ijkl} + \Delta t u^b_{ij}C^b_{klij} = q^n_{ij}A_{ijkl}, \tag{7.79}$$

the solvent part of the extra stress,

$$(T_s)^{ab}_{ij}A_{ijkl} = u^c_{ij}\left[(\mu_s)_{kl}(C^b_{klij}\delta^{ac} + C^a_{klij}\delta^{bc}) + (\nu_s)_{kl}C^c_{klij}\delta^{ab}\right], \tag{7.80}$$

the polymeric part of the extra stress, discretised using scheme A,

$$\left(1 + \frac{3(We)_{kl}}{2\triangle t}\right)P^{ab}_{ij}A_{ijkl} = u^c_{ij}\left[(\mu_p)_{kl}(C^b_{klij}\delta^{ac} + C^a_{klij}\delta^{bc}) + (\nu_p)_{kl}C^c_{klij}\delta^{ab}\right] + (We)_{kl}(B^n)^{ab}_{ij}A_{ijkl}, \tag{7.81}$$

and then scheme B,

$$\begin{aligned}\left(1 + \frac{(We)_{kl}}{\triangle t}\right)P^{ab}_{ij}A_{ijkl} &= u^c_{ij}\left[(\mu_p)_{kl}(C^b_{klij}\delta^{ac} + C^a_{klij}\delta^{bc}) + (\nu_p)_{kl}C^c_{klij}\delta^{ab} + (We)_{kl}\Gamma^{abcd}_{kl}C^d_{klij}\right] \\ &\quad + \frac{(We)_{kl}}{\Delta t}(P^n)^{ab}_{ij}A_{ijkl},\end{aligned} \tag{7.82}$$

where Γ^{abcd}_{kl} in Equation (7.82), is given by

$$\Gamma^{abcd}_{kl} = \delta^{ac}(P^n)^{bd}_{kl} + \delta^{bc}(P^n)^{ad}_{kl}. \tag{7.83}$$

In the above equations the summation convention is employed over i, j and c, d.
Substituting the stresses T^{ab}_s, P^{ab} and the density q, into the conservation of momentum yields the following linear system for u^b_{ij},

$$M^{ab}_{ijkl}u^b_{ij} = v^a_{kl}. \qquad \text{(sum over } i,\ j,\ b) \tag{7.84}$$

where M is the stiffness matrix, given by

$$M^{ab}_{ijkl} = \delta^{ab}A_{ijkl}+\Delta t[(\Lambda^{ab}_{pq}C^{c}_{pqij}+\Lambda^{cb}_{pq}C^{a}_{pqij}+\Upsilon^{ac}_{pq}C^{b}_{pqij}+\Phi^{abcd}_{pq}C^{d}_{pqij})C^{c}_{pqkl}+\Delta t c^2 C^{b}_{pqij}C^{a}_{pqkl}]A^{-1}_{pqpq}, \tag{7.85}$$

with summation over p, q and c, d.
Here, the matrix of dilatational viscosity coefficients Υ^{ab}_{ij} is given by

$$\Upsilon^{ab}_{ij} = \left((\nu_s)_{ij} + \frac{(\nu_p)_{ij}}{(C_T)_{ij}}\right)\delta^{ab}, \tag{7.86}$$

while the matrix of shear viscosity coefficients is

$$\Lambda^{ab}_{ij} = \left((\mu_s)_{ij} + \frac{(\mu_p)_{ij}}{(C_T)_{ij}}\right)\delta^{ab}. \tag{7.87}$$

Φ^{abcd}_{ij} contains the non-linear convection terms from the constitutive equation and arises only in the semi-implicit treatment (scheme B). Hence

$$\Phi^{abcd}_{ij} = \begin{cases} 0 \qquad \text{for scheme A,} \\ \\ (We)_{ij}/(C_T)_{ij}(\delta^{ab}(P^n)^{cd}_{ij} + \delta^{bc}(P^n)^{ad}_{ij}) \qquad \text{for scheme B.} \end{cases}$$

The right-hand side of Eq. (7.84), v^a_{kl}, is given by

$$v^a_{kl} = (u^n)^a_{ij}A_{ijkl} + c^2\Delta t q^n_{ij}C^a_{ijkl} + \Delta t y^a_{kl} - \Delta t G^{ab}_{ij}C^b_{ijkl}, \tag{7.88}$$

where G^{ab}_{ij} is given by,

$$G^{ab}_{ij} = \begin{cases} \frac{(We)_{ij}}{(C_T)_{ij}}(B^n)^{ab}_{ij} \qquad \text{for scheme A,} \\ \\ \frac{(We)_{ij}}{\Delta t(C_T)_{ij}}(P^n(x^n))^{ab}_{ij} \qquad \text{for scheme B.} \end{cases}$$

The stiffness matrix M needs to be calculated at every time step, since parameters like viscosity and Weissenberg number are permitted to vary. Hence M^{-1} needs to be calculated at each time step used in the iterative process to calculate $\mathbf{u}^{n+1}$.
It is for this reason that scheme B is not fully implicit in $\mathbf{P}$, because to use $\mathbf{P}^{n+1}$

within the stiffness matrix would require compilation, factorisation, and inversion of the matrix for each iteration within each time step. Such an approach is far too costly in terms of computation time. Note that for scheme A, the stiffness matrix becomes symmetric in the sense that, $M^{ab}_{ijkl} = M^{ba}_{klij}$, although this is not true for scheme B. Hence at each time step M is factorised once, using LU decomposition in the asymmetric case, and Cholesky decomposition in the symmetric case. Given the sparsity of the stiffness matrix following a spectral element discretisation, the parallel direct sparse solver routine PARDISO* is used to factorise and invert M. This first requires that the stiffness matrix be recast in terms of three full one dimensional arrays, detailing the value and position of the non-zero elements.

7.3.3 Marker Particle Method

The marker particle method is a Lagrangian scheme to track multiple fluid phases and interfaces. A large number of particles placed within the domain act as "markers", providing the identity of the fluid at a point in time and space. The approach was first suggested by Rider and Kothe [128, 129] and shows favourable comparisons with VOF and level set methods. Particular benefits include the absence of numerical diffusion and numerical surface tension, and the ability to handle severe topological changes with ease. Furthermore, the scheme is straightforward to implement and is very robust [128]. It has been subsequently applied in Newtonian drop dynamics studies by Bierbrauer and Zhu [14] and Bierbrauer and Phillips [13].

The fluid domain Ω is filled with initially equally spaced massless particles - a specified number per unit area. Every marker particle p is initially located at a unique position (x_p, y_p), and assigned a colour, or identity, C^m_p defined by

$$C^m_p = \begin{cases} 1 & \text{if particle p is in fluid } m, \\ 0 & \text{if particle p is not in fluid } m. \end{cases} \tag{7.89}$$

Assuming no change in phase, particles initially of fluid m will remain so indefinitely and will be advected with fluid m. Hence the colour function satisfies the advection equation viz.

$$\frac{DC^m_p}{Dt} = 0. \tag{7.90}$$

Note the similarity with VOF and level set methods. Here (7.90) is ensured through the Lagrangian treatment of the marker particles, whereas VOF/level set methods solve an analogous equation to (7.90) explicitly in an Eulerian manner for the volume fraction/level set function. As the particles remain of type fluid m, they can be assigned the constant material properties associated with fluid m. In this study, the material properties constant within each fluid are the viscosities $\mu_{p,s}$, $\nu_{p,s}$, the relaxation time λ_1 (which we have non-dimensionalised to the Weissenberg number) and the speed of sound c^2.

Grid to particle interpolation.

The marker particles, and hence the position of the relative phases, are updated using the velocities calculated on the Eulerian spectral element grid. The velocities are interpolated to each marker particle and the particles are advected with these velocities according to $\mathbf{u} = D\mathbf{x}/Dt$. The benefits of a spectral element formulation mean that internodal velocities can be found with ease and high accuracy using the Lagrange interpolant expansions (7.70). Therefore a particle at (x_p, y_p) can be easily and accurately assigned a velocity $\mathbf{u}(x_p, y_p)$ and hence updated in position accordingly.

Particle to grid interpolation

The fluids' material properties, carried with the marker particles, then need to be projected onto the grid before solving the governing equations for the next time step. Analogous to the many articles in the literature on volume-of-fluid (VOF) methods (for example [61]), it seems reasonable to assign material properties, such as viscosities and relaxation times, to each Gauss-Lobatto-Legendre node using the following averaging process

$$\phi_{ij} = \sum_{m=1}^{M} \phi^m C_{ij}^m. \tag{7.91}$$

Here ϕ_m denotes a material constant within fluid m, and M the total number of separate phases/fluids. Note that in this study $M = 2$, as we have only two distinct phases - the bubble and the ambient fluid.

The quantity C_{ij}^m is the interpolated colour function at the point (i, j) given by,

$$C_{ij}^m = \frac{\sum_{p=1}^{Np} S(x_p - x_i, y_p - y_j) C_p^m}{\sum_{p=1}^{Np} S(x_p - x_i, y_p - y_j)}, \tag{7.92}$$

where Np is the total number of particles and $S(x, y)$ a bilinear weighting function given by,

$$S(x - x_i, y - y_i) = \begin{cases} (1 - \left|\frac{x-x_i}{\Delta x}\right|)(1 - \left|\frac{y-y_i}{\Delta y}\right|) & \text{if } 0 \leq \left|\frac{x-x_i}{\Delta x}\right|, \left|\frac{y-y_i}{\Delta y}\right| \leq 1, \\ 0 \qquad \text{otherwise.} \end{cases}$$

Also, note that by definition,

$$\sum_{m=1}^{M} C_{ij}^m = 1. \tag{7.93}$$

Although C_{ij}^m is found by summing over all particles in the domain (see Eq. (7.92)), only those within a square of area $4\Delta x \Delta y$ contribute to determine the average colour function at GLL node (i, j). The average colour function will be weighted towards the colour function (Eqn. (7.89)) of the majority of particles which are in close proximity to point (i, j). Consequently, by Eqn. (7.91), the material constants will be weighted toward those of the dominant fluid about (i, j). Of course this is important only in regions near the interface where two distinct fluid types are present. Within the bulk of fluid $m = 1$ say, $C_p^1 = 1$, while $C_p^2 = 0$ for all particles p near (i, j). So $C_{ij}^1 = 1$ and $C_{ij}^2 = 0$ and hence $\phi_{ij} = \sum_{m=1}^{2} \phi^m C_{ij}^m = \phi^1$.

We have some choice in specifying the size of the search square $4\Delta x \Delta y$. For regular finite difference meshes, Δx, Δy are taken to be the regular grid spacings. However, the GLL points are unequally spaced. Consequently it seems prudent to leave the size of the search square as an independent parameter, which can be altered to suit the problem at hand, under the restriction that

$$\min(\Delta\xi_i) \leq \Delta x, \Delta y \leq \max(\Delta\xi_i), \tag{7.94}$$

where $\Delta\xi_i = |\xi_{i+1} - \xi_i|$, $i = 0, ..., N-1$, is the spacing between consecutive GLL points. In most instances, setting the search lengths Δx, Δy to be an average of the $\Delta\xi_i$, gives very reasonable results.

Particle boundary conditions

It may be the case that particles near the boundary in the current time step, may step outside the boundary in the next. To remedy this the particles are simply reflected back into the domain by the amount at which they exceed it. This exact approach is used by Bierbrauer and Zhu [14] in their finite difference study.

7.4 Validation

7.4.1 Marker Particle Test Solutions

In this section the marker particle scheme will be validated through the employment of some standard interface tracking tests. In particular, the simple rotation, the time reversed vortex, and the Zalesak slotted disk rotation test will be considered. In each test, an initially circular body of fluid type 1 is surrounded by a fluid of type 2, within a domain Ω. The identity of each fluid can be determined by its constituent marker particles according to definition (7.89). The fluid is advected by some analytical velocity field before returning to its initial position. Error measurements are made on differences in data between the initial and final states. Specifically we measure the L_1 error in the initial and final interpolated colour functions,

$$E_C = \int_\Omega |C^1_{ij}(T) - C^1_{ij}(0)| \, d\Omega \tag{7.95}$$

and the error in the mass of fluid 1,

$$E_M = |M_{exact} - M_{numerical}| \tag{7.96}$$

where

$$M_{numerical} = \int_\Omega C^1_{ij} \, d\Omega. \tag{7.97}$$

The exact mass is known from the analytical initial conditions: for example, $M_{exact} = \pi r^2$, where r is the radius of a circle of fluid 1. We also monitor the size of the transition region between fluids 1 and 2. Ideally this transition region should be as small as possible, and remain so, in order to resemble the discontinuous boundary between two fluid phases. A transition function ΔT_{ij} is defined such that,

	Mesh				MP Density	E_C	E_M	Max A_{tr}
	No of GLL points	$(\hat{\alpha}+1)$	$(\hat{\beta}+1)$	N	(particles/unit area)			
1.	101^2	10	10	10	101^2	6.23×10^{-4}	2.23×10^{-4}	1.50×10^{-2}
2.					201^2	6.33×10^{-4}	2.13×10^{-4}	2.02×10^{-2}
3.					301^2	6.23×10^{-4}	1.38×10^{-4}	2.25×10^{-2}
4.					601^2	6.43×10^{-4}	4.51×10^{-5}	2.35×10^{-2}
5.		20	20	5	301^2	6.47×10^{-4}	1.18×10^{-4}	2.22×10^{-2}
6.		5	5	20	301^2	6.14×10^{-4}	1.28×10^{-4}	2.17×10^{-2}
7.	201^2	10	10	20	201^2	6.42×10^{-4}	2.16×10^{-4}	7.05×10^{-3}
8.					601^2	6.34×10^{-4}	8.19×10^{-6}	1.09×10^{-2}

Table 7.1: Errors between initial and final states for the simple rotation problem.

$$\Delta T_{ij} = \begin{cases} 1 & \text{if } 0 < C_{ij} < 1 \\ 0 & \text{otherwise} \end{cases}$$

A measure of the area of the transition region at a point in time can then be found from

$$A_{tr} = \int_{\Omega} \Delta T_{ij} \, d\Omega. \tag{7.98}$$

Note that this by no means gives an accurate measure of the interfacial area, but provides an indication of its size and any variation thereof.

Simple rotation

An initially circular body of fluid 1, radius $r = 0.15$, is ensconced in fluid 2, within domain $\Omega = [0, 1]^2$. Both fluids are advected according to velocity field

$$u = -2\pi(y - 0.5), \tag{7.99}$$

$$v = 2\pi(x - 0.5), \tag{7.100}$$

causing all fluid elements to rotate about the point (0.5,0.5). The body will undergo a single rotation in 1 time unit, without changing shape. The initial interpolated colour function is shown in Figure 7.4.

The problem is studied for several different Gauss-Lobatto meshes and marker particle densities. The meshes are regular, containing equally sized spectral elements, and are defined by the number of elements $\hat{\alpha}+1$ and $\hat{\beta}+1$ in the x and y directions respectively, and the polynomial order N. Table 7.1 presents the meshes and the associated errors.

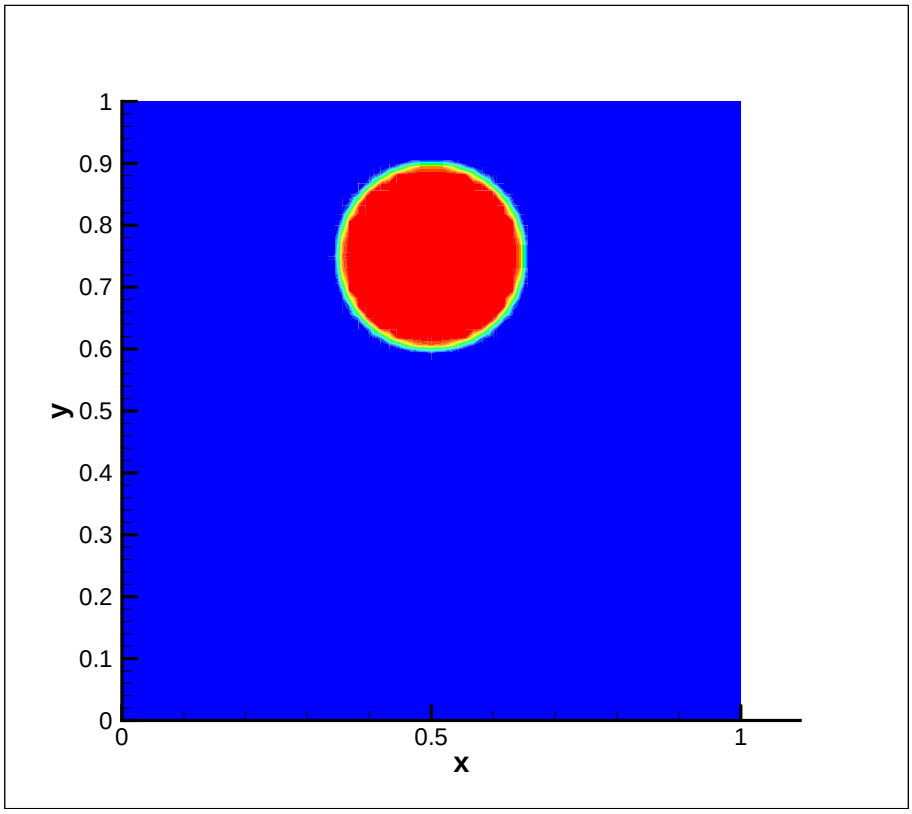

Figure 7.4: The initial colour function for the simple rotation and vortex test problems.

Importantly note the independence of the error in the colour function E_C from the mesh and marker particle density. This demonstrates perhaps the most alluring feature of the marker particle method. That once interpolation error from the particles to grid has been removed, numerical diffusion of the colour function is minimal as a fixed number of particles will carry the fluid information indefinitely. The primary source of error in E_C comes from the time stepping scheme used in updating each particle, which in this case is a second order trapezium rule with $\Delta t = 1 \times 10^{-2}$. This is corroborated by decreasing the time step to $\Delta t = 1 \times 10^{-3}$, in which case the error, E_C, for mesh 3 reduces to 6.23×10^{-6}. E_M provides an indication of the interpolation error from particle to grid, as we compare an interpolated mass, with the analytical $M_{analytical} = \pi r^2$. For mesh 1, increasing the density of marker particles results in increasingly accurate approximations to the mass. Refining the grid allows a more refined interface and a smaller transition region between the two fluids. However, to have accompanying improvements in E_M requires a corresponding increase in the particle density to ensure enough particle information is read in over the refined interpolation region. The maximum measure of the transition area A_{tr} is suitably small, with no

Mesh			MP Density	E_C	E_M	Max A_{tr}
$(\hat{\alpha}+1)$	$(\hat{\beta}+1)$	N	(particles/unit area)			
10	10	10	301^2	3.29×10^{-5}	2.22×10^{-4}	1.25×10^{-1}

Table 7.2: Errors between initial and final states for the time reversed vortex problem.

significant dependence on the choice of mesh. Increasing the marker particle density results in a very slight increase in the transition area as regions near the interface are more likely to contain particle contributions from another fluid (and so $\Delta T_{ij} = 1$). Expectedly, refining the grid results in a smaller transition area as the interpolation area decreases with the average grid spacing. Note that for all the above error measures, varying the number of spectral elements and polynomial order while keeping the total number of GLL points constant, does not have a significant effect.

Time reversed vortex

Using identical initial conditions to the simple rotation (see Fig. 7.4), the fluid is now distorted according to the vortex flow

$$u = -\sin(2\pi y)\sin^2(\pi x), \tag{7.101}$$

$$v = \sin(2\pi x)\sin^2(\pi y). \tag{7.102}$$

This is a far more stringent test, with significant stretching and deformation of the fluid. By multiplying the above velocity field by $\cos(\pi t/T_f)$, the flow will reverse at time $t = T_f/2$ and return to its initial position at $t = T_f$. Figure 7.5 shows the deformed fluid at $t = T_f/2$, where the final time $T_f = 8.0$.

Table 7.2 shows the errors associated with the flow for a single mesh. Once again, despite the severity of the flow, we note that the error in the initial and final solutions E_C, and in the mass E_M, remain very small. The transition area shows a marked increase in this test, which is to be expected given the strong deformation and stretching of the diffuse interface. Once again these errors compare well to other marker particle studies [12, 128].

In particular, note the error E_C^* in the scheme compared to other algorithms at similar mesh refinements (see Table 7.3). Error E_C^* is defined as E_C, but includes the interpolation error from an initial "exact" colour function. The scheme performs favourably,

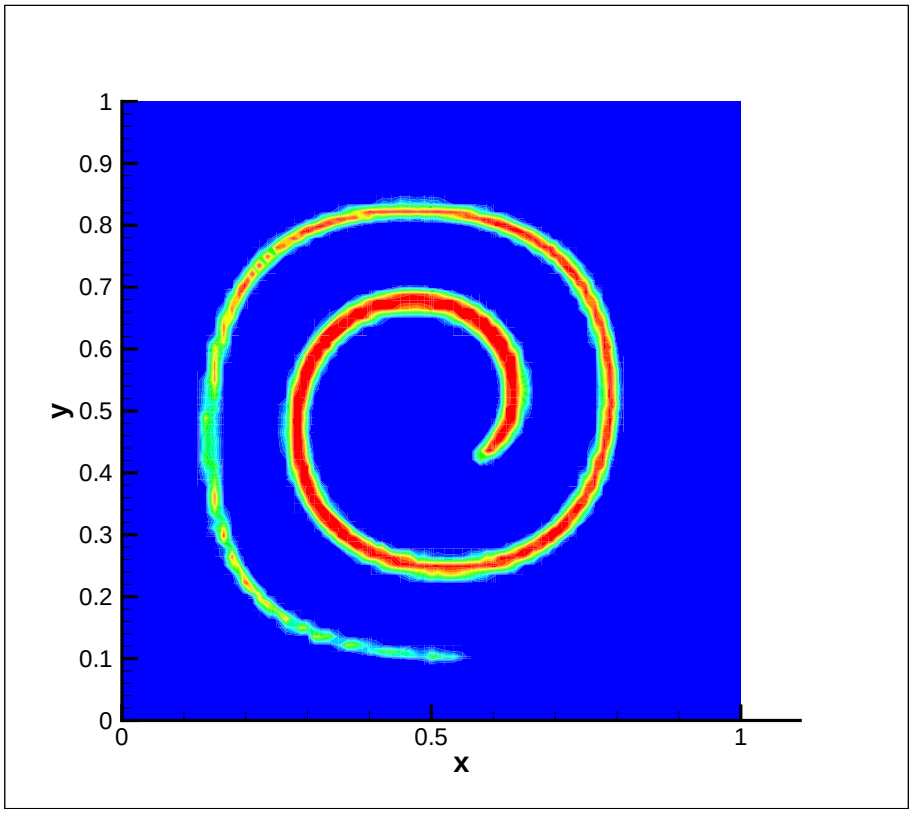

Figure 7.5: The colour function for the time reversed vortex problem at $t = T_f/2 = 4.0$.

with an error of a similar magnitude to other schemes. However, in subtracting the initial error we recognise the scheme's superior conservation properties. The remaining error E_C, which arises from the advection of the colour function between the initial and final states, is very small $E_C = 3.08 \times 10^{-5}$. This again demonstrates, interpolation aside, that numerical diffusion of the colour function over time is minimal, even under such a stringent test.

Zalesak slotted disk rotation

In this test a slotted disk is revolved once around the centre of the computational domain with a constant angular velocity, as in the simple rotation. The disk is of radius 0.5, with the rectangular slot having dimensions (0.12×0.6). The initial set up is given in Fig 7.6.

For comparison with previous studies, an additional measure of the error in the colour function is made,

Method	E_C^*
Rider and Kothe [130]	1.44×10^{-3}
EMFPA/Youngs [98]	2.13×10^{-3}
Adaptive triangular grid [168]	5.09×10^{-4}
THINC/WLIC [169]	2.75×10^{-3}
Present study	2.34×10^{-3}
Present study (initial error)	2.31×10^{-3}

Table 7.3: Error E_C^* (E_C including initial interpolation error) in colour function for time reverse vortex $T_f = 8.0$. In each case grid sizes are 128×128.

Mesh			MP Density	E_C	E_M	Max A_{tr}
$(\hat{\alpha}+1)$	$(\hat{\beta}+1)$	N	(particles/unit area)			
10	10	20	601^2	8.79×10^{-3}	3.16×10^{-4}	1.97×10^{-1}

Table 7.4: Errors between initial and final states for the Zalesak slotted disk rotation problem.

$$E_Z = \frac{\sum_\Omega |C_{ij} - C_{ij}^{exact}|}{\sum_\Omega C_{ij}^{exact}}. \tag{7.103}$$

Here C_{ij}^{exact} is the exact colour function at the nodal points (i, j), i.e. there is no interpolation over the boundary of the two phases. Hence, as well as the error arising from advection of the particles, E_Z contains the error associated with the interpolation from the particles to grid. The computation is also done on a more refined grid with 201^2 GLL points and 601^2 marker particles being used. The errors for this test are given in Table 7.4.

Once again, the marker particle scheme performs well with the error in the colour function E_C and mass E_M suitably small. The maximum transition area is somewhat larger than the rotating disk study, but only because the area of the slotted disk in this case is larger (the radius here is 0.5 compared to 0.15). Table 7.5 shows the error in the colour function E_Z compared with other studies in the literature at similar mesh refinements. Clearly the scheme compares favourably with the other methods, and particularly well when the initial interpolation error is subtracted. Again this emphasises a defining property of the marker particle method. While interpolation can introduce a significant source of error (which will indeed be present in all diffuse interface methods), subsequent error in the colour function is minimal.

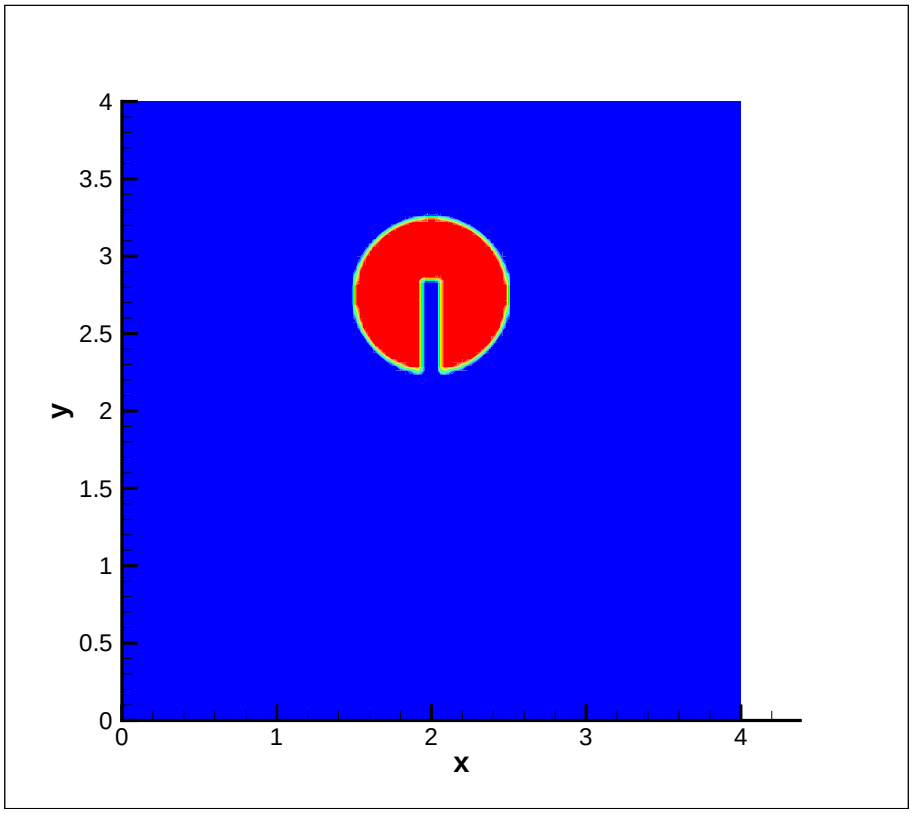

Figure 7.6: The initial colour function for the Zalesak slotted disk rotation problem.

7.4.2 Transient Poiseuille Flow of a near-incompressible Newtonian Fluid

To test the validity of the numerical solution of the governing equations, the velocity field is first compared with the analytical velocity for start up of Newtonian Poiseuille flow (in the near-incompressible limit). The analytical solution for an incompressible fluid viz.

$$u = -4y(y-1) - 32\sum_{n=1}^{\infty} \frac{\sin(ny/H)}{n^3} \exp(-n^2\mu_s t/H^2) \tag{7.104}$$

is prescribed at the inflow and outflow. Test points are chosen in the centre of the domain, where we compare the numerical and analytical velocity field, and on the boundary $y = 0$ where the error in the steady state stress is measured. The only non-trivial component of the stress is the shear stress

$$T_{xy} = \mu_s \frac{\partial u}{\partial y} = \mu_s(4 - 8y). \tag{7.105}$$

Method	E_Z
SLIC VOF [108]	8.38×10^{-2}
Hirt-Nichols VOF [67]	9.62×10^{-2}
Adaptive triangular grid [168]	1.25×10^{-2}
THINC/WLIC [169]	2.46×10^{-2}
Present study	4.87×10^{-2}
Present study (initial error)	4.69×10^{-2}

Table 7.5: Error E_Z for the Zalesak disk test for different multi-phase algorithms.

Figure 7.7 shows the numerical solution u at the test point $(0.5, 0.5)$ for a selection of (solvent) viscosities. In this case $\Omega = [0, 1]^2$ and is partitioned into four equally sized spectral elements with α,$\beta = 1$ and $N = 6$. The time step is $\Delta t = 1 \times 10^{-2}$. The time averaged error in the velocity, calculated using

$$E_u = \frac{\int |u_{analytical} - u_{numerical}| \, dt}{T_f}, \tag{7.106}$$

and the relative error in the stress E_T, are given in Table 7.6.

μ_s	E_u	E_T
0.1	4.26×10^{-5}	6.08×10^{-5}
0.5	1.00×10^{-4}	5.35×10^{-4}
1.0	1.78×10^{-4}	1.07×10^{-3}

Table 7.6: Errors for Newtonian Poiseuille Flow for a selection of viscosities.

It is interesting to note the relationship between the channel length L and the compressibility of the fluid. Consider the case $c^2 = 1 \times 10^3$, $\mu_s = 0.5$ with a longer channel length of $L = 10$. We see a significant difference in the numerical and analytical velocity at the domain centre (Fig. 7.8). The initial increase in the velocity from zero is delayed and then exhibits an overshoot of about 0.1, before oscillating down to the steady state value. This suggests that the value of c is not large enough to approximate an incompressible fluid in this extended geometry. What is being observed is the transient Poiseuille flow of a *compressible* Newtonian fluid. A truly incompressible fluid transmits information instantaneously, whereas a compressible fluid does so at some finite speed. In the shortened geometry, the speed of sound was sufficiently large in approximating the instantaneous transmission of the boundary conditions to the centre of the domain, and subsequently good agreement was obtained with the analyt-

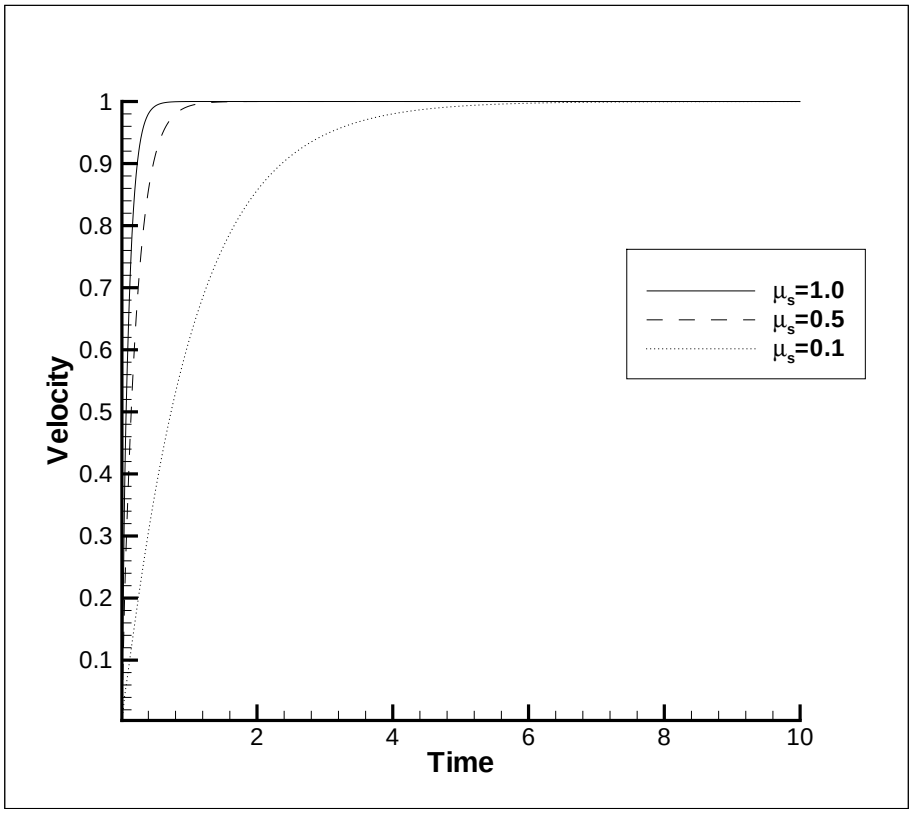

Figure 7.7: Numerical approximation of horizontal velocity component $u(0.5, 0.5, t)$ with time for Poiseuille flow. Here $c^2 = 1 \times 10^3$ and the channel length is $L = 1$.

ical incompressible solution. By lengthening the domain the effect of compressibility becomes apparent as the time to transmit information to the centre of the domain increases. This explains the time lag observed in the initial increase in the numerical velocity. As can be seen from Fig. 7.8, by increasing the speed of sound, the numerical compressible solutions converge toward the incompressible analytical solution, allowing one to recapture the incompressible solution in this longer channel.

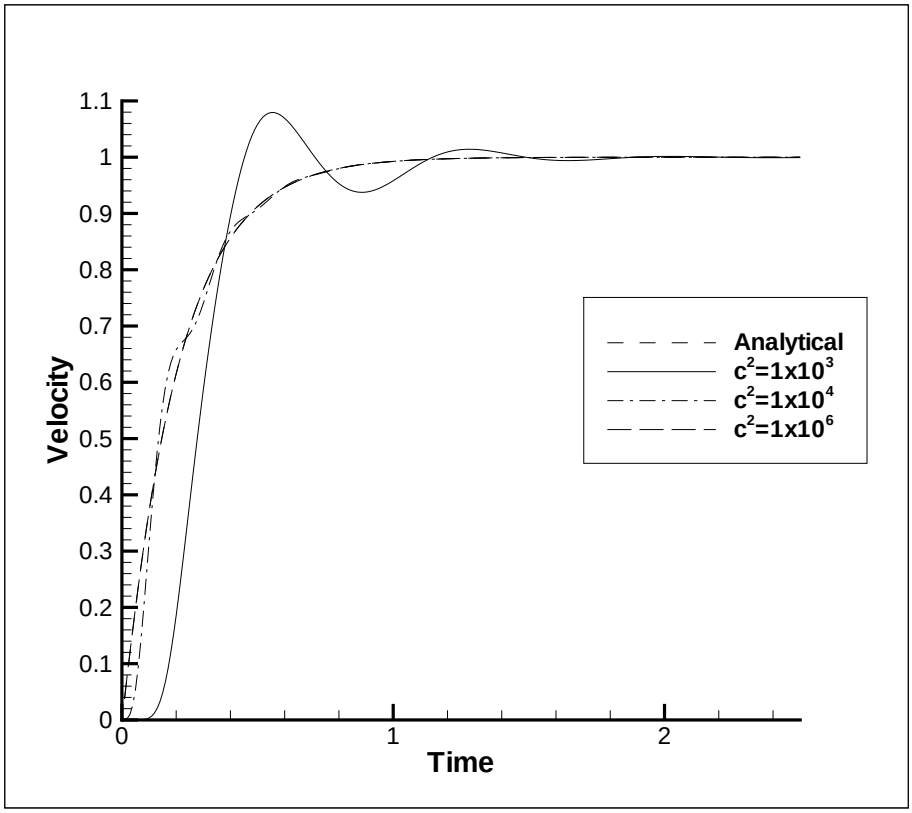

Figure 7.8: Incompressible analytical and compressible numerical solutions for velocity u for transient Poiseuille flow. By increasing the speed of sound the compressible solutions tend towards the incompressible solution. The channel length in this case is $L = 10$.

7.4.3 Transient Poiseuille Flow of a near-incompressible Oldroyd B fluid

The implementation of the Oldroyd B model, with the two temporal discretisations, will now be compared with the analytical solution for transient Poiseuille flow. The analytical solution for start-up transient Poiseuille flow of an incompressible Oldroyd B fluid was derived by Waters and King [162] for $Re \neq 0$. The non-trivial velocity component u is given by

$$u = -4y(y-1) - 32\sum_{n=1}^{\infty} \frac{\sin(Ny)}{N^3} \exp\left(-\frac{\alpha_N t}{2S_1}\right) G_N(t), \tag{7.107}$$

where $G_N(t)$ is defined as

$$G_N(t) = \cosh\left(\frac{\beta_N t}{2S_1}\right) + \left(\frac{1 + N^2(S_2 - 2S_1)}{\beta_N}\right) \sinh\left(\frac{\beta_N t}{2S_1}\right). \tag{7.108}$$

The remaining parameters are

$$N = (2n-1)\pi, \tag{7.109}$$

$$S_1 = \frac{We}{Re}, \tag{7.110}$$

$$S_2 = \beta S_1, \tag{7.111}$$

$$\alpha_N = 1 + S_2 N^2, \tag{7.112}$$

$$\beta_N = ((1 + S_2 N^2)^2 - 4S_1 N^2)^{1/2}. \tag{7.113}$$

Direct comparisons are made with the study by Van Os and Phillips [157], who employ a spectral element method in their solution of transient viscoelastic flows. Consider a 2×2 $(\alpha, \beta = 1)$ spectral element gird, with $N = 6$. The numerical solution is calculated for $\beta = 1/9$, $We = 1$ and $Re = 1$ for a channel length $L = 16$. Here we choose a large speed of sound ($c^2 = 1 \times 10^6$) to ensure compressibility effects are minimal. The numerical velocity and stress are measured on the penultimate vertical grid line, and compared with the boundary conditions at the inflow. Figure 7.9 shows the velocity and stress components calculated using both temporal discretisation schemes. One can see the divergence in the numerical solution using the second order explicit scheme (scheme A) at around $t \approx 22.0$ time units. The first order implicit scheme (scheme B) on the other hand seems to remain stable indefinitely, with a time averaged error

in the velocity of $E_u = 1.44 \times 10^{-4}$. Such a divergence in the explicit solution was observed by Van Os and Phillips [157], for identical mesh and material parameters, at approximately $t \approx 10.8$ time units. Decreasing the channel length to $L = 8$ (Fig. 7.10) sees the onset of divergence at an earlier stage for the explicit scheme, at $t \approx 3.8$ (Van Os and Phillips [157] observed divergence at $t \approx 4.2$). However, once again the implicit scheme demonstrates superior stability properties, showing no evidence of divergence. The time averaged error in this case is $E_u = 3.92 \times 10^{-4}$. Van Os and Phillips [157] found that keeping the channel length fixed, but increasing the number of streamwise elements, also decreases the time at which the solution diverges (Fig. 7.11). Using a 4×2 ($\alpha = 3, \beta = 1$) mesh with $L = 16$ (Fig. 7.11(a)) we find for the explicit scheme the solution diverges at $t \approx 3.9$, while once again, the implicit scheme remains stable with $E_u = 2.55 \times 10^{-4}$. Only by decreasing the channel length to $L = 8$ (Fig. 7.11(b)) do we see the implicit scheme succumb to numerical instability. The solution diverges at $t \approx 11.6$ for the implicit scheme, while at $t \approx 1.3$ for the explicit (Van Os and Phillips [157] observe divergence at $t \approx 1.0$).

Figures 7.12 and 7.13 display the velocities and stresses for Poiseuille flow for $We = 0.1$ and $We = 10$, respectively. Calculations are performed using the semi-implicit scheme with a single spectral element and $N = 4$. Despite the two orders of magnitude difference in We, the scheme maintains its integrity with the numerical approximation being indistinguishable from the analytical solution.

The implementation of the Oldroyd B constitutive equation has been validated through comparison with the transient analytical solution of Waters and King [162]. Despite being a compressible model, a near incompressible limit can be attained which provides accurate solutions to the incompressible flow. Broadly speaking, the spectral element scheme here exhibits similar stability properties seen in other spectral element studies [52, 157]. Namely, increasing the number of elements in the streamwise direction or shortening the channel length, brings forward the onset of instability. From the above discussion it is clear that the implicit scheme has more favourable stability properties, as well as being remarkably accurate in describing transient viscoelastic flows. It is for these reasons that the implicit scheme shall be used in the forthcoming study of viscoelastic multi-phase flows.

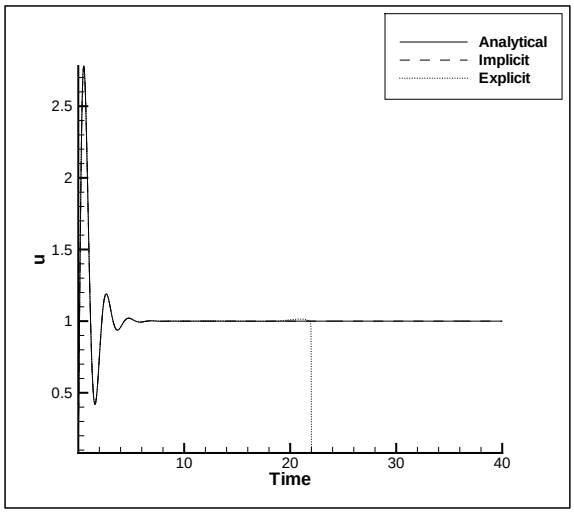

(a) Velocity u.

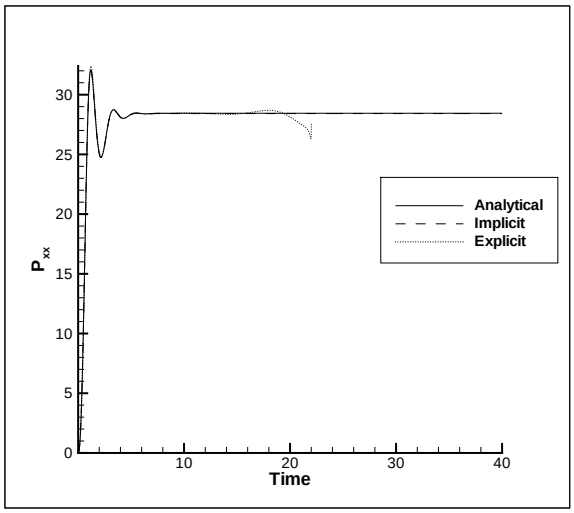

(b) Normal stress component P_{xx}.

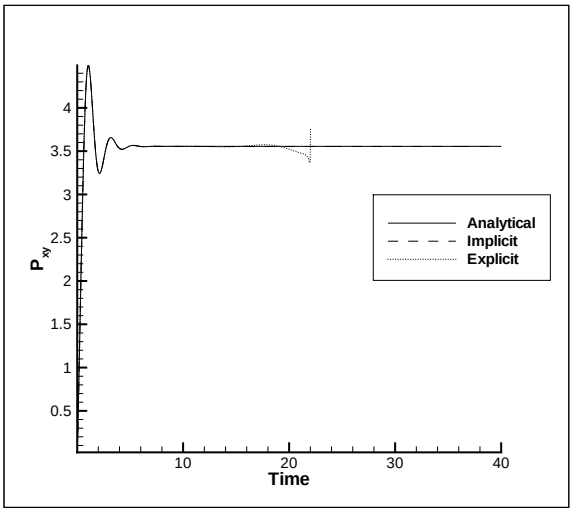

(c) Shear stress component P_{xy}.

Figure 7.9: Analytical and numerical solutions of an Oldroyd B fluid in Poiseuille flow for different numerical schemes. $L = 16$, $We = 1$, $Re = 1$, $\beta = 1/9$. The grid parameters are: $N = 6$, $\alpha = 1$, $\beta = 1$.

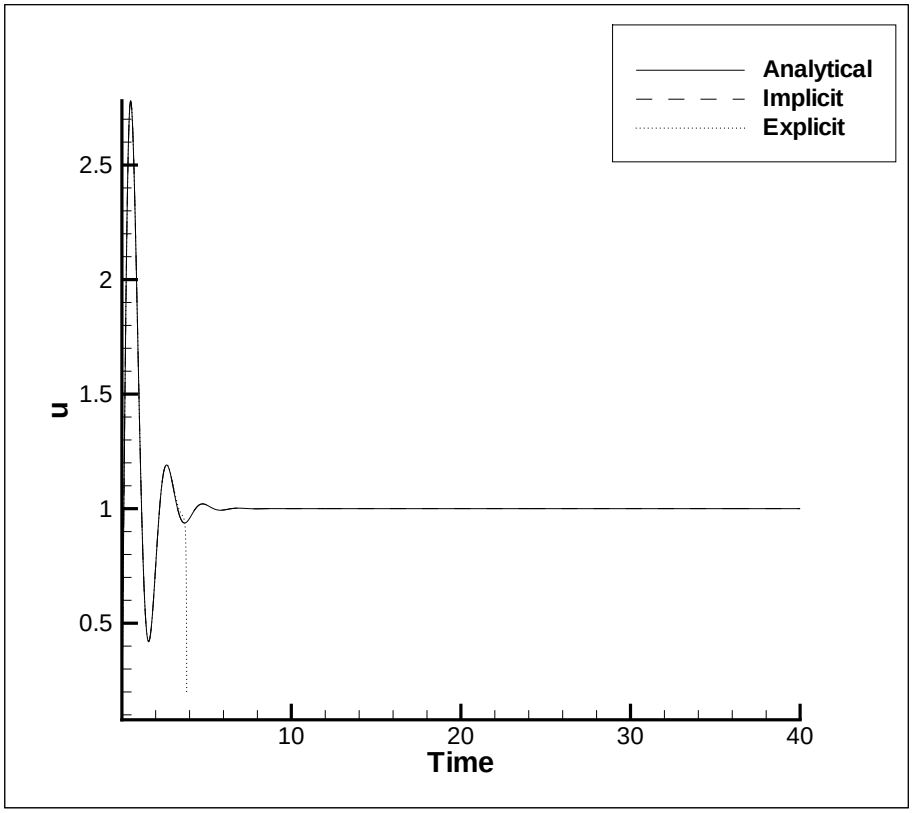

Figure 7.10: Analytical and numerical component of velocity u with time for an Oldroyd B fluid in Poiseuille flow. $L = 8$, $We = 1$, $Re = 1$, $\beta = 1/9$. The grid parameters are: $N = 6$, $\alpha = 1$, $\beta = 1$

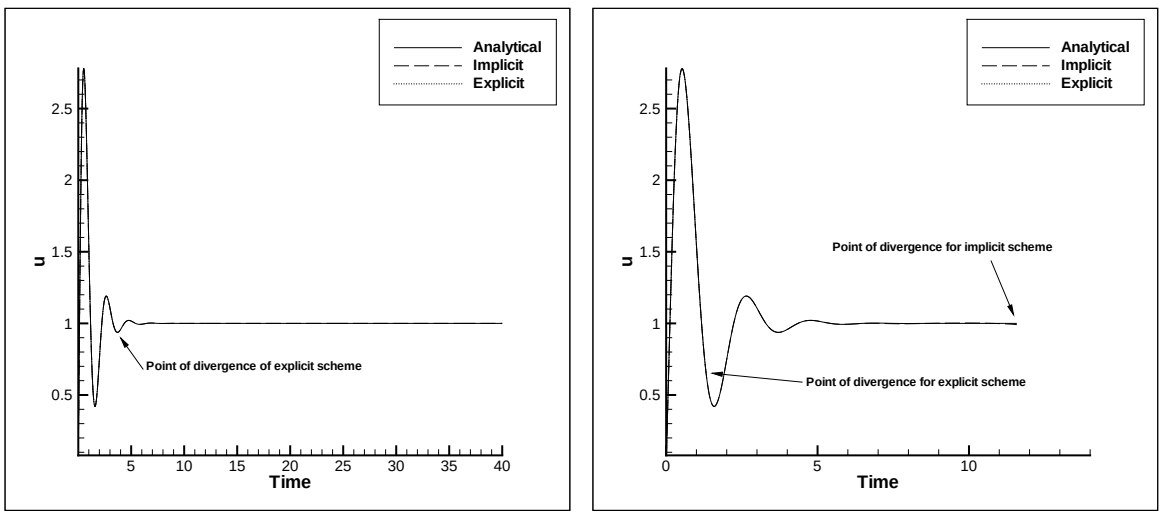

(a) $L = 16$. (b) $L = 8$.

Figure 7.11: Analytical and numerical solutions of an Oldroyd B fluid in Poiseuille flow for different numerical schemes at different channel lengths L, with increased streamwise mesh refinement. The grid parameters are: $N = 6$, $\alpha = 3$, $\beta = 1$.

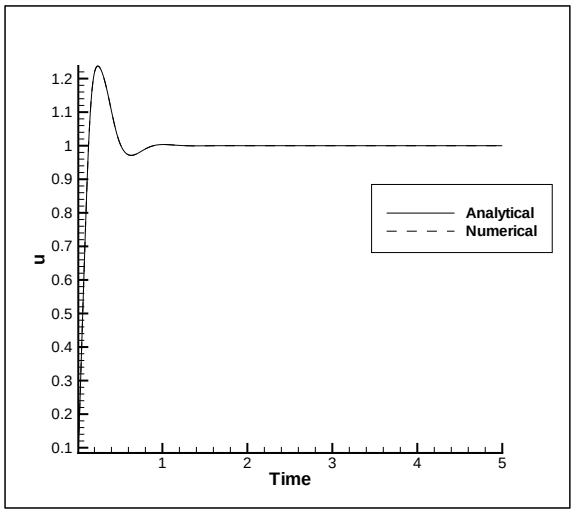

(a) Velocity u.

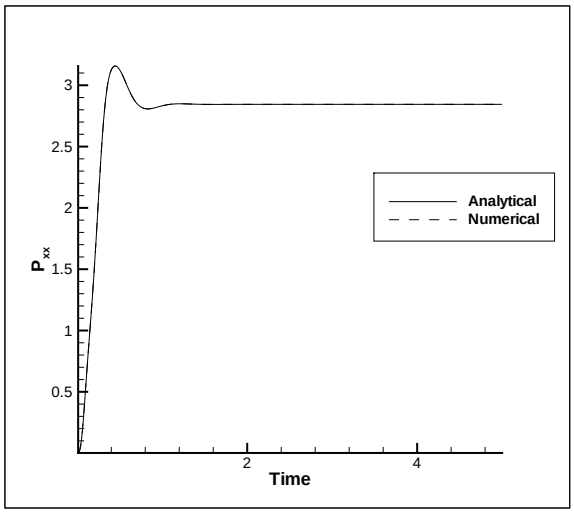

(b) Normal stress component P_{xx}.

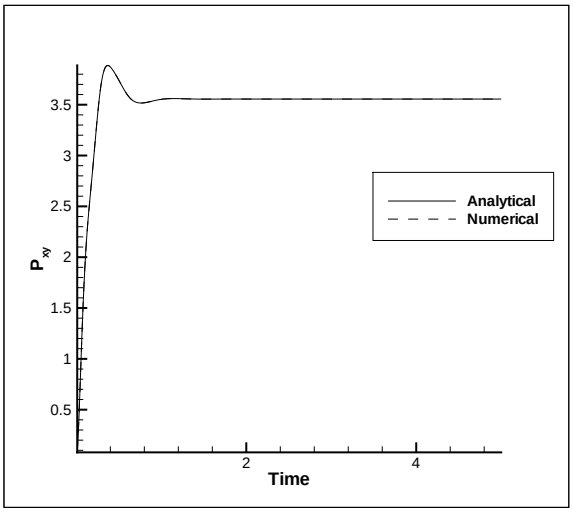

(c) Shear stress component P_{xy}.

Figure 7.12: Analytical and numerical solutions of an Oldroyd B fluid in Poiseuille flow. $L = 16$, $We = 0.1$, $Re = 1$, $\beta = 1/9$. The grid parameters are: $N = 4$, $\alpha = 0$, $\beta = 0$.

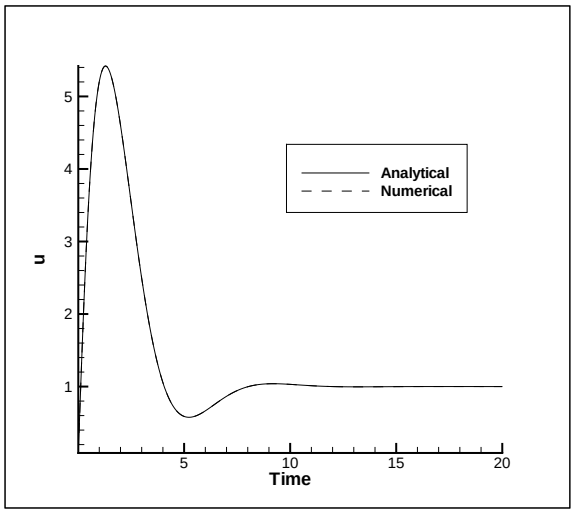

(a) Velocity u.

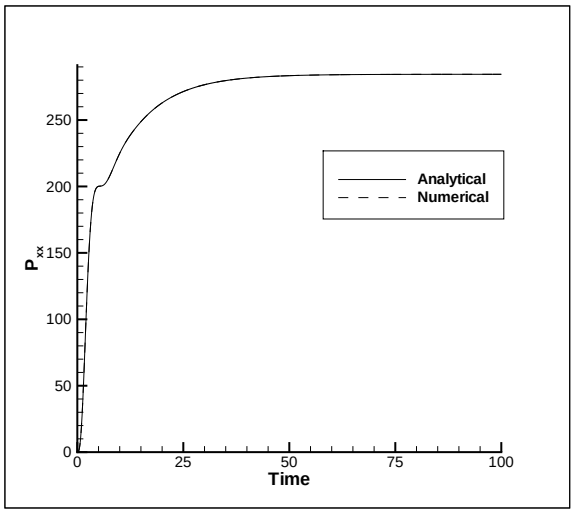

(b) Normal stress component P_{xx}.

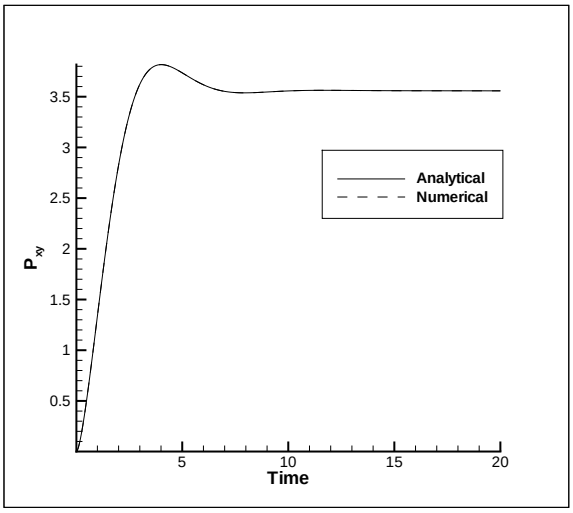

(c) Shear stress component P_{xy}.

Figure 7.13: Analytical and numerical solutions of an Oldroyd B fluid in Poiseuille flow. $L = 16$, $We = 10$, $Re = 1$, $\beta = 1/9$. The grid parameters are: $N = 4$, $\alpha = 0$, $\beta = 0$.

7.5 Numerical Results

7.5.1 Bubble Collapse in a Newtonian Fluid

In this section we present the numerical predictions for bubble collapse near a rigid boundary, within a Newtonian fluid. As described in the introduction, the bubble is initially represented as a circular region with a separate density and viscosity to the ambient fluid. Particles within this region are assigned an identity which they retain indefinitely. Hence the position of the bubble can be tracked by following these particles. We consider the bubble dynamics for a selection of ambient fluid viscosities and heights from the rigid boundary. In all cases, unless otherwise stated, we assume that the bubble contents consist of a compressible Newtonian fluid with viscosity $\mu_s = 1 \times 10^{-5}$ (an order of magnitude similar to air) and initial density $q = 0$. The initial density of the ambient fluid is taken to be $q = \ln 4 \approx 1.386$. Hence the density ρ of the ambient fluid is four times that of the bubble phase. The rigid boundary in question is taken to be the line $y = 0$ in a computational domain $D = [0, 10]^2$. On $y = 0$ and the remaining boundaries the no-slip condition applies. The mesh is refined around the area of interest, namely the bubble, with larger elements fanning outwards to the edges of the computational domain. An example mesh is given in Figure 7.14. Typical mesh parameters are $\alpha = \beta = N = 8$ and the time step used in the simulations is $\Delta t = 5 \times 10^{-3}$.

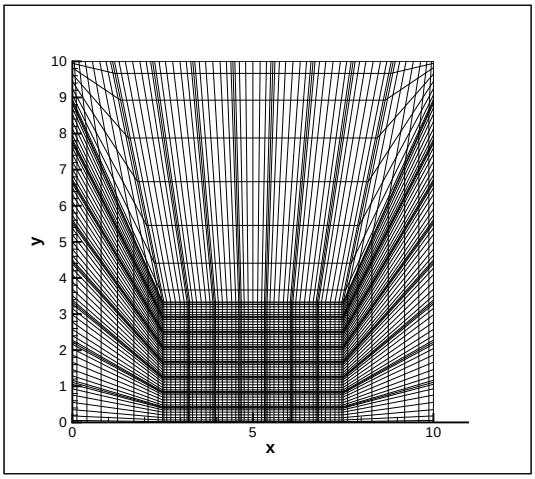

Figure 7.14: An example of the spectral element mesh used in the bubble collapse problems.

We consider first a bubble initially positioned to be just touching the rigid boundary.

Figure 7.15 shows the colour function at a selection of times for an ambient fluid viscosity $\mu_s = 1 \times 10^{-3}$. The initial difference in pressure between the bubble and ambient fluid initiates and drives bubble collapse. During collapse the bubble flattens, with its contents being pushed towards the wall by the greater bulk of fluid above it. As fluid follows most freely along the centre of the domain, a jet of fluid begins to form and then penetrate the body of the bubble. As the jet proceeds towards the wall, the bulk of the bubble is pushed out in either direction. The speed at which collapse occurs is so great that the outer edges of the bubble break up in an effect not dissimilar to "splashing". Splashing has been observed experimentally and predicted numerically, and is caused by the collision of fluid from the jet (travelling outwards from the centre) with the fluid from the oppositely directed ambient flow. Consequently, the fluid (or splash) is projected upwards from the boundary and can cause surface breaking and the formation of smaller cavities [151].

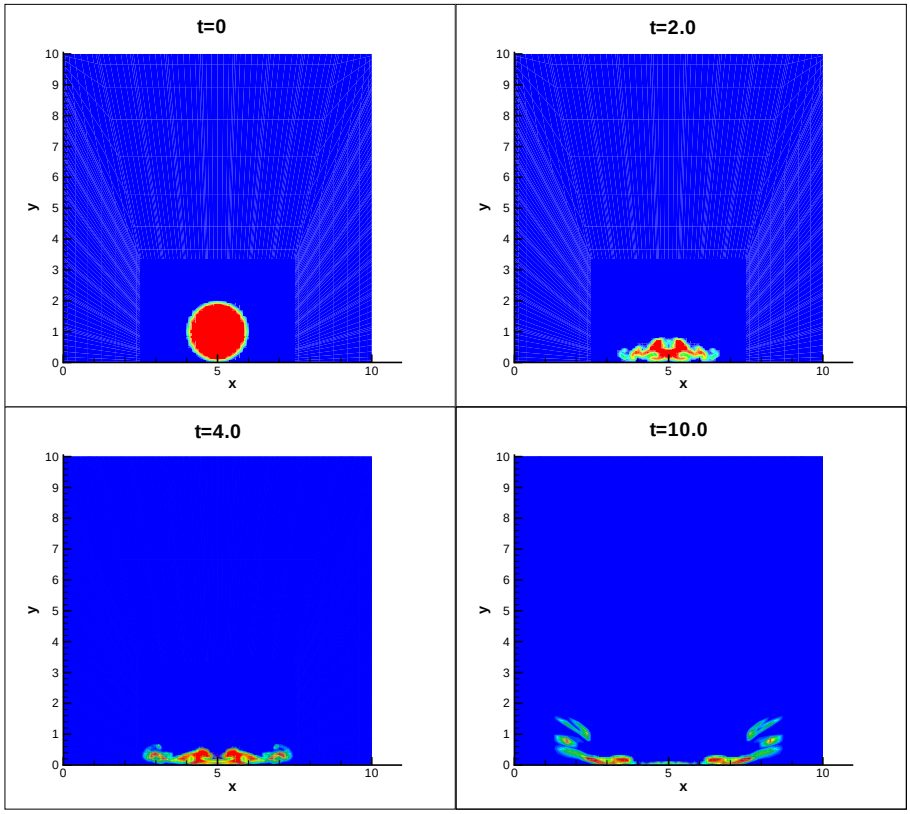

Figure 7.15: Bubble collapse near a wall in a Newtonian fluid with $\mu_s = 1 \times 10^{-3}$.

Evidently, besides predicting the well-known phenomenon of jet formation, phenomena such as splashing and bubble break up can be handled straightforwardly by the method. This is a clear advantage of the marker particle algorithm over the BEM,

where modelling bubble break up requires special treatment. By increasing the viscosity of the ambient fluid we see a similar response to that of our boundary element study. Figure 7.16 shows the colour function for $\mu_s = 1 \times 10^{-2}$. In this case jet formation is not as pronounced, with the top of the bubble being only slightly indented during collapse. However, a jet of sorts still forms, impinging on the boundary and pushing the bubble contents out towards the side walls. Also, bubble break up on the outer fringes is significantly reduced.

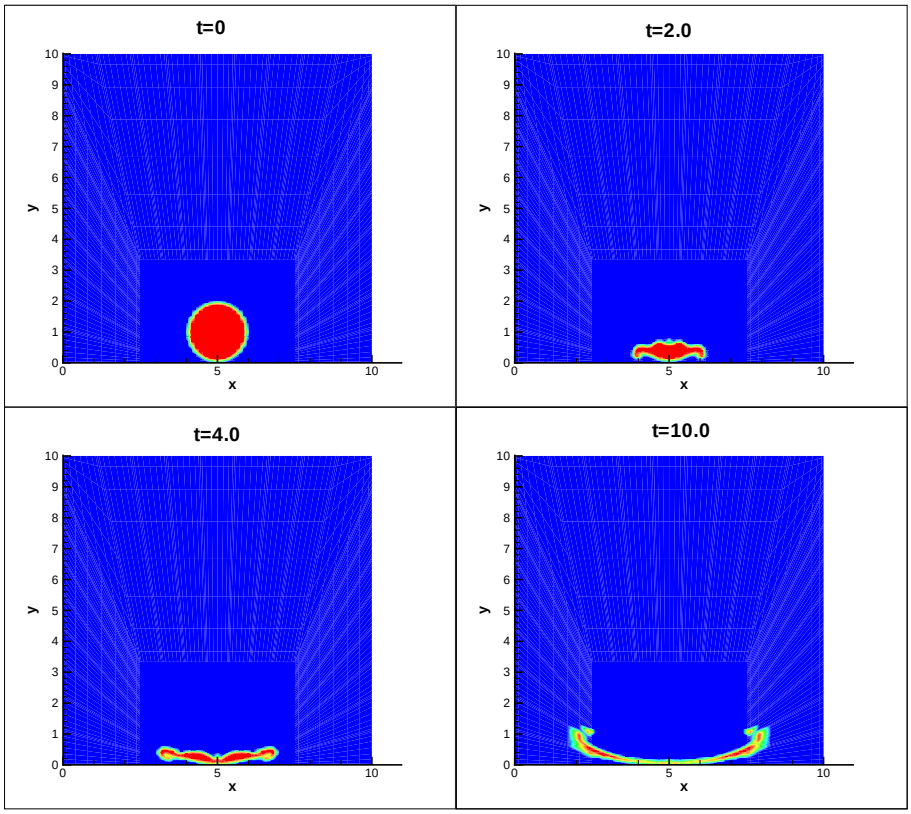

Figure 7.16: Bubble collapse near a wall in a Newtonian fluid with $\mu_s = 1 \times 10^{-2}$.

If the viscosity is increased further to $\mu_s = 0.1$ (Fig. 7.17) we see that jet formation is almost completely suppressed. As the bubble collapses, it deforms into a flattened, bowl like shape with no discernible jet formation. Any further spreading of the bubble and any bubble break up is also prevented.

Increasing the viscosity further to $\mu_s = 1.0$ (Fig. 7.18) we find that, not surprisingly, jet formation is once again prevented, although in this case, the effect of viscosity is so great that deformation in the bubble is minimal and it does not deviate significantly from sphericity. Following an initial decrease in volume, the bubble also quickly settles down into a steady state. Note that the bubble shape is such that the underside is

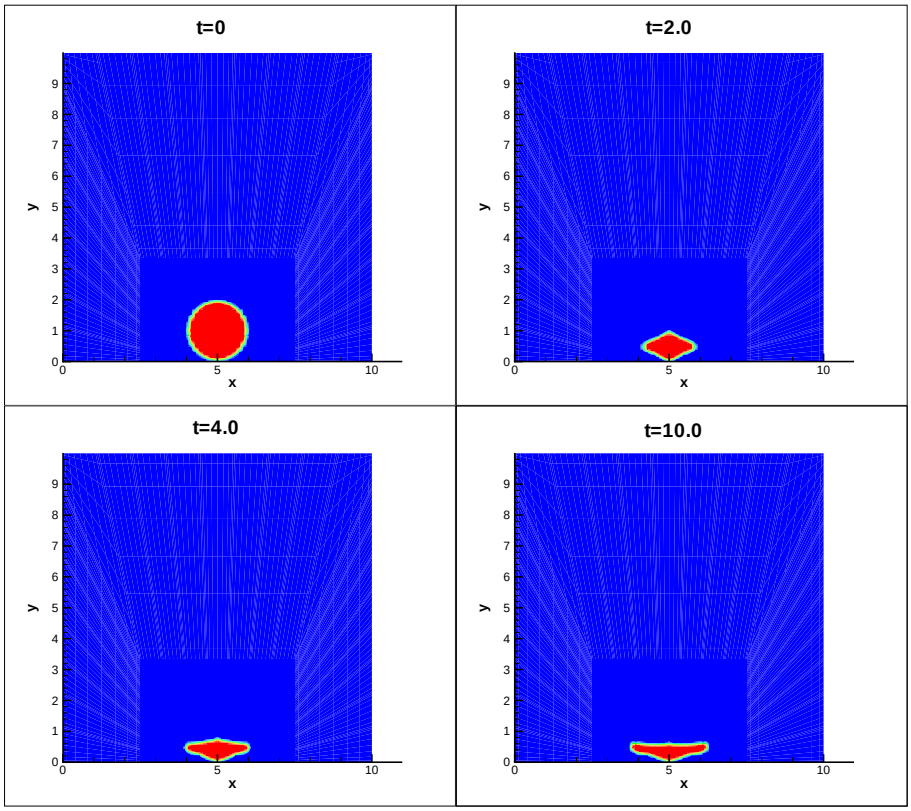

Figure 7.17: Bubble collapse near a wall in a Newtonian fluid with $\mu_s = 0.1$.

drawn inward, producing a more pointed bottom. Comparing this shape to those in Figure 3.10, one can see that these features, including jet prevention, are also predicted by the BEM for significant viscosities.

Figure 7.19 shows the variation of the jet position with time, for the aforementioned viscosities. As before, the jet position is defined as being the material point on the north pole of the bubble, where the jet is expected to form. In the very early stages of collapse, the profiles are indistinguishable as inertia dominates. The bubble collapses rapidly before rebounding due to the compressed fluid content within the bubble. After these initial stages, the effects of viscosity become more apparent. Expectedly, $\mu_s = 1 \times 10^{-3}$ shows the fastest decrease in position, with the jet proceeding toward the wall with the largest velocity. This rate decreases with increasing viscosity, with $\mu_s = 1.0$ attaining a steady state, as the jet position becomes constant and the jet velocity zero. Clearly, increasing viscosity can delay, slow and if large enough, prevent jet formation. This is well-known and has been observed in the previous boundary element study, and in other numerical studies such as that by Popinet and Zaleski [121]. While this behaviour is qualitatively similar to that predicted by the BEM, the jet position profiles are rather

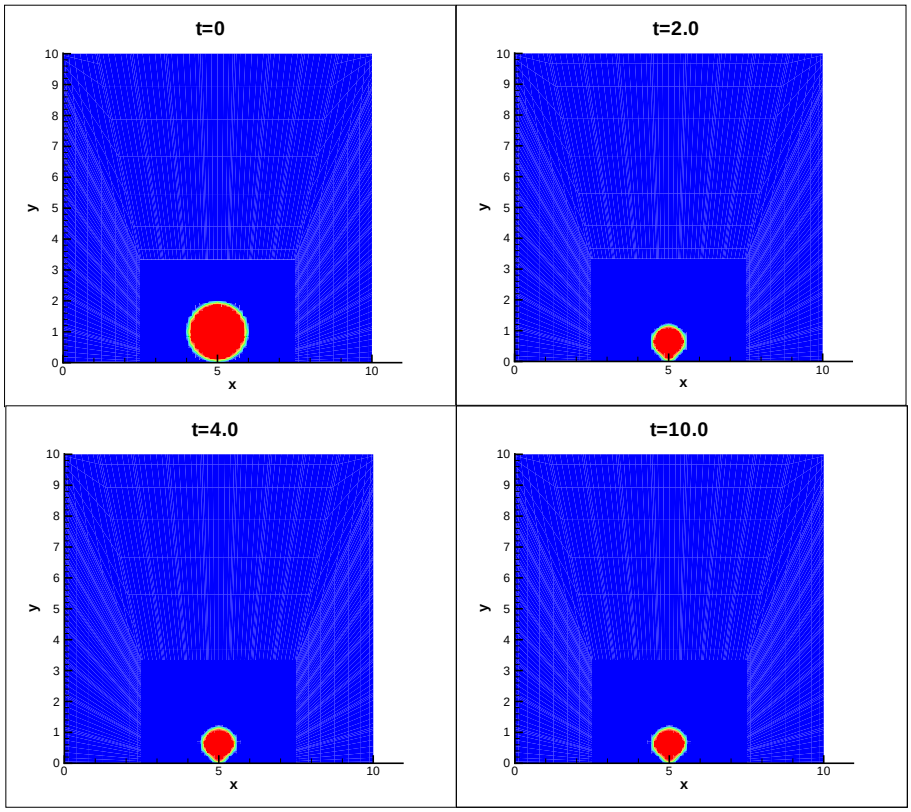

Figure 7.18: Bubble collapse near a wall in a Newtonian fluid with $\mu_s = 1.0$.

different. The liquid jet constantly accelerates during collapse in the previous BEM study, but can decelerate here. The reason for this is that the bubble in the BEM study was modelled as containing a constant pressure p_b. Here, the bubble is modelled as a compressible Newtonian fluid. Hence, as mentioned at the start of the paragraph, the bubble contents act to resist collapse and decelerate the surrounding fluid. The build up in pressure within the bubble can be sufficient to temporarily slow, stop, and even reverse collapse. This also explains the small, low amplitude oscillations in the jet position.

Figure 7.20 shows the variation of jet position with time for $\mu_s = 0.1$, for different mesh refinements. On varying the polynomial order N there is little change in the solution (to within an acceptable tolerance) for $N \geq 6$, suggesting that a choice of $N = 8$ does indeed provide a sufficient level of refinement.

We will now consider the effect of increasing the distance of the bubble from the rigid boundary. Figure 7.21 shows the colour function at different times for an ambient fluid viscosity $\mu_s = 0.1$, a distance $h = 1.1$ from the lower wall. Compared to Fig. 7.17, where the bubble was just attached to the wall, the small increase in distance causes

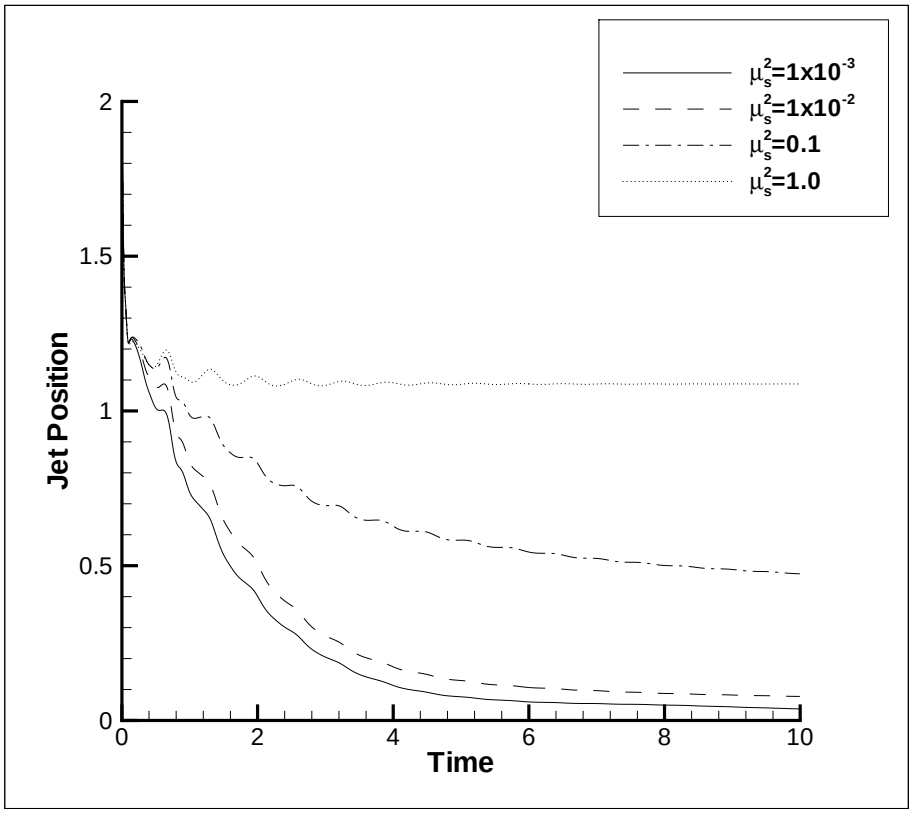

Figure 7.19: Position of jet with time for varying solvent viscosity μ_s.

the bubble shape to change quite substantially. As in the boundary element study (see Figure 3.11 for example), increasing distance from the wall causes a decrease in the deformation of the bubble. Closer to the wall, the bubble is more elongated along the x axis, with the topside more flattened. Increasing the distance to $h = 1.1$, the bubble has now deformed in a similar manner but to a lesser extent. For in the near wall case, fluid flows most easily from above the bubble, causing it to push down upon the bubble and create the more elongated shape and flatten topside. While this flow mechanism is still apparent for $h = 1.1$, it is not to the same extent. Fluid is able to flow more freely from all directions around the bubble, and so collapse is more uniform.

Increasing the distance from the wall further to $h = 2.0$ (Fig. 7.22) we note a further decrease in bubble deformation, as expected. In fact, the distance is such that deformation in the bubble is minimal, with it hardly changing from its initially circular shape. The fluid around the bubble is able to flow more freely from all sides, so the collapse is extremely uniform. This is also predicted in the equivalent Newtonian BEM case; see Figure 3.12. Here though the bubble collapses and decreases in volume, but given the fluid content of the bubble acting to resist collapse, it quickly settles down

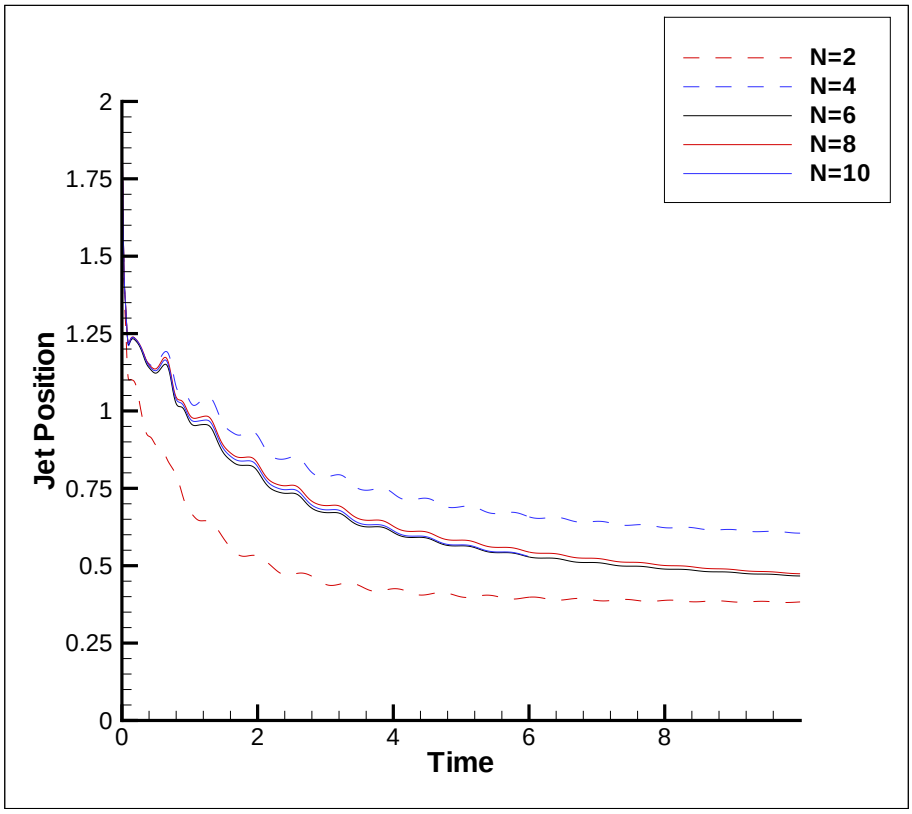

Figure 7.20: Dependence of the position of the jet on mesh refinement for $\mu_s = 0.1$.

to a steady state.

To conclude the discussion on Newtonian dynamics, we reiterate the qualitative agreement in the dynamics observed here, to those predicted by the boundary element study in Chapter 3. Close to the wall deformation in the bubble is severe as fluid flow is restricted near the wall, while unrestricted from above the bubble. In both cases, depending on viscosity, the preferential fluid flow from above can cause the bubble topside to flatten, with the possibility of jet formation. Further from the wall, as the flow around the bubble is more regular, the deformation in the bubble is more uniform, and can in fact remain near sphericity/circularity during collapse. Additionally, both methods predict a decrease in deformation and jet prevention for large enough viscosities.

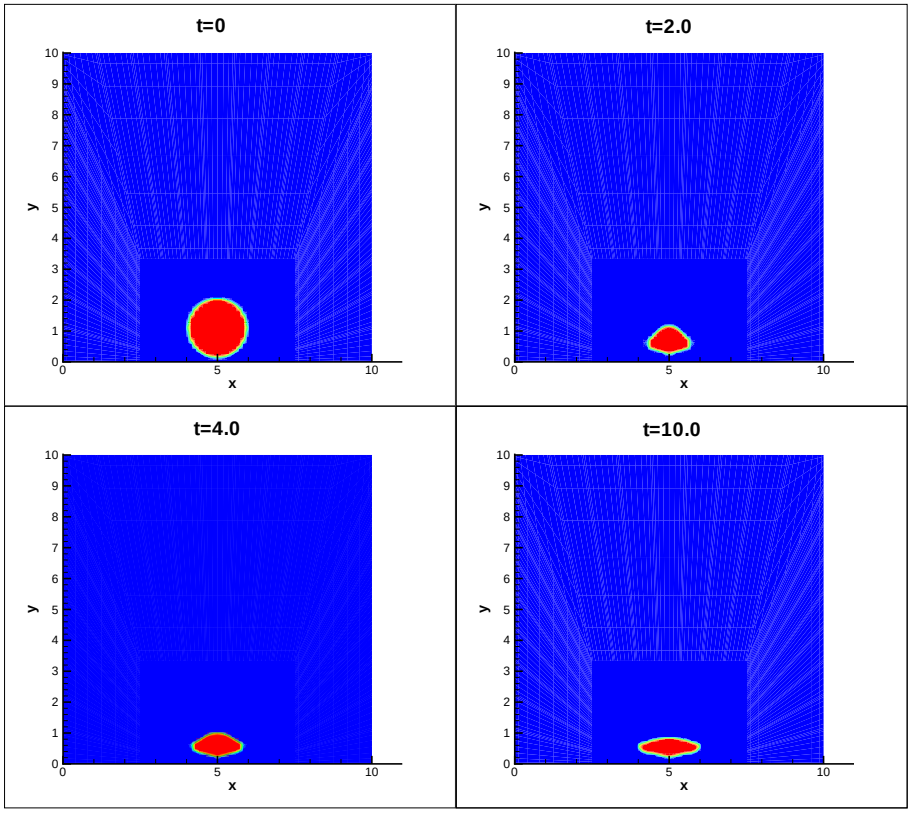

Figure 7.21: A plot of the colour function at different times, representing bubble collapse near a wall in a Newtonian fluid with $\mu_s = 0.1$, $h = 1.1$.

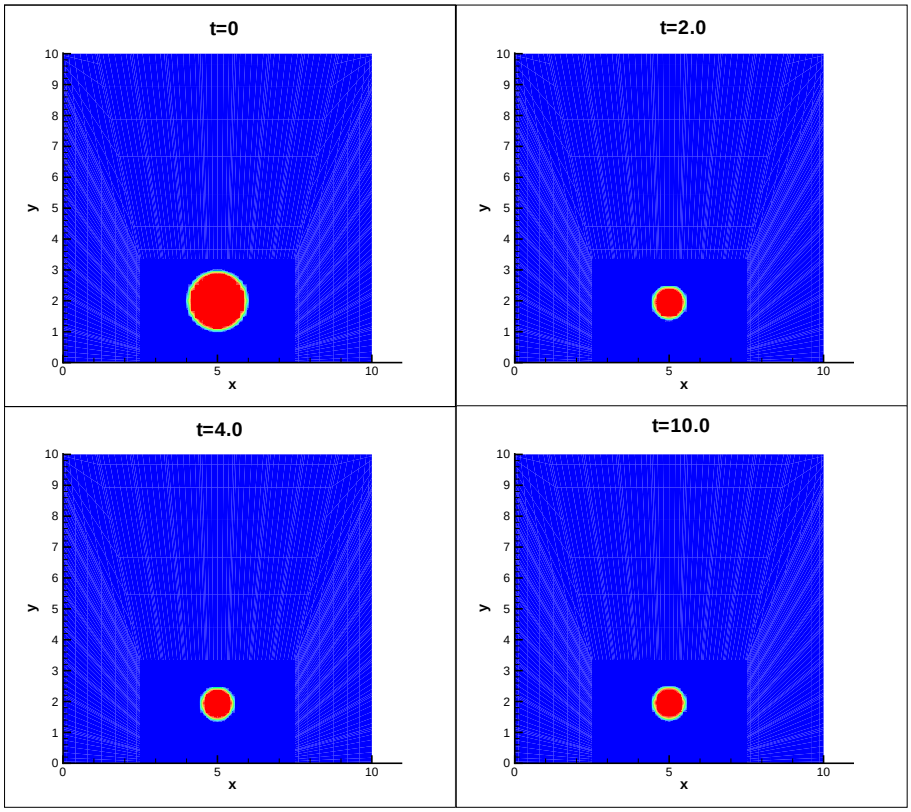

Figure 7.22: A plot of the colour function at different times, representing bubble collapse near a wall in a Newtonian fluid with $\mu_s = 0.1$, $h = 2.0$.

7.5.2 Bubble Collapse in an Upper Convected Maxwell Fluid

In this subsection we investigate the role of viscoelasticity on bubble collapse. The rheological properties of the ambient fluid are determined by the upper convected Maxwell (UCM) constitutive equation. The bubble contents remain Newtonian, with the parameters assigned previously. Figure 7.23 displays the colour function at various points in time, indicating bubble shape during collapse. The Weissenberg number of the ambient fluid is $We = 0.03$ and the polymeric viscosity $\mu_p = 0.1$. The bubble is initially positioned such that $h = 1.1$. Comparing Figure 7.23 with the corresponding Newtonian case (Fig. 7.21), one can see a notable difference in the bubble shapes due to the presence of viscoelasticity. During collapse, the bubble shapes are more prolate than their Newtonian counterparts and also form a marked cusp feature on their underside. Figure 7.24 shows a close up of the bubble for both the viscoelastic and Newtonian cases, at time $t = 0.5$.

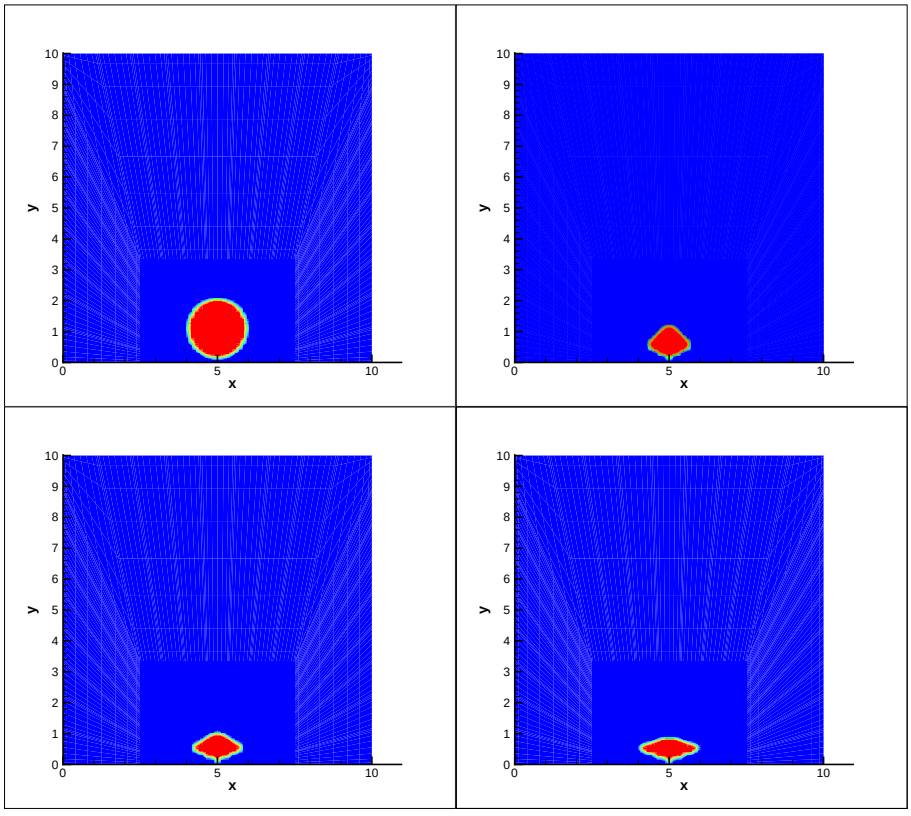

Figure 7.23: A plot of the colour function at different times, representing bubble collapse near a wall in a UCM fluid with $\mu_p = 0.1$, $We = 0.03$, $h = 1.1$.

In the viscoelastic case (on the left), a more elongated and cusped underside is clearly visible, in comparison to the Newtonian case on the right. The cusping and extensive

concavity of the bubble underside, when near the wall, is also predicted by the boundary element method (see Fig. 3.15, for example). It is interesting to note that over the course of this project, cusp formation has been a recurring feature in viscoelastic bubble dynamics.

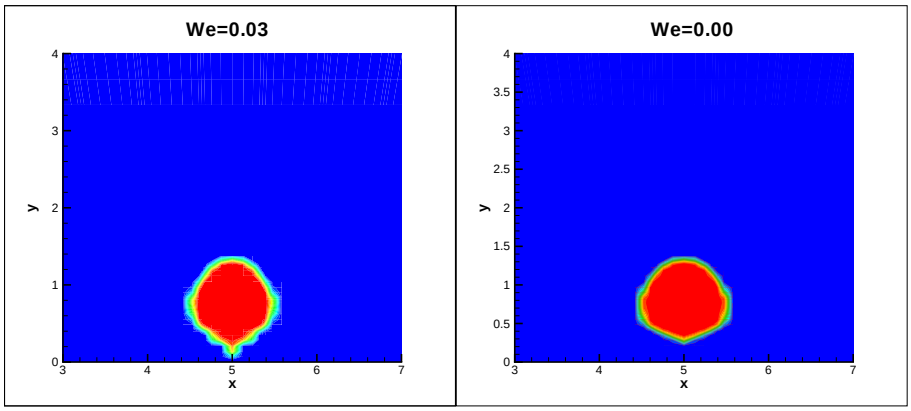

Figure 7.24: A plot of the colour functions in a UCM fluid (left) and Newtonian fluid (right) at time $t = 0.5$.

Evidently, near the wall there is a mechanism encouraging concavity in the bubble surface, which arises from the elastic properties of the surrounding fluid. While this also occurs in the BEM study, the full domain solution here can perhaps afford more insights into cusping mechanisms. A cusp forms when fluid just around the tip flows at a higher velocity than the tip itself, suggesting the presence of an additional stress that "squeezes" the bottom of the bubble from the sides. Figure 7.25 shows the contours of the different components of the extra stress near the wall. In the viscoelastic case, there is an extra stress layer in the T_{xx} component which is absent in the Newtonian case (see Fig. 7.26). This stress layer can become very large, particularly in the initial stages of collapse, where inertia is dominant and thin velocity boundary layers exist on the wall. In fact, this large stress layer can be a major source of numerical instability and the reason that results for Weissenberg numbers greater than $We \approx 0.03$ cannot be obtained in this case. This Weissenberg number limit will be discussed in more detail later. Though this value of Weissenberg number seems rather small, the alternative dimensionless measure of elasticity, the Deborah number $De = \lambda R_0 \left(\triangle p/\rho\right)^{1/2}$, yields an initial value of $De \approx 0.82$. This is a much more satisfactory upper bound and suggests that perhaps De provides a better measure of elastic effects for such problems. By our definition, the Deborah number provides a time scale associated with the flow process, while the Weissenberg number is associated with fluid characteristics. The

reason the Deborah number is not used here is because it is not constant, but varies with bubble density and pressure.

It seems that this build up of an elastic normal stress, which is directed along the x axis around the underside of the bubble, is the likely reason for cusp formation. The build up of normal stress in the vicinity of the cusp also occurs in the BEM study (see Fig 3.38, for example). Though quite different in structure, it is clear in both cases that additional viscoelastic stresses preferentially develop about the bubble underside. After all, the basic flow structure that exists between the bubble and rigid wall during collapse, should be similar in both cases.

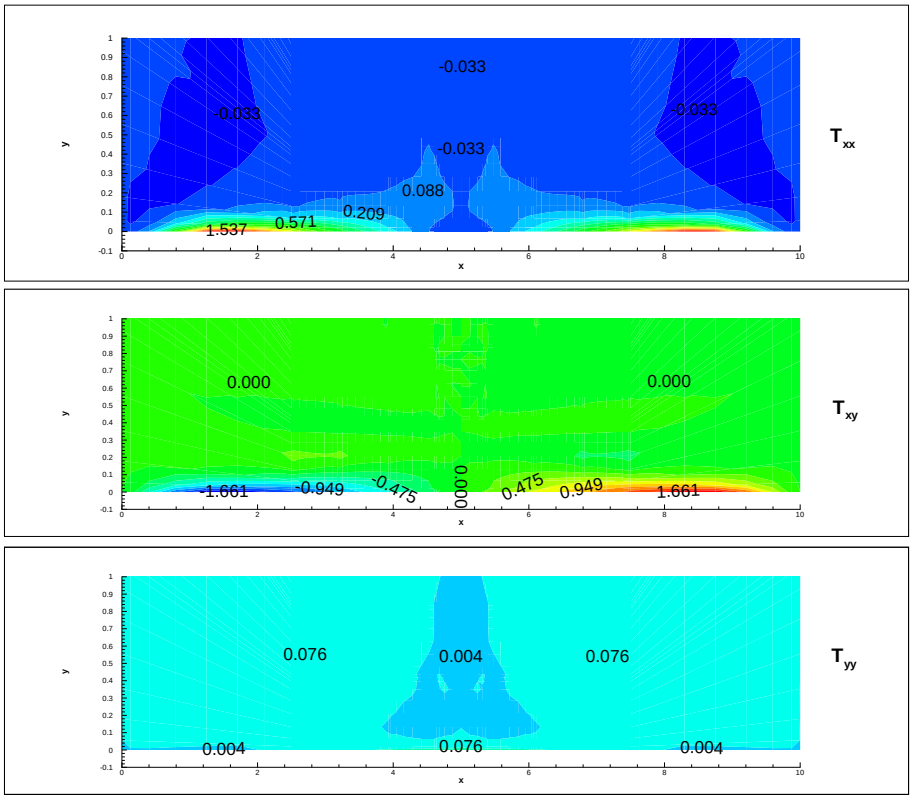

Figure 7.25: Contour plots of the extra stress components near the rigid boundary at time $t = 0.5$. It is a UCM fluid with $\mu_p = 0.1$, $We = 0.03$, $h = 1.1$.

The shear stress T_{xy} contours are similar to the Newtonian case (see Fig. 7.26) in both magnitude and structure, suggesting that T_{xy} plays a minor role in cusp formation. Similarly the normal stress T_{yy}, although different in structure, is small in both cases. Figure 7.27 shows the jet velocities in a Newtonian and UCM fluid. We compare the velocities after the initial collapse and rebound phase, as in this phase inertia dominates and the differences in dynamics are negligible. Even after this stage, the difference in

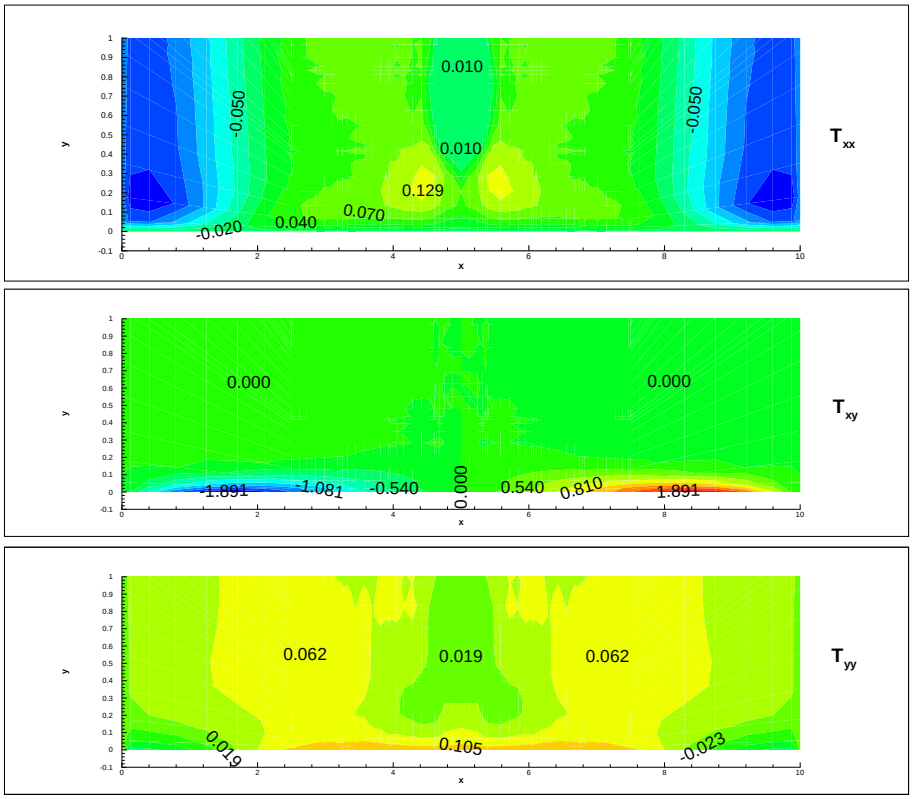

Figure 7.26: Contour plots of the extra stress components near the rigid boundary at time $t = 0.5$. The fluid is Newtonian with $\mu_s = 0.1$, $h = 1.1$.

the jet velocities is small, demonstrating that in this study the bubble content is the principal cause of bubble oscillation. The oscillations in the UCM fluid are fractionally larger in amplitude in most instances - alluding to the ability of the viscoelastic stresses to induce oscillation in the bubble. The combined effect of this and the bubble contents then create oscillations of a slightly larger amplitude. Increased amplitude oscillation with increased Deborah/Weissenberg number is of course a well known characteristic of viscoelastic bubble dynamics, and is predicted by the BEM in the spherical and non-spherical cases studied in the preceding chapters. See, for example, Figure 2.9.

Figure 7.28 shows the colour function at select times when the bubble has been moved from the wall to a distance $h = 2.0$. As in the Newtonian case, deformation in the bubble is markedly reduced and it remains very nearly circular during collapse.

Figure 7.29 shows the bubble jet velocities, after the initial collapse phase, at different distances from the wall. Expectedly, we see that further from the wall the amplitude of the oscillation in jet velocity is larger, because the fluid flow is less restricted and can flow at larger speeds. Increasing jet velocities with distance from the wall was also

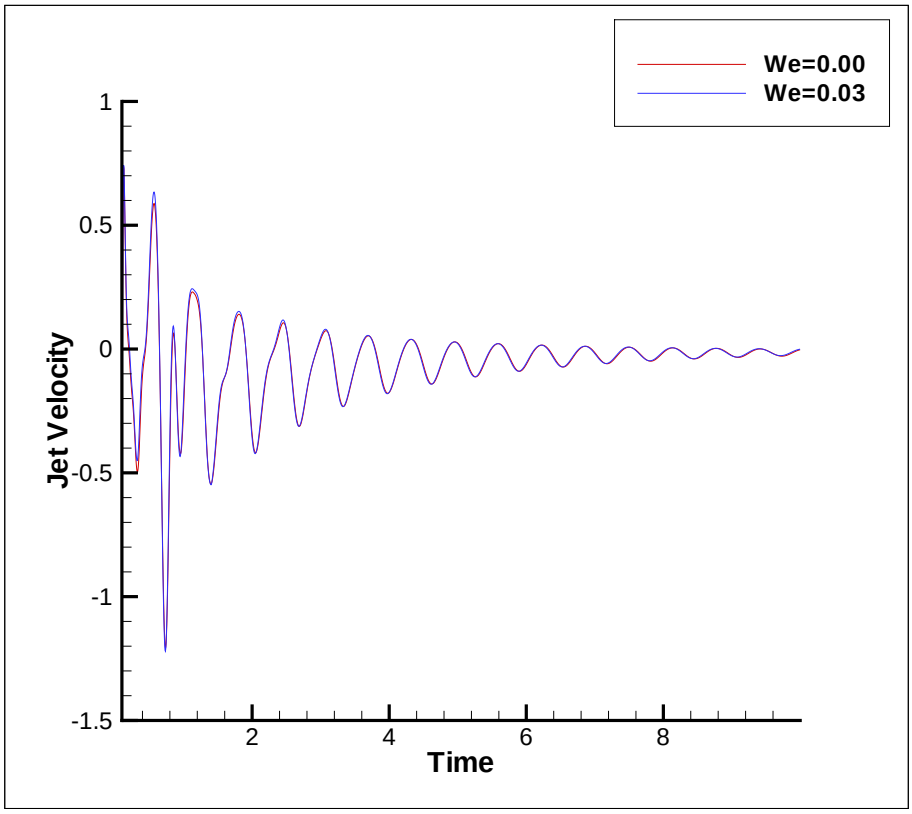

Figure 7.27: Variation of jet velocity with time (after the initial collapse) in a Newtonian and UCM fluid, $\mu_p = 0.1$, $h = 1.1$.

predicted by the BEM study (see Fig. 3.5, for example). Interestingly, note the small perturbations in the jet velocity for $h = 1.1$ at about $t = 2$, for example. These were also observed in the BEM study (see Fig. 3.17 and the accompanying paragraph), and result from the wall perturbing flow around the bubble and causing it to oscillate "out of phase", i.e. the lower part of the bubble may collapse, while the upper part expands. In turn, the unsynchronised flow field around the bubble produces perturbations in the jet velocity.

Additionally, at greater bubble distances from the wall, larger upper bounds on the Weissenberg number are permitted. For $h = 2.0$ for example, the maximum Weissenberg number for which stability is sustained is $We_{max} \approx 0.15$. This is not surprising, as a greater bubble distance from the wall means that the flow adjacent to the wall is less severe (reduced velocities and increased uniformity). Consequently, velocity gradients are significantly smaller and so the stress boundary layers, the most likely source of the numerical instability, are smaller in magnitude.

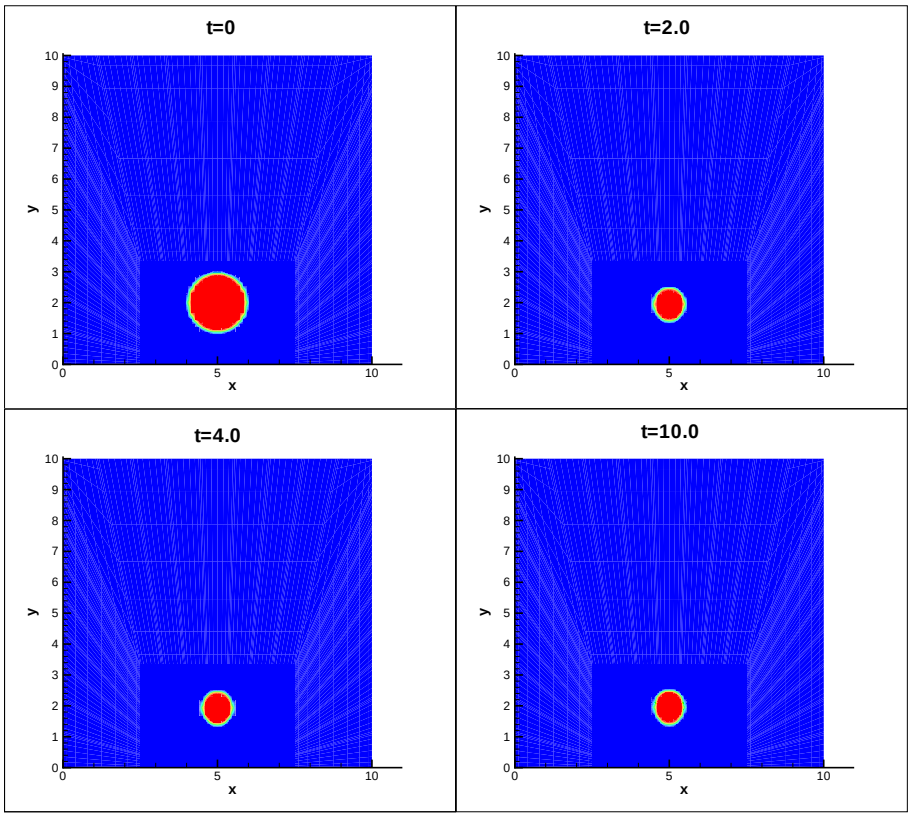

Figure 7.28: A plot of the colour function at different times, representing bubble collapse near a wall in a UCM fluid with $\mu_p = 0.1$, $We = 0.03$, $h = 2.0$.

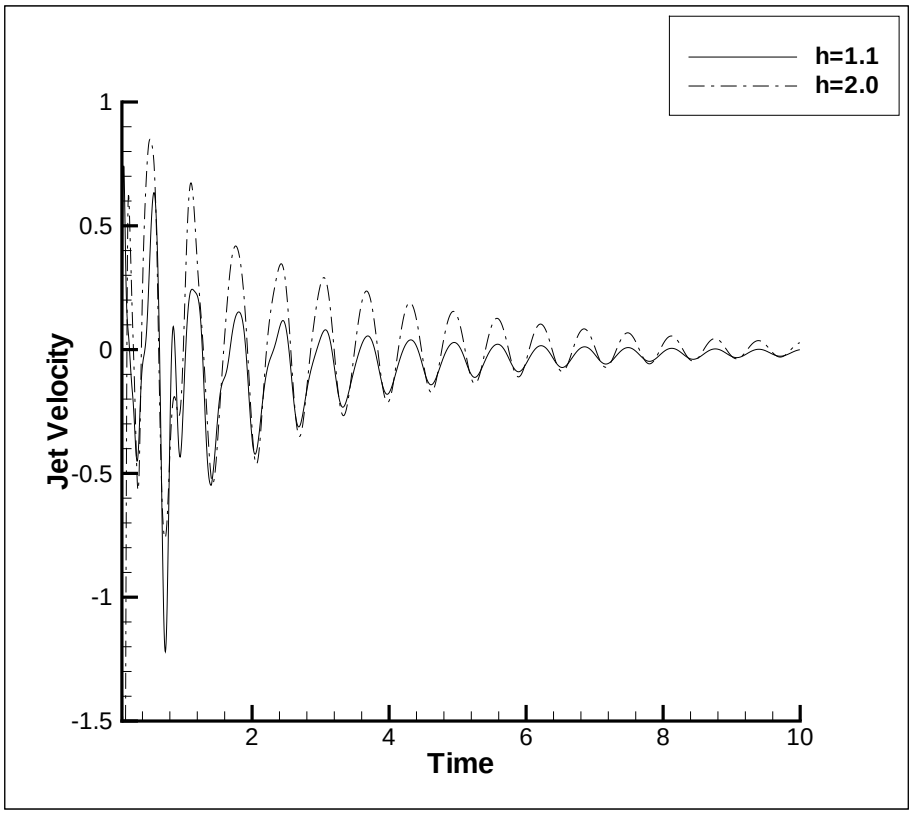

Figure 7.29: Variation of the jet velocity with time, at different distances h from the wall, in a UCM fluid with $\mu_p = 0.1$, $We = 0.03$.

7.5.3 Bubble Collapse in an Oldroyd B Fluid

Variation of Solvent Viscosity

In this section we investigate the dynamics of a bubble within a fluid whose rheological properties are governed by the Oldroyd B constitutive equation. It is well known that the Oldroyd B equation is comprised of the UCM model but with an additional Newtonian solvent stress contribution (see Equation (7.9)). It can be anticipated that, as is often observed in the literature, that this additional viscous stress will abate elastic effects and permit higher upper bounds on the Weissenberg number. Figure 7.30 shows the colour function at time $t = 0.5$ for a selection of solvent viscosities. The Weissenberg number is $We = 0.03$ (for comparison with the previous UCM studies) and the initial bubble distance from the wall is $h = 1.1$. Unsurprisingly, by increasing the solvent viscosity the small cusp on the bubble underside becomes less prominent and the somewhat sharpened underside becomes smoothed out. As expected, the elastic effects, which we know to be the reason for cusp formation, are suppressed with increasing solvent viscosity. This can be further appreciated by studying the stress component T_{xx} for each solvent viscosity.

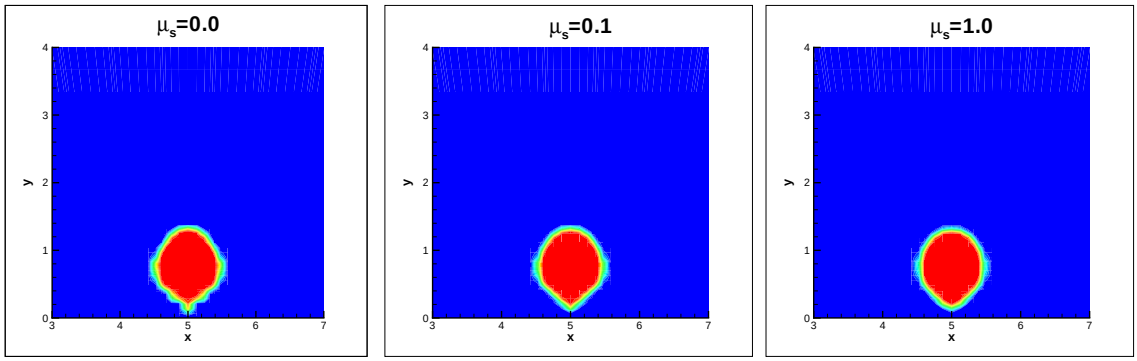

Figure 7.30: A plot of the colour function at $t = 0.5$ in an Oldroyd B fluid for different solvent viscosities μ_s. The remaining parameters are $\mu_p = 0.1$, $We = 0.03$, $h = 1.1$.

The contours of the stress component T_{xx} are shown in Figure 7.31. We know that this component of stress differs drastically in the Newtonian and viscoelastic cases, and that it is the dominant stress component in cusp formation. Expectedly we see significantly different stress contours for the different solvent viscosities. For $\mu_s = 0$ we see the thin, relatively high magnitude stress boundary layers observed in Fig. 7.25. By increasing the solvent viscosity to $\mu_s = 0.1$, viscous effects begin to abate elastic effects and the stress layers become thicker and decrease in magnitude. Increasing viscosity

to $\mu_s = 1.0$, we see that no discernible stress layers form and that the contour field resembles the Newtonian case (both in structure and magnitude). Evidently, increasing viscous effects increasingly suppress the elastic effects, thus providing an explanation of the transition in bubble shape from a cusped/concave to smoothed/convexed underside.

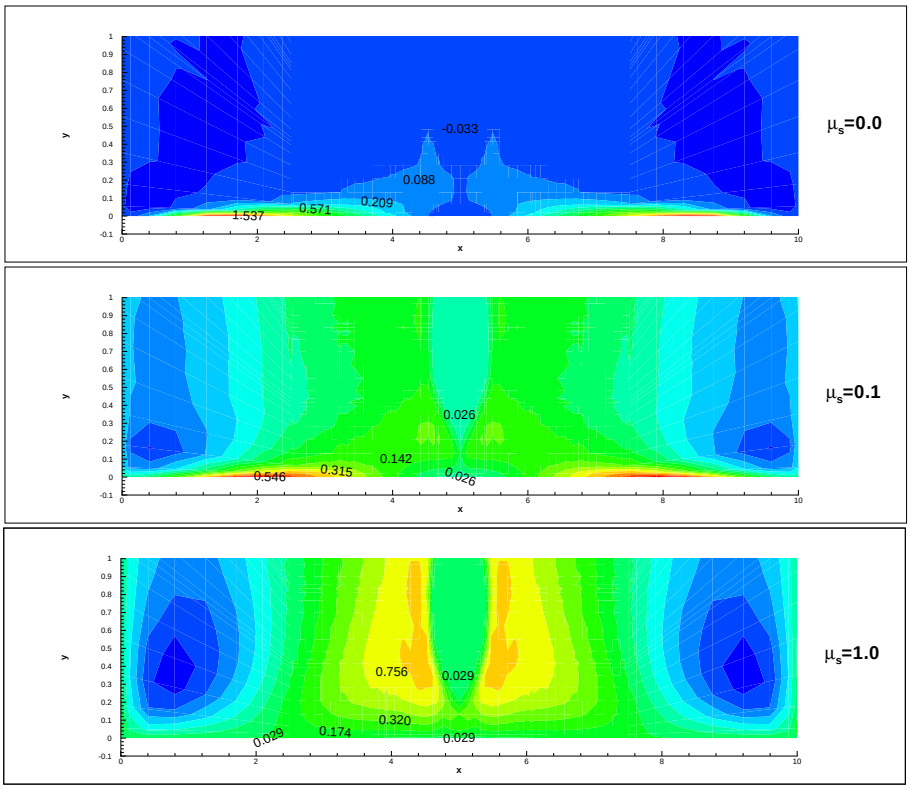

Figure 7.31: The stress contours of component T_{xx} for different solvent viscosities μ_s. The remaining parameters are $\mu_p = 0.1$, $We = 0.03$, $h = 1.1$.

Figure 7.32 shows the variation of the jet velocity with time for the different solvent viscosities discussed above. Once again, the behaviour is as expected. By increasing the viscosity the amplitude of oscillation decreases due to increased energy loss through viscous dissipation. Consequently, the bubble attains a zero kinetic energy steady state with $\mu_s = 1.0$, before the cases $\mu_s = 0, 0.1$. A similar response to increasing solvent viscosity has been predicted by the BEM when using the Jeffreys model, in the case of spherical bubble dynamics. Figure 2.15, for example, shows the increasingly damped oscillations of the radius with time.

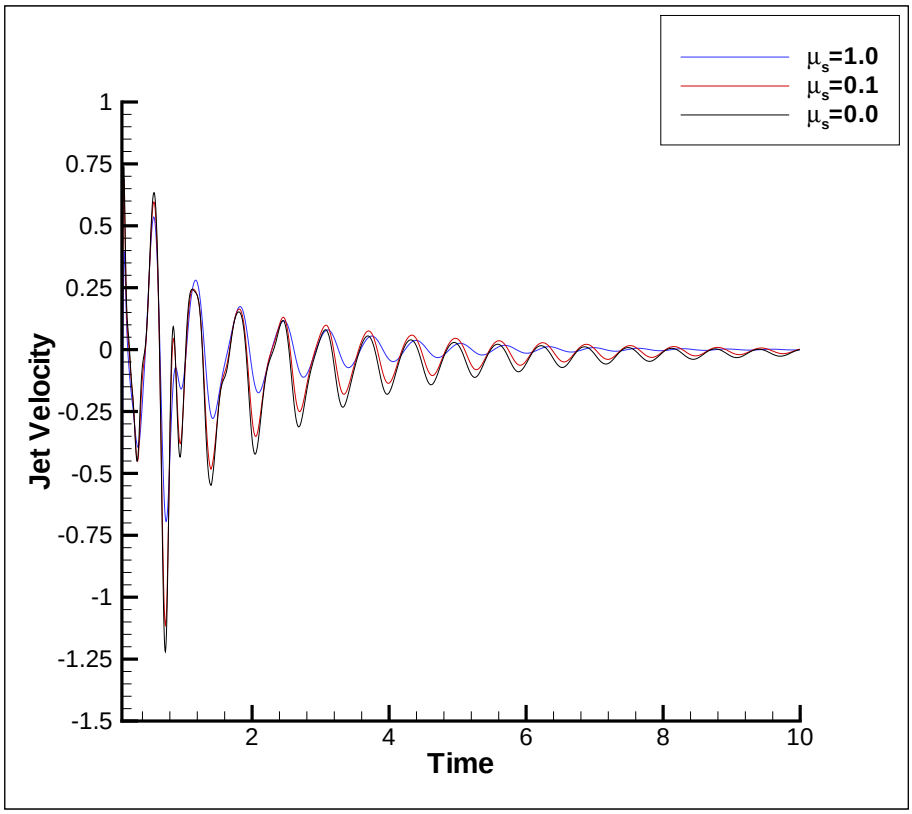

Figure 7.32: Variation of the jet velocity with time for different solvent viscosities, with $\mu_p = 0.1$, $We = 0.03$, and $h = 1.1$.

Variation of Weissenberg Number

Considering the case $\mu_p = \mu_s = 0.1$, $h = 1.1$, we shall now investigate the effect of varying the Weissenberg number. As we have mentioned, it is well known that the inclusion of a solvent stress can permit larger upper bounds on the Weissenberg number. Such is the case in this study. The inclusion of a solvent viscosity $\mu_s = 0.1$ has allowed an order of magnitude increase in the maximum attainable Weissenberg number, with $We_{max} \approx 0.65$. Figure 7.33 shows the colour function at $t = 0.5$ for a selection of Weissenberg numbers. The difference in the bubble shapes is not particularly striking, but one does notice an increasingly cusped underside for Weissenberg numbers $We = 0.1$ and 0.5. Once again, this highlights the role of elasticity in the formation of cusps.

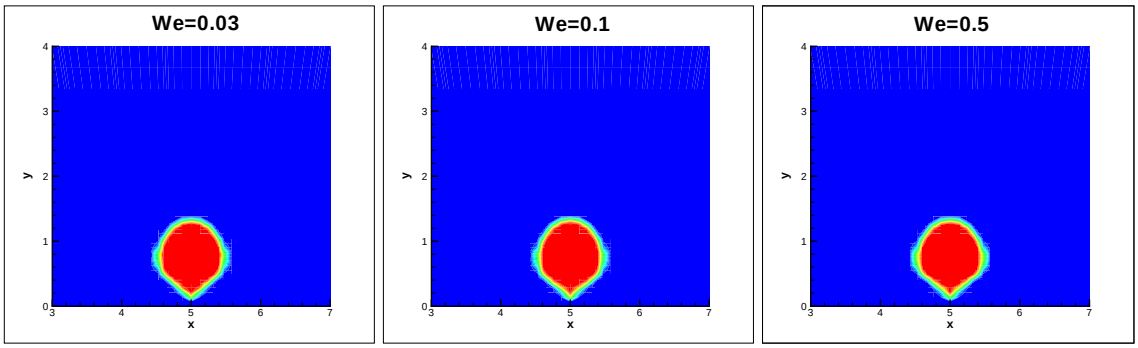

Figure 7.33: A plot of the colour function at $t = 0.5$ for different Weissenberg numbers. The remaining parameters are $\mu_p = \mu_s = 0.1$, $h = 1.1$.

The contours of stress component T_{xx} are given in Fig. 7.34. For $We = 0.03$, we see the thickest layers and smallest in magnitude. Increasing the Weissenberg number to $We = 0.1$, results in slightly thinner and more elongated layers with values of T_{xx} which are larger in magnitude. The increased magnitude of the stress is evidently responsible for the increased cusping. Increasing the Weissenberg number further to $We = 0.5$, we see yet thinner layers develop, with values of T_{xx} which are again significantly larger in magnitude. Such behaviour of the stress boundary layers, when varying Weissenberg number, has been well documented in the literature. For example, for the UCM model, Renardy [127] noted that boundary layer thickness decreased as We^{-1} with increasing Weissenberg number. Under-refinement of these layers can result in numerical instability, and in many studies in computational rheology this is cited as the reason for the high Weissenberg number problem [112]. This also seems the case here. For $We = 0.5$, accompanying the thin boundary layers, are lower amplitude spurious oscillations originating from the boundary. Though these are not significant enough

to pollute and destroy the whole solution, it clearly indicates that we are nearing the limiting Weissenberg number for this problem. As stated, this was found to be at around $We_{max} \approx 0.65$. Further refinement of these layers is possible and while it may allow increases in Weissenberg number, it merely postpones the issue.

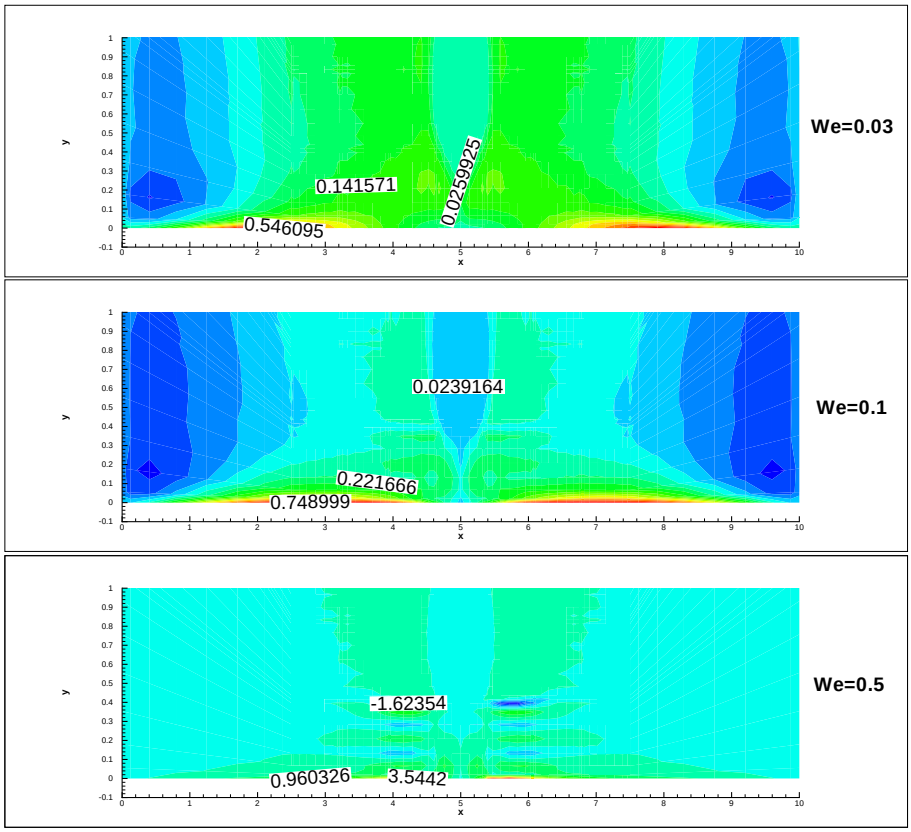

Figure 7.34: The stress contours of component T_{xx} for different Weissenberg numbers. The remaining parameters are $\mu_p = \mu_s = 0.1$, $h = 1.1$.

Despite considerable differences in the stress contours for varying Weissenberg numbers, as we can see in Figure 7.35, the difference in the jet velocities is not as pronounced. It seems elastic effects are most significant near the wall and primarily act to alter bubble shape in this region. We do, however, see a slight increase in the amplitude of oscillation with increasing Weissenberg number, due to the increased elastic energy in the system over viscous dissipation. Of course, we know this to be a quintessential characteristic of viscoelastic bubble dynamics.

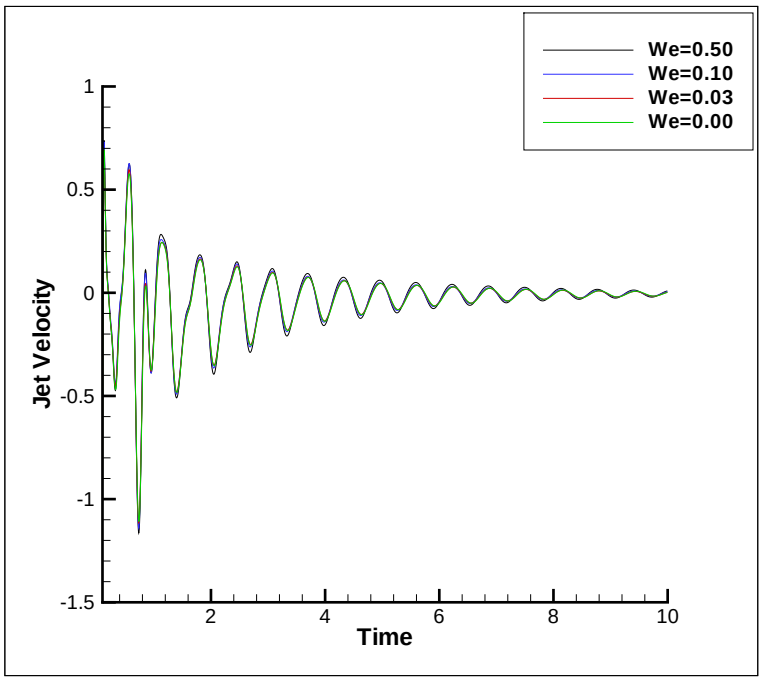

(a)

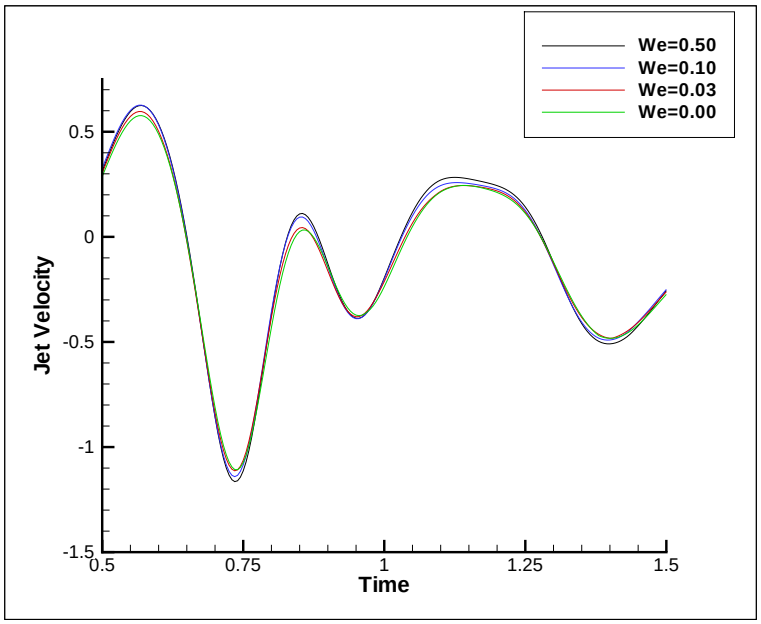

(b)

Figure 7.35: (a) Variation of jet velocity with time (after initial collapse) for different Weissenberg numbers, with $\mu_p = \mu_s = 0.1$, $h = 1.1$. (b) Close up of the jet velocities, indicating the increasing amplitude oscillations with We.

Variation of Polymeric Viscosity

Now the solvent viscosity and the Weissenberg number will be keep fixed at $We = \mu_s = 0.1$, but the polymeric viscosity will be varied. Figure 7.36 shows plots of the colour function at $t = 0.5$ for various polymeric viscosities. By increasing the polymeric viscosity, the bubble goes from having a more rounded shape with an appreciable cusped tail, to a more prolate (squashed along the y axis shape), with a less distinguishable cusp. Once again the stress contours T_{xx} can provide important insights into the formation of these different shapes.

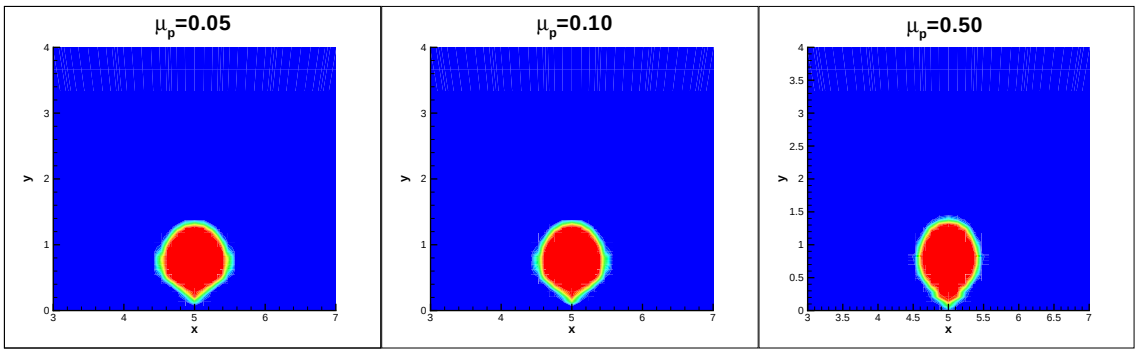

Figure 7.36: A plot of the colour function at $t = 0.5$ for different polymeric viscosities. The remaining parameters are $We = \mu_s = 0.1$, $h = 1.1$.

Figure 7.37 shows the T_{xx} contours for the different polymeric viscosities. Increasing the polymeric viscosity does not particularly effect the thickness or length of the stress boundary layer, for as we have discussed, this is primarily determined by the Weissenberg number. However, an increase in μ_p does result in stresses of increased magnitude, which vary in structure further from the boundary. For $\mu_p = 0.05$ and $\mu_p = 0.1$ the stress field in the region around the bubble, just away the wall, is quite uniform. Consequently, in both cases, the uniform distribution of stress results in the bubble shape, away from the wall, remaining relatively circular. For $\mu_p = 0.5$, besides the sizable increase in the overall magnitude of T_{xx}, there is a notable difference in structure, with a region of high stress around the bottom half of the bubble and a lower stress region around the top half. The increased magnitude, particularly around the lower half of the bubble, has the effect of squashing the bubble and producing a more prolate shape with no definite cusp formation.

Figure 7.38(a) shows the jet velocities for the selection of polymeric viscosities. As expected, increasing μ_p sees a decrease in the amplitude of oscillation, as elastic effects which would act to encourage oscillation, are suppressed due to increased viscous dis-

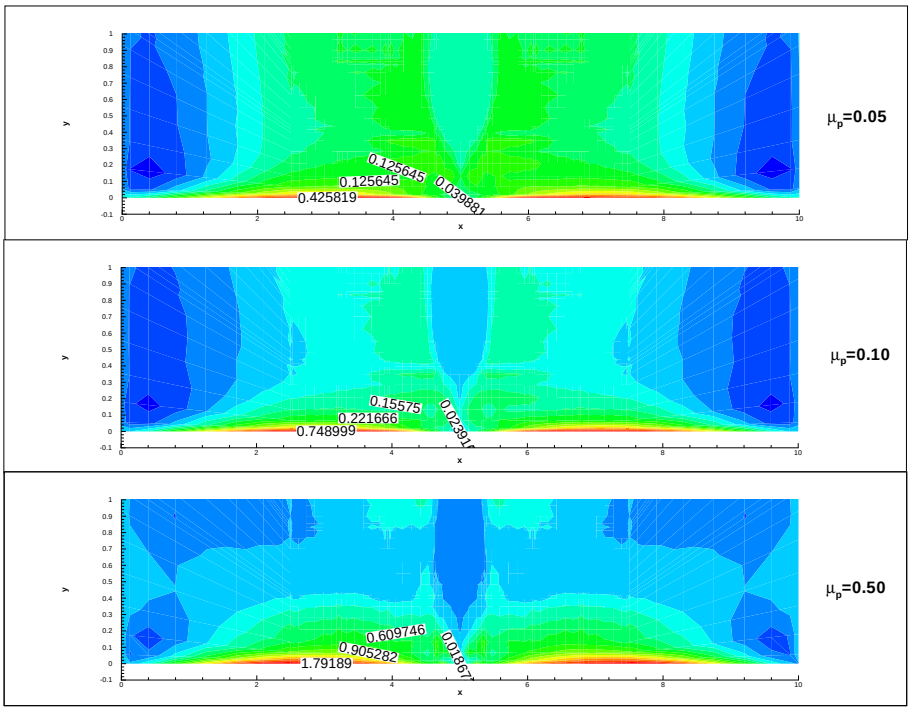

Figure 7.37: The stress contours of component T_{xx} for different polymeric viscosities. The remaining parameters are $We = \mu_s = 0.1$, $h = 1.1$.

sipation. Of course, such a response is well known and has been observed in the BEM study in the spherical and non-spherical cases (see, for example, Figure 2.10)

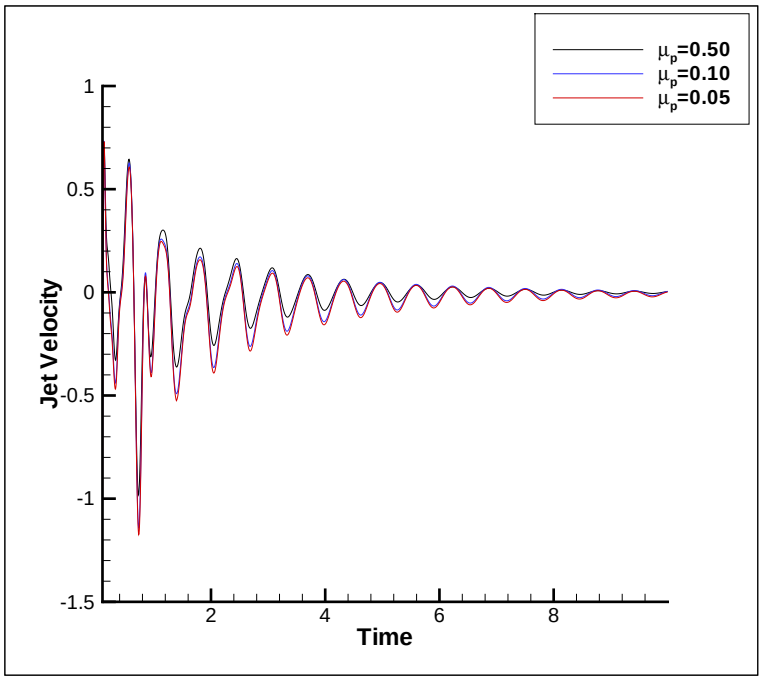

(a)

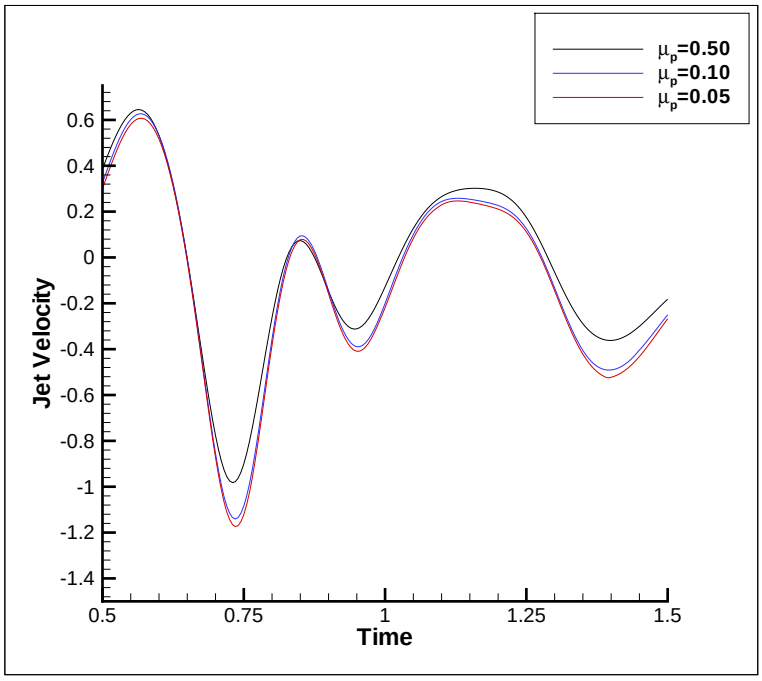

(b)

Figure 7.38: (a) Variation of jet velocity with time (after initial collapse) for different polymeric viscosities, with $We = \mu_s = 0.1$, $h = 1.1$. (b) Close up of the jet velocities, indicating the decrease in the amplitude of oscillations with increasing viscosity.

Variation of the Speed of Sound

We shall now investigate the bubble dynamics for different fluid compressibilities. This property is parameterised by the speed of sound. Figure 7.39 shows the colour function at $t = 0.5$ for different speeds of sound c^2. The material parameters are $\mu_s = \mu_p = We = 0.1$, with $h = 1.1$. Decreasing the speed of sound causes a notable change in bubble shape. At $c^2 = 1000$ we see the usual rounded bubble with a protruding cusped tail. At $c^2 = 500$, the cusped tail is no longer visible but the underside is at the limit of concavity. For $c^2 = 100$ there is no sign of concavity in the surface and the bubble has assumed a more prolate form. This transition from initial to final shape is not dissimilar to that observed when one increases the solvent or polymeric viscosity (as in Figures 7.30 and 7.36, respectively). Since the equation of state is $p = c^2\rho$, and the initial density difference $\Delta\rho$ is a constant, this means that the initial pressure difference Δp between to two phases varies linearly with c^2. Hence a large c^2 implies a large initial pressure difference, and consequently, produces large initial inertias and collapse velocities. By decreasing the speed of sound, the initial pressure difference and hence the inertia also decrease. Of course, increasing the viscosity produces a similar effect, as can be seen by considering the alternative definition of Reynolds number used in the preceding chapters, $Re^* = R_0(\rho\Delta p)^{1/2}/\mu$. Despite the similar inertial effects, compressibility and viscosity are of course two different fluid properties and do produce different physical effects. The unique role of compressibility can be readily seen from the jet velocity profiles shown in Fig. 7.40.

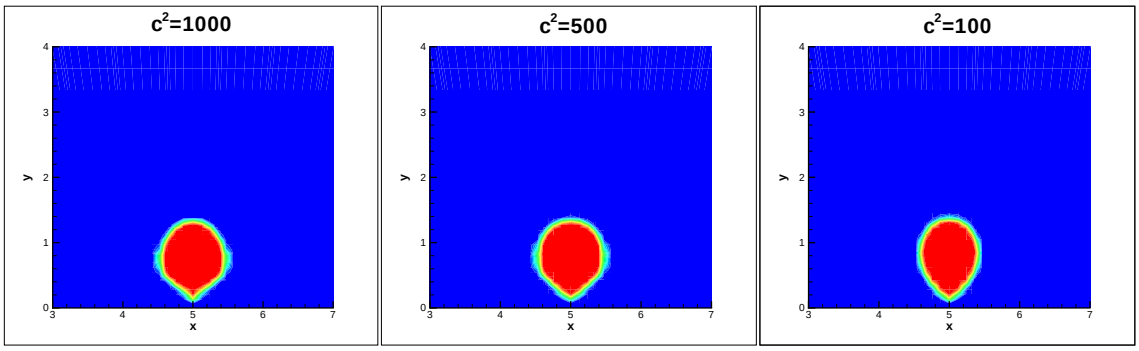

Figure 7.39: A plot of the colour function at $t = 0.5$ for different speeds of sound c^2. The remaining parameters are $We = \mu_s = \mu_p = 0.1$, $h = 1.1$.

The most notable difference in the jet velocities is the frequency of the oscillations. Decreasing the speed of sound c^2, results in a decrease in the frequency of bubble oscillation. This is essentially due to the pressure differences between the bubble and

ambient fluid. For large speeds of sound the pressure difference is large, which causes the bubble to collapse rapidly. However, as the bubble collapses and decreases in volume, there is a rapid increase in bubble density, and hence a rapid increase in pressure within the bubble as $p = c^2\rho$. This large pressure then halts collapse and causes the bubble to rapidly expand, with this process of rapid expansion/contraction then continuing, but becoming progressively slower due to viscous dissipation. At lower speeds of sound, collapse is not as rapid and it takes longer for the bubble density to increase to the point where the pressure is large enough to cause bubble rebound. Consequently, the frequency of the bubble oscillations is much lower.

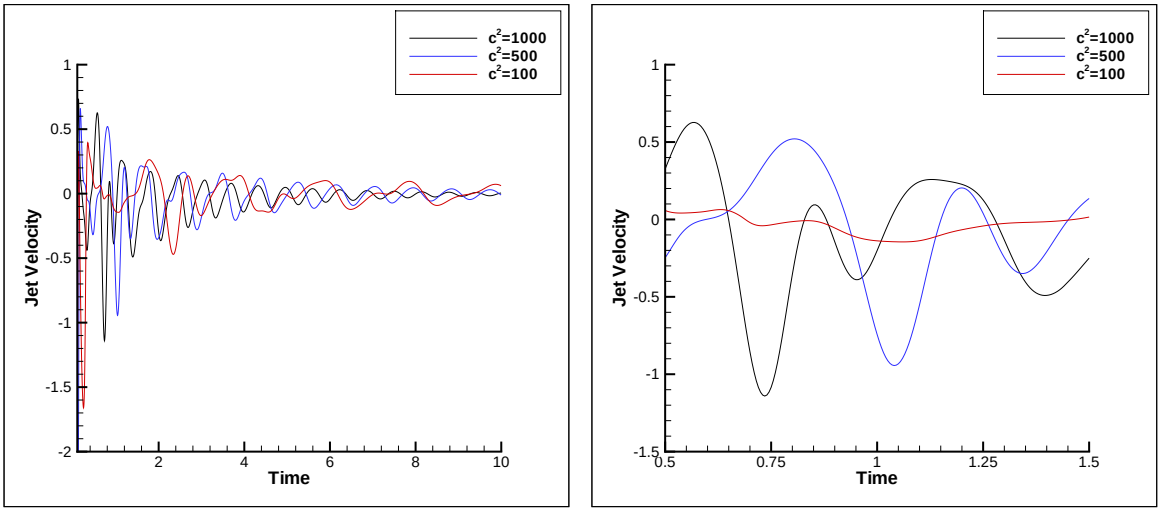

(a) (b)

Figure 7.40: (a) Variation of jet velocity with time (after initial collapse) for different speeds of sound, with $We = \mu_s = \mu_p = 0.1$, $h = 1.1$. (b) Close up of the jet velocities, indicating the increase in the frequency of oscillations with increasing sound speed.

Due to the smaller pressure difference at lower speeds of sound and the subsequently smaller initial collapse velocities, the associated reduction in the severity of the flow suggests that larger Weissenberg numbers can be obtained. This is indeed found to be the case. In fact, reducing the speed of sound to $c^2 = 100$ seems to eliminate any upper bound on the Weissenberg number. Figure 7.41 shows the jet velocities for different We with $c^2 = 100$. As usual, we see an increase in the amplitude of oscillation resulting from the increasing elastic effects. However, continually increasing We sees progressively smaller changes in the amplitude as the solution tends to a Hookean elastic limit. The reduced inertia and smaller velocity gradients mean that upon increasing the Weissenberg number, the constitutive equation for the polymeric

stress

$$\overset{\triangledown}{\mathbf{P}} + We^{-1}\mathbf{P} = We^{-1}\mu_p(\nabla\mathbf{u} + \nabla\mathbf{u}^T) \tag{7.114}$$

becomes increasingly better approximated by

$$\overset{\triangledown}{\mathbf{P}} = 0. \tag{7.115}$$

It seems that the velocity gradients are small enough to permit increases in We without amplifying the troublesome deformation terms in the upper convected derivative. Such a high Weissenberg number limit was observed in the BEM study and in other studies of viscoelastic bubble dynamics (e.g. [54]). The models predicted an elastic limit that resembles the inviscid solution for bubble collapse (see Figure 2.7, and the accompanying explanation, for example). Similarly, according to Equation (7.115), the polymeric stress $\mathbf{P}$ remains constant on following a deforming parcel of fluid. Since we have a zero initial stress condition, $\mathbf{P} = 0$ indefinitely. The solution is not inviscid however, as we still have a non-zero Newtonian solvent stress contribution.

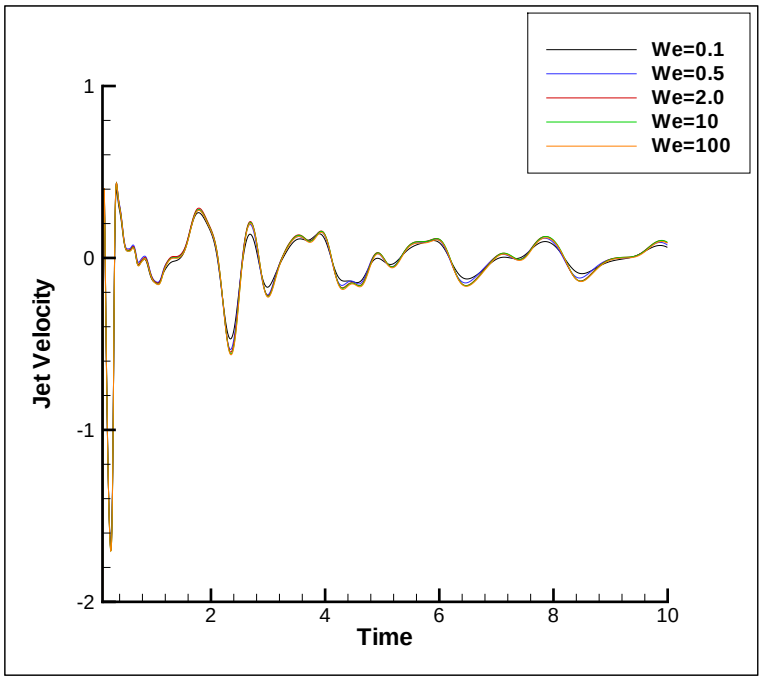

(a)

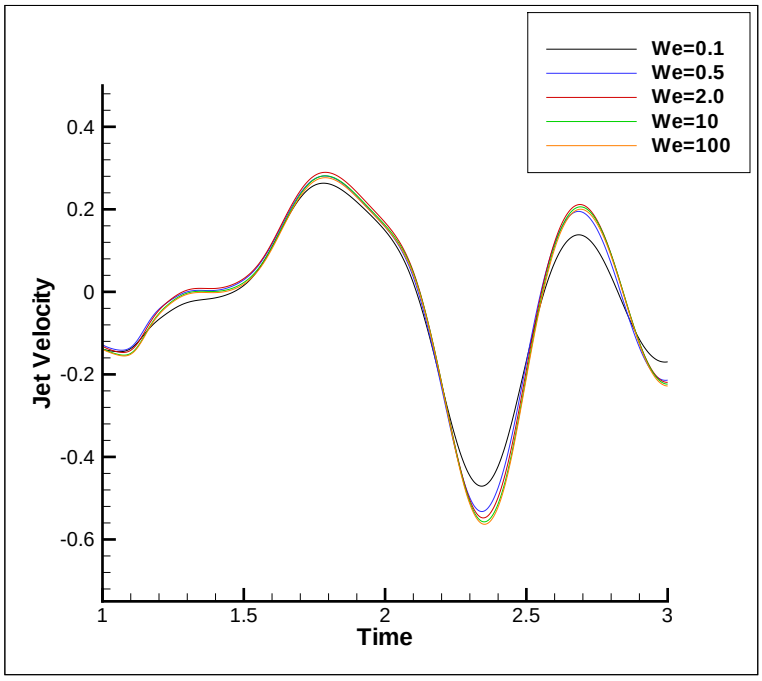

(b)

Figure 7.41: (a) Variation of jet velocity with time (after initial collapse) for different Weissenberg numbers, with $\mu_s = \mu_p = 0.1$, $c^2 = 100$, $h = 1.1$. (b) Close up of the jet velocities, indicating a limiting elastic solution at larger Weissenberg numbers.

7.6 Conclusions

In this chapter we have developed a numerical method to simulate two-phase viscoelastic flows. The full compressible, two-dimensional governing equations are solved using a spectral element method. The two phases are modelled using a marker particle method - a scheme which bears a strong resemblance to volume of fluid techniques. On the understanding that compressibility can play an important role in bubble collapse, we briefly discuss the modelling of compressible viscoelastic fluids and subsequently propose a more complete model to those used previously in the literature. The marker particle method is validated using some standard test problems, and this has highlighted the beneficial properties of the scheme, including minimal numerical diffusion and robustness. The spectral element solution of the governing equations was validated through comparison with the analytical solution for transient Poiseuille flow, in both the Newtonian and viscoelastic (Oldroyd B) cases. The agreement in both cases is excellent. The compressible formulation can be used to approximate the solution of the incompressible problem to a high degree of accuracy by simply increasing the speed of sound. Two different temporal discretisations for the polymeric stress were investigated; a second order explicit scheme which has been used previously by Fiétier and Deville [52] and Van Os and Phillips [157], and a first order semi-implicit scheme. The semi-implicit scheme was found to be considerably more stable and was subsequently employed in the study of two-phase viscoelastic flows. The compressible formulation was found to enhance stability slightly compared to the incompressible approach, but in general it exhibited the same behaviour with varying polynomial order and number of spectral elements.

The results for bubble collapse near a rigid boundary qualitatively agree with the dynamics observed in the boundary element study, other numerical studies, and experimental observations. Given the differences in the different models, a good quantitative agreement was not expected, and indeed, not observed. In the Newtonian case, for low viscosities, the model predicts jet formation and a splashing-like phenomenon. As viscosity is increased, jet formation is suppressed and bubble deformation is restricted. Including viscoelastic effects, firstly in the form of the Upper Convected Maxwell model, we find that during collapse jet formation can be prevented and a cusp can form on the bubble underside. This was also observed in the BEM study of Chapter 3, and is due to a build up of (visco)elastic stresses around the cusp when near the wall. In this study

large stress boundary layers can form, which can cause the solution to breakdown if the Weissenberg number exceeds a certain value. This upper bound on the Weissenberg number was found to increase with increasing distance from the wall. As is generally the case, the Oldroyd B model proved able to support considerably higher Weissenberg numbers, due to the inclusion of a solvent viscous stress. As in the UCM case, predictions from the Oldroyd B model include cusp formation on the bubble underside and also larger amplitude oscillations in the jet velocity with increasing Weissenberg number. Once again, this behaviour was also predicted by the BEM study and has been well documented in other numerical studies of spherical bubble dynamics. It was found that increasing the compressibility of the two fluids (by decreasing the speed of sound) resulted in smaller inertial effects and smaller initial collapse velocities. The frequency of the oscillation of the bubble was also markedly reduced. Due to the smaller inertial effects, and subsequently smaller velocity gradients near the wall, the elastic boundary layers were also significantly smaller in magnitude. Consequently, because these layers are unable to grow enough in magnitude to induce numerical instability, there seems to be no upper limit on the Weissenberg number. There is however an "elastic" solution in the limit of large Weissenberg numbers, as the polymeric constitutive equation reduces to a simpler form. An elastic limit was observed in the BEM study for the particular model used, and has also been predicted in other numerical/theoretical work on spherical bubble dynamics.

In conclusion, this study confirms the role of viscoelasticity in the dynamics of bubble collapse near a wall; a role which was first ascertained in the BEM study. Such viscoelastic effects include increased bubble oscillation with Weissenberg/Deborah number, considerable deformation and cusping near the wall, and perhaps most importantly, the ability to prevent jet formation. One might say that this reaffirms the opinion that viscoelasticity has a mitigating effect on cavitation damage. As we have guessed, it appears that perhaps such a statement might not be so simple. Specifically in the case of viscoelasticity, we have seen that large stresses can build up on the boundary. It is very possible that these may have a detrimental effect on the surface. Evidently, more research needs to be carried out, and in particular with more advanced rheological models which can perhaps give a more physical description of dynamics near the wall. Another important modelling extension is the study of more advanced equations of state and thermodynamic effects. There are, of course, a plethora of equations of

state, such as the equation of Tait, which may be better suited to describing the thermodynamic properties of the system. Indeed, it may even be possible to combine two equations of state, one for each phase, in a manner like the viscosity. Further extensions include modelling multi-bubble dynamics, studying the dynamics of an array of bubbles above, below and adjacent to one other. For in reality, bubbles rarely form singly but as part of a bubble cloud, with substantially different dynamics and implications for cavitation damage. Improvements to the numerical scheme include being able to support a larger (and more realistic) difference in initial densities between the bubble and ambient fluid, while still being able to attain a satisfactory Weissenberg number. Perhaps including SUPG or similar schemes might be beneficial with regard to increasing the Weissenberg number limit.

Chapter 8

Conclusions

In this thesis two different models and numerical methods have been developed to investigate the dynamics of bubbles in viscoelastic fluids.

8.1 The First Model

In the interests of gaining some crucial initial insights into viscoelastic bubble dynamics, a simplified system of governing equations is considered. The bubble is modelled as a void in the computational domain and the ambient fluid is considered incompressible and the flow irrotational. Viscous and viscoelastic effects then appear through the normal stress balance at the bubble surface. The model can be a good approximation, particularly for moderate to high velocity phenomena such as bubble collapse, due to the small amount of vorticity generated at free surfaces and the confinement of viscous/viscoelastic effects to thin boundary layers. Following experimental observations of bubble dynamics, axisymmetry is assumed, effectively reducing the problem from a three-dimensional one to a two-dimensional one. An efficient and versatile boundary element method is then developed to solve the governing equations.

8.1.1 Spherical Bubble Dynamics

In Chapter 2 the predictions of the model for spherical viscoelastic bubble dynamics are investigated. The model is first validated through comparison with the inviscid and viscous solutions for collapse of a spherical cavity, as described by the Rayleigh-Plesset equation. The predictions of the model with regard to spherical viscoelastic bubble dynamics are then discussed for several different constitutive equations. Even

though viscoelastic effects only appear through the normal stress condition on the free surface, the model predicts all the important phenomena seen in other spherical dynamics studies. More specifically, the Maxwell model predicts the damped oscillation of the bubble radius with time, the near elastic oscillations in the high Deborah number limit, and the no-rebound condition. Furthermore, the results are in good quantitative agreement with full solutions of the viscoelastic Rayleigh-Plesset equation. This supports the argument that surface effects alone can offer a comprehensive description of bubble dynamics. Considering the Jeffreys constitutive relation, predictions include an increasingly damped radius with increasing solvent viscosity. A generalised Maxwell model is also investigated, with empiricisms relating to Rouse and Doi-Edwards molecular theories prescribing the parameters. The Doi-Edwards model does not exhibit any oscillation in bubble radius - only a slow decay of bubble radius with time is predicted. In comparison, the Rouse model predicts a small low amplitude rebound before being completely damped. This is in stark difference to the more elastic behaviour predicted by the Maxwell and Jeffreys models. The majority of the work in this chapter has been published in the Journal of Non-Newtonian Fluid Mechanics [94]

8.1.2 Bubble Dynamics Near a Rigid Wall

In Chapter 3, the numerical scheme is modified to study bubble collapse near a rigid wall. When a bubble collapses near a rigid wall, a liquid jet can form which can penetrate the bubble and possibly impact upon the wall. It is well known that this jet plays an important role in the creation of cavitation damage. The numerical scheme is validated through comparison with the inviscid results available in the literature. Viscous Newtonian investigations confirm the effect of viscosity in inhibiting jet formation and jet speed, as reported in other numerical studies. For the values of Reynolds number and Deborah number necessary to induce oscillation, we find that during collapse near a wall the liquid jet will not form. Instead, the underside of the bubble can cusp and cause parts of the bubble surface to oscillate out of phase. The incoherent oscillations disrupt flow around the bubble causing perturbations in its position and velocity profiles. The cusping and perturbations become less perceptible as one moves further from the wall. Increasing viscous effects can prevent large deformations in bubble shape, regardless of distance from the rigid wall; and so reduce the incoherent oscillations and perturbations in the velocity. Crucially, viscoelasticity can prevent catastrophic bubble collapse. Instead the bubbles can oscillate near the wall for a significant period

of time, without significant changes in volume. For some parameters, steady states can be attained. The suppression of the liquid jet suggests that viscoelasticity has a mitigating effect on cavitation damage. A version of this chapter has been submitted to Theoretical and Computational Fluid Dynamics [92]

8.1.3 Two Bubble Dynamics Near a Rigid Wall

Chapter 4 is an extension of Chapter 3 and considers the dynamics of two bubbles near a rigid wall. The motivation is that bubbles in nature rarely form singly, but as part of bubble clouds. Hence bubble-bubble interaction near a wall requires consideration. The dynamics are interesting and varied, and strongly depend on initial bubble size, the fluid properties, and the distances between the bubbles and the wall. Jets readily form in certain situations in viscoelastic fluids (a sign of greater wall influence) but not in the corresponding Newtonian case (suggesting bubble-bubble interaction dominates). Though this behaviour seems to contradict the findings of the previous chapter, it in fact highlights the importance bubble-bubble interactions have on the overall dynamics. This may provide some explanation for the ambiguity present in the experimental literature, where direct measurements of cavitation damage in viscoelastic fluids have been contradictory. Cavitation dynamics depends as much on neighbouring bubbles as it does on the fluid properties.

8.1.4 Bubble Dynamics Near a Free Surface

In Chapter 5, the effect of viscoelasticity on bubble dynamics near a free surface is investigated. The situation is pertinent to biological applications and has implications for cell damage and drug delivery. A range of dynamics is seen to occur, with a subtle dependance on the Deborah number, Reynolds number and the distance from the free surface. In the presence of viscoelasticity, the motion of free surface jets can be significantly retarded compared to the Newtonian cases, and the bubbles take a wide range of shapes. On including viscoelastic effects, the usual axial jet observed in so many instances in the Newtonian dynamics, is no longer seen. Instead, an annular, ring like jet can form and can penetrate the bubble to produce mushroom-like shapes. Similar shapes are observed in bubbles collapsing near purely elastic boundaries, and are due to perturbations in the bubble surface resulting from elastic responses in the free surface. Further from the free surface however, the bubble can collapse in a near-

spherical, oscillatory manner, before reaching some steady state. The conclusions are similar to those of bubble collapse near a rigid wall: Given that no high speed jets can form in the bubble or free surface, the implications for cavitation/cell damage are mitigatory. Brief comparisons with the experimental work of Williams et al. [165] have also been made. The model was extended to include the propagation of shock waves and shock-induced bubble collapse. The results are promising in the early stages, but to recreate the observed free surface jets, the theory needs to be extended to include evolution to a toroidal geometry, to allow the liquid jet to fully penetrate the bubble and form the free surface jet. A version of this chapter is in preparation for submission to the Journal of Fluid Mechanics [91]

8.1.5 Rising Gas Bubbles

In Chapter 6, we apply the model to the study of rising bubbles in viscoelastic fluids. The bubble is assumed to be constant in volume, rising through an incompressible fluid under an irrotational flow. Results for the Newtonian rising bubble show good agreement with previous studies and steady state bubble shapes qualitatively match full domain solutions. In the viscoelastic case, the results predict the bubble's prolate shape and the formation of the trailing end cusp. The method allows for high curvatures and deformations and so can capture the sharpness of the cusp to a higher degree than seen in other numerical schemes. Furthermore, the cusped bubble profile bears a good qualitative agreement with experimental observations. Proposed reasons for the velocity jump include drag reduction due to cusping [95], the action of surface forces [133] and the negative wake [66]. Here, we include the appropriate surface effects and inertia terms and observe cusping, but detect no velocity jump discontinuity. This suggests that the negative wake is primarily responsible for its occurrence, corroborating previous experimental and numerical findings [66, 117]. Much of the work in this chapter is to appear in a paper that has been accepted for publication in the Journal of Non-Newtonian Fluid Mechanics [90]

8.2 The Second Model

In Chapter 7, we return to the problem of Chapter 3, that of bubble collapse near a rigid wall. However, a new model and numerical method are devised. The intention being to gain further insight into the role of viscoelasticity, but also to corroborate the

findings of Chapter 3. The second model employs the full compressible equations of motion in a two dimensional domain. In contrast to the boundary element method, the governing equations are solved on a fixed Eulerian grid using the spectral element method. The two phases are modelling using a marker particle method. On the understanding that compressibility can play an important role in bubble collapse, we briefly discuss the modelling of compressible viscoelastic fluids and subsequently propose a more complete model to those used previously in the literature. The marker particle method is validated using some standard test problems, and this has highlighted the beneficial properties of the scheme, including its minimal numerical diffusion and robustness. The spectral element solution of the governing equations was validated through comparison with the analytical solution for transient Poiseuille flow, in both the Newtonian and viscoelastic (Oldroyd B) cases. The agreement in both cases is excellent.

The results for bubble collapse near a rigid boundary qualitatively agree with the dynamics observed in the boundary element study, other numerical studies, and experimental observations. Given the differences in the different models, a good quantitative agreement was not expected, and indeed, not observed. In the Newtonian case, for low viscosities, the model predicts jet formation and a splashing-like phenomenon. As viscosity is increased, jet formation is suppressed and bubble deformation is restricted. Including viscoelastic effects, firstly in the form the Upper Convected Maxwell model, we find that during collapse jet formation can be prevented and a cusp can form on the bubble underside. This was also observed in the BEM study of Chapter 3, and results from a build up of (visco)elastic stresses near the wall. In this case large stress boundary layers can form, which can cause the solution to breakdown if the Weissenberg number exceeds a certain value. This upper bound on the Weissenberg number was found to increase with increasing distance from the wall. As is generally the case, the Oldroyd B proved able to support considerably higher Weissenberg numbers, due to the inclusion of a solvent viscous stress. As in the UCM case, predictions of the Oldroyd B model include cusp formation on the bubble underside and also larger amplitude oscillations in the jet velocity with increasing Weissenberg number. Once again, this behaviour was also predicted by the BEM study and has been well documented in other numerical studies of spherical bubble dynamics. It was found that increasing the compressibility of the two fluids (by decreasing the speed of sound) resulted in smaller inertial effects and smaller initial collapse velocities. The frequency of the os-

cillation of the bubble was also markedly reduced. Due to the smaller inertial effects, and subsequently smaller velocity gradients near the wall, the elastic boundary layers were also significantly smaller in magnitude. Consequently, because these layers are unable to grow enough in magnitude to induce numerical instability, there seems to be no upper limit on the Weissenberg number. There is however an "elastic" solution in the limit of large Weissenberg numbers, as the polymeric constitutive equation reduces to a simpler form. Similarly, an elastic limit was observed in the BEM study for the particular model used, and has also been predicted by other numerical/theoretical works on spherical bubble dynamics. A version of this chapter is in preparation for submission to the Journal of Computational Physics [93].

8.3 Model Comparisons

As already mentioned, the models are too different to expect good quantitative agreement. The first model assumes a 3D axisymmetric irrotational flow with viscoelastic effects included at the bubble surface, while the second model solves the 2D governing equations and employs an ideal gas equation of state for the fluid and bubble. However, despite these considerable differences, it is reassuring to see that both models predict the same qualitative behaviour, including:

- Increased amplitude bubble oscillations with increasing We, De.
- Jet prevention.
- The formation of a cusped bubble underside when near the wall.
- The existence of an elastic limit solution for large enough We, De.
- Identical responses to increases in viscosity or distance from the wall.

This helps to confirm that the findings presented in this thesis are a veracious account of viscoelastic bubble dynamics near a rigid wall.

Both models have their pros and cons. It can be argued that the second model provides a fuller description of the physics, by making no restrictions on the structure of the ambient flow. However, the more developed model can pose further modelling issues, such as determining an appropriate equation of state. The ideal gas equation is a less

than satisfactory choice. The model is also a two dimensional approximation to a three dimensional problem. Computationally, the BEM method is quick and efficient and requires little memory. Conversely, the spectral element marker particle method (SEMP) is computationally expensive and requires substantial computing resources due to the increased domain calculations and the large numbers of particles involved. Currently, without further parallelisation, the extension to a three dimensional system would be computationally prohibitive. As a free surface model, the BEM has the advantage that the bubble surface is a true density/pressure discontinuity, far more representative of real situations. The accurate surface discretisation also means that surface physics and boundary conditions can be included to a high degree of accuracy. In contrast, the bubble surface in the SEMP method is not well defined, and is essentially an average of the different fluid properties over a finite distance. Furthermore, from a numerical point of view, SEMP does not permit large discontinuities, for example in density, between phases. Spectral methods are at their most powerful when approximating problems that have smooth solutions, in which case exponential convergence can be achieved. A major advantage of the scheme however is the ability to handle topology changes, such as jet penetration and bubble break-up, with ease. Though possible with the BEM method, topology changes require cumbersome, ad-hoc mesh treatments.

The two methods developed in this thesis originate from two very different approaches in modelling multiphase flows. As mentioned, the fact they predict the same qualitative behaviour is an assurance that findings in this work are a faithful description of viscoelastic bubble dynamics. The above discussion highlights the fact that no method is perfect. In choosing to accurately or efficiently describe one aspect of your system, you sacrifice accuracy or efficiency elsewhere. This is one reason why multiphase flows remain the subject of intense research. They pose some of the greatest numerical and computational challenges in science and engineering, and will continue to do so, for many years to come.

8.4 Further Work

There is a great deal of scope for further work with both the boundary element and spectral element marker particle method. Work common to both studies, is firstly, the necessity to investigate dynamics for more complex rheological constitutive equations.

In this thesis the models were restricted to Maxwell/Oldroyd type in order to gain important initial insights into the role of viscoelasticity. There are a range of more physical constitutive equations which deserve investigation. Secondly, both methods need to be extended to include general multi-bubble configurations. Bubbles often form as a part of bubble clouds and, as highlighted in Chapter 4, bubble-bubble interaction is crucial in providing further insight into the mechanisms of cavitation damage. Ideally, this extension would include development to fully 3D models in both cases.

With regard to the BEM method only, further work includes the ability to model post-jet impact toroidal dynamics. This would allow computations to continue and permit phenomena such as the free surface jets that form under shock-waves (see Section 5.3.5, Chapter 5). For the second model, further work to be done includes an investigation into an appropriate thermodynamic equation of state. Indeed, a separate thermodynamic relation may need to be applied in each phase. With regard to the numerical scheme, improvements include the ability to support larger (and more realistic) density differences between the bubble and ambient fluid, while still being able to attain a satisfactory Weissenberg number. Perhaps including SUPG or similar schemes might be beneficial with regard to increasing the Weissenberg number limit.

Appendix A

Cubic Spline Construction

The cubic spline is an extremely effective tool in interpolation.

Given a set of points P_i, $i = 1, ..., (n+1)$ on surface S, q_i is cubic spline in $[P_1, P_{n+1}]$ if:

1. S, when restricted to $[P_i, P_{i+1}]$, is a polynomial of degree at most 3, and
2. $S \in C^2[P_1, P_{n+1}]$

Let $q_i(s)$ be defined parametrically w.r.t arclength s on $[P_i, P_{i+1}]$ by

$$q_i(s) = a_i(s - s_i)^3 + b_i(s - s_i)^2 + c_i(s - s_i) + d_i \tag{A.1}$$

for $i = 1, .., n$.
Then by point 2 above, the following conditions must be enforced:

1. $q_i(s_{i+1}) = q_{i+1}(s_{i+1})$ to ensure function continuity.
2. $q_i'(s_{i+1}) = q_{i+1}'(s_{i+1})$ to ensure continuity in the first derivative.
3. $q_i''(s_{i+1}) = q_{i+1}''(s_{i+1})$ to ensure continuity in the second derivative.

Therefore, applying these conditions to equation (1), gives the following restriction on the coefficients a_i, b_i, c_i, d_i,

$$\begin{aligned} d_{i+1} &= a_i\tilde{s}_i^3 + b_i\tilde{s}_i^2 + c_i\tilde{s}_i + d_i, \\ c_{i+1} &= 3a_i\tilde{s}_i^2 + 2b_i\tilde{s}_i + c_i, \\ b_{i+1} &= 3a_i\tilde{s}_i + b_i, \end{aligned} \tag{A.2}$$

where $\tilde{s}_i = s_{i+1} - s_i$.

A.1 Natural Spline

The natural cubic spline imposes a zero second derivative condition at the end points viz.,

$$q_1''(s_1) = 0 \tag{A.3}$$
$$q_n''(s_{n+1}) = 0. \tag{A.4}$$

This implies that $b_1 = 0$ and $3a_n\tilde{s}_n + b_n = 0$.
Substituting into (A.2) and rearranging, one can obtain a linear system of equations for b_i:

$$\begin{pmatrix} 2(\tilde{s}_1+\tilde{s}_2) & \tilde{s}_2 & 0 & & & 0 \\ \tilde{s}_2 & 2(\tilde{s}_2+\tilde{s}_3) & \tilde{s}_3 & & & 0 \\ 0 & & \ddots & & & \\ & & & \ddots & & \\ & & & \tilde{s}_{n-2} & 2(\tilde{s}_{n-2}+\tilde{s}_{n-1}) & \tilde{s}_{n-1} \\ & & & 0 & \tilde{s}_{n-1} & 2(\tilde{s}_{n-1}+\tilde{s}_n) \end{pmatrix} \begin{pmatrix} b_2 \\ b_3 \\ \vdots \\ \vdots \\ b_{n-1} \\ b_n \end{pmatrix} = 3 \begin{pmatrix} \tilde{d}_2 \\ \vdots \\ \vdots \\ \vdots \\ \vdots \\ \tilde{d}_n \end{pmatrix} \tag{A.5}$$

Where $\tilde{d}_i = \frac{d_{i+1}-d_i}{\tilde{s}_i} - \frac{d_i-d_{i-1}}{\tilde{s}_{i-1}}$, $i = 2, \ldots, n$.

A.2 Clamped Spline

The clamped cubic spline imposes a zero first derivative condition at the end points viz.,

$$q_1'(s_1) = 0 \tag{A.6}$$
$$q_n'(s_{n+1}) = 0. \tag{A.7}$$

Consequently, $c_1 = 0$ and $3a_n\tilde{s}_n^2 + 2b_n\tilde{s}_n + c_n = 0$. Substituting into (A.2) and rearranging yields the following linear system;

$$\begin{pmatrix} 2\tilde{s}_1 & \tilde{s}_1 & 0 & & & 0 \\ \tilde{s}_1 & 2(\tilde{s}_1+\tilde{s}_2) & \tilde{s}_2 & & & 0 \\ 0 & & \ddots & & & \\ & & & \ddots & & \\ & & & \tilde{s}_{n-1} & 2(\tilde{s}_{n-1}+\tilde{s}_n) & \tilde{s}_n \\ & & & 0 & \tilde{s}_n & 2\tilde{s}_n \end{pmatrix} \begin{pmatrix} b_1 \\ b_2 \\ \vdots \\ \vdots \\ b_n \\ b_{n+1} \end{pmatrix} = 3 \begin{pmatrix} \frac{d_2-d_1}{\tilde{s}_1} \\ \vdots \\ \tilde{d}_i \\ \vdots \\ \vdots \\ \frac{d_n-d_{n+1}}{\tilde{s}_n} \end{pmatrix} \tag{A.8}$$

The above tri-diagonal systems can be solved with ease and efficiency for b_i using the Thomas algorithm [123]. The remaining spline coefficients can then be found from substitution into (A.2).

Appendix B

Treatment of the Logarithmic Singularity in the Boundary Integral

As mentioned in Section 2.3, the azimuthal integration of the Green's function $G(\mathbf{p}, \mathbf{q})$ and its normal derivative can be calculated analytically and give

$$\int_0^{2\pi} G \, d\theta = \frac{4r(s)K(k(s))}{[(r(s)+r_i)^2 + (z(s)-z_i)^2]^{1/2}}, \tag{B.1}$$

and

$$\int_0^{2\pi} \frac{\partial G}{\partial n} \, d\theta = \\ -4\frac{r}{[(r+r_i)^2 + (z-z_i)^2]^{3/2}} \left(\left[\frac{dz}{ds}(r+r_i) - \frac{dr}{ds}(z-z_i) - \frac{2r_i}{k^2}\frac{dz}{ds} \right] \frac{E(k)}{1-k^2} + \frac{2r_i}{k^2}\frac{dz}{ds}K(k) \right), \tag{B.2}$$

where

$$k^2(s) = \frac{4r(s)r_i}{(r(s)+r_i)^2 + (z(s)-z_i)^2}, \tag{B.3}$$

and $K(k)$ and $E(k)$ are complete elliptical integrals of the first and second kind, respectively. These integrals are approximated by

$$K(k) = P(1-k^2) - Q(1-k^2)\log(1-k^2), \tag{B.4}$$

$$E(k) = R(1-k^2) - S(1-k^2)\log(1-k^2), \tag{B.5}$$

where P, Q, R, S are tabulated polynomials [1].

From equation (B.3) we can see that if collocation point $(r_i, z_i) = (r(s), z(s))$ then $k^2 = 1$ and a logarithmic singularity will occur in the elliptical integrals $K(k)$ and $E(k)$. Evidently, this will only occur if the collocation point lies on a segment over with we want to integrate - and then only at the endpoints of the segment. To demonstrate this we consider the singularity at the point $(r(s_j), z(s_j))$ over segment $\triangle s = s_{j+1} - s_j$. To deal with this singularity the logarithm in (B.4) is split into a singular and non-singular contribution viz.

$$\log(x) = \log\left(\frac{x}{((s-s_j)/\triangle s)^2}\right) + 2\log((s-s_j)/\triangle s), \tag{B.6}$$

where $x = 1-k^2$. The singular contribution is now contained in the second term on the right hand side of (B.6). Substituting (B.6) into (B.4) and subsequently into integrals (B.1) and (B.2), one is then able to factor out the singular component. For example,

$$\int_{s_j}\int_0^{2\pi} G\, d\theta = \int_{s_j} \frac{4r(s)}{[(r(s)+r_i)^2 + (z(s)-z_i)^2]^{1/2}} \left(P - Q\log\left(\frac{x}{((s-s_j)/\triangle s)^2}\right)\right) ds + \int_{s_j} \frac{8r(s)}{[(r(s)+r_i)^2 + (z(s)-z_i)^2]^{1/2}} \left(P - Q\log\left((s-s_j)/\triangle s\right)\right) ds \tag{B.7}$$

The first integral is not singular and can be treated with standard Gaussian quadrature. The second integral can be integrated using a special quadrature scheme that incorporates the singularity; the details of which (the appropriate quadrature points and weights) are found in [142].

Bibliography

[1] M. Abramowitz and I. A. Stegun. *Handbook of Mathematical Functions*. Dover, 1965.

[2] J.S. Allen and R.A. Roy. Dynamics of gas bubbles in viscoelastic fluids. Linear viscoelasticity. *J. Acoust. Soc. of Am.*, 107(6):3167–3178, 2000.

[3] M. T. Arigo and G. H. McKinley. An experimental investigation of negative wakes behind spheres settling in a shear-thinning viscoelastic fluid. *Rheol Acta*, 37:307–327, 1998.

[4] V. Ashworth and R. P. M. Procter. Cavitation in dilute polymer solutions. *Nature*, 258, 1975.

[5] G. Astarita. Spherical gas bubble motion through Maxwell liquids. *Ind. Eng. Chem. Fundamen.*, 5(4):548–553, 1966.

[6] G. Astarita and G. Apuzzo. Motion of gas bubbles in non-Newtonian liquids. *A.I.Ch.E Journal*, 11(5):815–820, 1965.

[7] G. K. Batchelor. *An introduction to Fluid Dynamics*. Cambridge University Press, 1967.

[8] D. W. Beard and K. Walters. Elastico-viscous boundary-layer flows. I. Two-dimensional flow near a stagnation point. *Proc. Camb. Phil. Soc.*, 60:667, 1964.

[9] T. B. Benjamin and A. T. Ellis. The collapse of cavitation bubbles and the pressures thereby produced against solid boundaries. *Phil. Trans. R. Soc. Lond. A*, 260:221, 1966.

[10] J.P. Best. The formation of toroidal bubbles upon the collapse of transient cavities. *J. Fluid Mech.*, 251:79–107, 1993.

[11] J.P. Best and A. Kucera. A numerical investigation of non-spherical rebounding bubbles. *J. Fluid Mech.*, 245:137–154, 1992.

[12] F. Bierbrauer. *Mathematical modelling of water-droplet impact on hot galvanised steel surfaces.* PhD thesis, University of Wollongong, Australia, 2004.

[13] F. Bierbrauer and T. N. Phillips. The numerical prediction of droplet deformation and break-up using the Godunov marker-particle projection scheme. *Int. J. Num. Meth. Fluids*, 58(8):1155–1160, 2007.

[14] F. Bierbrauer and S. Zhu. A numerical model for multiphase flow based on the GMPPS formulation. Part I: Kinematics. *Comput. Fluids*, 36:1199–1212, 2007.

[15] R.B. Bird, R.C. Armstrong, and O. Hassager. *Dynamics of Polymeric Liquids.* John Wiley & Sons, 1987.

[16] J. R. Blake, P. B. Robinson, A. Shima, and Y. Tomita. Interaction of two cavitation bubbles with a rigid boundary. *J. Fluid Mech.*, 255:707–721, 1993.

[17] J.R. Blake and D.C Gibson. Growth and collapse of a vapour cavity near a free surface. *J. Fluid Mech.*, 111:123–140, 1981.

[18] J.R. Blake and D.C. Gibson. Cavitation bubbles near boundaries. *Ann. Rev. Fluid Mech.*, 19:99–123, 1989.

[19] J.R. Blake, B.B. Taib, and G. Doherty. Transient cavities near boundaries. Part 1. Rigid boundary. *J. Fluid Mech.*, 170:479–497, 1986.

[20] J.R. Blake, B.B. Taib, and G. Doherty. Transient cavities near boundaries. Part 2. Free surface. *J. Fluid Mech.*, 181:197–212, 1987.

[21] J.R. Blake, Y. Tomita, and R.P. Tong. The art, craft and science of modelling jet impact in a collapsing cavitation bubble. *App. Sci. Res.*, 58:77–90, 1998.

[22] P. C. Bollada and T. N. Phillips. On the effects of a compressible viscous lubricant on the load-bearing capacity of a journal bearing. *Int. J. Num. Meth. Fluids*, 55:1091–1120, 2007.

[23] P. C. Bollada and T. N. Phillips. An anisothermal, compressible, piezoviscous model for journal bearing lubrication. *Int. J. Num. Meth. Fluids*, 58:27–55, 2008.

[24] J. M. Boulton-Stone. *Application of boundary integral methods to rising and bursting bubbles*. PhD thesis, University of Birmingham, 1993.

[25] J. M. Boulton-Stone. The effect of surfactants on bursting gas bubbles. *J. Fluid Mech.*, 302:231–257, 1995.

[26] J. M. Boulton-Stone and J. R. Blake. Gas bubbles bursting at a free surface. *J. Fluid Mech.*, 254:437–466, 1993.

[27] J. M. Boulton-Stone, P. B. Robinson, and J. R. Blake. A note on the axisymmetric interaction of pairs of rising, deforming gas bubbles. *Int. J. Multiphase Flow*, 21(6):1237–1241, 1995.

[28] D. C. Brabston. *Part I. Numerical solutions of steady viscous flow past spheres and gas bubbles*. PhD thesis, California Institute of Technology, 1974.

[29] C.E. Brennen. *Cavitation and Bubble Dynamics*. Oxford University Press, 1995.

[30] E. A. Brujan. A first order model for bubble dynamics in a compressible viscoelastic liquid. *J. Non-Newtonian Fluid Mech.*, 84:83–103, 1999.

[31] E. A. Brujan. The equation of bubble dynamics in a compressible linear viscoelastic liquid. *Fluid Dynamics Research*, 29:287–294, 2001.

[32] E. A. Brujan. Cavitation bubble dynamics in non-Newtonian fluids. *Polymer Engineering and Science*, 49:419–431, 2009.

[33] E. A. Brujan, A. F. H. Al-Hussany, R. L. Williams, and P. R. Williams. Cavitation erosion in polymer aqueous solutions. *Wear*, 264:1035–1042, 2008.

[34] E. A. Brujan, T. Ikeda, and Y. Matsumoto. Dynamics of ultrasound-induced cavitation bubbles in non-Newtonian liquids and near a rigid boundary. *Phys. Fluids*, 16:2402, 2004.

[35] E. A. Brujan, K. Nahen, P. Schmidt, and A. Vogel. Dynamics of laser-induced cavitation bubbles near an elastic boundary. *J. Fluid Mech.*, 433:251–281, 2001.

[36] E. A. Brujan, K. Nahen, P. Schmidt, and A. Vogel. Dynamics of laser-induced cavitation bubbles near an elastic boundary: influence of the elastic modulus. *J. Fluid Mech.*, 433:283–314, 2001.

[37] E. A. Brujan, C. D. Ohl, W. Lauterborn, and A. Philipp. Dynamics of laser-induced cavitation bubbles in polymer solutions. *Acustica*, 82:423–430, 1996.

[38] E. A. Brujan, A. Pearson, and J. R. Blake. Pulsating, buoyant bubbles close to a rigid boundary and near the null final Kelvin impulse state. *Int. J. Multiphase Flow*, 31:302–317, 2005.

[39] B. Bunner and G. Tryggvason. Dynamics of homogeneous bubbly flows Part 1. Rise velocity and microstructure of the bubbles. *J. Fluid Mech.*, 466:17–52, 2002.

[40] E. Canot and L. Davoust. Numerical simulation of the buoyancy-driven bouncing of a 2D bubble at a horizontal wall. *Theor. Comput. Fluid Dyn.*, 17:51–72, 2003.

[41] G. L. Chahine and D. Fruman. Dilute polymer solution effects on bubble growth and collapse. *Phys. Fluids*, 22:1406–1407, 1979.

[42] A. J. Coleman, J. E. Saunders, L. A. Crum, and M. Dyson. Acoustic cavitation generated by an extracorporeal shock wave lithotripter. *Ultrasound in medicine and biology*, 13(2):69–76, 1987.

[43] N. Curle and H. J. Davies. *Modern Fluid Dynamics*, volume 1. D. Van Nostrand, 1968.

[44] D. Dawson and C. M. Taylor. Cavitation in bearings. *Ann. Rev. Fluid Mech.*, 11:35–66, 1979.

[45] M. M. Denn. Boundary layer flows for a class of elastic fluids. *Chem. Eng. Sci.*, 22(3):395–405, 1967.

[46] D. G. Dommermuth and D. K. P. Yue. Numerical simulation of nonlinear axisymmetric flows with a free surface. *J. Fluid Mech.*, 178:195–219, 1987.

[47] M. Dular, B. Bachert, B. Stoffel, and B. Sirok. Relationship between cavitation structures and cavitation damage. *Wear*, 257(11):1176–1184, 2004.

[48] B. J. Edwards and A. N. Beris. Remarks concerning compressible viscoelastic fluid models. *J. Non-Newtonian Fluid Mech.*, 36:411–417, 1990.

[49] M. Gad el Hak. Questions in fluid mechanics: Stoke's hypothesis for a Newtonian, isotropic fluid. *J. Fluids Eng.*, 117:3–5, 1995.

[50] A. T. Ellis and R. Y. Ting. Non-Newtonian effects on flow generated cavitation in a pressure field. *Fluid Mechanics Acoustics and Design of Turbomachinery*, (1):403–421, 1974.

[51] A. Evan, L. Willis, J. McAteer, M. Bailey, B. Connors, Y. Shao, J. Lingeman, J. Williams Jr., N. Fineberg, and L. Crum. Kidney damage and renal functional changes are minimized by waveform control that suppresses cavitation in shock wave lithotripsy. *J. Urology*, 4(1):1556–1562, 2002.

[52] N. Fiétier and M. O. Deville. Time-dependent algorithms for the simulation of viscoelastic flows with spectral methods: applications and stability. *J. Comput. Phys.*, 186:93–121, 2003.

[53] H. S. Fogler and J. D. Goddard. Oscillations of a gas bubble in viscoelastic liquids subject to acoustic and impulsive pressure variations. *J. Appl. Phys.*, 42(1):259–263, 1971.

[54] H.S. Fogler and J.D. Goddard. Collapse of spherical cavities in viscoelastic fluids. *Phys. Fluids*, 13(5):1135–1141, 1970.

[55] X. Frank and H. Z. Li. Complex flow around a bubble rising in a non-Newtonian fluid. *Phys. Rev. E*, 71:036309, 2005.

[56] T. Funada and D. D. Joseph. Viscous potential flow analysis of capillary instability. *Int. J. Multiphase Flow*, 28(9), 2002.

[57] T. Funada and D. D. Joseph. Viscoelastic potential flow analysis of capillary instability. *J. Non-Newtonian Fluid Mech.*, 111:87–105, 2003.

[58] D. Funfschilling and H. Z. Li. Flow of non-Newtonian fluids around bubbles: PIV measurements and birefringence visualisation. *Chemical Engineering Science*, 56:1137–1141, 2001.

[59] X. Gao. A promising boundary element formulation for three dimensional viscous flow. *Int. J. Numer. Meth. Fluids*, 47:19–43, 2005.

[60] S.-C. Georgescu, J.-L. Achard, and E. Canot. Jet drops ejection in bursting gas bubble processes. *Euro. J. Mech. B/Fluids*, 21:265–280, 2002.

[61] D. Gueyffier, J. Li, A. Nadim, R. Scardovelli, and S. Zaleski. Volume of fluid interface tracking with smoothed surface stress methods for three dimensional flows. *J. Comput. Phys.*, 152:423–456, 1999.

[62] J. Hadamard. Movement permanent lent d'une sphere liquide et visqueuse dans un liquide visqueux. *Comptes Rendus*, 152:1735, 1911.

[63] O. G. Harlen. The negative wake behind a sphere sedimenting through a viscoelastic fluid. *J. Non-Newtonian Fluid Mech.*, 108:411–430, 2002.

[64] F. H. Harlow and J. E. Welch. Numerical calculation of time-dependent viscous incompressible flow of fluid with a free surface. *Phys. Fluids.*, 8:2182–2189, 1965.

[65] O. Hassager. Negative wake behind bubbles in non-Newtonian liquids. *Nature*, 279:402, 1979.

[66] J. R. Herrera-Velarde, R. Zenit, D. Chehata, and B. Mena. The flow of non-Newtonian fluids around bubbles and its connection to the jump discontinuity. *J. Non-Newtonian Fluid Mech.*, 111:199–209, 2003.

[67] C. W. Hirt and B. D. Nichols. Volume of fluid (VOF) methods for the dynamics of free boundaries. *J. Comput. Phys.*, 39:201–225, 1981.

[68] D. D. Joseph. *Fluid Dynamics of Viscoelastic Liquids*. Springer-Verlag, 1990.

[69] D. D. Joseph. Rise velocity of a spherical cap bubble. *J. Fluid Mech.*, 488:213–223, 2003.

[70] D. D. Joseph. Potential flow of viscous fluids: Historical notes. *Int. J. Multiphase Flow*, 32:285–310, 2006.

[71] D. D. Joseph, G. S. Beavers, and T. Funada. Rayleigh-Taylor instability of viscoelastic drops at high Weber numbers. *J. Fluid Mech.*, 453:109–132, 2002.

[72] D.D. Joseph and T.Y. Liao. Potential flows of viscous and viscoelastic fluids. *J. Fluid Mech.*, 265:1–23, 1994.

[73] M. Kemiha, X. Frank, S. Poncin, and H.Z. Li. Origin of the negative wake behind a bubble rising in non-Newtonian fluids. *Chemical Engineering Science*, 61:4041–4047, 2006.

[74] I. J. Keshtiban, F. Belblidia, and M. F. Webster. Numerical simulation of compressible viscoelastic liquids. *J. Non-Newtonian Fluid Mech.*, 122:131–146, 2004.

[75] R. E. Khayat. A boundary element analysis of multiply connected three dimensional cavity mixing flow of polymer solutions. *Int. J. Numer. Meth. Fluids*, 31:1173–1194, 1999.

[76] R. E. Khayat. Three-dimensional boundary element analysis of drop deformation in confined flow for Newtonian and viscoelastic systems. *Int. J. Numer. Meth. Fluids*, 34:241–275, 2000.

[77] R. E. Khayat and K. Marek. An adaptive boundary element approach to 3D transient free-surface flow of viscous fluids. *Engineering Analysis with Boundary Elements*, 23:111–122, 1999.

[78] C. Kim. Collapse of spherical cavities in Maxwell fluids. *J. Non-Newtonian Fluid Mech.*, 55:37–58, 1994.

[79] S. J. Kim, K. H. Lim, and C. Kim. Deformation characteristics of spherical bubble collapse in Newtonian fluids near the wall using the finite element method with ALE formulation. *Korea-Australia Rheol. J.*, 18(2):109–118, 2006.

[80] E. Klaseboer, K. C. Hung, C. Wang, C. W. Wang, B. C. Khoo, P. Boyce, S. Debono, and H. Charlier. Experimental and numerical investigation of the dynamics of an underwater explosion bubble near a resilient/rigid structure. *J. Fluid Mech.*, 537:387–413, 2005.

[81] E. Klaseboer and B. C. Khoo. Boundary integral equations as applied to an oscillating bubble near a fluid-fluid interface. *Computat. Mech.*, 33(2):129–138, 2004.

[82] E. Klaseboer and B. C. Khoo. An oscillating bubble near an elastic material. *J. Appl. Phys.*, 96(10):5808, 2004.

[83] E. Klaseboer, C. Turangan, S. W. Fong, T. G. Liu, K. C. Hung, and B. C. Khoo. Simulations of pressure pulse-bubble interaction using boundary element method. *Comput. Meth. Appl. Mech. Eng.*, 195:4287–4302, 2006.

[84] K. T. Knapp, J. W. Daily, and F. G. Hammitt. *Cavitation*. McGraw-Hill, 1970.

[85] T. Kodama and K. Takayama. Dynamic behavior of bubbles during extracorporeal shock-wave lithotripsy. *Ultrasound in medicine and biology*, 24(5):723–738, 1998.

[86] W. Lauterborn and H. Bolle. Experimental investigations of cavitation-bubble collapse in the neighbourhood of a solid boundary. *J. Fluid Mech.*, 72(2):391–399, 1975.

[87] M. Lee, E. Klaseboer, and B. C. Khoo. On the boundary integral method for the rebounding bubble. *J. Fluid Mech.*, 507:407–429, 2007.

[88] V. G. Levich. The motion of bubbles at high Reynolds numbers. *Zh. Eksp. Teor. Fiz.*, 19:8, 1949.

[89] J. Li. General explicit difference formulas for numerical differentiation. *J. Comput. Appl. Math.*, 183:29–52, 2005.

[90] S. J. Lind and T. N. Phillips. The effect of viscoelasticity on a rising gas bubble. *J. Non-Newtonian Fluid Mech.*, doi:10.1016/j.jnnfm.2010.04.002, 2010.

[91] S. J. Lind and T. N. Phillips. The effect of viscoelasticity on bubble dynamics near a free surface. *J. Fluid Mech. (in preparation)*, 2010.

[92] S. J. Lind and T. N. Phillips. The influence of viscoelasticity on the collapse of cavitation bubbles near a rigid boundary. *Submitted to Theor. Comput. Fluid Dyn.*, 2010.

[93] S. J. Lind and T. N. Phillips. Predictions of bubble dynamics using a spectral element marker particle method. *J. Comput. Phys. (in preparation)*, 2010.

[94] S. J. Lind and T. N. Phillips. Spherical bubble collapse in viscoelastic fluids. *J. Non-Newtonian Fluid Mech.*, 165:56–64, 2010.

[95] Y. J. Liu, T. Y. Liao, and D. D. Joseph. A two-dimensional cusp at the trailing edge of an air bubble rising in a viscoelastic liquid. *J. Fluid Mech.*, 304:321–342, 1995.

[96] D. Lohse, B. Schmitz, and M. Versluis. Snapping shrimp make flashing bubbles. *Nature*, 413:477–478, 2001.

[97] M. S. Longuet-Higgins and E. D. Cokelet. The deformation of steep surface waves on water. I. A numerical method of computation. *Proc. R. Soc. Lond. A.*, 350:1–26, 1976.

[98] J. López, J. Hernández, P. Gómez, and F. Faura. A volume of fluid method based on multidimensional advection and spline interface reconstruction. *J. Comput. Phys.*, 195:718–742, 2004.

[99] J. Lu, A. Fernndez, and G. Tryggvason. The effect of bubbles on the wall drag in a turbulent channel flow. *Phys. Fluids.*, 17, 2005.

[100] T. S. Lundgren and N. N. Mansour. Vortex ring bubbles. *J. Fluid Mech.*, 224:177–196, 1991.

[101] C. W. Macosko. *Rheology - Principles, measurements, and applications.* Wiley-Vch, 1994.

[102] C. Málaga and J. M. Rallison. A rising bubble in a polymer solution. *J. Non-Newtonian Fluid Mech.*, 141:59–78, 2007.

[103] F. Mashayek and N. Ashgriz. A hybrid finite-element-volume-of-fluid method for simulating free surface flows and interfaces. *Int. J. Num. Meth. Fluid.*, 20:1363–1380, 1995.

[104] S. Matušů-Nečasová, A. Sequeira, and J. H. Videman. Existence of classical solutions for compressible viscoelastic fluids of Oldroyd type past an obstacle. *Math. Meth. Appl. Sci.*, 22:449–460, 1999.

[105] M. J. Miksis, J.-M. Vanden-Broeck, and J. B. Keller. Rising bubbles. *J. Fluid Mech.*, 123:31–41, 1982.

[106] D. W. Moore. The rise of gas bubble in a viscous liquid. *J. Fluid Mech.*, 6:113–130, 1959.

[107] D. W. Moore. The boundary layer on a spherical gas bubble. *J. Fluid Mech.*, 16:161–176, 1963.

[108] W. F. Noh and P. Woodward. *Lecture notes in Physics*, volume 59, chapter SLIC (simple line interface calculation), pages 330–340. Springer, 1976.

[109] J. G. Oldroyd. On the formulation of rheological equations of state. *Proc. R. Soc. Lond. A*, 200(1063):523–541, 1950.

[110] J. G. Oldroyd. Note on the hydrodynamic and thermodynamic pressures. *Proc. R. Soc. Lond. A*, 226:57–58, 1954.

[111] S. Osher and J. A. Sethian. Fronts propagating with curvature-dependent speed: Algorithms based on Hamilton-Jacobi formulations. *J. Comput. Phys.*, 79(1):12–49, 1988.

[112] R. G. Owens and T. N. Phillips. *Computational Rheology*. Imperial College Press, 2005.

[113] F. Paris and J. Canas. *Boundary Element Method Fundamentals and Applications*. Oxford University Press, 1997.

[114] A. Pearson, E. Cox, J.R. Blake, and S.R. Otto. Bubble interactions near a free surface. *Engineering analysis with boundary elements*, 28:295–313, 2004.

[115] A. Philipp and W. Lauterborn. Cavitation erosion by single laser-produced bubbles. *J. Fluid Mech.*, 361:75–116, 1998.

[116] S. B. Pillapakkam and P. Singh. A level-set method for computing solutions to viscoelastic two-phase flow. *J. Comput. Phys.*, 174:552–578, 2001.

[117] S. B. Pillapakkam, P. Singh, D. Blackmore, and N. Aubry. Transient and steady state of a rising bubble in a viscoelastic fluid. *J. Fluid Mech.*, 589:215–252, 2007.

[118] C. Pilz and G. Brenn. On the critical bubble volume at the rise velocity jump discontinuity in viscoelastic fluids. *J. Non-Newtonian Fluid Mech.*, 145:124–138, 2007.

[119] M. Plesset and R. Chapman. Collapse of an initially spherical vapour cavity in the neighbourhood of a solid boundary. *J. Fluid Mech.*, 47(2):283–290, 1971.

[120] M. S. Plesset. The dynamics of cavitation bubbles. *ASME J. Appl. Mech.*, 16:228–231, 1949.

[121] S. Popinet and S. Zaleski. Bubble collapse near a solid boundary: a numerical study of the influence of viscosity. *J. Fluid Mech.*, 464:137–163, 2002.

[122] C. Pozrikidis. Three-dimensional oscillations of rising bubbles. *Engineering Analysis with Boundary Elements*, 28:315–323, 2004.

[123] W. H. Press, B. P. Flannery, S. A. Teukolsky, and W. T. Vetterling. *Numerical Recipes*. Cambridge University Press, 1988.

[124] A. Prosperetii and G. Tryggvason. *Computational Methods for Multiphase flow*. Cambridge University Press, 2007.

[125] R. K. Prud'homme and R. B. Bird. The dilatational properties of suspensions of gas bubbles in incompressible Newtonian and non-Newtonian fluids. *J. Non-Newtonian Fluid Mech.*, 3:261–279, 1978.

[126] Lord Rayleigh. On the pressure developed in a liquid during the collapse of a spherical cavity. *Phil. Mag.*, 34:94–98, 1917.

[127] M. Renardy. *Mathematical analysis of viscoelastic flows*. SIAM, 2000.

[128] W. J. Rider and D. B. Kothe. A marker particle method for interface tracking. *6th ISCFD conference paper*, 1995.

[129] W. J. Rider and D. B. Kothe. Stretching and tearing interface tracking methods. Technical report, Los Alamos National Laboratory, 1995.

[130] W. J. Rider and D. B. Kothe. Reconstructing volume tracking. *J. Comput. Phys.*, 141:112–152, 1998.

[131] P. B. Robinson, J. M. Boulton-Stone, and J. R. Blake. Application of the boundary integral method to the interaction of rising two-dimensional deformable gas bubbles. *J. Eng. Math.*, 29:393–412, 1995.

[132] P.B. Robinson, J.R. Blake, T. Kodama, A. Shima, and Y. Tomita. Interaction of a cavitation bubble with a free surface. *J. Appl. Phys.*, 89(12):8225–37, 2001.

[133] D. Rodrigue, D. De Kee, and C. F. Chan Man Fong. An experimental study of the effect of surfactants on the free rise velocity of gas bubbles. *J. Non-Newtonian Fluid Mech.*, 66:213–232, 1996.

[134] D. Rodrigue, D. De Kee, and C. F. Chan Man Fong. Bubble velocities: further developments on the jump discontinuity. *J. Non-Newtonian Fluid Mech.*, 79:45–55, 1998.

[135] B.M. Rush and A. Nadim. The shape oscillations of a two-dimensional drop including viscous effects. *Engineering Analysis with Boundary Elements*, 24:43–51, 2000.

[136] W. Rybzynski. Über die fortschreitende bewegung einer flüssigen kugel in einem zähen medium. *Bull. Acad. Sci. Cracovie*, A:40, 1911.

[137] G. Ryskin and L. G. Leal. Numerical solution of free-boundary problems in fluid mechanics. Part 2. Buoyancy-driven motion of a gas bubble through a quiescent liquid. *J. Fluid Mech.*, 148:19–35, 1984.

[138] A. Shima, K. Takayama, Y. Tomita, and N. Miura. An experimental study on effects of a solid wall on the motion of bubbles and shock waves in bubble collapse. *Acustica*, 48:293–301, 1981.

[139] A. Shima, T. Tsujino, H. Nanjo, and N. Miura. Cavitation damage in polymer aqueous solutions. *J. Fluids Eng.*, 107:134–138, 1985.

[140] E. Soto, C. Goujon, R. Zenit, and O. Manero. A study of velocity discontinuity for single air bubbles rising in an associative polymer. *Phys. Fluids*, 18:121510, 2006.

[141] G. G. Stokes. On the effect of the internal friction of fluids on the motion of pendulums. *Trans. Camb. Phil. Soc.*, 9:8, 1851.

[142] A. H. Stroud and D. Secrest. *Gaussian Quadrature Formulas*. Prentice Hall, 1966.

[143] R. Sureshkumar. Stability analysis using compressible viscoelastic formulation. *J. Non-Newtonian Fluid Mech.*, 116:471–477, 2004.

[144] M. Sussman, E. Fatemi, P. Smereka, and S. Osher. An improved level set method for incompressible two-phase flows. *Comput. Fluids*, 27(5-6):663–680, 1998.

[145] M. Sussman and P. Smereka. Axisymmetric free boundary problems. *J. Fluid Mech.*, 341:269–294, 1997.

[146] B. B. Taib. *Boundary integral methods applied to cavitation bubble dynamics*. PhD thesis, University of Wollongong, Australia, 1985.

[147] E. Taliadoroua, G. C. Georgioua, and I. Moulitsas. Weakly compressible Poiseuille flows of a Herschel-Bulkley fluid. *J. Non-Newtonian Fluid Mech.*, 158:162–169, 2009.

[148] I. Tanasawa and W. J. Yang. Dynamic behaviour of a gas bubble in viscoelastic liquids. *J. Appl. Phys.*, 41(11):4526–4531, 1970.

[149] L. Tisza. Supersonic absorption and Stokes' viscosity relation. *Phys. Rev.*, 61:531, 1942.

[150] Y. Tomita, P.B. Robinson, R.P. Tong, and J.R. Blake. Growth and collapse of cavitation bubbles near a curved rigid boundary. *J. Fluid Mech.*, 466:259–283, 2002.

[151] R. P. Tong. The role of 'splashing' in the collapse of a laser-generated cavity near a rigid boundary. *J. Fluid Mech.*, 380:339–361, 1999.

[152] C. Truesdell. The present status of the controversy regarding the bulk viscosity of fluids. *Proc. R. Soc. Lond. A*, 226:59–65, 1954.

[153] C. Truesdell. *Continuum Mechanics I. The Mechanical Foundations of Elasticity and Fluid Mechanics.* Gordon and Breach, 1966.

[154] G. Tryggvason, B. Bunner, A. Esmaeeli, D. Juric, N. Al-Rawahi, W. Tauber, J. Han, S. Nas, and Y.-J. Jan. A front tracking method for the computations of multiphase flow. *J. Comput. Phys.*, 169:708–759, 2001.

[155] C. K. Turangan, G. P. Ong, E. Klaseboer, and B. C. Khoo. Experimental and numerical study of transient bubble-elastic membrane interaction. *J. Appl. Phys.*, 100(054910), 2006.

[156] S. O. Unverdi and G. Tryggvason. A front-tracking method for viscous, incompressible, multi-fluid flows. *J. Comput. Phys.*, 100:25–37, 1992.

[157] R. G. M. van Os and T. N. Phillips. Spectral element methods for transient viscoelastic flow problems. *J. Comput. Phys.*, 201:286–314, 2004.

[158] A. Vogel, W. Lauterborn, and R. Timm. Optical and acoustic investigations of the dynamics of laser-produced cavitation bubbles near a solid boundary. *J. Fluid Mech.*, 206:299–338, 1989.

[159] A. J. Wagner, L. Giraud, and C. E. Scott. Simulation of a cusped bubble rising in a viscoelastic fluid with a new numerical method. *Comput. Phys. Comm.*, 129:227–232, 2000.

[160] Q. X. Wang, K. S. Yeo, B. C. Khoo, and K. Y. Lam. Nonlinear interaction between gas bubble and free surface. *Computers and fluids*, 25(7), 1996.

[161] Q. X. Wang, K. S. Yeo, B. C. Khoo, and K. Y. Lam. Strong interaction between a buoyancy bubble and a free surface. *Theor. Comput. Fluid Dyn.*, 8:73–88, 1996.

[162] N. D. Waters and M. J. King. Unsteady flow of an elastico-viscous liquid. *Rheol. Acta*, 9:345–355, 1970.

[163] P. P. Wegener and J-Y. Parlange. Spherical cap bubbles. *Annu. rev. Fluid Mech.*, 5:79–100, 1973.

[164] P. R. Williams, P. M. Williams, and S. W. J. Brown. A technique for studying liquid jets by cavitation bubble collapse under shockwaves, near a free surface. *J. Non-Newtonian Fluid Mech.*, 72:101–110, 1997.

[165] P. R. Williams, P. M. Williams, and S. W. J. Brown. A study of liquid jets formed by bubble collapse under shock waves in elastic and Newtonian liquids. *J. Non-Newtonian Fluid Mech.*, 76:307–325, 1998.

[166] J. Wu and W. L. Nyborg. Ultrasound, cavitation bubbles and their interaction with cells. *Advanced drug delivery reviews*, 60:1103–1116, 2008.

[167] W. Q. Xi. Numerical simulation of violent bubble motion. *Phys. Fluids*, 16(5):1610–1919, 2004.

[168] X. Yang, A. J. James, J. Lowengrub, X. Zheng, and V. Cristini. An adaptive coupled level-set/volume-of-fluid interface capturing method for unstructed triangular grids. *J. Comput. Phys.*, 217:364–394, 2006.

[169] K. Yokoi. Efficient implementation of THINC scheme: A simple and practical smoothed VOF algorthim. *J. Comput. Phys.*, 226:1985–2002, 2007.

[170] S. Zhang, J.H. Duncan, and G.L. Chanine. The final stage of the collapse of a cavitation bubble near a rigid wall. *J. Fluid Mech.*, 257:147–181, 1993.

[171] Z. Zhang and H. Zhang. Surface tension effects on the behaviour of a cavity growing, collapsing, and rebounding near a rigid wall. *Physical Review E*, 70, 2004.

[172] Z. Zhang and H. Zhang. Surface tension effects on the behaviour of two cavities near a rigid wall. *Physical Review E*, 71, 2005.